ENERGY DISSIPATION IN ORTHOGONAL ULTRA-PRECISION MACHINING OF DUCTILE MATERIALS

By

YONGWIE SEO

Bachelor of Science in Engineering
The Korea University
Seoul, Korea
1976

Master of Science in Engineering
The Ohio State University
Columbus, Ohio
1990

Submitted to the Faculty of the
Graduate College of the
Oklahoma State University
in partial fulfillment of
the requirements for
the Degree of
DOCTOR OF PHILOSOPHY
May, 1993

ENERGY DISSIPATION IN ORTHOGONAL
ULTRA-PRECISION MACHINING
OF DUCTILE MATERIALS

Thesis Approved:

Don A. Lucca
Thesis Adviser

Dean of the Graduate College

To my Father, Mother,

Wife,

Son, and Daughter

For

Their Sacrifices, Support,

and Encouragement

ACKNOWLEDGMENTS

The author expresses his deepest gratitude and sincere appreciation to his advisor, Dr. Don A. Lucca. His exceptional guidance and warm encouragement throughout this research have been invaluable. The helpful advice and suggestions of the other committee members, Drs. Ranga Komanduri, Peter M. Moretti, John W. Nazemetz, and Yuh-Cheng Shiau, are also gratefully appreciated. The author also expresses his appreciation to William L. Edwards, S. Craig Dickson and Perry Bowen for their help in diamond tool edge characterization.

The author gratefully acknowledges the financial support of the Division of Design and Manufacturing Systems of the National Science Foundation through Grant No. DDM-8909489. Thanks also go to the School of Mechanical and Aerospace Engineering and the Oklahoma Center for Advancement of Science and Technology (OCAST) for their support. Research support from the National Center for Super Computing Applications is gratefully acknowledged.

Special gratitude is expressed to the author's father, Jongsup Seo, and his late mother, Insoon Moon, his wife, Eunja Kim, proud son, Sunghun, and pretty daughter, Alice (Aera). Their countless sacrifices and years of patience have helped him throughout this study.

TABLE OF CONTENTS

Chapter Page

Chapter Page

LIST OF TABLES

LIST OF FIGURES

Figure Page

Figure Page

Figure Page

Figure Page

Figure Page

Figure Page

Figure Page

NOMENCLATURE

b	half width
C	wave speed
E	Young's modulus
F	force
f	function
k	flow stress
K	thermal conductivity
l	half contact length
m	strain rate sensitivity
M	mach number
N	ratio of dilatation wave speed to shear wave speed
n	repetition index
P, p	normal load, normal pressure
Pe	Peclet number
Q, q	tangential load, tangential pressure or heat flux
r	ratio, radius, distance
R	resultant force, energy partition
s	Fourier variable, deviatoric stress
t	depth, thickness
T	temperature
u	specific energy, x-directional displacement
v	y-directional displacement

V	speed
w	width, strain energy
x	x coordinate
y	y coordinate
Y	uniaxial yield strength
α	rake angle, thermal expansion ratio
δ	thickness
ε	strain
ϕ	normalized temperature, stress function
γ	shear strain, normalized heat flux
κ	thermal diffusivity
λ	Lamé constant
μ	shear modulus (Lamé constant), friction coefficient
ν	Poisson's ratio
θ	angle
ρ	mass density
σ	stress
ξ	normalized local coordinate in x-direction
η	normalized local coordinate in y-direction

Subscripts

0	initial, original
c	chip, cutting
d	dilatation, deformation
e	edge, effective, elastic
eq	equivalent
f	friction, flank

K	conductivity
m	sequential number, mass
p	plastic
pl	plowing
s	shear
sl	sliding
t	thrust, total, tool
w	workpiece

Superscripts

M	mechanical
T	thermal

CHAPTER I

INTRODUCTION TO ULTRA-PRECISION MACHINING

1.1 Introduction

Over the last two decades, advanced technologies in manufacturing processes have become key strategies to competitive economic development as well as technological survival in the world. Now, the need for advanced technology is challenging current microtechnology (capability of 1 μm accuracy) and nanotechnology (capability of 1 nm accuracy) for form accuracies and tolerances, along with the further development of machine tools, control equipments, material science, and process mechanics involved [Taniguchi, 1983; McKeown, 1987].

The definition of ultra-precision machining is not an absolute one. In other words, as technology advances machining accuracy is also changing as shown in Fig. 1-1 [Taniguchi, 1983]. This figure, called the "Taniguchi Curve", represents a progression of machining accuracy. Further development of process accuracies are extrapolated in the figure beyond the year of 2000. In the figure, machine tools indicate the equipment by which the corresponding accuracy can be achieved. Taniguchi's definition for ultra-precision machining is "those processes or machines by which the highest possible dimensional accuracy is or has been achieved at a given point in time". In the figure, for example, 1 μm

accuracy was ultra-precision machining in 1930's, however, this accuracy was precision machining in 1950's, and it would be nothing but normal machining in the year 2000. General trends of the three machining accuracies are gradually tending towards smaller achievable machining accuracies with time. Also, the figure shows that achievable machining accuracy of ultra-precision machining in the 1990's would be precision machining in early 2000's.

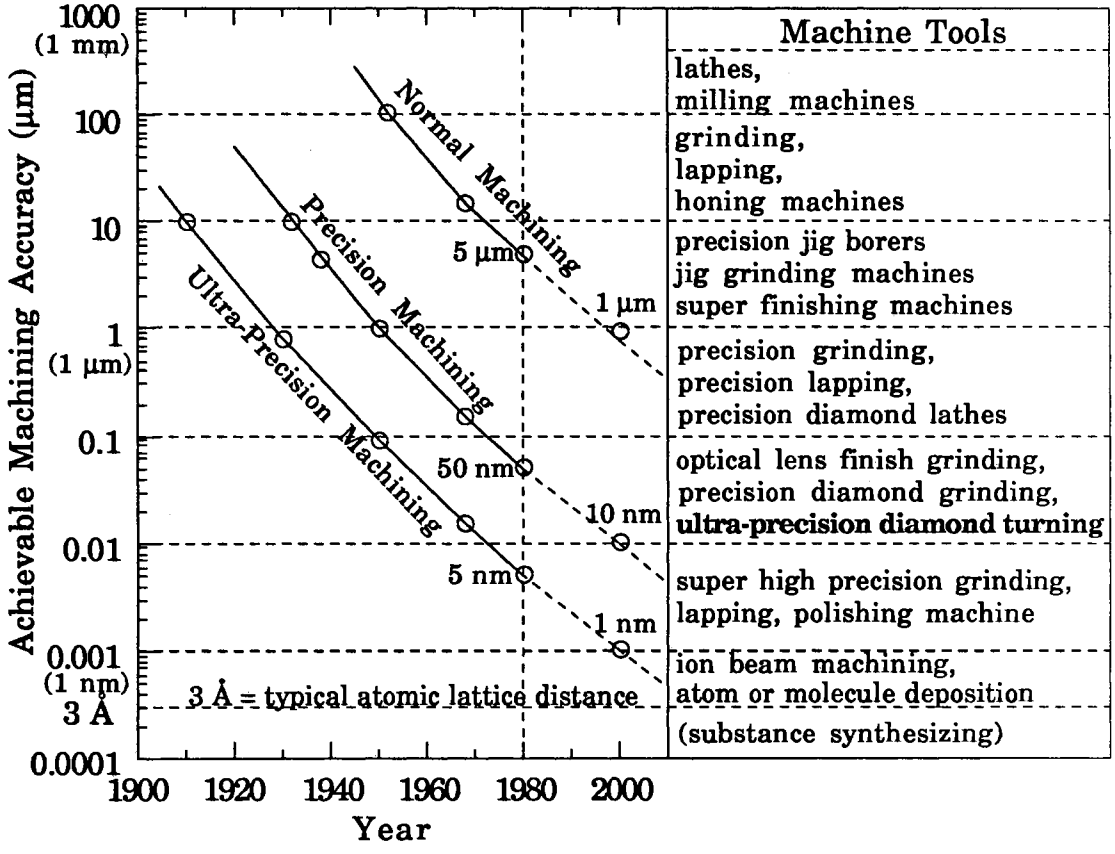

Figure 1-1. Progressive Development of Achievable Machining Accuracy [Taniguchi, 1983]

In the 1980's, achievable ultra-precision machining was on the order of 0.01 μm for dimensional tolerances and 1 nm for surface roughnesses. In the early 2000's, we could have the capability of machining a subnanometer accuracies. The next generation of precision engineering will be "atomic-bit" engineering which includes elastic emission machining, ion beam machining, and synthesis of materials at the atomic scale.

Economics are one of the important factors to select a particular machining process. According to the Machining Data Handbook [Machinability Data Center, 1972, 1980], annual labor and overall costs for operating metal cutting machine tools in the United States alone have been estimated to exceed $40 billion per year in 1972. This amount has increased to $115 billion per year in 1980. Even if there is no available statistic data for 1990 yet, an estimate of a linear increase of this amount results in approximately more than $200 billion in the United States alone. This amount corresponds to about 14 % of the total Federal Budget of $1.45 trillion in 1992. There are many factors affecting the cost of machining. Among them, surface finish and dimensional tolerance are important. For steel workpieces, the approximate machining cost for improvement of surface finish from 1.6 μm (finish turn) to 0.4 μm (honing) is about 4 times that of 1.6 μm finish. Even if the direct statistics are not yet available for ultra-precision machining alone, this process is much more costly due to high cost of equipment and low productivity. Since the fundamental mechanics in ultra-precision machining are similar to that in conventional machining, improved process technology in ultra-precision machining can be applied to the conventional metal cutting process. If such is the case, a small improvement of the process could bring

significant savings in total operating costs. Furthermore, diamond turning has emerged as an economically "viable" technique recently for the machining of a wide range of components particularly for optical parts due to its unique capabilities for dimensional accuracy and surface quality [Chapman, 1988].

Ultra-precision diamond turning can be considered an extension of the conventional machining process, which utilizes a specially prepared single crystal diamond tool together with a machine tool of extreme-accuracy, and high stiffness. The cutting process is performed under precisely controlled conditions of temperature and vibration isolation. High technology components involving computer disk substrates, metal optics, and precision contact machine elements require ultra-precision dimensional accuracies ranging from micrometers to nanometers [Sugano, 1987; Furukawa, 1988; Moriwaki, 1989].

Ultra-precision diamond turning has the following advantages over other machining processes:

- high form accuracy and repeatability,
- superior local surface roughness as well as global flatness (or form accuracy),
- no possibility of imbedding foreign materials such as grit in the machined surface (as would be the case for grinding),
- relatively large machinable workpiece surface,
- machining with low energies (less than 5 kw) and, as a result, low process temperature during machining (hence less thermal damage and expansion of the workpiece surface),
- no environmental contamination due to by-products such as chemicals and noises,

- moderate material removal rate, and
- minimum operating skill due to computerization.

Some limitations include:

- high machine tool and diamond tool cost,
- dependent accuracy upon the mechanical movement resulting from the control system and physical tool edge geometry, and
- not adequate for fine groove formation (limited to flat or curved surface).

Some of these limitations are under study and should be eliminated in the near future.

To remove some of these limitations and to improve the accuracy in the ultra-precision diamond turning process, balanced research and development must move forward in the related areas such as accurate measurements of geometry and surface quality, characterization of material behavior, and mathematical modeling and simulations of the process mechanics.

1.2 Historical Background

Even though copper mirrors were made in the 6th century BC, and polished diamond tooling was well known in the mid-19th century, the technology recognized as "diamond turning" today has emerged only after the World War II. As a newly emerging technology, research and development in ultra-precision machining has been very active worldwide. In 1960's, as an alternative process to grinding of optical components, single point diamond turning was introduced in industries and laboratories including Philips Research in the Netherlands, Bryant-

Simmons in the United Kingdom, as well as Union Carbide Co., Perkin-Elmer Co., Lawrence Livermore National Laboratory and Battelle Pacific Northwest Laboratory in the United States. Brief historical background of ultra-precision machining in some of the advanced countries in ultra-precision machining is provided below.

1.2.1 Japan

Since the Japan Society of Precision Engineers (JSPE) was established in 1933, technology in precision machining has made rapid progress. Aided also by the Japan Society of Grinding Engineers which was established in 1956, high precision machining of semi-conductor materials, ferrite, quartz, ceramics and non-metallic materials including germanium and silicon has been made by grinding, lapping and polishing in 1960's [Iizuka, 1988; Kobayashi, 1988].

After the first report on diamond cutting made by Union Carbide, which appeared in the 7th International Machine Tool Design and Research Conference in 1966, the terminology of "ultra-precision machining" was first used in Japan by Tsuwa of Osaka University in the Bulletin of the JSPE in 1972. A special committee for ultra-precision machining was founded within the JSPE in 1981 (60 members in 1988) and it became the center of ultra-precision technology in Japan. In 1986, a special group for diamond tool edge characterization was founded within the JSPE. Presently, the Electrotechnical Laboratory (ETL) and Electrical Communication Laboratory (ECL) are the centers for the micro-fabrication technology in Japan.

1.2.2 The United Kingdom

In the United Kingdom, nanotechnology efforts were initiated to meet the need to manufacture precision optics when the UK National Initiative On Nanotechnology (NION) was established at National Physical Laboratory (NPL) under the Department of Trade and Industry [Franks, 1988]. In 1986, a Strategy Committee was formed to support the development of science and technology. The core areas are the technology of positioning and control to nanometer accuracy, ultra-precision machining, new energy beam techniques and nanometer metrology, nanostructures, surface treatment and analysis, X-ray optics, and super smooth surfaces. Metrological instrumentation has been developed for both contact and non-contact measuring methods for surface wavelengths down to 50 nm.

1.2.3 Germany

In West Germany, high precision machining technology has been supported mainly in optics by the Bundesministerium für Forschung and Technologie from early 1970's [Heynacher, 1983]. Fields of applications are cameras, night vision equipment, spectral and astronomical optics. A diamond turning machine was fabricated for workpiece sizes of 800 mm in diameter and 400 mm in height by Zeiss early in 1980's.

1.2.4 The United States

The first ultra-precision machine tool is reported to have been fabricated by Du Pont at the Oak Ridge National Laboratory Y-12 plant operated by Union Carbide for the U.S. Department of Energy in 1962

[Richards, 1966; Whitten, 1966]. An aluminum alloy hemisphere having a 4 inch diameter was machined with a geometric accuracy of 25 μin (0.635 μm) and roundness tolerance at the equator of below 2 μin (0.05 μm). Diamond turning machines DTM-1 and DTM-2 followed in 1969 ~ 1971 at Lawrence Livermore National Laboratory, later followed by PERL (Precision Engineering Research Lathe) also at Livermore in 1982 [Brown, 1983]. In the mid-1980's, DTM-3 was completed. It was capable of machining parts up to 84 inches in diameter and weighed 7000 lbs. Taking the opportunity of US-Japan Joint Seminar on Ultra-Precision Machining, the American Society of Precision Engineers (ASPE) was founded in 1985 in the United States. Since then, nanotechnology has become a rapidly emerging research and development area [Teague, 1988].

1.3 Uniqueness and Applications

Ultra-precision machining has several unique features due to its characteristically small dimensional scale (as compared with conventional machining) as shown in Fig. 1-2. The depth of cut (uncut chip thickness) can range from a few micrometers down to nanometers. Typical achievable dimensional tolerances are at least one-half the wavelength of visible light (0.25 μm) and arithmetic average roughnesses range from 50 nm to 1 nm [Krauskopf, 1984]. Elastic recovery at the flank face may be comparable with the depth of cut, thus the contact at the flank face may not be negligible. The tool edge radius is also important for the process mechanics when the depth of cut is on the order of the edge radius. Diamond tools are usually employed due to their capability of maintaining a sharp edge and because of their superior thermal properties.

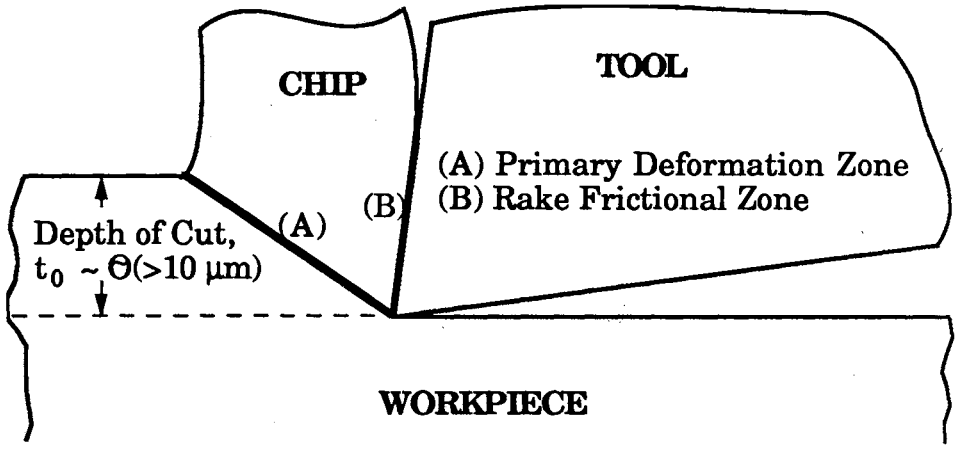

a) Orthogonal Conventional Machining Geometry

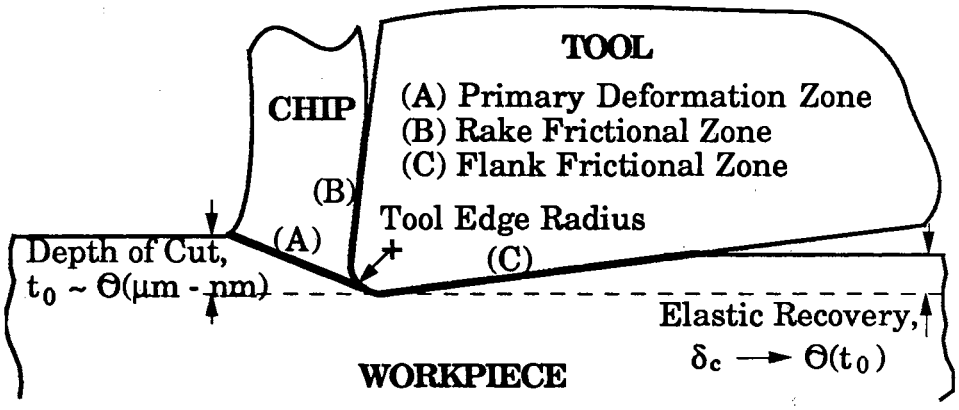

b) Orthogonal Ultra-precision Machining Geometry

Figure 1-2. Comparison of Conventional Machining and Ultra-Precision Machining

Applications of the diamond turning process depends on part shape, part size, and process repeatability, but superior surface quality (local roughness as well as global flatness) and long tool life are unique characteristics of the ultra-precision diamond turning process. Currently, ultra-precision diamond turning is utilized to produce components requiring high dimensional accuracy and surface finish, e.g., metal mirrors for lasers, computer magnetic memory hard disc substrates, contact lens molds, and VCR heads, etc.

1.4 Outline of the Dissertation

In Chapter I, a time progression of increasing accuracies in normal, precision and ultra-precision machining was described. Some of the uniquenesses and applications of present day ultra-precision machining, and in particular, single point diamond turning were also described.

The ultra-precision diamond turning process is described in terms of the machine tool, diamond tool and diamond turnable materials in Chapter II. The mechanics involved in the process are also discussed together with the energy models proposed in the literature. After careful review of the previous studies, some problems needing further study were defined as focal points of the present study for both the experimental and analytical approaches in Chapter III.

The results of an initial experimental study using Al 6061-T6 are discussed in Chapter IV together with comparisons of cutting geometries, experimental set-ups and cutting conditions. Tool characterization using a scanning electron microscope (SEM) technique was also described. In this initial experimental study, force behavior with depth of cut,

measurement of contact length at the tool-workpiece using a AuPd coating technique and preliminary investigation of the effect of tool edge radius on resulting forces and energies was performed.

Based on the observation of a significant tool edge effect on the measured forces, further experimental study of the tool edge profile effect was performed using various tools and cutting conditions. The investigation of the edge profile effect on the energy dissipation when machining tellurium copper (Te-Cu) is described in Chapter V. The seven tools employed were characterized using atomic force microscopy (AFM). The measured tool edge radii (profiles) obtained from the AFM were used to investigate the effect of cutting forces, thrust forces and specific energies measured at various cutting conditions. These conditions included various tool rake angles (0°, -10°, -20°, -30°), cutting distances (up to 3 km), tool conditions (new tool and considerably worn tool), and cutting speeds (one order of magnitude difference). For the study of the process mechanics in ultra-precision machining, attention was focused in the range of depths of cut where the cutting force signals are nonlinear with depth of cut. These depths of cut ranged from 20 μm to 10 nm. The 2D cutting force components and specific energy variation with depth of cut were examined in this range. From careful investigation of the experimental results, it was observed that the cutting process transitions from a cutting-dominant to plowing/sliding-dominant process at submicrometer depths of cut. It was also recognized that the measured tool-workpiece contact length at the flank interface becomes the characteristic length scale at submicrometer depths of cut. The experimental results described above indicated that the machining process at submicrometer depths of cut resembles a sliding indentation problem.

Based on the experimental study, a simplified analytical model was developed and is described in Chapter VI. This allowed investigation of the elastoplastic stress fields at the subsurface of the workpiece. Elastostatic stress fields due to a stationary surface pressure were formulated using Airy's stress function as a first step. Also, elastodynamic stress fields using a Fourier integral transform method for a loaded slider on a semi-infinite moving non-insulated body was formulated. The heat partition at the contacting interface and corresponding temperature rises of both the stationary and moving bodies were formulated. Extension from the elastodynamic stress solution to elastoplastic stress solution was made by employing the Prandtl-Reuss equation and solving by a Runge-Kutta method. The elastoplastic stress fields calculated were compared with results obtained using the FEM code ABAQUS for the same conditions. The subsurface plastically deformed layer was on the order of micrometers and the temperature rise at the interface was about 0.1 °C at conditions representing submicrometer depths of cut for both the workpieces.

Both experimental and analytical results and observations are summarized in Chapter VII. From the experimental study, both the cutting and thrust forces were seen to depend significantly on the tool edge contour. The nonlinearity of force components, severe rotation of the resultant force vector, dramatic increase in total specific energy, and characteristic length scale shift as depth of cut decreases were found to be the unique process characteristics in ultra-precision machining. The developed slider model was shown to be useful to predict the stress fields and resulting temperatures. Finally, recommendations for improvements or extensions to the present study were given.

CHAPTER II

STATE OF PRESENT UNDERSTANDING

2.1 Introduction

Single point diamond turning of soft materials is a well established technology having been used over the last two decades, however, due to the lack of understanding of the governing process physics, further advances in machining performance, dimensional accuracy and surface finish are now being limited. Goals of improving the machined surface quality and extending the range of diamond turnable materials to possibly include ferrous and brittle materials, significant interest has motivated further study of the governing mechanisms of the process. The mechanisms of chip formation, the temperatures generated, and the resultant tool wear and subsurface workpiece plastic deformation all represent areas in which fundamental understanding must be developed in ultra-precision machining.

With the characteristic length scale of the process being several orders of magnitude smaller than conventional machining, it is necessary to re-examine the process mechanics which govern in ultra-precision machining. For example, unlike in conventional machining where shear along the shear plane and friction at the rake face of the tool dominate, ultra-precision machining may involve significant plowing and sliding along the flank face of the tool due to the tool edge radius and elastic

recovery of the workpiece material. The trend of force components with depth of cut may be quite different as depth of cut decreases. In conventional metal cutting with continuous chip formation, it is well established that the majority of heat (about 80 %) is carried away by the chip [Shaw, 1983]. With the decrease in thermal mass of the chip as the depth of cut decreases, the partitioning of thermal energies at the tool-chip and tool-workpiece in ultra-precision machining may be quite different from conventional machining. Due to flank face rubbing, the subsurface plastic deformation in the workpiece may be significant relative to the depth of cut as well.

In this chapter, ultra-precision machining is reviewed and contrasted with conventional machining. Some aspects of the process mechanics including the size effect, and plowing and sliding processes in microcutting are reviewed and discussed. Several conceptual geometric models for energy dissipation are investigated. Based on a review of the literature, some problems are identified and proposed as research areas in need of further study.

2.2 Process Components of Ultra-Precision Machining

2.2.1 Machine Tool

Diamond turning machine tools are designed and fabricated using state-of-the-art machine tool technology. Machine tool accuracy has been improved using air bearings and hydrostatic slides to isolate the dynamic effects. Laser-interferometry and a CNC controller are used to obtain required positioning accuracies. To prevent the diamond tool from chipping resultant from dynamic effects, the machine tool must have

special characteristics. These characteristics are essential not only for the machine tool but for the workpiece supporting fixtures and tool holding devices as well. General design requirements are listed below [Krauskopf, 1984; Chapman, 1988]:

- high rigidity and stability,
- superior spindle and slide accuracy and repeatability,
- accurate positioning of tool and workpiece,
- extreme vibration isolation and precise temperature control, and
- strong support and set-up of tool and workpiece.

For high stiffness of the machine tool, granite or alumina ceramic beds are used, and they are usually supported by air mounts to isolate it from vibration [Furukawa, 1986; Masuda, 1989]. Typical stiffnesses of the machine tool are about 10^6 lb/in and the sliding accuracy is on the order of nanometers. Environmental temperature control is also critical due to the thermal expansion of the machine tool and workpiece system. The design and fabrication technology of the machine tool is relatively well established, thus the machine tool is not a limiting factor for improvement of accuracy of the workpiece [McKeown, 1982; Donaldson, 1983].

2.2.2 Diamond Tool

Natural diamond is used as a cutting tool because of its high hardness, superior thermal properties, low coefficient of friction, and high wear resistance. Due to its high hardness and strength, a very sharp edge can be maintained. Diamond does show however, orientation sensitive friction coefficient and differences in hardness for different types [Krauskopf, 1984; Hurt, 1984]. The wear of diamond tools is known to be

dependent on the crystallographic orientation. Some results of wear tests have suggested that a tool with a {100} or {110} rake face and a {100} nose face has better wear characteristics than other orientations [Wada, 1980; Hurt, 1984, 1986]. Typical physical and mechanical properties of diamonds, together with some comparable materials, are shown in Table 2-1.

TABLE 2-1

MECHANICAL AND PHYSICAL PROPERTIES OF DIAMOND

Properties	Values	Comparable Materials
Density (g/cm^3) at 25 °C	3.51 ~ 3.52	SiC : 3.217
Heat Capacity (cal/mol °C)	1.46 at 20 °C 2.52 at 125 °C	Si at 20 °C : 4.3 W at 20 °C : 5.97
Thermal Conductivity (cal/cm sec °C)	1.9 at 227 °C 1.1 at 427 °C	Cu : 0.91 at 25 °C Ag : 0.99 at 25 °C
Thermal Diffusivity (cm^2/sec)	10 at 25 °C	Ag : 1.66 at 25 °C
Thermal Expansion (/ °C) x 10^6	1.34 at 20~100 °C 3.29 at 20~400 °C	W : 4.6 at 20 °C SiC : 7.3 at 20 °C
Temp. for Stability	600 °C	
Young's Modulus (GPa)	1000	WC:720
Poisson's Ratio	0.1~0.29	
Hardness (Hv: GPa)	90~150	
Shear Strength (MPa)	340	
Compressive Strength (GPa)	9	WC: 4.3

Diamond has about 4 times higher hardness and is known to have about 20 times longer tool life than carbide tools. When heated to 600 °C, diamond begins to form a black coating on the surface and at 1500 °C,

graphitization begins. Thus, maintaining the process temperature below 600 °C is important for longer tool life during machining. Also, due to high hardness and low shock and impact resistance, the diamond edge can easily be chipped. Therefore, special care must be given to the proper handling and mounting of the tool. Gem quality natural single crystal diamonds are the best for use as a tool material. Diamonds are known not to promote built-up edge, although some can occur as the tool wears, especially for aluminum materials.

The sharpness of the diamond tool edge is one of its advantages for use in ultra-precision machining. The tool edge radius (profile) determines the minimum depth of cut, below which, the tool disturbs the workpiece surface structure without effective material removal. Burnham [1976] estimated a theoretical diamond tool edge radius as 0.3 nm based on interatomic spacing, and Ikawa and Shimada [1977] calculated the theoretical value as 2 nm based on a surface tension approach. The smallest edge radius reported to have been used so far is for Moriwaki and Okuda's [1989] tool of 20 ~ 50 nm (estimated). Low rake angle or negative rake angle tools are used to provide stronger cutting edges. Typically, 0 ~ 2° rake and 5 ~ 10° clearance angle tools are used. Larger nose radius or straight nose tools are known to achieve better surface roughnesses than smaller nose radii tools, possibly due to the suppression of a vibration effect during machining [Sugano, 1987; Masuda, 1989].

Tool life depends on the cutting conditions such as depth of cut, cutting speed, workpiece material and cutting fluid. It has been generally said that single crystal diamond tool life is about 300 ~ 400 km in cutting distance. Sugano [1987] used single crystal diamond tools for cutting an aluminum alloy up to 900 km in cutting distance under conditions of depth

of cut of 20 μm at 720 m/min with volatile oil used as a cutting fluid. However, beyond 400 km in cutting distance, the force components, especially thrust force, increased significantly due to severe tool wear.

As a cutting fluid, kerosene or light-weight machine oil is commonly used [Wada, 1980; Nishiguchi, 1988; Masuda, 1989]. Pure water is also reported to have been used for acrylic resin [Furukawa, 1988] and single crystal silicon [Syn, 1988].

2.2.3 Workpiece Materials

Literature on fundamental studies of the chip formation and machinability of single point diamond turning has only recently begun to emerge. Experimental studies have been performed to investigate the mechanisms of micro chip formation [Ueda, 1980; Nishiguchi, 1988], and diamond tool wear [Hurt, 1986; Syn, 1986; Sugano, 1987]. Other studies have been reported on the ultra-precision machining of copper [Iwata, 1984; Moriwaki, 1989], aluminum [Atkin, 1986; Sugano, 1987], stainless steel [Iwata, 1986; Iwata, 1987a], and electroless nickel [Syn, 1986; Taylor, 1986]. Successful attempts have been made at machining silicon [Blake, 1987, 1988; Taylor, 1987; Syn, 1988], germanium [Furukawa, 1988; Gerchman, 1988], and molybdenum [Donaldson, 1985]. Diamond turnable materials include ductile metals, polymers, and crystals. Steels and nickel alloys have shown not to be diamond turnable because of high tool wear rates [Delingat, 1983; Hurt, 1984].

Generally, face-centered-cubic materials are diamond turnable, but materials containing carbon are generally not, due to thermo-chemical reactions which occur during the cutting process. At high temperature,

TABLE 2-2

OPTICAL MATERIALS AND COMPARISON OF THEIR MACHINING PROCESSES [Delingat, 1983]

	Material	Precision Molding or Pressing	Grinding Lapping Polishing	Diamond Turning
Optical Glasses	FK 54	Q	G	Q
	F4	Q	G	Q
	SF59	Q	G	Q
	LaK N17	Q	G	Q
	Fused quartz (SiO_2)	Q	G	Q
Crystals	$CaCO_3$	N/A	A	N/A
	SiO_2	N/A	A	N/A
	KH_2PO_4	N/A	A	A
	Al_2O_3	N/A	A	N/A
	$MgAl_2O_4$	N/A	A	N/A
	CaF_2	N/A	A	Q
	LiF	N/A	A	Q
	NaCl	N/A	A	Q
	KBr	N/A	A	Q
	ZnS	N/A	A	G
	ZnSe	N/A	A	A
	Silicon	N/A	A	A
	Ge	N/A	A	A
Optical Plastics	PMMA	G	Q	A
	PC	G	Q	A
	PS	G	Q	A
	CR-39	G	Q	A
Materials for Mirrors	Glass - Ceramics	N/A	G	N/A
	Cu	N/A	A	G
	Ag	N/A	A	G
	Au	N/A	A	G
	Al	N/A	G	G
	Ni	N/A	A	N/A

N/A: not applicable, A: applicable, G: good, Q: not known
PMMA: polymethyl-methacrylate, PC: polycarbonate
PS: polystyrene, CR-39: allyldiglycol-carbonate

diamond reacts with materials such as tungsten, tantalum, titanium, and germanium, and forms a carbide of the workpiece material. In an oxygen environment, materials such as ferrite, cobalt, manganese, nickel, beryllium, chromium react and graphitize the diamond. However, some of these materials have been test machined in a laboratory.

Some optical materials and applicable processes for generating mirror surfaces are shown in Table 2-2. Generally, precision molding or pressing is employed for optical plastics and glasses. Diamond turned molding and press dies are also used for improved surface roughness. Grinding or lapping and polishing are usually used for optical glasses and crystals due to their high brittleness. Ductile materials and some crystals and plastics are typically diamond turned. The criteria for "diamond tunability" may be tool wear, process temperature, or machined surface quality.

2.3 Some Considerations on the Mechanics of the Ultra-Precision Machining Process

2.3.1 Chip Formation

Merchant [1945a, 1945b] was the first to establish the relationships between tool forces and cutting geometry. He developed a shear strain expression at the primary shear zone using Piispanen's [1948] card deck analogy, and derived a shear angle from the minimum energy principle. His force diagram using the geometrical relationships between force components became the basic force model in metal cutting, and is shown in Fig. 2-1. The figure shows primary shear at the shear plane, and secondary shear at the tool-chip interface. Tool-workpiece frictional

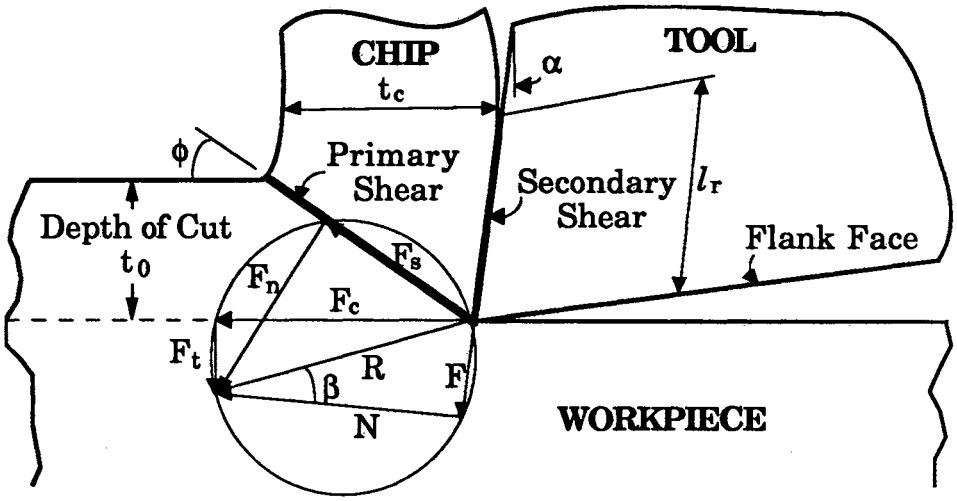

Figure 2-1. Merchant's Force Diagram for Conventional Orthogonal Cutting [Merchant, 1945a, 1945b]

contact is neglected in the mechanics of conventional machining.

Albrecht [1960, 1963] developed a new force diagram by introducing the concept of ploughing. Spaans [1967a, 1967b, 1970, 1971] considered a 3D equilibrium equation to find the "parasitic" force at the cutting edge in three perpendicular directions. However, no study has modeled the cutting process for submicrometer depths of cut. Here, the process mechanics related to ultra-precision machining is reviewed and discussed from the view point of energy dissipation at decreased depths of cut.

2.3.1.1 Primary Shear. The shear plane is the main region where plastic deformation occurs in conventional machining. According to Merchant's result, the shear stress is a function of cutting force (F_c), thrust force (F_t), shear angle (ϕ) and depth of cut (t_0), but is not affected by the cutting speed (V). Kobayashi [1960] also showed that the speed effect is

negligible. According to the results of von Turkovich [1967], the shear stress also depends on the workpiece temperature.

Using Merchant's shear plane angle from the minimum energy principle of $\phi = 45 - (\beta - \alpha)/2$, Albrecht [1963] investigated the effect of this angle on the resultant cutting force. In the plot of resultant force vs. shear angle, for a 26.8% change in shear angle, the resultant force changes only 7.5%. This means the effect of the change of the shear plane angle on the energy dissipation may not be significant.

2.3.1.2 Secondary Shear. Secondary shear occurs at the chip due to contact between the chip and tool rake face. This friction problem is still not yet well understood because of the uncertainty of the friction coefficient and the contact (apparent vs. real) at the rake face [Kobayashi, 1960; Oxley, 1976; Venuvinod, 1983; Tabor, 1987]. Kobayashi [1960] found that the friction coefficient for strong junction contacting asperities ranges from 0.4 to 1.0 but there is no general solution for other conditions.

Albrecht [1960, 1963] modeled this zone by introducing a ploughing process in which a small portion of the material in front of the cutting edge is pressed into the tool-chip interface thus contributing to a built-up edge and/or built-up layer, and chip curling. The remaining portion of the material is pressed into the workpiece, and results in residual stresses in the subsurface of the machined workpiece. Accordingly, the magnitude of the ploughing force is increased with edge radius. He also observed that the ploughing force is nonlinear as the depth of cut decreases. Similar nonlinearity was observed by Armarego [1961] and Thomsen [1953].

The contact length at the rake face (l_r) was estimated by Hastings [1974] using the cutting geometry as:

$$l_r \geq t_0 \sin(\phi + \beta - \alpha)/ (\cos \beta \sin \phi) \qquad (2\text{-}1)$$

When the rake angle $\alpha = 0$, using Merchant's minimum work principle, this reduces to:

$$l_r \geq t_0 (1 + r \cot \phi) = 2 t_0 \qquad (2\text{-}2)$$

This equation indicates that contact length at the tool-chip can be as small as only twice the depth of cut for zero rake angle tools. Therefore, the contact at the tool-chip interface may not be significant as depth of cut decreases. The assumption here was that the resultant cutting force vector is parallel to the line connecting the point where the workpiece material changes to a chip on the free surface and the point where the chip-tool contact is separated.

2.3.1.3 Flank Friction. Usually the contact at the flank face is neglected in conventional machining. However, several investigators emphasized the importance of flank friction on the dissipation of energy as depth of cut decreases [Nakayama, 1968; Hurt, 1984; Moriwaki, 1989; Lucca, 1991b]. Due to the elastic behavior of the workpiece material, elastic recovery of the newly created surface and hence tool-workpiece contact at the flank face is not negligible compared to the depth of cut in micro-cutting. This sliding contact may have considerable impact on the total energy dissipation during the micro-machining process [Lucca, 1989].

Ikawa [1977] found that elastic recovery at the flank face and the thickness of plastically deformed layer were 17% and 120 % of the tool edge radius respectively for a 3 degree rake angle and a material having 1% strength of the Young's modulus. He used the analogy between the

cutting edge penetration and the deformation of a thick walled tube subjected to an internal pressure. He explained that the difference between the nominal depth of cut and the effective depth of cut comes from the rubbing or sliding of the tool edge without material removal at smaller depths of cut. This rubbing was thought to affect the workpiece subsurface damage and temperature rise significantly. However, no estimation of the contact length at the tool-workpiece interface was made, and this frictional contact was neglected for modeling the process mechanics.

2.3.2 "Size Effect"

In machining, the so called "size effect" was observed by many investigators as depth of cut decreases [Backer, 1952; Albrecht, 1960; Armarego, 1961; Nakayama, 1968; Sugano, 1987; Furukawa, 1988; Moriwaki, 1989]. In the grinding process, Malkin [1974a, 1974b] also observed the size effect. The "size effect" is the phenomenon that specific energy increases dramatically as depth of cut decreases. Specific energy is defined as the energy required for the removal of a unit volume of the workpiece ($u_t = F_c V/(t_0 w V)$. Here, F_c is the cutting force, V is the cutting speed, t_0 is the depth of cut, and w is the width of cut. Furukawa and Moronuki [1988] investigated the size effect for a variety of materials as shown in Fig. 2-2. In the figure, specific energy is normalized by dividing the specific energy at 10 μm depth of cut for each material. They used a single crystal diamond tool having a nose radius of 0.5 mm, rake angle of 0°, and clearance angle of 2 ~ 3° for this experiment. Depths of cut ranged from 0.5 to 10 μm and cutting speed was 100 mm/sec. The normalized specific energies increase significantly as depth of cut decreases for all the

materials however, above about 3 μm depth of cut, the energies stabilize and reach the values for conventional machining. This dissipation of mechanical energy at decreased depths of cut, not directly responsible for material removal, is very important in its effect on tool performance, workpiece surface integrity and subsurface plastic deformation, but the mechanisms involved are still not yet well understood.

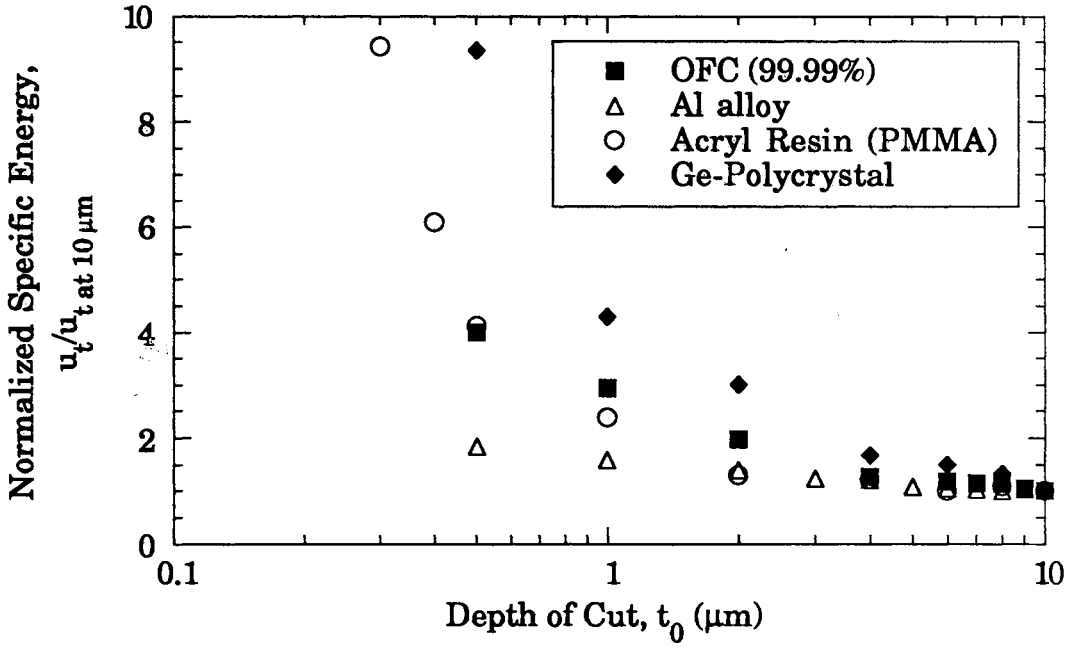

Figure 2-2. Normalized Specific Energies for Various Materials Showing the Size Effect [Furukawa, 1988]

Armarego and Brown [1961] explained that the size effect is dependent on the tool profile and material. The change in cutting tip geometry and creation of a built-up edge result in the change of rake angle during cutting.

Backer et al. [1952] argued that the size effect resulted from the theoretical strength of the material in which the strength of a small deformation zone is greater than the strength of the bulk material due to a reduced dislocation density.

Williams and Gane [1977] explained the size effect as a tensile strength effect of high strain (>1) and strain rate (>10^5/sec) during metal cutting. Dugdale and Enahoro [1964] identified the causes of the size effect as tool bluntness, friction on the tool flank, a work-hardened layer on the specimen and increase in shear strength due to plastic deformation. Recently, Taminiau and Dautzenberg [1991] observed a higher yield shear stress in the high-precision cutting of free-turning brass using a diamond tool. They found it to be almost twice as high as the value in rough cutting. They attributed this to a higher strain rate in high-precision cutting.

The increase of flow stress due to strain rate can be expressed as:

$$\frac{\sigma_2}{\sigma_1} = \left[\frac{\dot{\varepsilon}_2}{\dot{\varepsilon}_1}\right]^m \tag{2-3}$$

where σ is the flow stress, $\dot{\varepsilon}$ is the strain rate, and m is the strain rate sensitivity. When the process temperature is less than 50 % of the melting point of the material on the absolute scale, the strain rate effect on the flow stress is not significant. For copper and aluminum, m is about 0.02 below 200 °C [Altan, 1973]. An order of magnitude increase in strain rate increases flow stress less than 5 %, and a 100 times higher strain rate results in only less than 10 % increase in flow stress. However, the specific energy observed at submicrometer depths of cut is at least one order of magnitude higher than that of at large depths of cut. Thus, the

strain rate effect may not be a significant contributor to the energy dissipation at reduced depths of cut.

According to Nakayama [1968], the subsurface plastic flow of workpiece material which he attributed to the extension of the shear zone below the machined surface, becomes important at small depths of cut. The energy dissipated in this subsurface flow was seen not to be proportional to the depth of cut and hence one source of the size effect. He also found that the change in effective rake angle made a contribution to the size effect. Malkin [1974a, 1974b] also pointed out the effects of severe negative rake angles in grinding processes.

As depth of cut approaches the order of the tool edge radius, the effective rake angle becomes negative. Conventional machining is assumed to have constant rake angle because the depth of cut is much larger than the edge radius of the tool (if no built-up edge is present). Further decrease of depth of cut below the tool edge radius results in plowing and sliding of the tool on the workpiece surface without effective material removal. The redundant energy dissipation of plowing and sliding is reported to contribute to the considerable increase in the specific energy as depths of cut decreases [Malkin, 1974a, 1974b; Lucca, 1991b].

2.3.3 Plowing and Sliding

In ultra-precision machining, plowing and sliding at the flank face may be considered as a mechanism of energy dissipation. Plowing is resultant from either a negative rake angle or an "effective" negative rake which results when the edge radius of the tool is of the order of the depth of cut as shown in the bottom of Fig. 2-3 [Lucca, 1991b]. Sliding is due to the

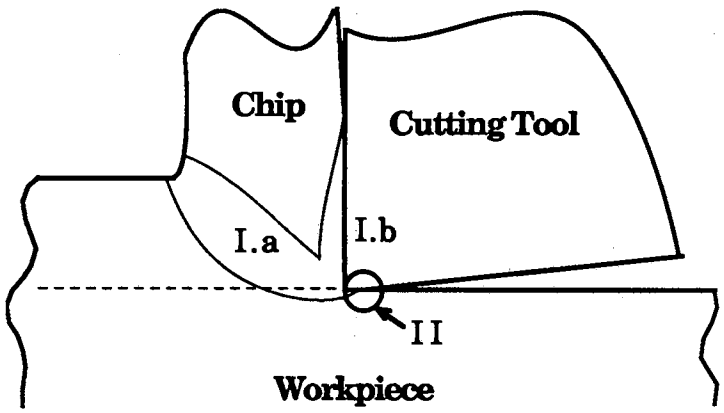

I.Chip Formation: a. Shear Throughout the Shear Zone
b. Sliding of Chip along the Rake Face

II. Sliding: Tool/Workpiece Interaction by Flank Wear or Elastic Recovery of Workpiece Material

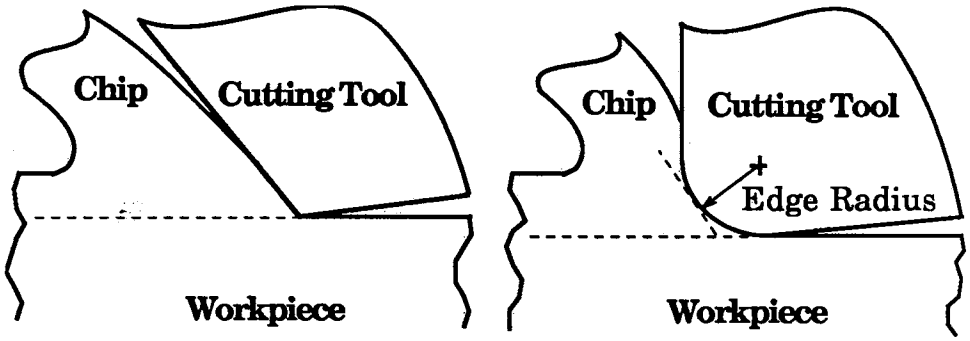

Plowing: Due to Negative or "Effective" Negative Rake angle

Figure 2-3. Chip Formation, Sliding and Plowing in Orthogonal Metal Cutting [Lucca, 1991b]

subsequential tool-workpiece interaction caused by either flank wear or elastic recovery of the workpiece material as shown in zone II of Fig. 2-3. When plowing and sliding processes dominate over the chip formation process, the subsurface of the machined workpiece is in elastoplastic stress state and may be a major zone of energy dissipation.

Hamilton [1963] observed that the plastic shear energy in rolling contact is much greater than that of simple shear. From an experimental study of fully work-hardened, cold-rolled copper discs, he observed that plastic flow occurred in a narrow layer below the surface toward the entrance of the roll. Using Radzimovsky's solution [1953] for the stress fields, he calculated the position where yielding first occurs for a metallic material. The plastic onset begins at 0.704 times the half contact length below the center of contact.

Merwin and Johnson [1963], and Johnson and Jefferis [1963] investigated the plastic flow and residual stresses in rolling and sliding contact using a step-by-step numerical analysis. They observed a forward flow of material due to shear strain. A variety of metals exhibiting forward flow suggests that the influence of hardening properties is not of primary importance. The analytical prediction of Merwin and Johnson shows good agreement with Hamilton's observation [1963] for forward flow. They observed that the energy dissipated in plastic deformation for rolling contact which is subject to forward and backward plastic flow at the entrance and exit of rolling contact is 3 ~ 4 times as great as would be required in simple shear.

In grinding processes, it is well established that the mechanism of material removal changes from chip formation to plowing or rubbing as depths of cut decrease [Malkin, 1974a, 1974b; Doyle, 1980]. Malkin

separated the total specific energy into chip formation, sliding and plowing energy components. In metal cutting with a sharp and well-ground tool, Spaans [1967a, 1967b] observed that the parasitic axial cutting force reaches to about 40% of the total axial cutting force, which also indicates the importance of plowing and sliding process. From the process mechanics point of view, chip formation, sliding and plowing in grinding can be viewed as similar to those mechanisms active in ultra-precision machining. The difference in the two processes would be the tool geometry, i.e., in grinding, the wheel has irregular shaped multi-point tools (grit) whereas in diamond turning, the tool is well defined and is a single point.

Similarities between the mechanisms involved in rolling and sliding, and the cutting process in ultra-precision machining can be seen. As the depth of cut decreases, from a certain critical depth of cut of about a few micrometers, the thrust force component does not decrease and is larger than the cutting force in magnitude. The thrust force is the major force component in the material removal process below this depth of cut. Hence, this may be considered as a plowing and sliding dominant process rather than a chip formation dominant process.

2.3.4 Geometric Models for Energy Dissipation

2.3.4.1 Eugene's Model. In order to investigate machinability in terms of specific cutting energy, Eugene [1963] performed experiments using several steels. He used high speed steel tools with 15°, 25°, 35° rake angles, and depths of cut from 0.05 to 2.0 mm to study the relationship between the specific cutting energy and workpiece mechanical properties.

He proposed a conceptual energy model which consisted of four energy zones as depicted in Fig. 2-4. Total specific cutting energy, w_c is the sum of elastic and plastic deformation, friction at the chip/tool interface, and energy dissipated in front of the tool (at A) as shown in the figure.

$$w_c = w_{de} + w_{dp} + w_f + w_e \tag{2-4}$$

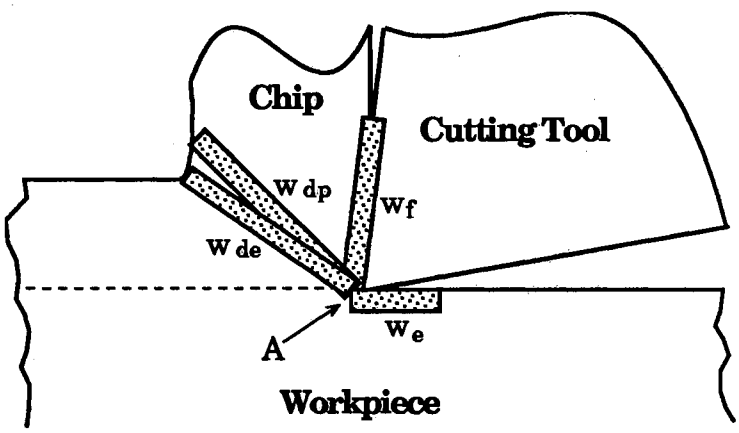

Figure 2-4. Eugene's Geometric Model for Energy Dissipation [Eugene, 1963]

The energy in front of the tool (at A) comes from three sources, i.e., cold working, the decohesion energy of the specimen, and the frictional energy between the tool nose and newly machined surface. It depends on the nature of the specimen, tool geometry and cutting speed.

From his experimental results, he observed:

- there is a critical depth of cut below which the linearity between the depth of cut and force components does not hold, and this

value depends upon the material being cut, tool rake angle, and cutting speed, and

- higher rake angles result in higher critical depths of cut, and as cutting speed decreases, the critical depth of cut increases.

It should be noted that Eugene observed nonlinearity of the force behavior even in steel workpieces cutting with high speed steel tools. Also, he clearly recognized the importance of the role of the tool edge on the energy dissipation.

2.3.4.2 Nakayama and Tamura's Model. Nakayama and Tamura [1968] used high speed steel tools with rake angles of 0°, -20°, and -40° and tool edge radii of 3 ~ 4 μm and 17 μm. In order to avoid built-up edge, temperature, and strain rate effects, brass was used with a low cutting speed of 0.1 m/min, and the depths of cut ranged from 2 to 40 μm.

In their model, five types of energy dissipation were considered, i.e., surface energy of the newly created surfaces, w_1, shear deformation energy in the shear zone, w_2, frictional energy on the tool face, w_3, frictional energy on the tool flank, w_4, and kinetic energy of the chip, w_5. These are shown in Fig. 2-5. Shear deformation energy, w_2, is divided again into simple shear, w_{21} and extended shear energy, w_{22}. Frictional energy on the tool face, w_3, is divided into tool-chip interface frictional energy, w_{31}, and secondary frictional energy in the chip subsurface, w_{32}. Frictional energy on the tool flank, w_4, is divided into tool flank face frictional energy, w_{41}, and flank subsurface plastic deformation energy, w_{42}. They neglected w_1, w_4 and w_5. Therefore, the total cutting energy was expressed as:

$$w = w_{21} + w_{22} + w_{31} + w_{32} \tag{2-5}$$

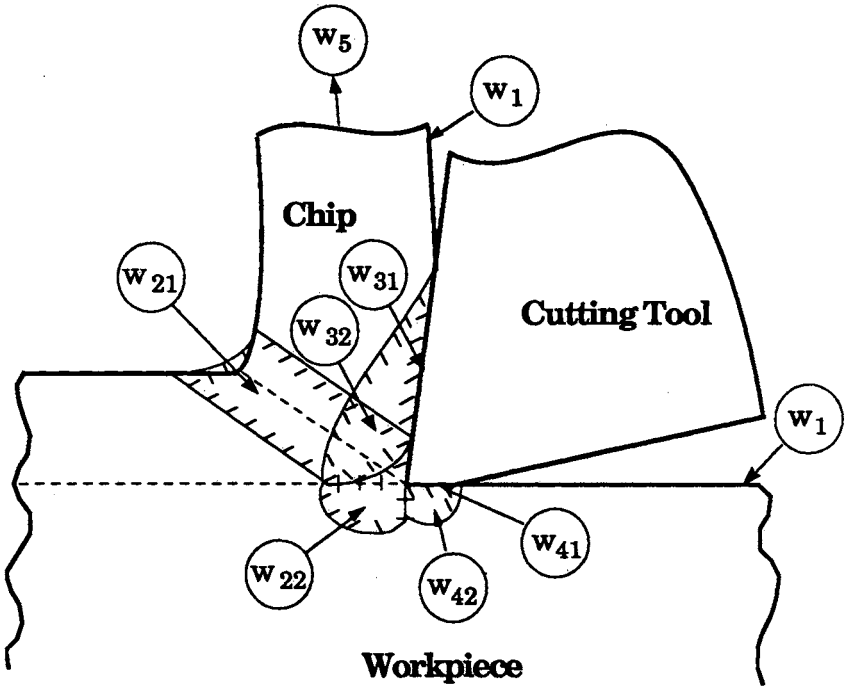

Figure 2-5. Nakayama and Tamura's Geometric Model for Energy Dissipation [Nakayama, 1968]

From experimental data, Nakayama and Tamura observed the ratio of plastic deformation of the machined surface to the contact length at the flank face to be from 1 to 2 for -40° and 0° rake angle respectively. They assumed that these ratios are too large to be due to flank friction, and thought this large plastic flow should be attributed to the extended shear zone effect. Even though they neglected w_4 as well as w_1 and w_5, they emphasized the importance of the energy due to the subsurface plastic flow

of the workpiece due to the extension of the shear zone below the subsurface as depth of cut decreases. They concluded that the size effect is caused by the subsurface plastic flow of the workpiece, decrease of shear angle, and negative increase of effective rake angle as the depth of cut decreases.

Through the systematic investigation of the energy dissipating zones for the possible causes of the size effect, Nakayama and Tamura introduced several important aspects of the mechanics of ultra-precision machining. Without relying on the traditional theory of the size effect such as theoretical strength, dislocation theory, and strain rate, they introduced a concept of extended shear zone below the subsurface of the workpiece and plastic deformation as well as tool edge effect. Their findings can be summarized as:

- an extended shear zone into the workpiece (subsurface plastic deformation) is introduced as an important energy dissipating zone when depth of cut decreases,
- the extended shear zone concept generates a question on the validity of the thin shear plane theory in micro-cutting, and
- the increased importance of the role of tool edge profile on energy dissipation at reduced depths of cut.

2.3.4.3 Moriwaki and Okuda's Model. Moriwaki and Okuda [1989] proposed two conceptual models depending on the depth of cut as shown in Fig. 2-6. For the case of a large depth of cut relative to the edge radius as shown in Fig. 2-6 a), the workpiece material is removed by the conventional cutting process and chip formation and surface integrity are

mostly influenced by the orientation and structure of the grains of the workpiece material.

When the depth of cut is comparable or less than the tool edge radius as shown in Fig. 2-6 b), the material is pushed with a large negative rake angle rather than removed efficiently. Thus, rubbing or burnishing dominates over cutting. Due to the rubbing or burnishing process, grain boundaries are no longer visible on both the chip surface and the newly created surface when depth of cut is reduced to the order of 0.1 μm. This depth of cut corresponds to 2-5 times the estimated tool edge radius. At lower depths of cut, plastic deformation involving burnishing and rubbing generates a larger thrust force than that is expected due to the decreased volume of the workpiece removed. In addition, a negative rake angle also affects the force components.

Through their experimental study using diamond tools, Moriwaki and Okuda found the importance of tool edge geometry. They found:

- the machining process at submicrometer depths of cut changes from a chip formation-dominant process to a rubbing and burnishing-dominant process,
- the transition depth of cut from a chip formation to a rubbing and burnishing-dominant process is about 2-5 times the tool edge radius, and
- the nonlinear thrust force with depth of cut may be due to the plastic deformation of the workpiece associated with the rubbing and burning process at decreased depth of cut.

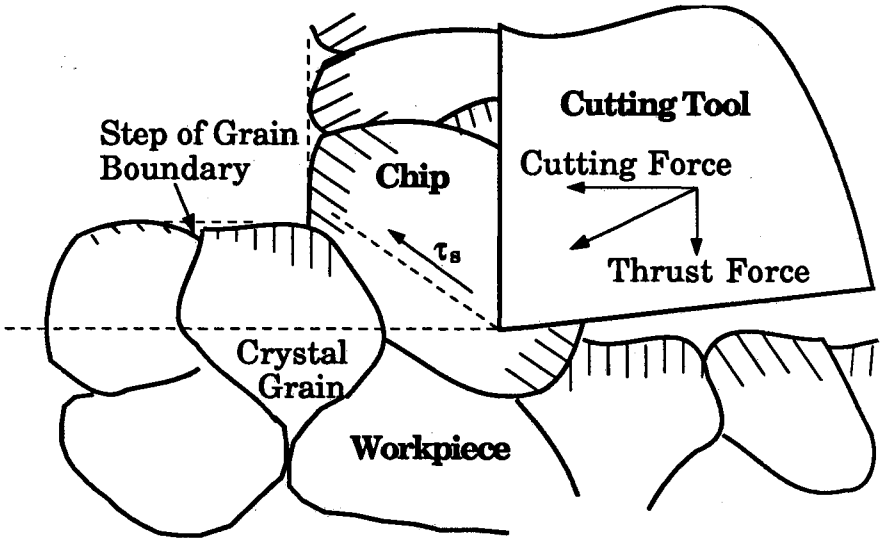

a) Model for Large Depth of Cut

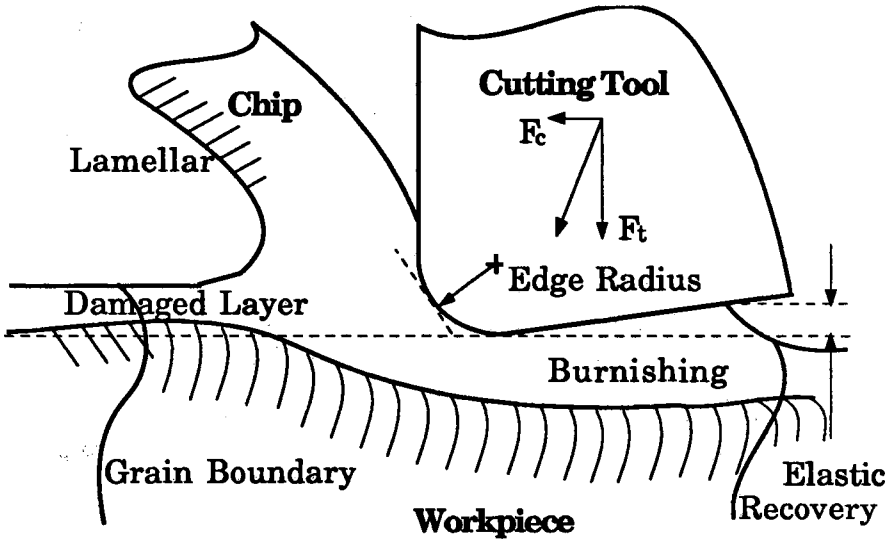

b) Model for Small Depth of Cut

Figure 2-6. Moriwaki and Okuda's Geometric Model for Energy Dissipation [Moriwaki, 1989]

2.4 Summary of the Present Understanding

2.4.1 Components of the Machining System

Machine tools for ultra-precision diamond turning are designed and fabricated using state-of-the-art technology to achieve nanometer accuracy. The accuracy of the machine tool is not a limiting factor for achieving dimensional accuracy and optimal surface finish of a workpiece.

Natural single crystal diamond tools are best suited for ultra-precision turning due to their superior mechanical and physical properties however, brittleness, sensitivity to crystallographic orientation, and low temperature for stability are limitations. The sharpest diamond tool edge reported is about 20 ~ 50 nm [Moriwaki, 1989].

Ductile, non-ferrous metals, polymers and some crystals are diamond turnable. Some brittle materials are successfully diamond turned in the laboratory. Steels and nickel alloys are known not to be diamond turnable due to severe tool wear. Through a better understanding of the governing process mechanics, the number of the diamond turnable materials could possibly be extended.

2.4.2 Process Mechanics

The lack of understanding of the process mechanics in ultra-precision diamond turning appears to be a major obstacle for improving workpiece quality. In ultra-precision machining, a dramatic increase in specific energy as depths of cut decreases (size effect) is one of the unique characteristics of the process. Increased shear energy alone is unable to account for the dramatic increase of the specific energy [Lucca, 1991b].

This result is identical with Albrecht's shear angle effect on the resultant cutting force, i.e., change of shear angle is not significant for the change of resultant cutting force [Albrecht, 1963].

Two orders of magnitude higher strain rate results in only less than 10 % increase in flow stress. This increase is much smaller than the observed increase in the specific energy at reduced depths of cut. Therefore, the strain rate effect may not be a significant contributor to the energy dissipation as depth of cut decreases.

2.4.3 Plowing and Sliding

Energy dissipation in ultra-precision machining can be divided into chip formation, and plowing and sliding energies similar to the grinding process. Sliding contact at the flank face of the tool is neglected in conventional machining however, as depth of cut decreases, the contact length at the tool-workpiece interface due to elastic recovery of the workpiece and tool flank wear may take a increased role in energy dissipation. For a quantitative understanding of the effect of the tool flank contact, measurement of this sliding length together with accurate force component measurement are essential.

The relative importance of the plowing and sliding process at decreased depth of cut necessitates the study of the plastic deformation of the workpiece. The neglected plastic deformation energy at the subsurface of the workpiece in conventional machining may take on an increased importance as depth of cut decreases.

2.4.4 Energy Models

Systematic work has been presented by Nakayama and Tamura in assessing energy dissipation in metal cutting. Even though they failed to analyze the effect of depth of cut on energy dissipation at submicrometer depths of cut (because of the limitation of the equipment), they pointed out the importance of energy dissipation due to subsurface plastic deformation of the workpiece by introducing the extended shear zone below the subsurface as depth of cut decreases. They recognized the importance of the tool edge radius as depth of cut decreases.

Through experimental work, Moriwaki and Okuda found that the process mechanics changes from a chip formation dominant process to rubbing and burnishing dominant process at submicrometer depths of cut. They also found that plastic deformation coupled with rubbing and burnishing may generate larger thrust forces than expected at smaller depths of cut.

2.5 Conclusions

The classical understanding of the mechanics of cutting is only good for the case of large depths of cut relative to the tool edge radius. As depth of cut decreases to the order of the tool edge radius, the validity of the classical theory of metal cutting needs to be re-examined. Through a review of the literature, the following is observed:

1) the energy dissipation in ultra-precision machining can be divided into chip formation, sliding and plowing,
2) the decrease of shear plane angle due to change in effective rake angle is unable to account for the size effect,

3) the effect of cutting speed on the specific energy needs to be examined further,

4) further experimental studies need to be performed to study the nonlinear force behavior and energy dissipation,

5) to study the effects of the tool geometry and flank contact, the tool edge should be characterized and the flank contact length must be measured precisely, and

6) workpiece behavior due to sliding contact which is neglected in conventional metal cutting must be examined. This includes both the elastoplastic deformation and resulting temperature rise.

CHAPTER III

PROBLEM DEFINITION

3.1 Problem Definition

3.1.1 Areas Where Questions Arise

3.1.1.1 Behavior of Forces with Depth of Cut. Knowledge of the force behavior in the cutting process is essential to understanding the process mechanics. Very little work has been done on the measurement of the force components for depths of cut in the submicrometer range (mainly due to machine tool limitations until recently). Accurate measurement of the force components is very difficult in ultra-precision machining due to their very low magnitudes. In conventional machining, the behavior of force with depth of cut is linear however, from a depth of cut which is on the order of or below the tool edge radius, the behavior seems to be nonlinear. This is believed to be related to the tool edge contour. The nonlinearity of the cutting force components must be examined further.

3.1.1.2 Tool Edge Characterization. To understand the behavior of forces with depth of cut, the geometry of the tool edge profile must be known accurately. Typical edge radii of newly sharpened single crystal diamond tools can range from submicrometers for commercially prepared tools down to tens of nanometers for specially prepared tools. Some specially sharpened diamond tools have been estimated to have edge radii

in the range of 20 ~ 50 nm [Moriwaki and Okuda, 1989; Shimada et al., 1992]. Due to such small edge radii, accurate measurement of the diamond tool edge radius is a formidable task. Scanning electron microscopy (SEM) technique can be employed to examine diamond tools, but charging effects of electrons with uncoated tools, and coating thickness uniformity on the tools which have been coated limit the accuracy of measured edge contours. The use of a specially configured SEM with two secondary electron detectors has also been reported [Asai, 1990], but a gold coating thickness of several tens of nanometers on the tool edge generates a question on the measured accuracy of a 20 ~ 45 nm edge radius. Other profiling instruments such as the laser interferometric microscope or step height profilometer which can vertically resolve atomic scale features are limited by their lateral spatial resolution. Recently, the use of atomic force microscopy (AFM) for mapping the 3D topography of surfaces with atomic lateral and vertical scale resolution has made it possible to examine the tool edge [Binnig, 1986].

3.1.1.3 Effect of Tool Edge (profile). Due to the lack of information about the tool edge, a study of the effect of tool edge contour on the measured force behavior was not previously possible. By knowing the tool edge profile or radius accurately, behavior of the obtained force components can be analyzed using the measured edge profile.

3.1.1.4 Effect of Cutting Speed. There have been some argument on the cause of the size effect. Among the reasons given, the effect of strain rate on the substantial increase in specific energy due to cutting speed has

not been experimentally examined. The effect of the speed on the force behavior needs to be examined further.

3.1.1.5 Plowing and Sliding. The mechanisms of energy dissipation in ultra-precision machining can be divided into chip formation, plowing and sliding (similar to the mechanisms in grinding [Malkin, 1974a]). At large depths of cut, the plowing and sliding process has been neglected relative to the dominant chip formation process. Based on measured forces, the significance of the plowing and sliding needs to be further investigated.

3.1.1.6 Contact at the Tool-Workpiece Interface. The mechanics of conventional machining has been formulated for the case of continuous chip formation in which flank frictional contact and heating at the tool-workpiece interface is neglected. It has been proposed that the flank contact in this case may cause a significant shift in the partition of energy between energy dissipating zones [Lucca, 1989]. For single point diamond turning, the literature shows that substantial flank wear occurs when machining an aluminum alloy [Sugano, 1987]. However, the effect of tool-workpiece contact on energy dissipation, if any, has not been investigated.

3.1.1.7 Plastic Deformation and Temperature Rise of the Workpiece. Mechanical energy dissipation due to plastic deformation at the surface of the workpiece is known to be significant in rolling and sliding processes [Merwin, 1963]. The mechanical energy dissipation and the resulting temperature rise affects not only the mechanics involved but also the tool performance, workpiece dimensional accuracy, and surface integrity. Based on an experimental study, a simplified analytical model for the

prediction of the elastoplastic stresses and resulting temperatures should be developed.

3.2 Objectives and Scope of the Study

3.2.1 Research Objectives and Significance

The objectives of the present study are:

- experimental investigation of the effect of energy dissipation in orthogonal ultra-precision machining due to the change of tool edge conditions, cutting speeds, and workpiece materials, and
- development of an analytical model which will enable prediction of workpiece stresses and temperature fields in single point diamond turning at submicrometer depths of cut.

The study will attempt to explain the mechanism of energy dissipation by investigating dependence of measured force components and predicted stress and temperature fields on the process variables and the workpiece materials. The uniqueness of the process mechanics in the ultra-precision machining will be studied through experimentation and analytical modeling.

Understanding the effects of process conditions on the ultra-precision machining process could possibly enable extension of the range of tool-workpiece combinations and diamond turnable materials. If developed, an elastoplastic stress and temperature model would contribute to the understanding some of the process mechanics in ultra-precision machining.

3.2.2 Scope of the Research

The experimental approach includes investigation of the effect of cutting conditions on force behavior through the measurement of 2D cutting force components. Carefully characterized single point diamond tools will be employed to study the effect of tool edge contour on the resulting cutting force components. For workpieces, ductile materials including copper and aluminum will be used. Tool flank contact length will be measured using a AuPd coating technique.

Theoretical model development will include calculation of stress and temperature fields. Based on an elastic model, the final elastoplastic formulation can be obtained using Merwin and Johnson's [1963] step-by-step numerical technique. Using the measured contact length at the tool-workpiece contact and force components as an input data for the model, the elastoplastic stress and temperature rise will be estimated.

The specific goals of the present research are to:

- develop a technique for accurate force measurement during orthogonal ultra-precision diamond turning;
- accurately characterize the tool edge (profile) using SEM and/or AFM;
- perform experimental studies for the effects of tool geometry, cutting speed, and depth of cut on forces in single point diamond turning of aluminum 6061-T6 and/or tellurium copper;
- measure the tool-workpiece contact length at submicrometer depths of cut using a AuPd coating technique; and
- develop an analytical model for the workpiece subsurface elastoplastic stress distributions and temperature fields.

CHAPTER IV

EXPERIMENTAL STUDY OF ENERGY DISSIPATION AND CONTACT LENGTH AT THE FLANK INTERFACE IN ORTHOGONAL FLYCUTTING OF AL 6061-T6

4.1 Introduction

The objectives of this initial experiment were to measure the cutting and thrust forces accurately and to investigate the significance of the contact length at the tool-workpiece interface as depth of cut decreases from tens of micrometers down to tens of nanometers on energy dissipation. The cutting and thrust forces in metal cutting is of primary importance because they govern the phenomena occurring in the cutting process. It is well known that in machining, most of the mechanical energy which is imparted to the tool-workpiece system is transformed into heat (97 - 99 %) [Shaw, 1983]. This dissipation of mechanical energy and the subsequent temperature rises is known to affect the chip formation process, tool wear, the resulting workpiece subsurface damage, and the final metallurgical state of the material.

In this chapter, the initial shakedown experiments for the orthogonal flycutting of Al 6061-T6 are described. The machine tool, diamond tool, and data acquisition system which were used during the machining

experiments are also described. Before machining, a single crystal diamond tool was coated with AuPd and measured edge radius using the SEM. This was to study the effect of tool edge radius on resulting forces and energies. The characterization capability was limited to 2D. Cutting and thrust forces were measured during machining Al 6061-T6 from 10 nm to 20 μm depth of cut. Contact length at the tool-workpiece interface was measured at three different depths of cut, i.e., 0.01, 0.1 and 1 μm. This was to investigate the significance of the contact length at submicrometer depths of cut. An initial study on the effects of new and worn tools on energy dissipation were also performed.

4.2 Experimental Diamond Turning Configuration

Accurate measurement of the cutting force components is critical in understanding the governing physical mechanisms in metal cutting. In order to measure the force components accurately at very small depth of cut, careful attention must be paid to the method of cutting and data collection. Here, some of the important aspects of the cutting experiment are discussed.

4.2.1 Cutting Geometry

4.2.1.1 Orthogonal Cutting vs. Oblique Cutting. Most practical cutting processes are complex in geometry. Cutting operations can be divided into two categories, i.e., orthogonal cutting and oblique cutting. Orthogonal cutting is the simpler case where cutting is performed with the tool edge perpendicular to the cutting velocity. In oblique cutting, the cutting edge is inclined some angle to the cutting velocity. Thus, orthogonal cutting

creates a two dimensional force system and oblique cutting generates a three dimensional cutting force system. Due to its simpler cutting force system, orthogonal cutting is used in the experiment of the present study.

4.2.1.2 Flycutting vs. Plunge Cutting. In flycutting, the workpiece is stationary and the tool is rotating. Usually, rectangular shaped workpiece specimens are used. In addition to the flycutting, plunge cutting is sometimes used to achieve orthogonal cutting condition [Rhorer, 1986]. In the plunge cutting, a serrated disk is rotated and a tool is fed in the radial direction. The full width of the disk is cut as the disk rotates. Flycutting configuration has some advantages over plunge cutting:

- a force transducer can be placed directly behind the stationary workpiece. Thus, accurate force measurement can be achieved, and
- a wide range of cutting speeds can be obtained by changing the radius of tool's rotation.

For the present study, all the experiments were performed using an orthogonal flycutting geometry.

4.2.2 Experimental Set-Up

4.2.2.1 Overall Set-Up. A state-of-the-art commercial diamond turning machine was used. The fixture for holding tool and workpiece including a tool holding plate, tool holder, workpiece holder, and dynamometer holding block were designed and fabricated. The overall experimental set-up which was used throughout the current study is shown in Fig. 4-1. The diamond tool is clamped to the tool holder which is bolted to the tool holding plate. This plate is held by the vacuum chuck of

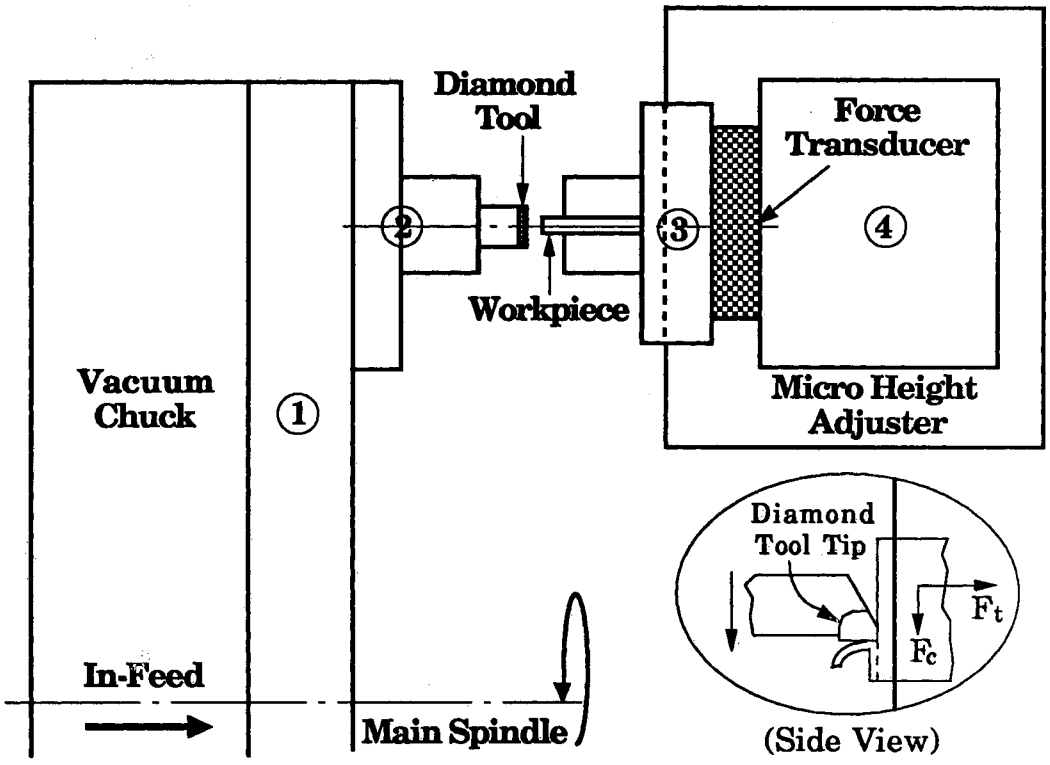

1: Tool holding plate, 2: Tool holder, 3: Workpiece holder,
4: Dynamometer holding block

Figure 4-1. Schematic Diagram of Experimental Set-Up of Orthogonal Flycutting Geometry (Top View)

the machine tool main spindle which rotates to produce a desired cutting speed and in-feeds to produce a desired depth of cut. The workpiece is clamped in the workpiece holder. Directly behind the holder is the dynamometer used to measure the 2D force components during machining. The two channels of the force signals from the dynamometer enter into amplifiers and then go into the oscilloscope and then to the personal computer for data storage and processing.

A flat nose, single crystal diamond tool is rotated 76.2 mm off the spindle axis to provide the cutting motion, and a rectangular workpiece is held on top of a dynamometer which allows the measurement of the cutting and thrust forces. The experimental set-up provided orthogonal flycutting to be performed on a stationary workpiece.

4.2.2.2 Machine Tool. A submicron turning and grinding machine (Rank Pneumo Model ASG-2500) was used throughout the current experimental study. The overall features and capabilities of the machine tool are shown in Table 4-1 (turning specifications only).

4.2.2.3 Diamond Tool. Two flat nosed, single crystal diamond tools made by Norton Co. were used. The width of the nose was about 2 mm along the cutting edge and was used to cut a 1 mm thick workpiece. The included angle of the nose at the rake face was about 60°. The diamond crystal was vacuum brazed to a carbon steel shank and was oriented such that the rake face was a {110} plane with a {100} plane parallel to the cutting direction.

TABLE 4-1

FEATURES AND CAPABILITIES OF THE ASG 2500
SUBMICRON AND GRINDING MACHINE
[Rank-Pneumo, 1990]

Description		Features and Capabilities
Control System		Allen Bradley Series 8200 CNC
Feedback System (Closed-Loop)		Hewlett Packard Model 5518 Laser Interferometer
System Resolution		10 nm (0.4 μin)
Vibration Isolation		Passive Air Isolator (3 Points)
Slideways	Design Slideway Travel Main Spin Travel Velocity	Hydrostatic Oil Bearing 254 mm (10 in) 152 mm (6 in) 0.25 ~ 760 mm/min (0.01 ~ 30 in/min)
Workpiece Spindle	Design Speed Range Load Capacity	Air Bearing 100 ~ 2400 rpm 450 N (100 lbs)
Max. Machinable Workpiece Dimensions	Diameter Length	304 mm (12 in) 152 mm (6 in)
Utilities	Electrical Power Air Supply	230 VAC/3 KVA 0.7 MPa (100 psi) /15 CFM
Required Floor Space		1.83 x 2.74 m (72 x 108 in)

4.2.2.4 Workpiece. A rectangular shaped 1 mm thick, 15 mm long, 12 mm wide Al 6061-T6 workpiece was used. The maximum variation of the thickness was ± 5 %. The workpiece was positioned with its length tangent to the tool rotation, and was 76.2 mm off axis which is also the tool's radius of rotation. The 15 mm long workpiece occupied 11.28° of the 76.2 mm radius circle of the tool rotation. The initial overhang length of the workpiece from the workpiece holder was 2 mm in width direction, and remaining width of about 10 mm was inserted and clamped into the workpiece holder. The rotating tool's constant infeed rate corresponded to the depth of cut. The magnitude of the off axis dimension compared to the length and width of the workpiece allowed for orthogonal "planing" of the workpiece to be achieved. A constant infeed assured a known depth of cut, independent of any elastic recovery of the material behind the tool edge. The interrupted cutting avoids the problems associated with the DC drift of the force signals during cutting.

4.2.2.5 Dynamometer. A Kistler 9251A piezoelectric force transducer (dynamometer) was positioned directly behind the workpiece holder to measure 2D force signals during machining. Since the cutting force components must be transmitted through the friction at the mounting interface, the transducer must be heavily preloaded. It is recommended that the preload must be greater than a maximum expected force by at least a factor of 10. Also, a thin coating of oil or grease was recommended to be applied on both the mating surfaces of the transducer to provide the transmission of high frequency forces. The technical data for the Kistler 9251A force transducer are listed in Table 4-2.

TABLE 4-2

TECHNICAL DATA FOR KISTLER 9251A
FORCE TRANSDUCER
[Kistler]

Description	Data
Measuring Range (with 25 kN preload) Compression and Traction Shearing	 ±5000 N ±2500 N
Resolution	0.01 N
Sensitivity Compression and Traction Shearing	 3.87 pC/N 8.03 pC/N
Stiffness Axial Transverse	 1000 N/μm 300 N/μm
Natural Frequency (with 4 N in axial)	8 kHz
Linearity (max. error)	± 1 %
Insulation Resistance	$5x\ 10^{13}\ \Omega$
Capacity	30 pF
Operating Temperature	- 60 to 250° C
Max. allowable Bending Moment	 100 Nm
Weight and Dimension	0.32 N (24x24x10 mm)
Material	Stainless Steel

4.2.2.6 Amplifier. Kistler 5004 dual mode signal amplifiers were employed for each channel. The maximum specified amplifier DC drift was 0.03 pC/sec. To eliminate the drift, the amplifier was reset just before each measurement of the force components.

4.2.2.7 Oscilloscope. The force signals from the force transducer were displayed on a Lecroy 9400 oscilloscope via amplifier, and were saved or processed using a personal computer. The sampling rate corresponded to sampling of about 250 data points during cutting (excluding uncut time period) at 7.62 m/min cutting speed which is used for most of the current experimental study.

4.2.2.8 Assembly. In order to provide a better contact and alignment, all mating surfaces were lapped using No 3600 abrasive paste on the lapping plate before assembly. A micro-height adjuster was mounted on the slideway table of the machine tool. The dynamometer holding block was clamped on top of the micro-height adjuster. Using a dynamometer clamping bolt, the workpiece holder (which has a threaded blind hole on the sides mating with the dynamometer, and the dynamometer holding block were clamped together through their center holes. Before the assembly, a special lubrication grease (type 1063 supplied by the Kistler Co.) was applied on both of the mating surfaces of the force transducer. An axial preload of 4000 N was applied to the clamping bolt in tightening the force transducer, which is about 3 orders of magnitude greater than the anticipated resultant force. This is to assure the stiffness of the system. The applied preload was checked using the signal output from the force transducer during the clamping. Also, the perpendicularity of the

workpiece holder to the surface of the machine tool slideway was carefully adjusted using a level gage with a square block. This was done to assure the tool-workpiece alignment. The workpiece was clamped to the workpiece holder after lapping the mating sides with the workpiece holder.

The tool holding plate with tool holder (pre-assembled) was mounted on the vacuum chuck of the machine tool's main spindle. The mating surface of the vacuum chuck was also stoned with an ultra-fine stone to remove possible debris on the surface. Finally, the tool was mounted on the tool holder and was aligned with workpiece such that the 2 mm flat tool edge could cut the entire 1 mm width of the workpiece.

4.2.2 9 Programming of the Cutting Operation. For the cutting operation, a simple program was made:

```
G01G71G90G95
M04S100
X-76.2Z2.0
Z0F3
Z-0.01F0.001
Z0F3M02
```

The first line or "block" is the master control block. G01 represents linear interpolation of the motion, G71 is for mm units, G90 is for absolute position, G95 is for mm/rev for feed. In the second block, M04 is for counter clock-wise rotation of the main spindle and S100 is the spindle speed in rpm. The blocks from the third to 6th represent the coordinates to move when the block is executed by the controller of the machine tool. Here, Z is the axial direction of the main spindle, X is the transverse slide

direction, and F is the feed rate in mm/rev respectively. M02 in the last block represents the end of the program. The depth of cut can be assigned by F in the 5th block.

4.2.3 Tool Edge Characterization Using SEM

From low magnification under a Normarski microscope, rake and clearance angles were measured. The edge radii were estimated using the SEM at 20,000 times magnification. The geometry of the tools used are shown in Table 4-3.

TABLE 4-3

SINGLE CRYSTAL DIAMOND TOOLS USED IN ORTHOGONAL FLYCUTTING OF AL 6061-T6

Tool	Rake Angle	Clearance Angle	Edge Radius
Tool 1	0°	6°	0.2 μm
Tool 2	-2.0°	6°	0.2 μm

Before the cutting experiment, two new single crystal diamond tools, Tool 1 and Tool 2 were coated with approximately 5 nm in thickness of AuPd and then examined under the SEM. The coating thickness was controlled using a coating rate, i.e., the tools were placed under the SEM Coating System Model SC502 for 15 sec at a coating rate of 3 Å/sec. Fig. 4-2 shows the observed edge geometry for Tool 1. Since the tool is flat-nosed, it is positioned in the SEM with the line of sight along the cutting edge.

Normal viewing could be assured by slightly tilting the tool such that both the rake and flank faces appeared as lines. The two-dimensional tool geometry was characterized before cutting, and the measured edge radii for both tools were estimated to have about 0.2 μm as shown in Table 4-3.

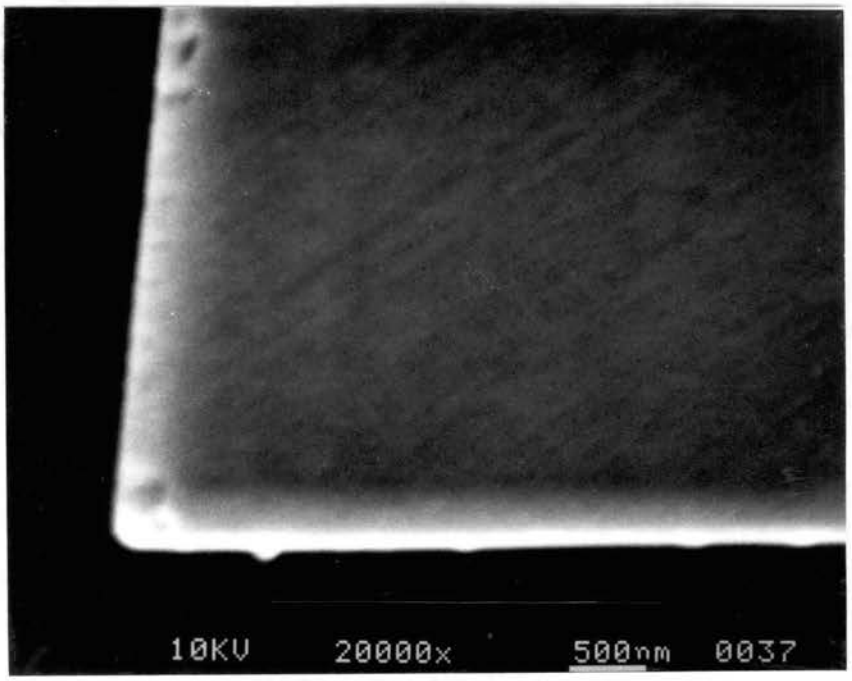

Figure 4-2. SEM Photo of Single Crystal Diamond Tool Edge

The coating thickness of about 5 nm was negligible relative to the estimated tool edge radius of 0.2 μm. Asai et al. [1990] used a conventional SEM which was configured to have two secondary electron detectors for measuring tool edge radius. They used a Au coating technique to prevent the diamond from charging however, the coating thickness of 17 nm to measure 20 ~ 45 nm edge radius raises questions about the accuracy of the measured edge radius. Coating techniques and SEM observation may not be good for nanometer edge resolution.

4.2.4 Cutting Conditions

For all the experiments described in this initial shakedown, cutting was performed on 6061-T6 aluminum specimens at a cutting speed of 7.6 m/min. The depth of cut ranged from 0.01 μm to 20 μm. Cutting was performed without lubricant. Careful attention was paid to the potential presence of a built-up edge, however, both microscopic examination of the tool before and after cutting verified that no built-up edge at the diamond tool tip was formed. Also the consistency of the measured forces was additional evidence that a built-up edge was not present under these cutting conditions.

4.3 Initial Experimental Results

4.3.1 Measured Force Signals

Two 6061-T6 aluminum specimens were cut using Tool 1. During machining, cutting and thrust force signals were recorded on a personal computer via the dynamometer, amplifier, and oscilloscope. Typical unfiltered signals are shown in Figs. 4-3, 4-5, 4-7 and 4-9, and averaged signals are in Figs. 4-4, 4-6, 4-8, and 4-10 for 0.01, 0.1, 1.0, and 10 μm depth of cut respectively. As shown in the figures, very repeatable force signals were obtained from the interrupted orthogonal flycutting geometry. The base line corresponds to the time when the tool is out of the cut, and the signals representing the forces during cutting are the step heights above the base line. For efficient data storage, the total out-of-cut signal has not been saved. At a depth of cut of 0.01 μm, the thrust force is much greater than the cutting force. However, at 10 μm depth of cut, the cutting force is

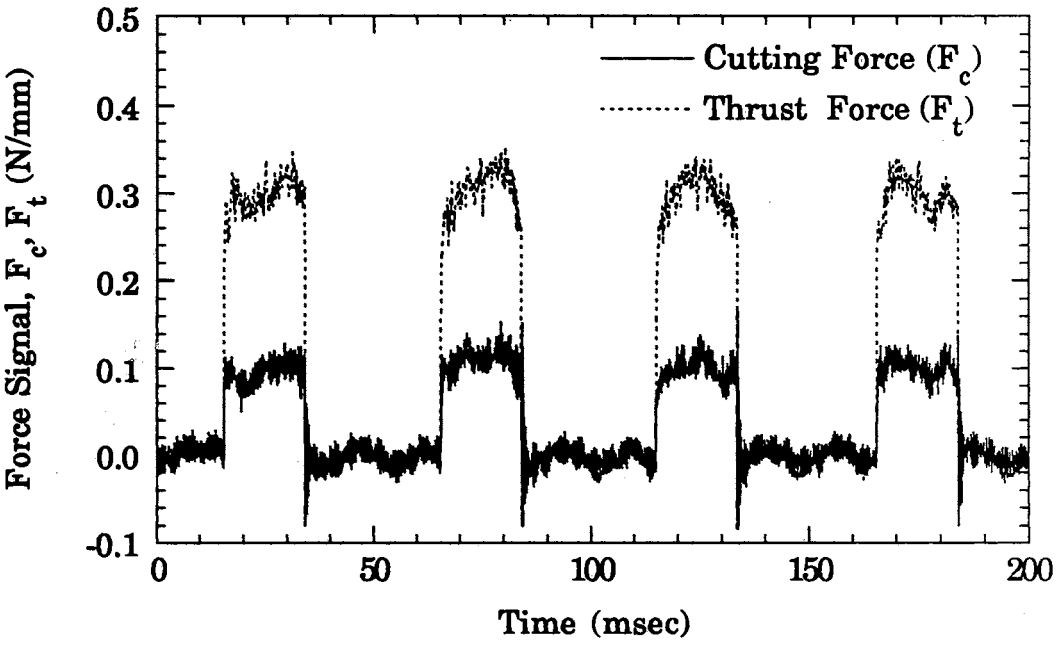

Figure 4-3. Measured Cutting and Thrust Force Signals During Machining of 6061-T6 Aluminum at 0.01 μm Depth of Cut

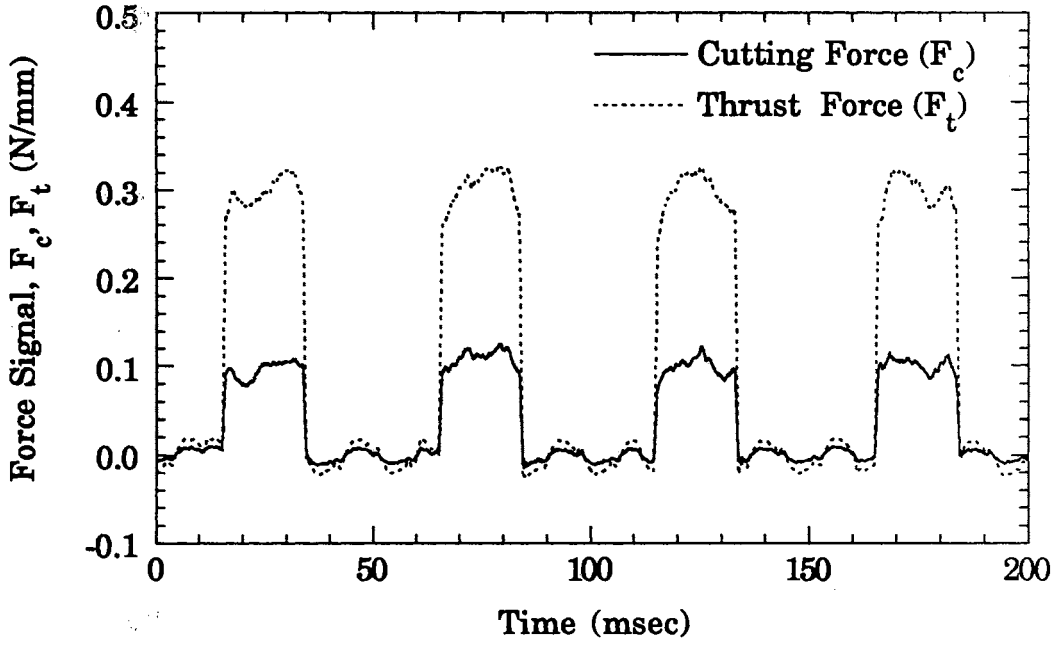

Figure 4-4. Averaged (19 points) Cutting and Thrust Force Signals in Machining of 6061-T6 Aluminum at 0.01 μm Depth of Cut

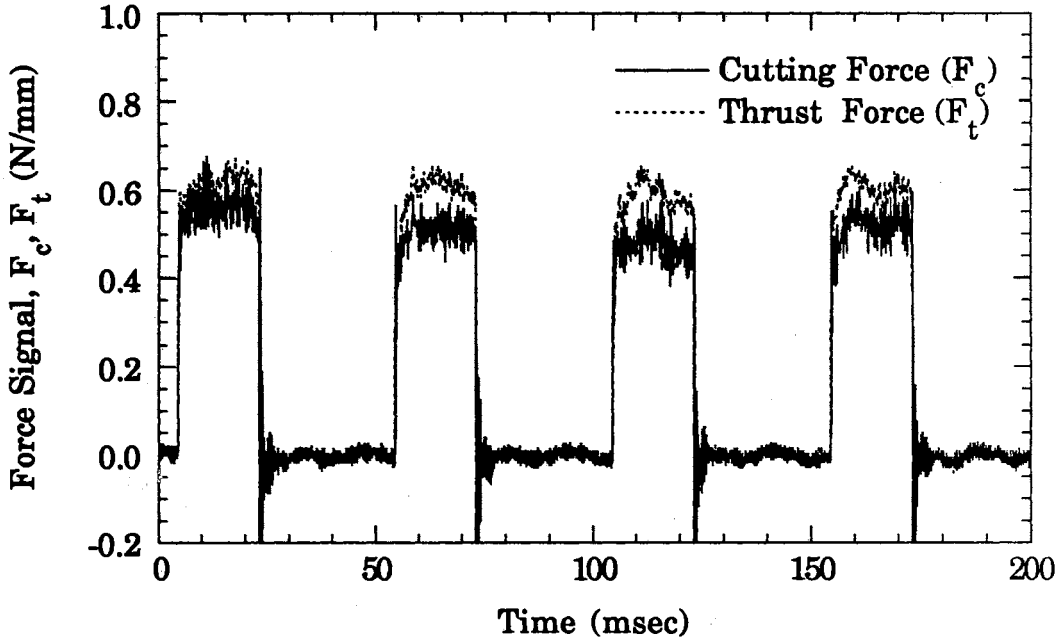

Figure 4-5. Measured Cutting and Thrust Force Signals During Machining of 6061-T6 Aluminum at 0.1 μm Depth of Cut

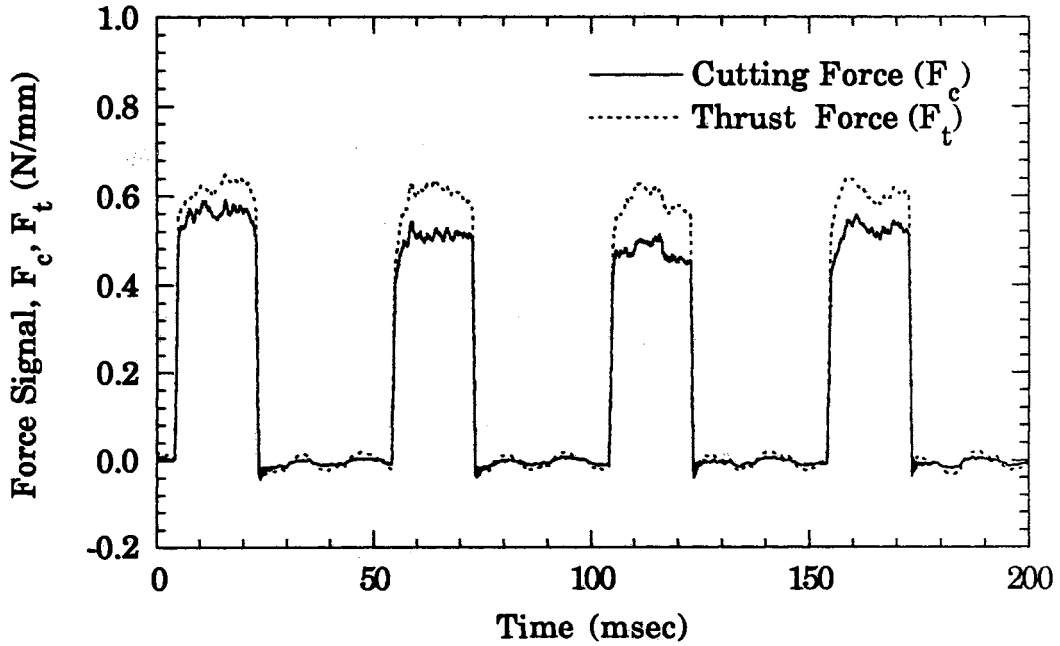

Figure 4-6. Averaged (19 points) Cutting and Thrust Force Signals in Machining of 6061-T6 Aluminum at 0.1 μm Depth of Cut

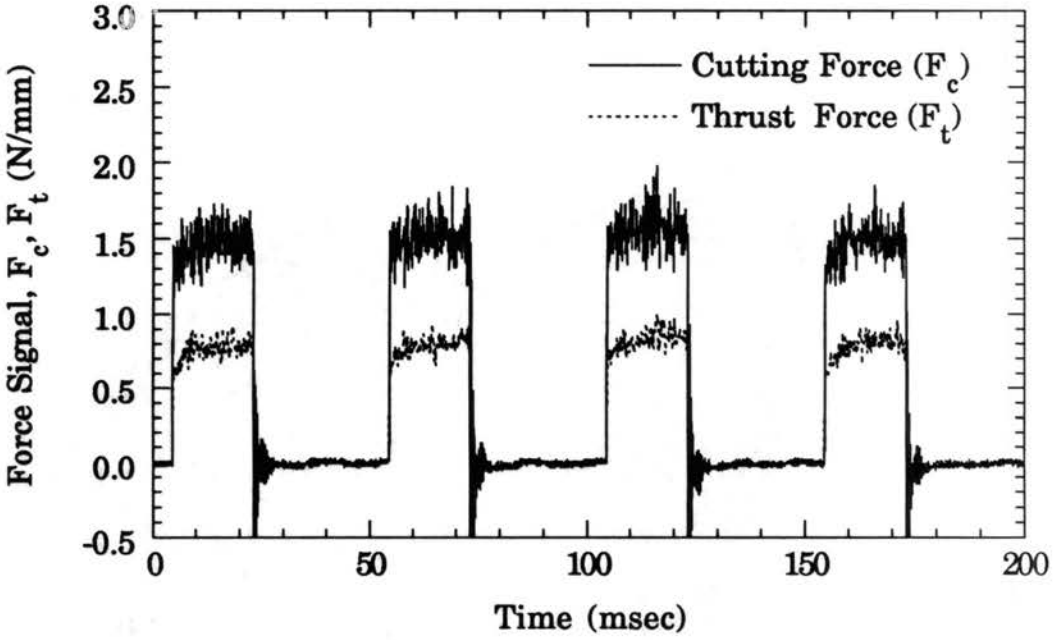

Figure 4-7. Measured Cutting and Thrust Force Signals During Machining of 6061-T6 Aluminum at 1 μm Depth of Cut

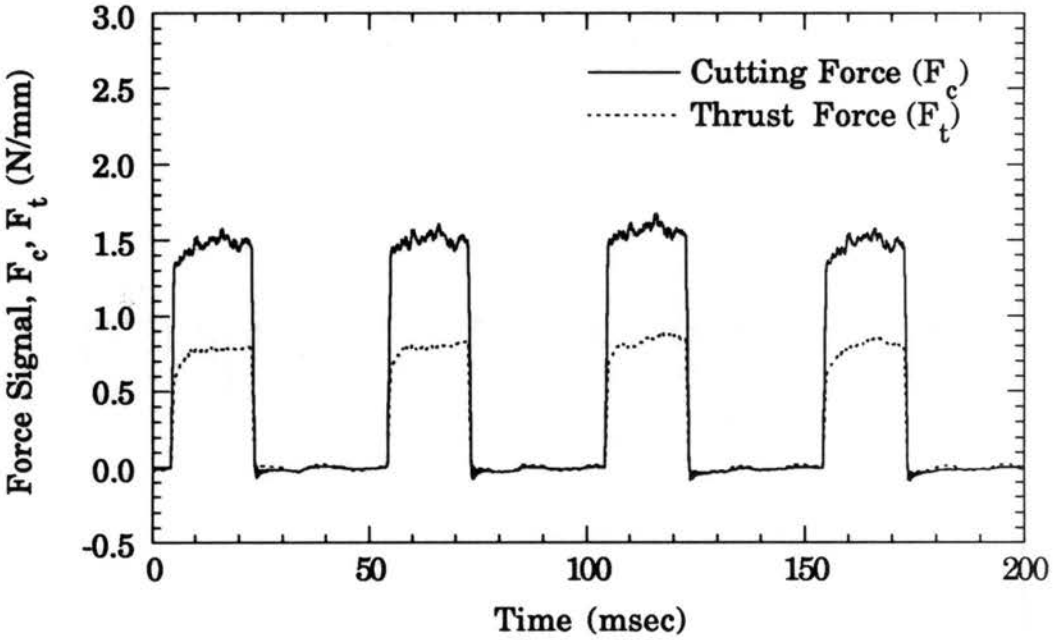

Figure 4-8. Averaged (19 points) Cutting and Thrust Force Signals in Machining of 6061-T6 Aluminum at 1 μm Depth of Cut

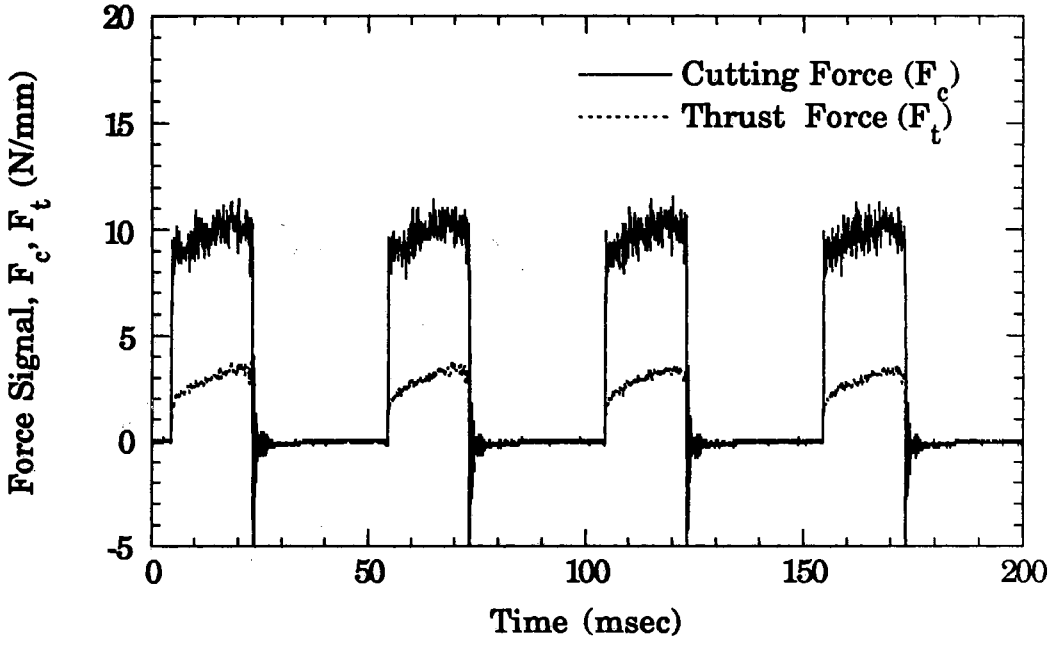

Figure 4-9. Measured Cutting and Thrust Force Signals During Machining of 6061-T6 Aluminum at 10 μm Depth of Cut

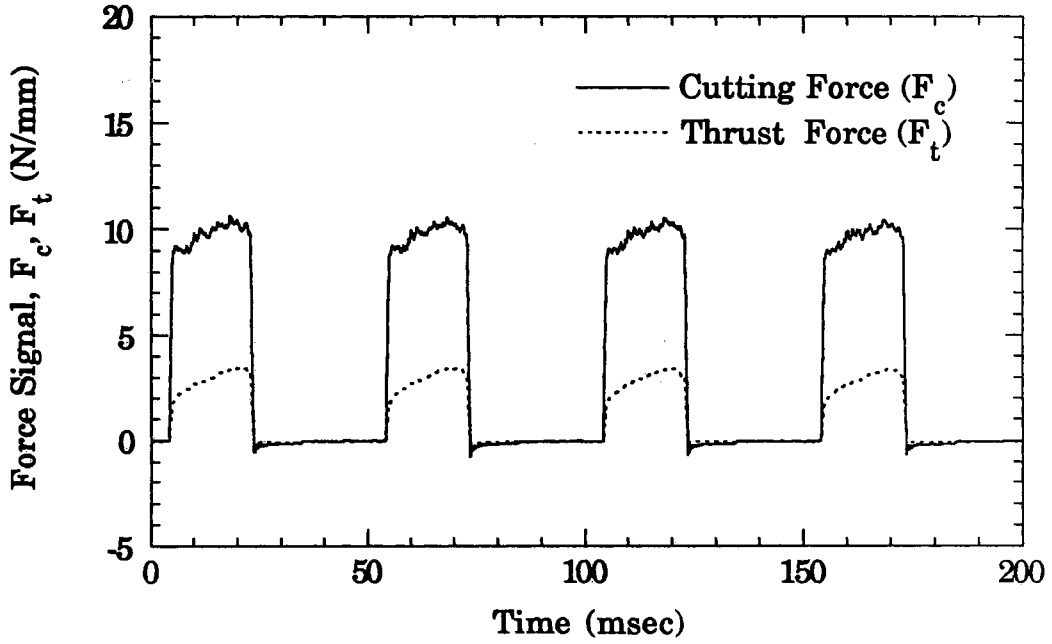

Figure 4-10. Averaged (19 points) Cutting and Thrust Force Signals in Machining of 6061-T6 Aluminum at 10 μm Depth of Cut

much greater than the thrust force. The base line variation of cyclic change is due to the power line frequency of 60 Hz noise with a magnitude of about the resolution of the dynamometer (0.01 N). Also, the total force in the cutting direction, that from which the total specific energy is based upon, is quite small, i.e., about 0.1 N for cutting a 1 mm thick 6061-T6 aluminum workpiece. Some of the initial results in this chapter have been reported elsewhere [Lucca, 1993c].

4.3.2 Measured Force Components

The magnitudes of the cutting and thrust forces were obtained from the average heights in the cyclic signals from the oscilloscope from 0.01 to 20 μm depth of cut using Tool 1. Cutting was performed at 7.6 m/min without cutting fluid. For depths of cut below 1 μm, cutting was performed continuously until stable step heights were obtained at a given depth of cut. The fluctuation seems to be due to the unstable cutting action at reduced depths of cut. The unstable cutting action may be resultant from the effect of the tool's local profile interaction with the microcracks and/or secondary particles of the workpiece. Four consecutive step heights which represented the stable cutting, were taken from the oscilloscope for the cutting and thrust force at each depth of cut. An average of those four step heights were taken as a cutting or thrust force at that depth of cut. The results are shown in Figs. 4-11 ~ 4-14. In Fig. 4-11, cutting and thrust forces are shown as a function of depth of cut. These data are obtained from two different aluminum workpieces of Specimen 1 and Specimen 2. The repeatability of the force components from Specimens 1 and 2 was ± 5 % with respect to the mean value of the two. The curves show the same

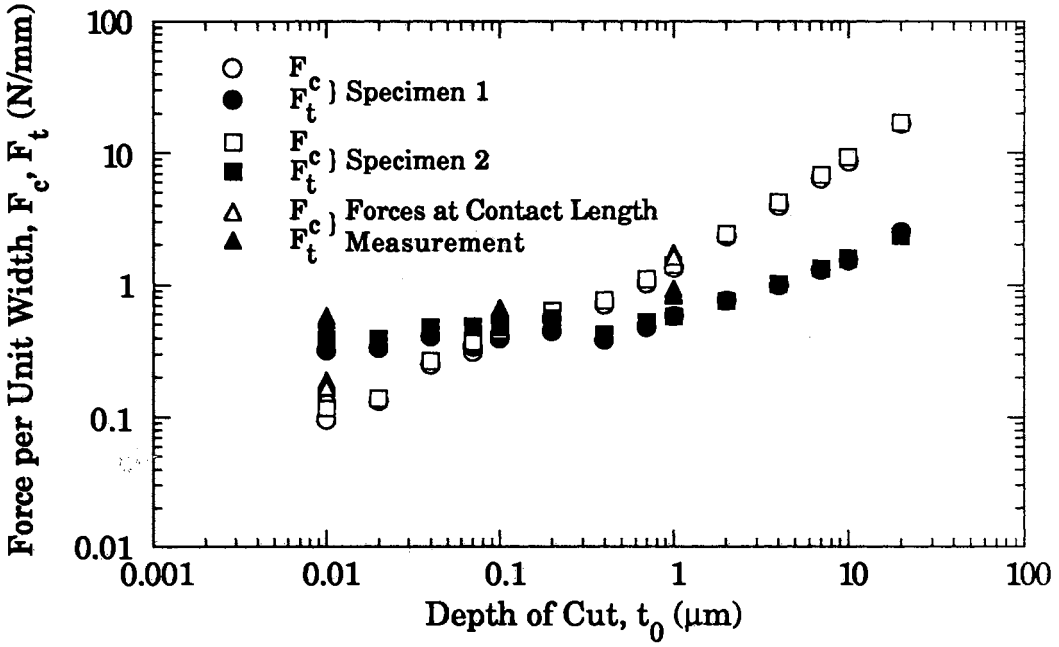

Figure 4-11. Effect of Depth of Cut on Force Components in Machining of 6061-T6 Aluminum

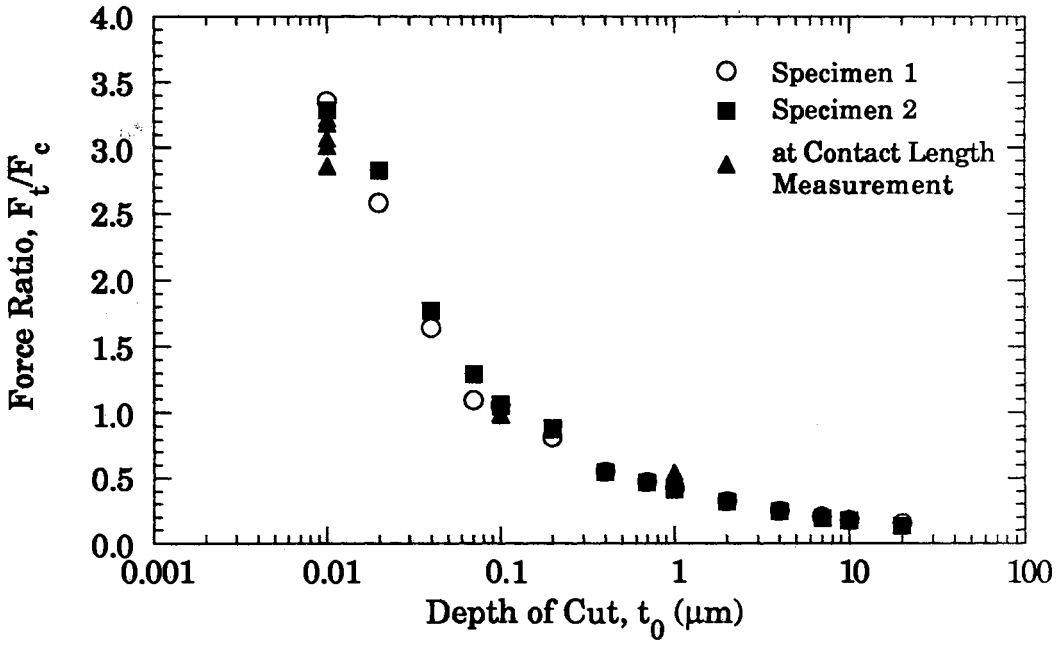

Figure 4-12. Effect of Depth of Cut on Force Ratio in Machining of 6061-T6 Aluminum

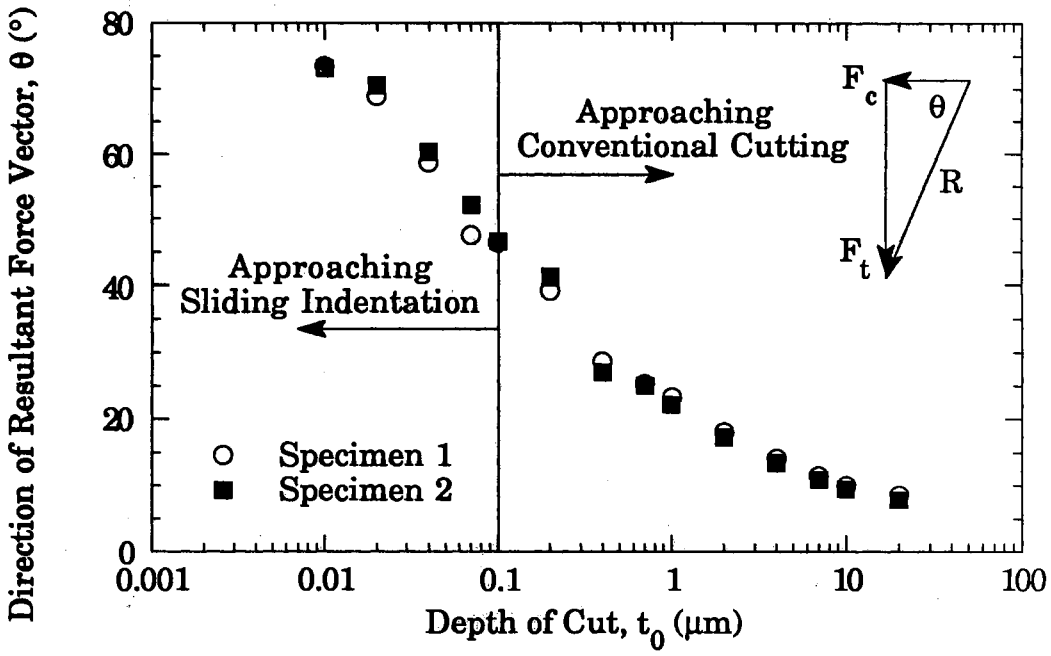

Figure 4-13. Effect of Depth of Cut on the Direction of Resultant Force Vector in Machining of 6061-T6 Aluminum

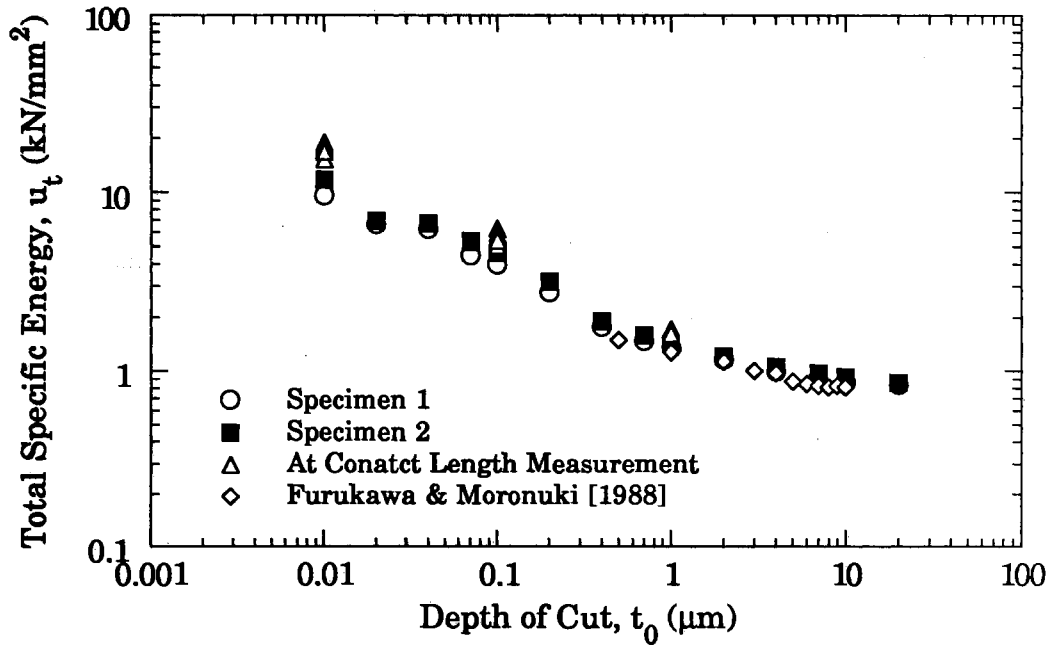

Figure 4-14. Effect of Depth of Cut on Total Specific Energy in Machining of 6061-T6 Aluminum

trends as that of copper [Moriwaki, 1989; Lucca, 1991a, 1991b, 1992], viz, a linear decrease in both cutting and thrust force down to 1 ~ 2 μm but nonlinear below that, and a cross-over of the cutting and thrust force curves at about 0.15 μm depth of cut. The magnitude of the thrust force dominates over the cutting force below this depth of cut. At 10 nm depth of cut, the magnitudes of the cutting and thrust forces are about 0.1 N and 0.4 N, which are more than 10 times the resolution of the force transducer. From the cutting force data, it can be seen that the total energy dissipated in the process decreases two orders of magnitude over the range of depth of cut from 10 μm to 10 nm, however the thrust force decreases less than one order of magnitude in this range.

Fig. 4-12 shows the ratio of thrust to cutting force as a function of depth of cut. This again shows the thrust force is the dominant force component for the depths of cut below the depth of cut of cross over of force components. The thrust force is about 3.3 times the cutting force at 10 nm depth of cut however, at 10 μm depth of cut, the ratio is about 0.2, which approaches a typical value for conventional machining.

When the force ratios are converted to the direction of resultant force vector using $\theta = \tan^{-1}(F_t/F_c)$, this direction vs. depth of cut is plotted as shown in Fig. 4-13. Here, a severe rotation of the resultant force vector downward towards the workpiece as depth of cut decreases is observed. At 10 nm depth of cut, the direction of resultant force vector is about 75° downward from the cutting direction. At the high end of depth of cut (20 μm), the direction is only several degrees off from the cutting direction. This change of the direction of the resultant force vector downward toward the workpiece can be viewed as resulting in a sliding indentation problem from the depth of cut below the cross-over point of the cutting and thrust

force ($\theta = 45°$). At the lower end of the depth of cut, the direction of resultant force vector would reach the value of pure sliding indentation. At the high end of depth of cut, the direction approaches the cutting direction, which is the case for conventional metal cutting. This trend seems to be a characteristic of all the experimental results obtained in the microcutting of ductile materials.

Fig. 4-14 shows the total specific energy calculated from the cutting force using $u_t = F_c\, V/(t_0\, wV)$. This value represents the energy expended per unit volume of the material removed. Included in Fig. 4-14 is the result of Furukawa and Moronuki [1988] for aluminum alloy cutting using a 0° rake and 2 ~ 3° clearance angle tool. The overall trend of increasing specific energy with decreasing depth of cut is consistent with the result of Furukawa and Moronuki. This trend also agrees with that reported for the microcutting of a variety of ductile materials [Moriwaki, 1989; Lucca, 1991a, 1991b, 1992]. This figure clearly shows the size effect. As depth of cut decreases from 10 μm to 10 nm, the total specific energy increased from 1 kN/mm^2 to more than 10 kN/mm^2. The differences between the two experiments are the cutting speed of 7.6 m/min for the present experiment and 6 m/min for Furukawa and Moronuki's experiment. Cutting fluid was not used for the present study unlike the experiments of Furukawa and Moronuki which used kerosine. Also, the tool edge geometry was not specified for their experiments.

From Figs. 4-11 ~ 4-14, it is recognized that there are many uncertainties in machining below a depth of cut of about 30 nm. The uncertainties may be due to temperature variation, asynchronous motion of the spindle, in-feed motion during machining, and the atomic interaction of the tool and the workpiece. These uncertainties may result

in differences between the apparent depth of cut and the true depth of cut, and may not be negligible below about 30 nm [Lucca, 1993a]. However, the repeatability of the data, and the fact that the cutting force continues to drop, may indicate that accurate depths of cut down to 10 nm with the current set-up are achievable.

The temperature variation of the diamond turning machine environment is controlled within ± 2 °C however, small changes of the environment temperature is significant at small depths of cut. For an aluminum alloy, the thermal expansion is about 25 nm for a 1 mm long specimen (α = 2.52 x 10^{-5} mm/mm/°C) for a unit degree Celsius temperature rise. The asynchronous motion of the spindle affects the true rotational position of the spindle centerline. This motion would affect the control of the ultra-precision machine tool, in particular, the depth of cut. The atomic interaction could be a mechanical and chemical interaction between the tool and the workpiece where surface creation is predominant over a bulk material removal, however this is unlikely since the surface energy of metals is on the order of 1 ~ 2 J/m^2.

4.3.3 Contact Length at the Flank Interface

When cutting at submicrometer depths of cut, the possible significance of the contact length at the tool-workpiece interface needs to be examined as a zone of energy dissipation. Estimates of the contact length, based on the measured thrust force and an estimated flank contact stress (3 times the uniaxial yield strength of the workpiece material), indicate that this length could be of the order of or greater than the depth of cut. As an attempt at quantifying this length, a series of experiments were

performed using Tool 1 and an aluminum 6061-T6 workpiece material. The cutting conditions were the same as above. The flank face of Tool 1 was coated with a fresh coating of a AuPd about 5 nm in thickness again. Several careful cuts were performed at a prescribed depth of cut. Cutting and thrust forces were measured and then the tool flank face was examined under the SEM. The measured force components, force ratio and the specific energies during machining are shown in Figs. 4-11, 4-12, and 4-14. The force components during the contact length measurements were slightly larger than that of the series cut (Specimen 1 & 2) which is shown in Fig. 4-11. This may be due to the gradual change of the tool edge condition during machining. The effect of change of the tool edge condition on resulting forces and energies will be discussed further in next chapter.

Fig. 4-15 is an SEM photograph of the flank face of the tool giving an indication of the contact length at 10 nm depth of cut. The cutting edge is at the top, with the rake angle into the plane of the photo. The region of the worn-off coating is clearly seen. The minimum worn-off length from the tool edge of the flank face was measured at 10 locations along the cutting edge under the SEM. The minimum worn-off length among ten measured was taken as the contact length for each test. This procedure was repeated five times for 0.01, 0.1, and 1.0 μm depth of cut respectively. The results are shown in Table 4-4. Also included are the normalized contact length with respect to the depth of cut, and the contact stress calculated based on the measured thrust force and contact length at a given depth of cut, i.e., $\sigma = F_t/(l_f\ w)$.

At a 0.01 μm depth of cut, the magnitude of the measured force components may have some errors due to the uncertainties described

before. However, the thrust force appears to follow the overall trend in this range, thus the measured contact length and the thrust force component may be reasonable in the range below 30 nm depth of cut.

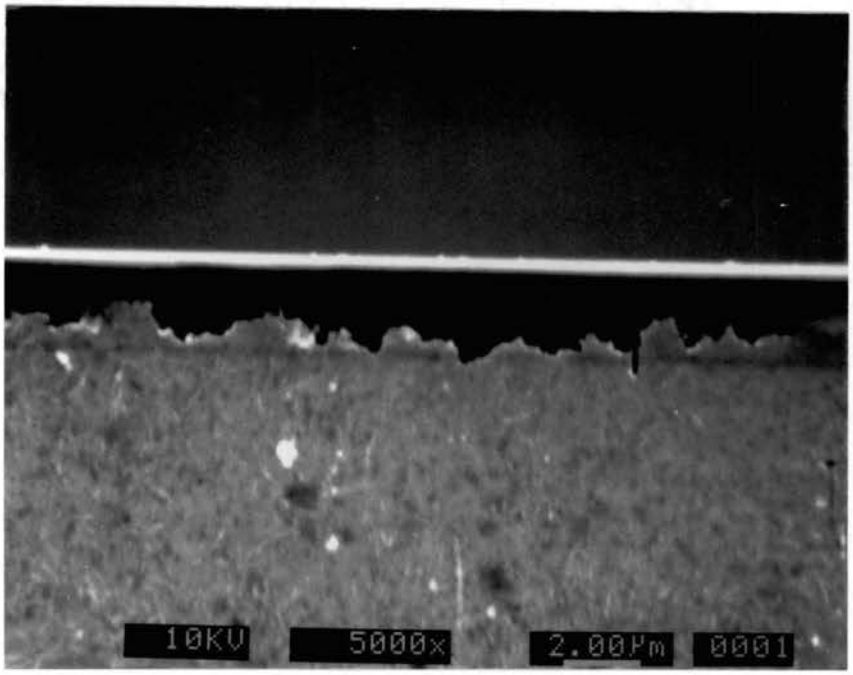

Figure 4-15. SEM Photo Representing a Contact Length at the Flank Interface in Machining of 6061-T6 Aluminum at 10 nm Depth of Cut

In Fig. 4-16 measured contact lengths and thrust forces are compared as a function of depth of cut. The contact length is seen to decrease with decreasing thrust force and depth of cut, and also follows the general trend of the thrust force. The measured contact length at 10 nm was 1.03 μm, and was on the same order for 0.1 and 1 μm depth of cut. This is due to the

nonlinearity of the thrust force with depth of cut in which the magnitude remains almost unchanged as the depth of cut decreases.

TABLE 4-4

MEASURED FORCE COMPONENTS, CONTACT LENGTHS, AND ESTIMATED CONTACT STRESSES IN ORTHOGONAL FLYCUTTING OF 6061-T6 ALUMINUM

Depth of Cut (μm)	Test No	F_c (N/mm)	F_t (N/mm)	l_f (μm)	l_f / t_0	σ (MPa)
0.01	1	0.172	0.548	0.97	97.0	564.9
	2	0.189	0.580	0.97	97.0	597.9
	3	0.182	0.548	1.33	133.3	411.1
	4	0.154	0.496	0.85	84.8	584.9
	5	0.169	0.484	1.03	103.0	469.9
	Ave	0.173	0.531	1.03	103.0	525.7
0.1	1	0.628	0.667	0.97	9.70	687.6
	2	0.580	0.613	1.09	10.91	561.9
	3	0.559	0.585	1.12	11.21	521.9
	4	0.542	0.568	1.09	10.91	520.6
	5	0.504	0.497	1.09	10.91	455.5
	Ave	0.563	0.586	1.07	10.73	549.5
1.0	1	1.635	0.828	1.33	1.33	621.2
	2	1.675	0.863	1.58	1.58	547.6
	3	1.667	0.835	1.33	1.33	626.4
	4	1.645	0.830	1.09	1.09	760.8
	5	1.720	0.932	1.09	1.09	854.3
	Ave	1.668	0.858	1.29	1.28	682.1

Whereas the measured contact length of worn-off coating can be viewed as an upper bound for the actual contact length, a calculated length based on the measured thrust force, assuming an interface pressure equal to 3 times the uniaxial yield strength, i.e., 3Y, could be considered a lower bound. Calculation of the contact length at the depth of cut of 10 nm,

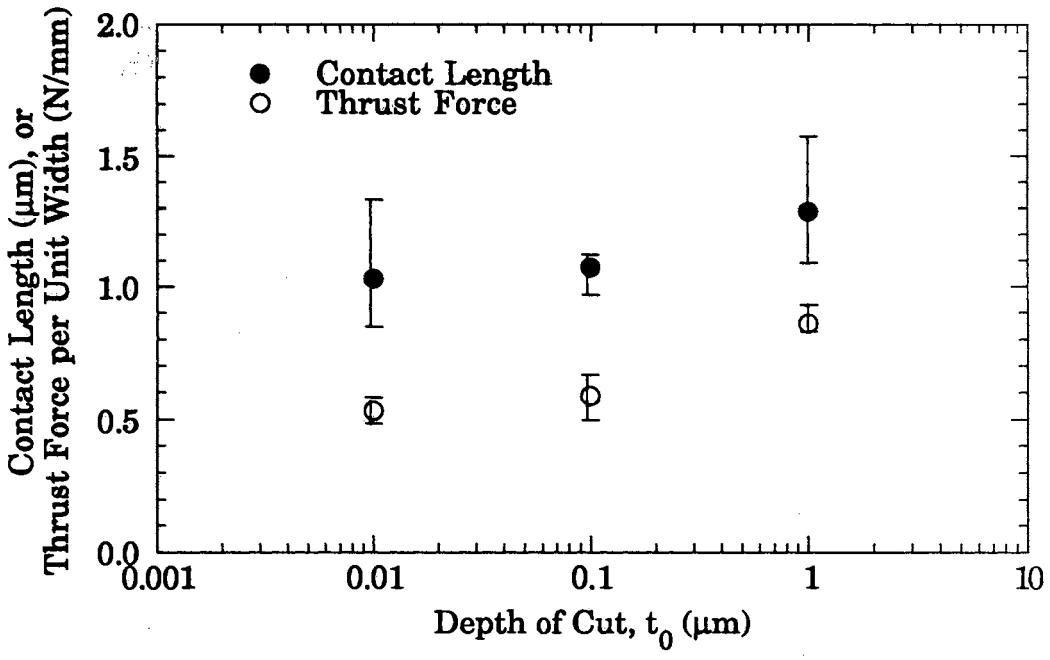

Figure 4-16. Measured Contact Length and Thrust Force in the Orthogonal Flycutting of 6061-T6 Aluminum

results in a length of 0.49 μm as compared to 1.03 μm which was measured (average of the five minimum values). This indicates that the contact length would still be between 49 and 103 times the depth of cut at 10 nm, and thus becoming a characteristic length scale.

The relative importance of the contact length to the depth of cut can be seen in Fig. 4-17. The ratio of the contact length at the flank face of the tool to the depth of cut increases significantly as depth of cut decreases. At 0.1 μm depth of cut, the contact length is about one order of magnitude greater, and at 0.01 μm it is two orders of magnitude larger than the depth of cut. This indicates that the contact length at submicrometer depths of cut becomes the characteristic length scale for this range of depth of cut. This, coupled with the rotation of the thrust force towards the workpiece

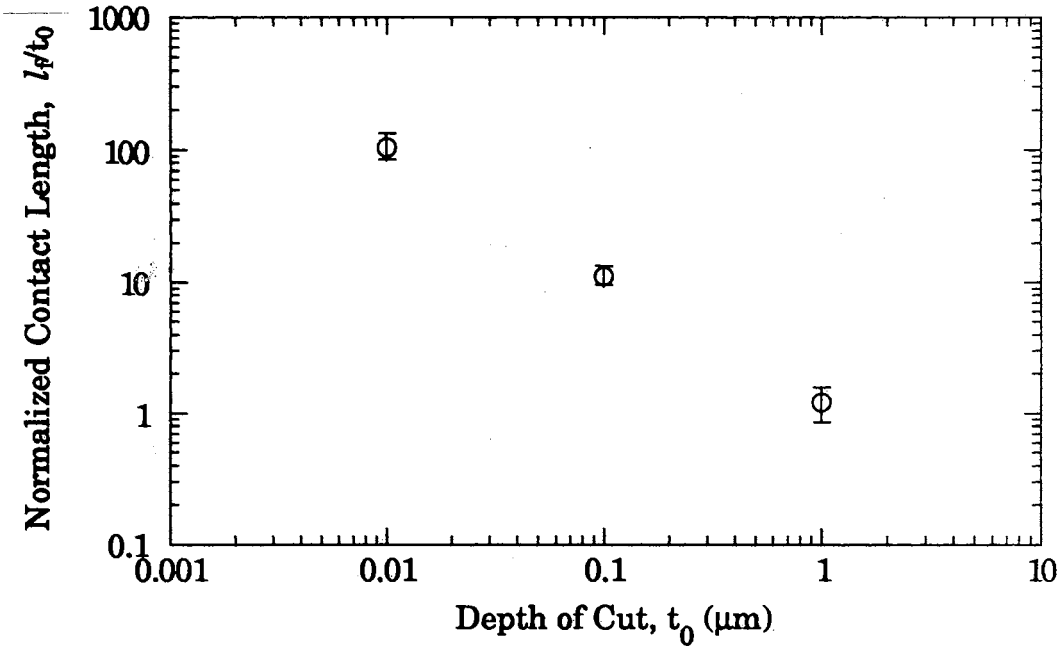

Figure 4-17. Normalized Contact Length with Respect to the Depth of Cut in Orthogonal Flycutting of 6061-T6 Aluminum

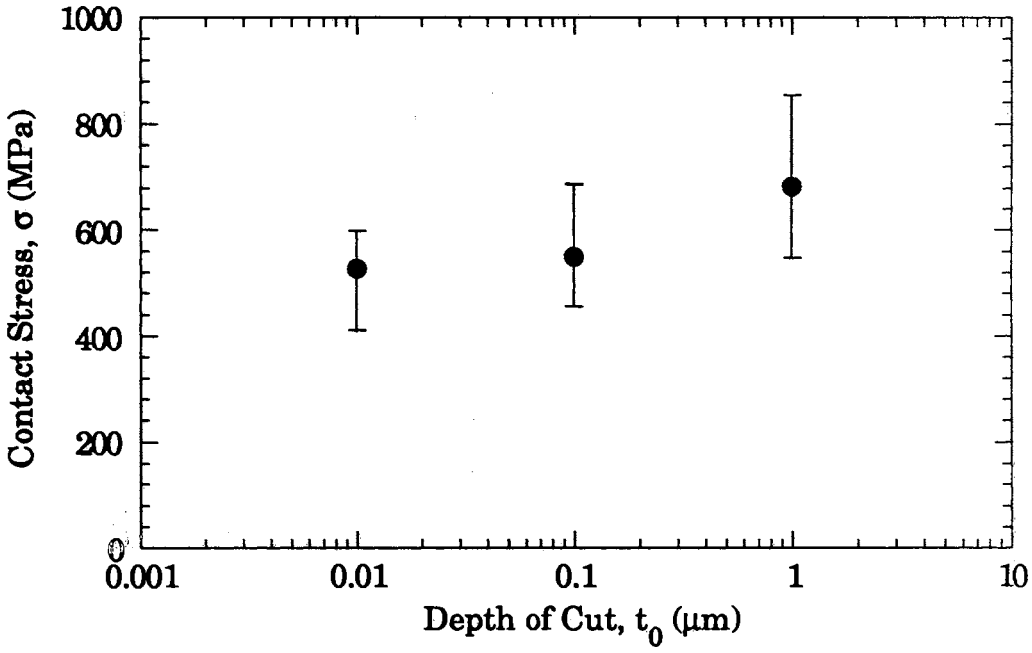

Figure 4-18. Contact Stress at the Tool-Workpiece Contact Based on Measured Contact Length and Thrust Force in Orthogonal Flycutting of 6061-T6 Aluminum

suggests that the process can be thought of as transitioning from a cutting-dominant to a sliding indentation (or plowing/sliding)-dominant process.

The validity of the measured contact length can be assured by investigating the contact stress at the interface. Contact stress based on the measured contact length and thrust force is shown in Fig. 4-18. The average contact pressures of the five measurements at the interface were between 1.5 and 1.9 times the measured uniaxial yield strength of the Al 6061-T6 workpiece of Y = 363 MPa when apparent area is assumed equal to the actual area. These values are comparable with the value of 3 times the uniaxial yield strength predicted for plane strain indentation, and this agreement would improve if the actual contact was in fact less than the apparent contact.

4.3.4 Initial Study of Edge Radius Effect on the Energy Dissipation

The possible significance of a tool edge effect on resulting forces and energies has been recognized however, very little study of this effect has been performed to date. In order to investigate the edge radius effect on force behavior, an initial experimental study was performed using Tool 2. Before cutting, the new tool was estimated to have a 0.2 μm edge radius using the SEM. The edge of the tool was first "broken in" by machining aluminum for a distance of about 0.5 km. Break-in cutting is also applied in actual production processes for the tools to be adjusted to produce acceptable parts [Atkin, 1986]. A series of cuts was then performed over the range of depths of cut from 0.01 ~ 10 μm. This result is denoted as "new tool", and is shown in Figs. 4-19 ~ 4-22. After machining about 2 km

in cutting distance, another series of cuts was performed. This data is also shown in Figs. 4-19 ~ 4-22, and is denoted as "worn tool". The effect of the tool wear is clearly seen in the figures. At depths of cut above about 0.4 μm, there is no change in the resulting forces, whereas at or below this depth, the forces are seen to rise significantly, e.g., the cutting force increased by a factor of two and the thrust force by three at 10 nm depth of cut. The force ratio increased from 2.5 to about 4 (1.6 times increased) at 10 nm depth of cut, and the increase of the specific energy is the same as that of the cutting force. This shift of force components may be due to the change of the edge radius of the tool because other cutting conditions remained the same. Even though evaluation of the edge radius was not

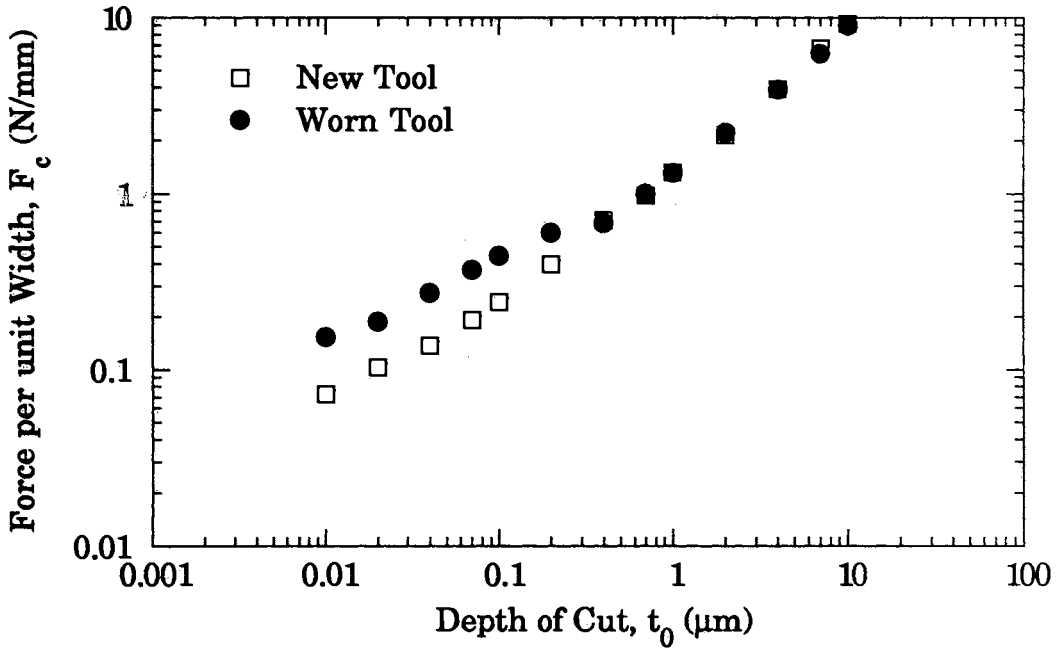

Figure 4-19. Effect of New Tool and Worn Tool on Cutting Force in Orthogonal Flycutting of 6061-T6 Aluminum

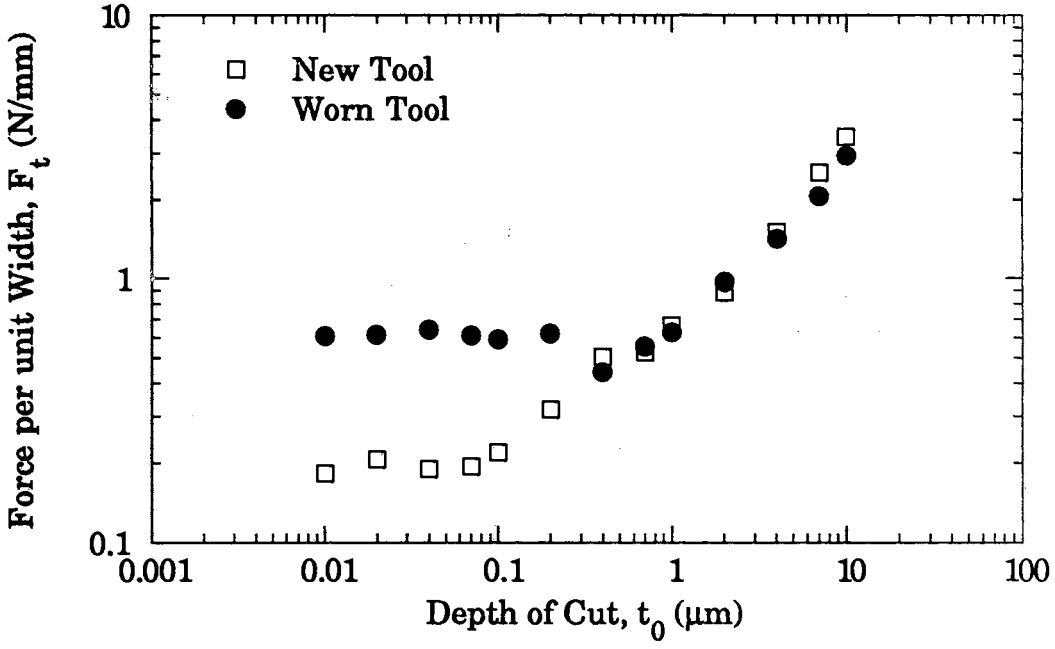

Figure 4-20. Effect of New Tool and Worn Tool on Thrust Force in Orthogonal Flycutting of 6061-T6 Aluminum

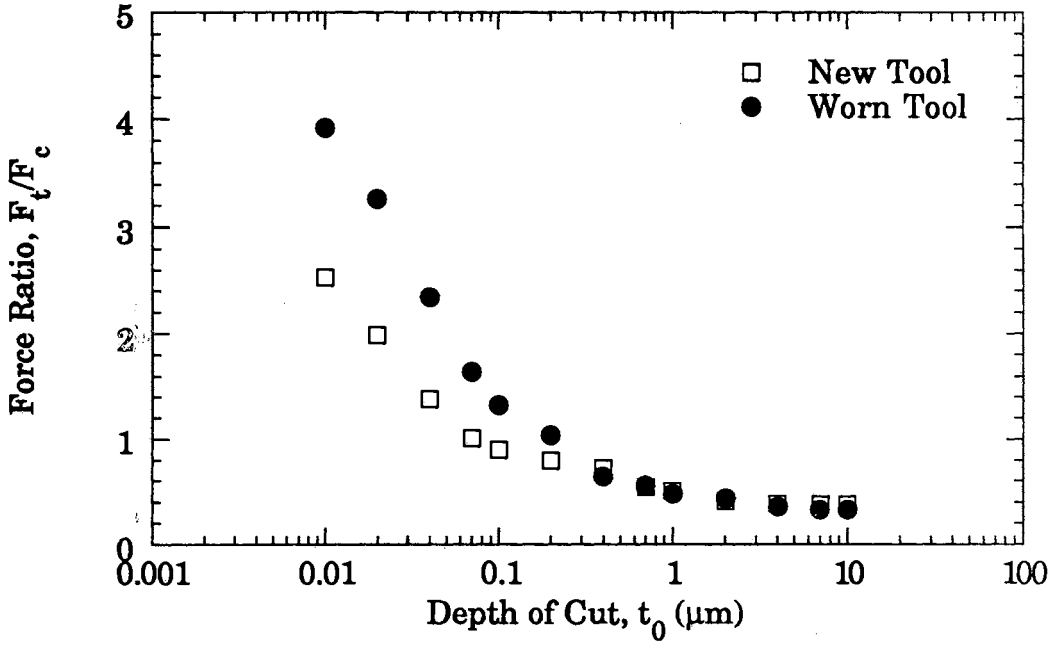

Figure 4-21. Effect of New Tool and Worn Tool on Force Ratio in Orthogonal Flycutting of 6061-T6 Aluminum

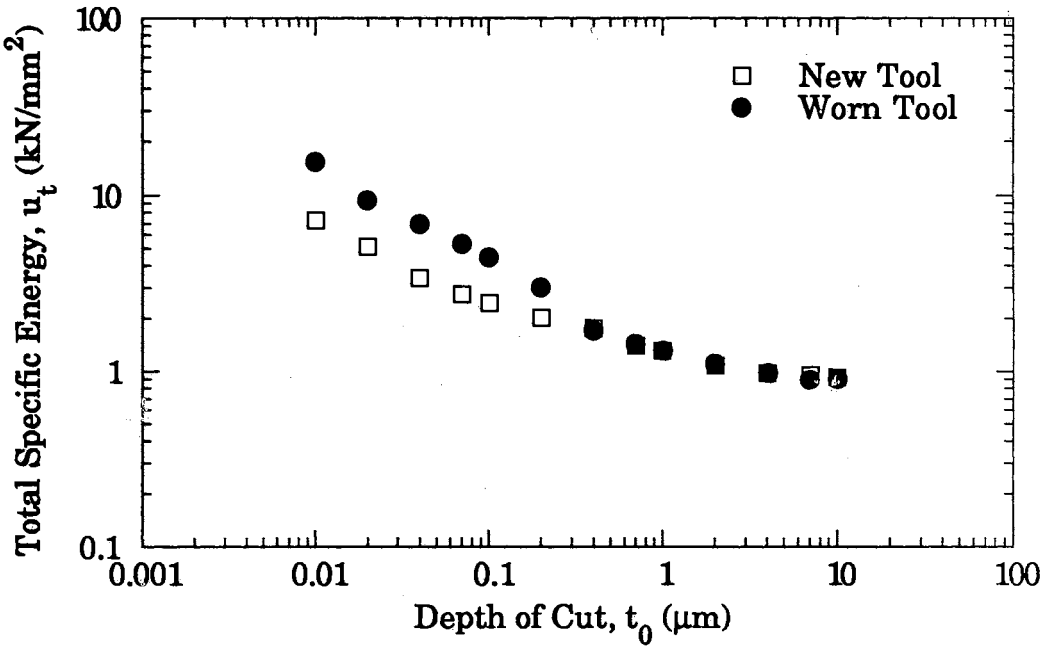

Figure 4-22. Effect of New Tool and Worn Tool on Total Specific Energy in Orthogonal Flycutting of 6061-T6 Aluminum

possible at this initial experiment, it is conceivable that the edge radius may be worn tenths of a micrometer. In Chapter V, the edge radius is shown to have increased from 0.2 to about 0.3 μm using AFM.

4.4 Conclusions

From the results of the initial orthogonal flycutting of Al 6061-T6, the following observations are made:

- the orthogonal flycutting geometry produced very repeatable cutting force components,
- at submicrometer depths of cut, thrust force was dominant over the cutting force. The force behavior with depth of cut shows

nonlinear behavior with a cross-over of the cutting force and thrust force. The size effect was observed and the overall trend was consistent with results reported in the literature,

- the rotation of the direction of the resultant force vector downward toward the workpiece was significant as depth of cut decreases,
- the measured contact lengths of 1 μm order appear to be consistent with estimates based on indentation stress, and become the characteristic length scale at submicrometer depth of cut,
- process mechanics at submicrometer depths of cut resembles the sliding indentation process,
- the effect of tool edge condition was found to be significant on the energy dissipation at decreased depths of cut, and
- the tool edge characterization technique using SEM with AuPd coating provided only 2D geometry and was limited by the coating technique.

The significance of the tool edge effect on the energy dissipation and the change of the process mechanics at submicrometer depth of cut suggested a further systematic experimental study of the energy dissipation in ultra-precision orthogonal diamond turning. For further experimental study of the edge effect, more reliable 3D tool edge characterization technique is required.

CHAPTER V

EXPERIMENTAL STUDY OF THE TOOL EDGE PROFILE ON ENERGY DISSIPATION IN ORTHOGONAL FLYCUTTING OF Te-Cu

5.1 Introduction

From the initial experimental study of the tool edge effect on energy dissipation using 6061-T6 aluminum as a workpiece material, a significant increase of force components and resulting energies was observed at submicrometer depths of cut due to about one tenth of micrometer increase in tool edge radius. Since the cutting distance of several kilometers used in the experiment was small relative to the tool life of about 300 ~ 400 km [Sugano, 1987], an increase of the energy dissipation may be significant at the early stages of the tool's life. From the initial experimental results, it was recognized that a more reliable technique for tool edge characterization and further systematic experimental approaches were needed to study the tool edge effect on the energy dissipation and the process mechanics at submicrometer depths of cut.

In this chapter, an experimental study of the tool edge geometry effect on the resulting forces and energies in the orthogonal ultra-precision flycutting of tellurium copper (Te-Cu) are described. Before the cutting experiments, the overall tool geometry was characterized using an optical

microscope. For the detailed tool edge characterization, an atomic force microscopy (AFM) technique was used. The tool edge profiles were measured down to tens of nanometers using the AFM. After the tool characterization, cutting was performed over a range of depth of cut from 10 nm to 20 μm, and then the tools were again characterized using the AFM.

Several effects of tool edge geometry and cutting conditions on the resulting forces and energies were investigated in these experiments. The effects studied were:

- geometric effect of nominal rake angles,
- effect of cutting distance (up to 3 km with 1 km intervals),
- effect of edge profiles of new and worn tools,
- effect of effective rake angle, and
- effect of cutting speed over an order of magnitude change.

From the results of the orthogonal ultra-precision flycutting of Te-Cu at various conditions described above, it was found that both the nominal rake angle and tool edge profile have significant effects on the resulting forces and energies. Some results of the experimental study have been reported [Lucca, 1993b].

5.2 Cutting Conditions

5.2.1 Workpiece Material

For all the experiments in this chapter, cutting was performed on Te-Cu having a nominal chemical composition of 99.4 ~ 99.5 % Cu and 0.5 ~ 0.6 % Te. Depth of cut ranged from 10 nm to 20 μm. A light mineral oil was brushed onto the workpiece as a cutting fluid. The size of the

specimen was 1 mm thick, 15 mm long, and 12 mm wide. Cutting speed was the same as the speed of the aluminum experiments, i.e., 7.6 m/min (except for the study of the cutting speed effect).

The workpiece specimen thickness of 1 mm was selected to ensure plane strain cutting even for the high effective negative rake angle conditions which would be present for cutting at submicrometer depths of cut. In addition, this allowed the resultant force components at 10 nm depth of cut to be above the resolution of the dynamometer of about 0.01 N. The cutting length was long enough to eliminate entrance or exit effects.

5.2.2 Diamond Tools

A total of seven single crystal diamond tools were used in this study. Based on the overall geometry, each tool was given an identifier as shown in Table 5-1. The overall geometries of the tools were characterized by tilting the tool such that the rake and flank faces appeared as lines under an optical microscope. Detailed characterization of the tool edge was performed using the AFM and will be described later. Other specifications such as crystallographic orientation, blazing method, and shank material were the same as in the aluminum cutting experiments. The measured angular deviation was about ± 0.5° for repeated measurements of the same tool. The Tools A1, B, C, and D were new tools as received from a tool manufacturer. The Tool A2 was the same tool as the Tool 2, and the Tool A4 was the Tool 1 for aluminum cutting in previous chapter.

5.2.3 Experimental Procedure

An overall experimental procedure for the study of rake angle, cutting distance and speed effect on energy dissipation is shown in Table 5-2 together with the tools used. After tool edge characterization using the AFM, two series of cuts were taken on two different workpiece specimens using four different tools (A1, B, C, and D) which had 0°, -10°, -20°, and -30° rake angles respectively. After cutting, the tool edges were again characterized.

TABLE 5-1

SINGLE CRYSTAL DIAMOND TOOLS USED IN ORTHOGONAL FLYCUTTING OF Te-Cu

Tool I.D.	Rake Angle (°)	Clearance Angle (°)	Remarks*
A1	0	6	New
B	-10	10	New
C	-20	10	New
D	-30	10	New
A2	-2	6	Used
A3	0	6	Used
A4	0	6	Used

* Indicates previous usage before current experiment

For the cutting distance study, Tool A1 was continuously used. After one kilometer of cutting of oxygen-free copper (OFC) at a depth of cut of 0.4 μm at a cutting speed of 15.2 m/min, a second series of cuts were performed on two Te-Cu workpiece specimens at a cutting speed of 7.6 m/min. During the machining of Te-Cu, force components were

TABLE 5-2

EXPERIMENTAL PROCEDURE FOR THE STUDY OF RAKE ANGLE, CUTTING DISTANCE, AND SPEED EFFECT ON THE ENERGY DISSIPATION IN ORTHOGONAL ULTRA-PRECISION FLYCUTTING OF Te-Cu

Cutting Distance (km)	Tool A1 (0° Rake)	Tool B (-10°)	Tool C (-20°)	Tool D (-30°)	Tool A2 (0°)	Tool A3 (0°)	Tool A4 (0°)
0	Ch. 1*	Ch. 1	Ch. 1	Ch. 1	Ch. 1	Ch. 1	Ch. 1
	Series Cut 1**	Series Cut	Series Cut	Series Cut		Series Cut	Series Cut
	Ch. 2	Ch. 2	Ch. 2	Ch. 2		Ch. 2	Ch. 2
	Wear (OFC)						
1.0	Series Cut 2 Ch. 3 Wear (OFC)						
2.0	Series Cut 3 Ch. 4 Wear (OFC)						
3.0	Series Cut 4 Ch. 5						
Speed Effect (m/min)	7.6, 22.9, 38.1, 76.2 (Series Cuts) Ch. 6						

* Ch. No; tool edge characterization number using AFM

** Series Cut No; cutting of Te-Cu to measure force components for the whole range of depths of cut (10 nm ~ 20 μm). Two specimens were used for each series cut

- Wear; cutting of oxygen-free copper at 15.2 m/min with 0.4 μm depth of cut to speed-up the wear in the tool edge profile

measured at depths of cut from 10 nm to 20 μm. The OFC was used to accelerate the change of the tool edge profile as it has greater strength than Te-Cu. The uniaxial tensile strength of OFC is 288 MPa, whereas Te-Cu is 225 MPa. As a cutting fluid, light mineral oil was applied. After the second series of cuts, tool edge characterization was again performed. This procedure was continued until 3 km of cutting distance was accumulated using Tool A1.

To investigate the speed effect, Tool A1 was continuously used after 3 km cutting. The examined cutting speeds were 7.6, 22.9, 38.1 and 76.2 m/min, which corresponded to 100, 300, 500, and 1000 rpm respectively for the experimental set-up of the present study. Two specimens were cut for the whole range of depth of cut at a given cutting speed. After all the cutting for the investigation of speed effect, Tool A1 was characterized.

For the study of the effect of new tool and worn tool, series cut data from Tool A1 in its "as-received" condition (new) was compared with the results from the Tools A3 and A4 since these tools had been used over considerable cutting distance before the current experiment.

5.3 Diamond Tool Edge Characterization Using Atomic Force Microscopy (AFM)

5.3.1 Atomic Force Microscopy Technique

In the present study, the StandAlone Atomic Force Microscope (Model No SAAFM-1) from Digital Instruments was employed for 3D diamond tool edge characterization. This configuration is similar to that recently reported by Donaldson and co-workers [1992]. Since its introduction in 1986 [Binnig, 1986], the study of surface topography using the AFM has been

widely initiated. Until recently, however, scanning of a large sample such as a diamond tool, was not possible with commercially available instruments. An AFM which uses a miniaturized diode interferometer to detect tip deflection during scanning now allows movement of the probe instead of the sample, therefore it can be placed directly on large stationary samples.

Fig. 5-1 depicts a schematic of the atomic force microscope set-up. The set-up was placed on a vibration isolation table. Before examination, tools were carefully cleaned with a solution of 70% methanol/30% ethanol and blown off with pure gas (AccuDuster II OS; chlorodifluoromethane) before drying. It was found that accurate cleaning is essential for nanometer scale resolution. Flat-nosed single crystal diamond tools of 2 mm width to be used in the cutting experiments were positioned under the microscope with the included angle between their rake and clearance (flank) faces centered about the vertical axis. Coarse positioning of the tool under the microscope was adjusted with two linear translation stages on which the tool was mounted. The tools were held such that a Si_3N_4 micro-fabricated cantilever tip could scan across the diamond tool edge normal to the rake and flank faces. For each characterization, five 3 μm x 3 μm area scans positioned 0.15 mm apart were taken. The 3 μm scan was taken to examine both the flank wear and edge radius which has been estimated to be on the order of one micrometer from the SEM characterization in the aluminum cutting experiments. The scan pattern was centered on the tool edge with one scan at the center of the tool's width and two on each side.

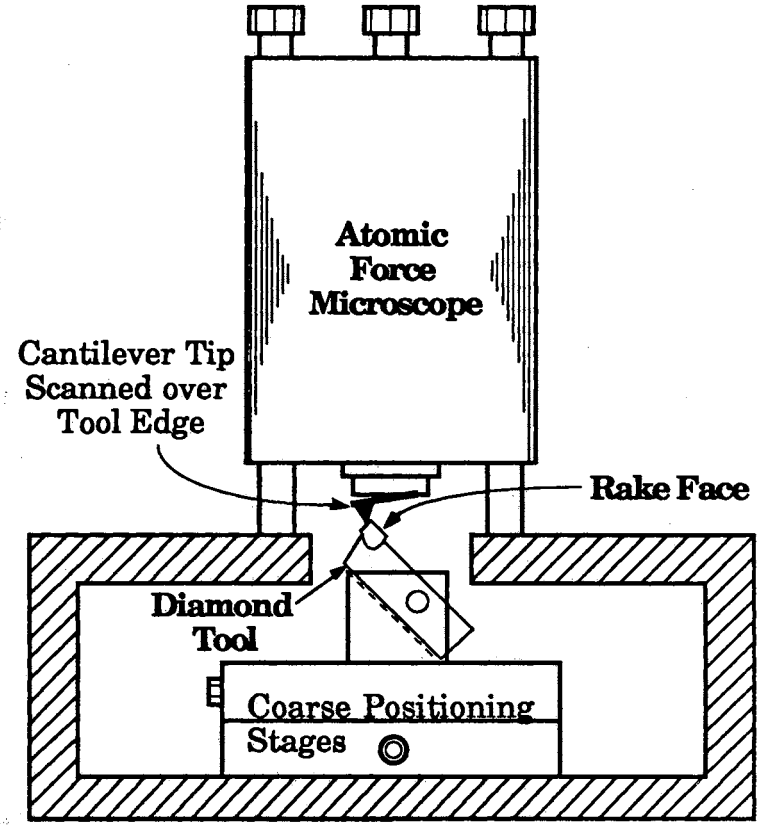

a) Configuration of Atomic Force Microscope

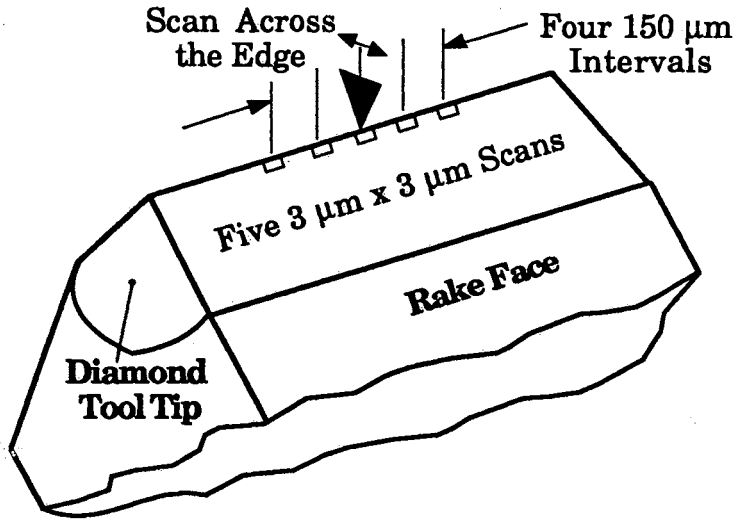

b) Diamond Tool Edge Scanned

Figure 5-1. Configuration of Atomic Force Microscope Used for Diamond Tool Edge Characterization

5.3.2 Measured Tool Edge Radii

In characterizing the overall geometry of a tool, the rake and clearance angles with respect to the shank of the tool were measured with an optical microscopy since the tools were to be mounted such that the shank is normal to the cutting direction. The repeatability of these measurements was about ± 1 degree. The detailed tool edge profile was then characterized with the atomic force microscope. The measured cross-sectional profiles were found to be consistently within ± 10 nm over the five scanned areas, and also within this range for repeated characterizations of a given tool using several new cantilever tips. For a 3 μm scan, this allowed for a measurement of the included angle of tool to ± 0.5 degrees. Whereas the force microscope can resolve much smaller features, the variations of edge profile across the tool limited the accuracy. Some error sources which could affect the results of the characterization were recognized. These were tool tip cleaning, the setting of the angle of a tool edge at the coarse positioning stage, electromagnetic fields of the environment, and acoustic noise from the surroundings. Some of these error sources may limit the accuracy of the characterization. Here, the result of the tool edge characterization was used to infer the overall edge contour of tens of nanometer, and not the atomic scale features of the edge.

The 3 μm x 3 μm scanned areas consisted of 128 individual line scans with 128 data points. The scanned tool edge profiles are shown in Figs. 5-2 ~ 5.8 for all the tools used in the present study. The figures represent the tool edge profiles after the final cutting, i.e., after speed effect cutting for Tool A1 and after cutting two specimens for the other tools. The wavy pattern seems to be due to the error sources discussed above. The profiles

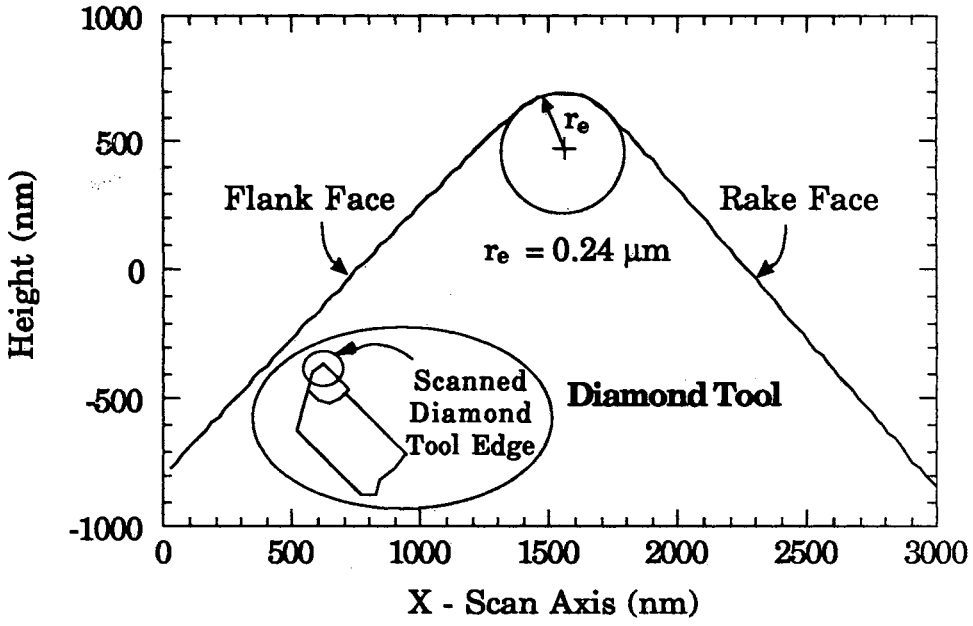

Figure 5-2. Measured Tool Edge Profile Using AFM for 0° Rake Angle Tool (Tool A1)

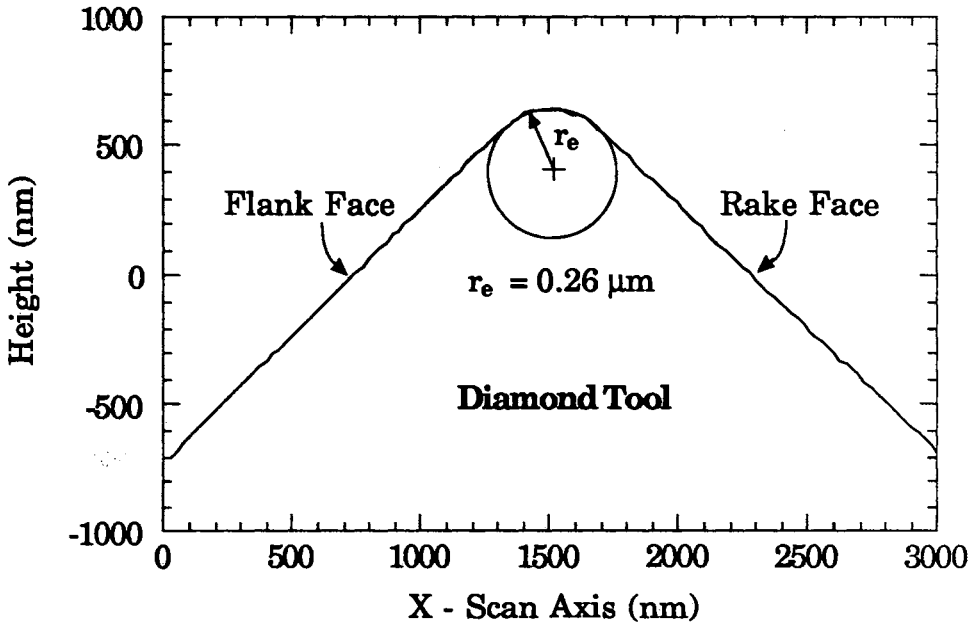

Figure 5-3. Measured Tool Edge Profile Using AFM for -10° Rake Angle Tool (Tool B)

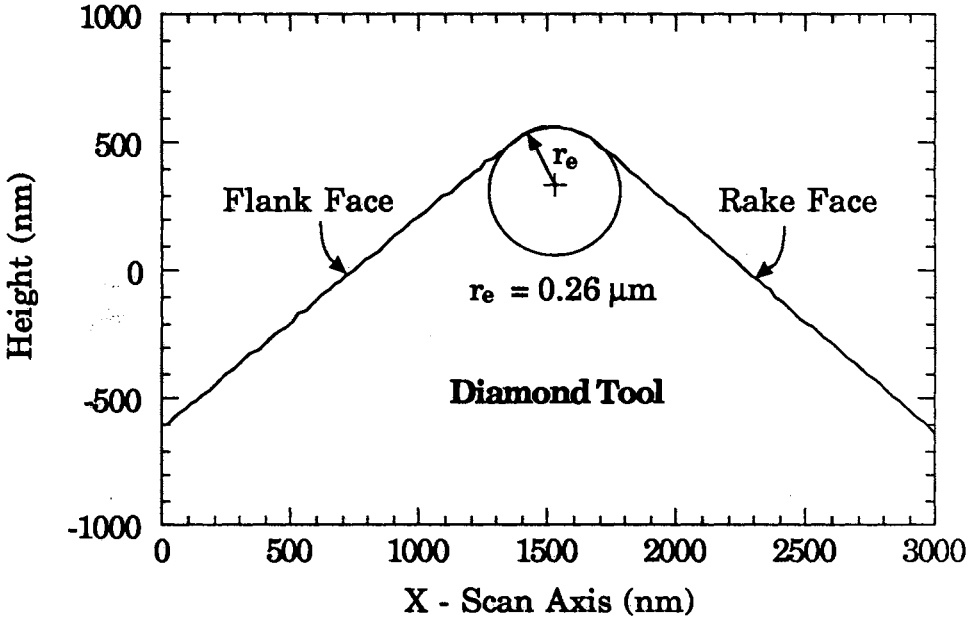

Figure 5-4. Measured Tool Edge Profile Using AFM for -20° Rake Angle Tool (Tool C)

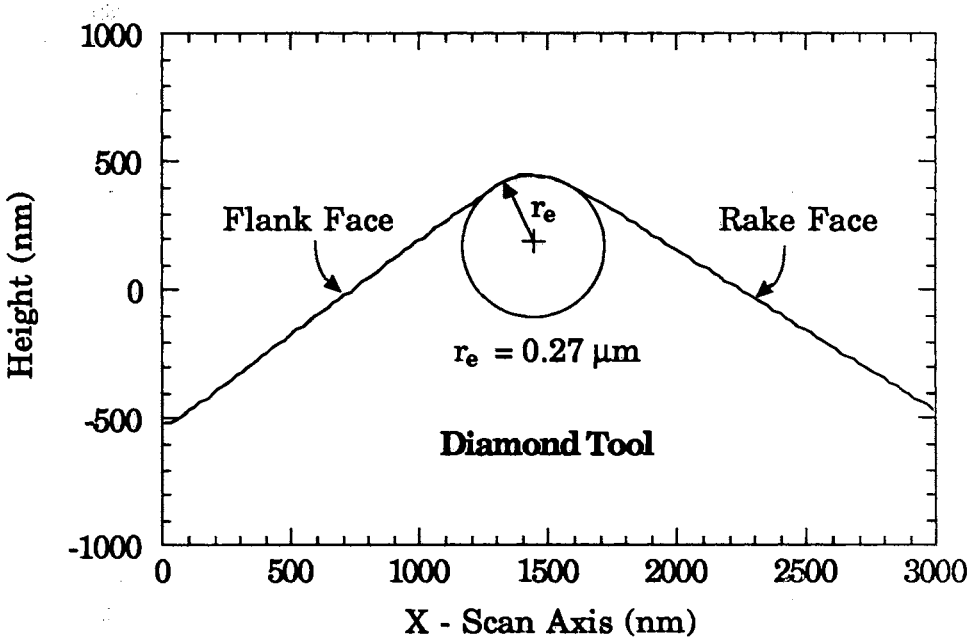

Figure 5-5. Measured Tool Edge Profile Using AFM for -30° Rake Angle Tool (Tool D)

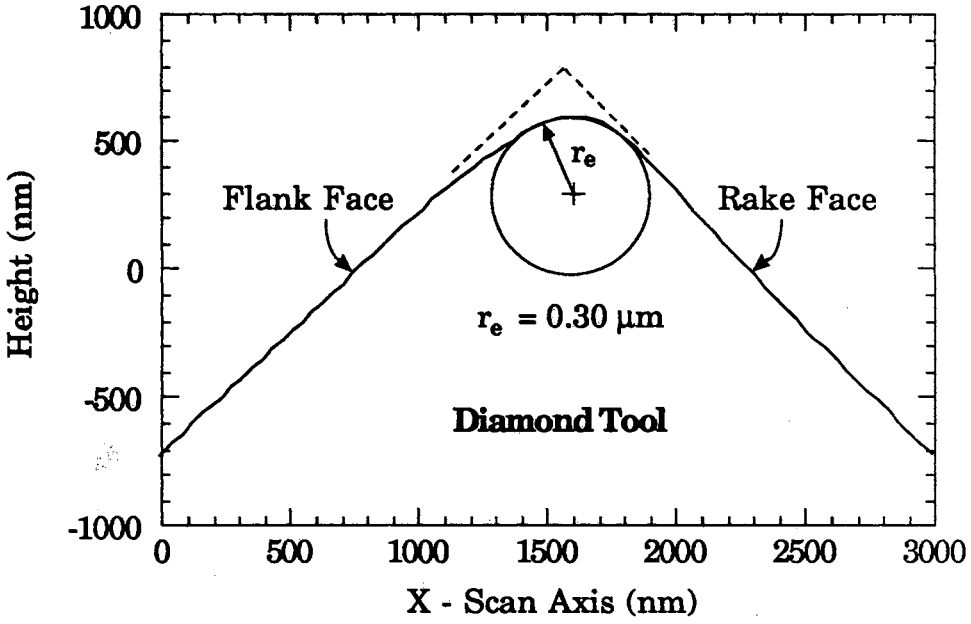

Figure 5-6. Measured Tool Edge Profile Using AFM for 0° Rake Angle Worn Tool (Tool A2)

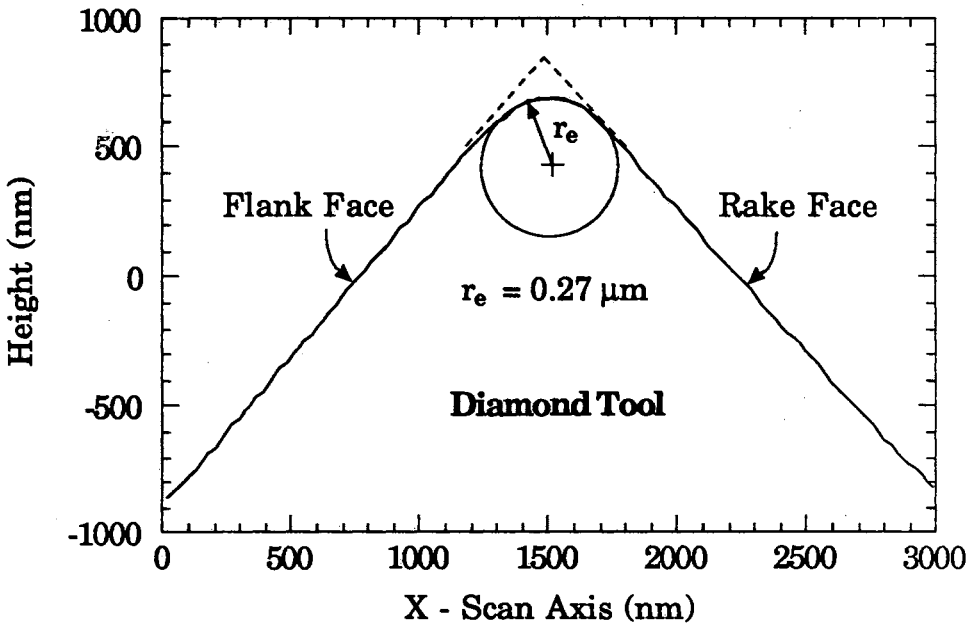

Figure 5-7. Measured Tool Edge Profile Using AFM for 0° Rake Angle Worn Tool (Tool A3)

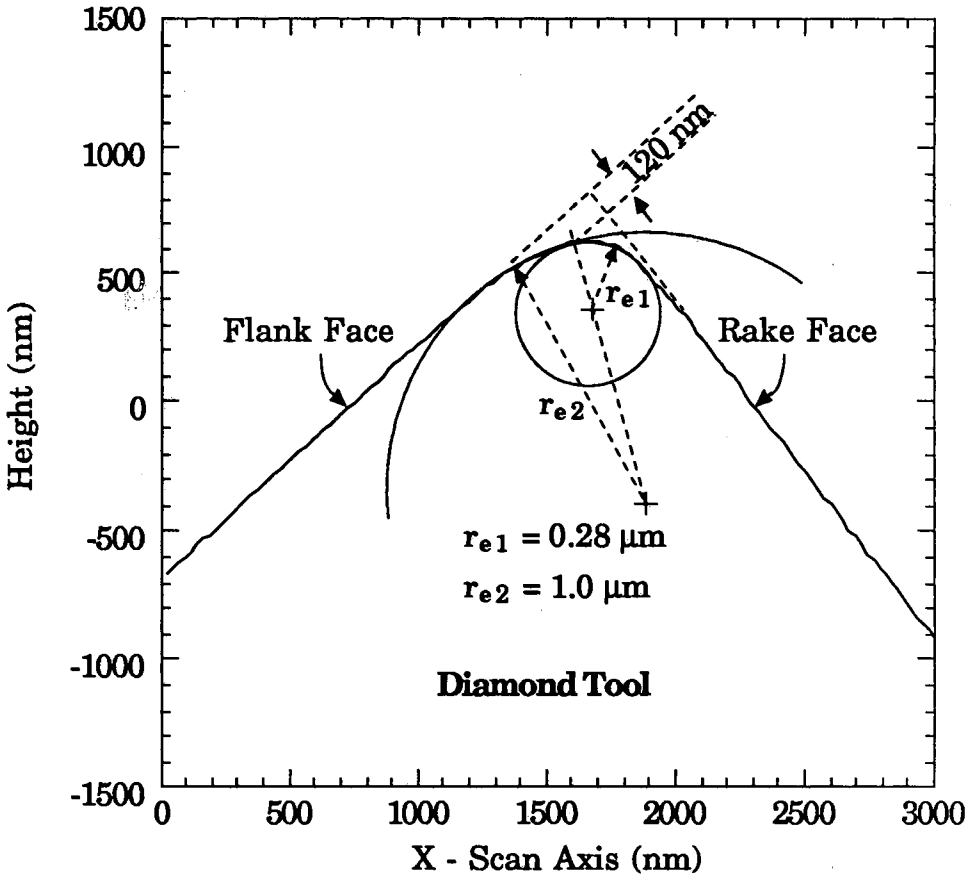

Figure 5-8. Measured Tool Edge Profile Using AFM for 0° Rake Angle Worn Tool (Tool A4)

shown in the figures represent one scan within the scan area, and was typical for all the line scans. The measured edge profile before and after cutting up to 3 km for A1 tool was within the repeatability of the scanning of ± 10 nm. If there is any change in the profile during the 3 km cutting, a smoothening of the edge profile at the tool flank seems to occur. The change was within the range of repeatability of ± 10 nm.

The AFM scans inferred the tool edge to be a part of a circle connecting the rake and flank faces for all new tools (A1, B, C, D). On the tool tip, a circle was made such that at least three points of the circle are to lie on top of the tool's flank, apex, and rake face respectively to estimate the tool edge radius for the tool. By adjusting the radius of the circle, the edge radius of each tool was estimated. All the new tools were estimated to have about the same edge radius (r_e) of 0.25 ± 0.02 μm.

Whereas the new tools had straight flank and rake faces with a circular arc at the tool tip, the worn tools (A2, A3, and A4) were characterized as having some wear at both the flank and rake faces near the apex. The tool edges was still approximately a circular shape. Here, Tool 2 was not used for the actual Te-Cu cutting experiment however, the edge radius determined by the AFM was compared with that from the SEM characterization. Reasonable agreement of both results of 0.2 μm from SEM at unused condition and 0.3 μm from the AFM after considerable cutting, indicates that both results were reliable. The edge profile of Tool A4 shown in Fig. 5-8 is also comparable with the SEM photo in the previous chapter when the tool was new. The circular shaped initial profile of the tool was changed to the contour shown at both sides of the flank and rake face with an increased radius in between. More wear at the flank than at the rake face was observed. This edge profile can be

idealized as having two edge radii which are tangent at about 120 nm depth up from the bottom of the flank face as shown in the Fig. 5-8. Even though it is less pronounced, similar contours can also be seen from the other two worn tools of Tools A2 and A3. These edge contours seem to be characteristics of worn tools.

5.4 Experimental Results and Discussion

5.4.1 Measured Force Signals

During orthogonal flycutting of Te-Cu, cutting and thrust force signals were measured at four depths of cut which are one order of magnitude different, i.e., 0.01, 0.1, 1.0, and 10 μm. The signals obtained using Tool A1 at about 3 km in cutting distance are shown in Figs. 5-9 ~ 5-16. The same, quite repeatable, force signals were obtained for Te-Cu as were obtained during cutting of 6061-T6 aluminum. At a depth of cut of 0.01 μm, the thrust force is greater than the cutting force but not much greater than the thrust force when cutting aluminum. This could be due to the difference in the tool edge profiles, viz., when cutting Te-Cu, the edge radius of Tool A1 was about 0.25 μm whereas, for aluminum cutting, edge of Tool A4 was contour shaped (primary edge radius was 0.28 μm and secondary edge radius was about 1 μm). Another explanation would be the difference in the workpiece materials. Unlike when cutting aluminum, spike shaped step heights were obtained for the Te-Cu cutting at decreased depths of cut however, at large depths of cut, the step height was very flat.

At 1.0 μm depth of cut, force signals highly oscillated within a given step height as shown in Fig. 5-13. This oscillation seemed to be a general trend for the depths of cut ranging from about 0.1 μm to 1 μm. These

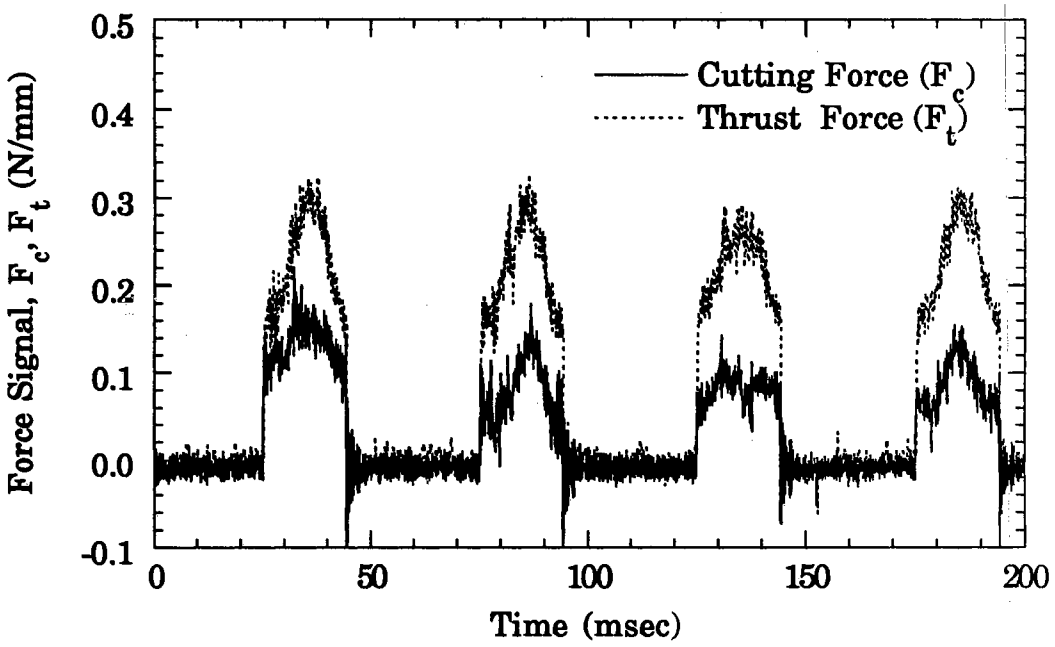

Figure 5-9. Measured Cutting and Thrust Force Signals During Orthogonal Flycutting of Te-Cu at 0.01 μm Depth of Cut

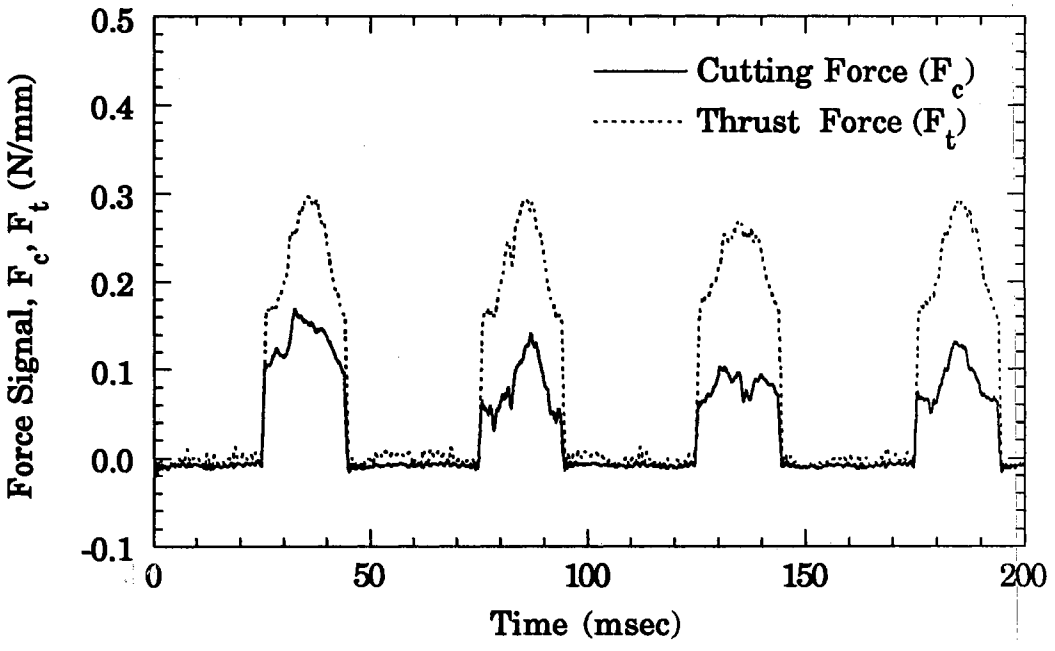

Figure 5-10. Averaged (19 points) Cutting and Thrust Force Signals in Orthogonal Flycutting of Te-Cu at 0.01 μm Depth of Cut

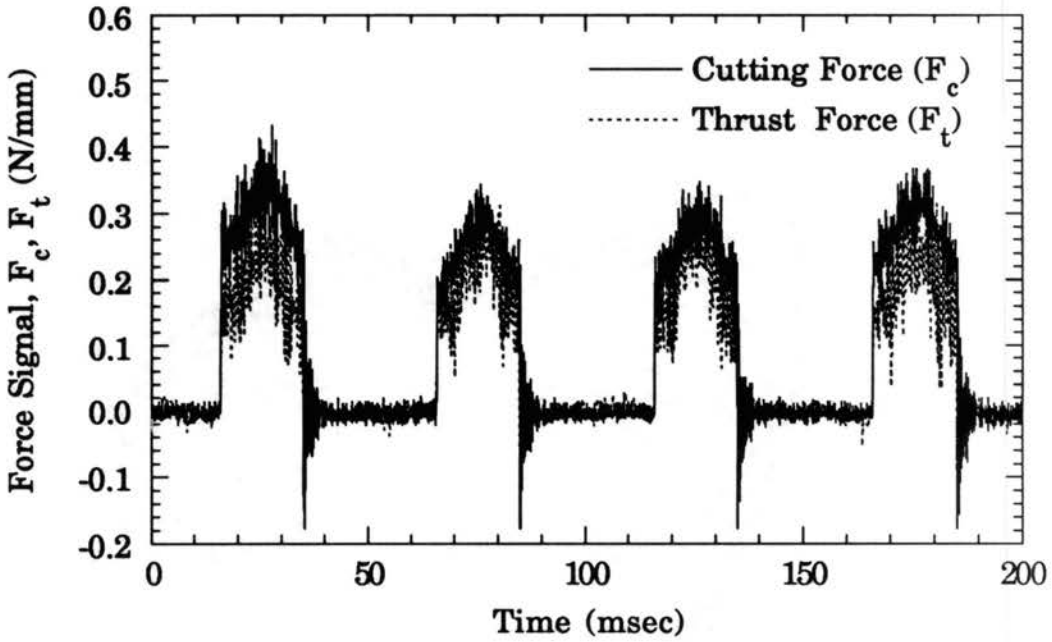

Figure 5-11. Measured Cutting and Thrust Force Signals During Orthogonal Flycutting of Te-Cu at 0.1 μm Depth of Cut

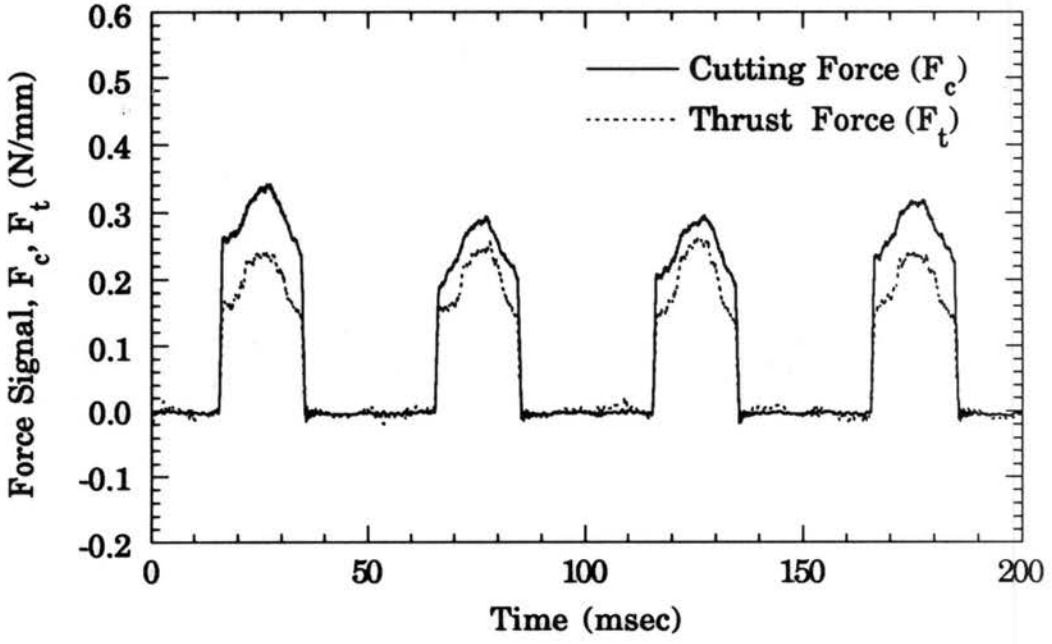

Figure 5-12. Averaged (19 points) Cutting and Thrust Force Signals in Orthogonal Flycutting of Te-Cu at 0.1 μm Depth of Cut

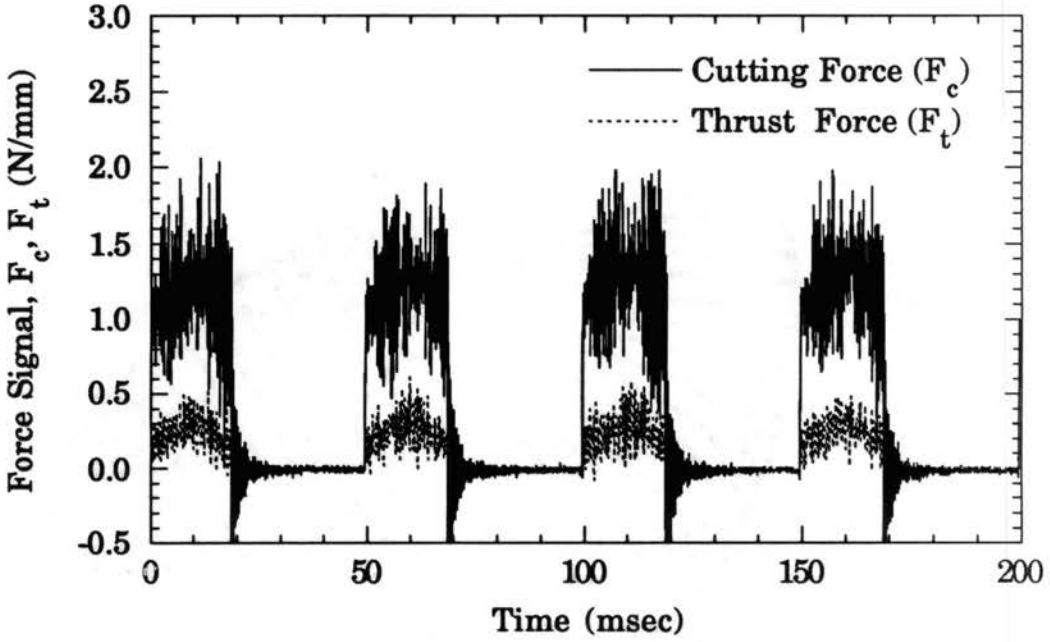

Figure 5-13. Measured Cutting and Thrust Force Signals During Orthogonal Flycutting of Te-Cu at 1 μm Depth of Cut

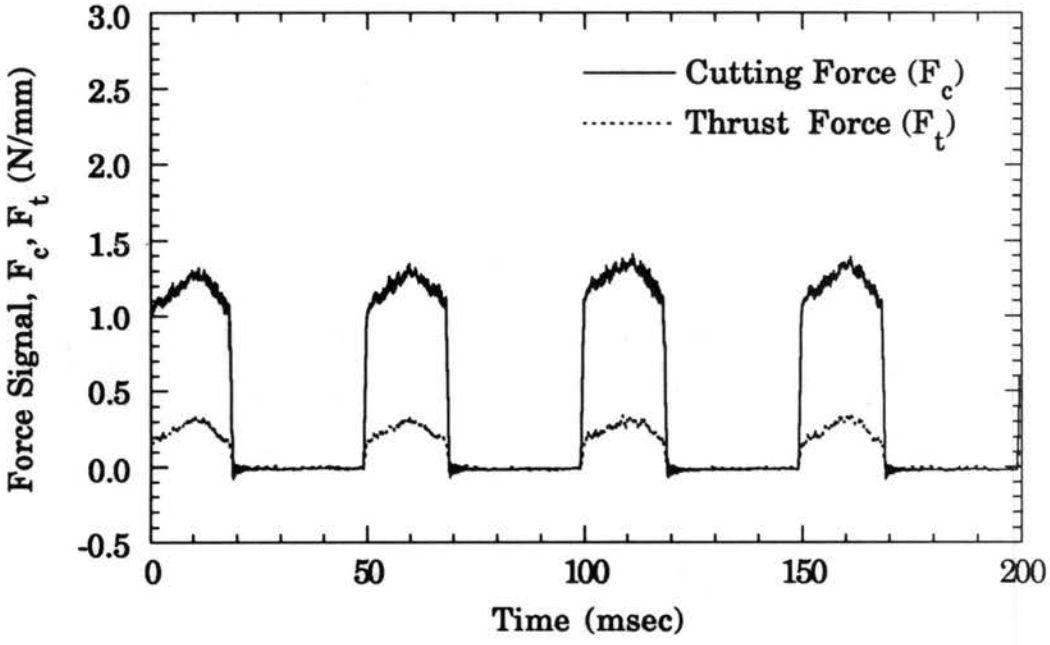

Figure 5-14. Averaged (19 points) Cutting and Thrust Force Signals in Orthogonal Flycutting of Te-Cu at 1 μm Depth of Cut

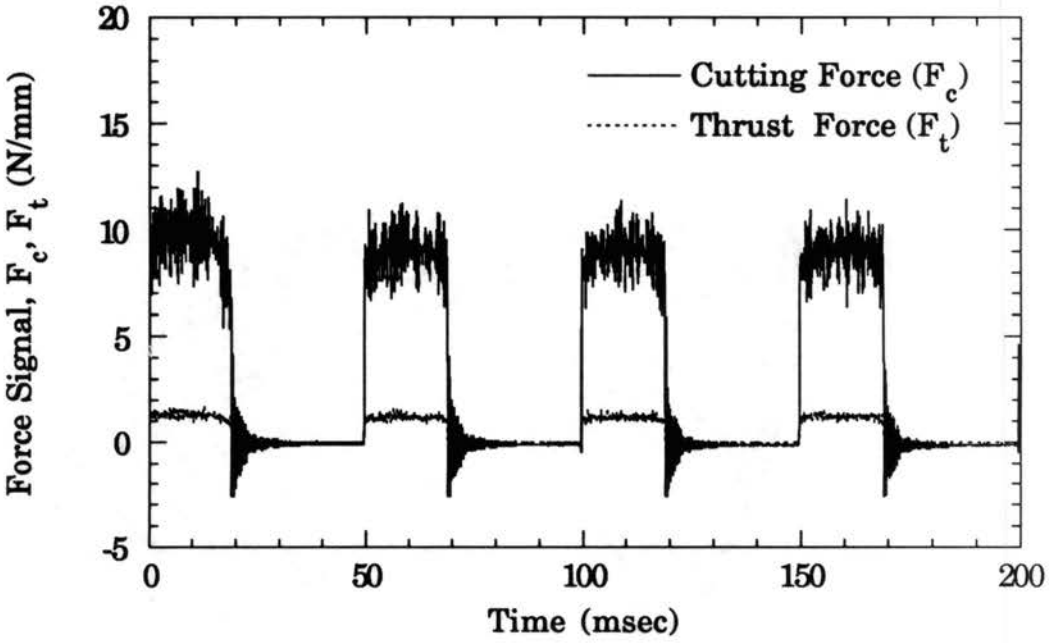

Figure 5-15. Measured Cutting and Thrust Force Signals During Orthogonal Flycutting of Te-Cu at 10 μm Depth of Cut

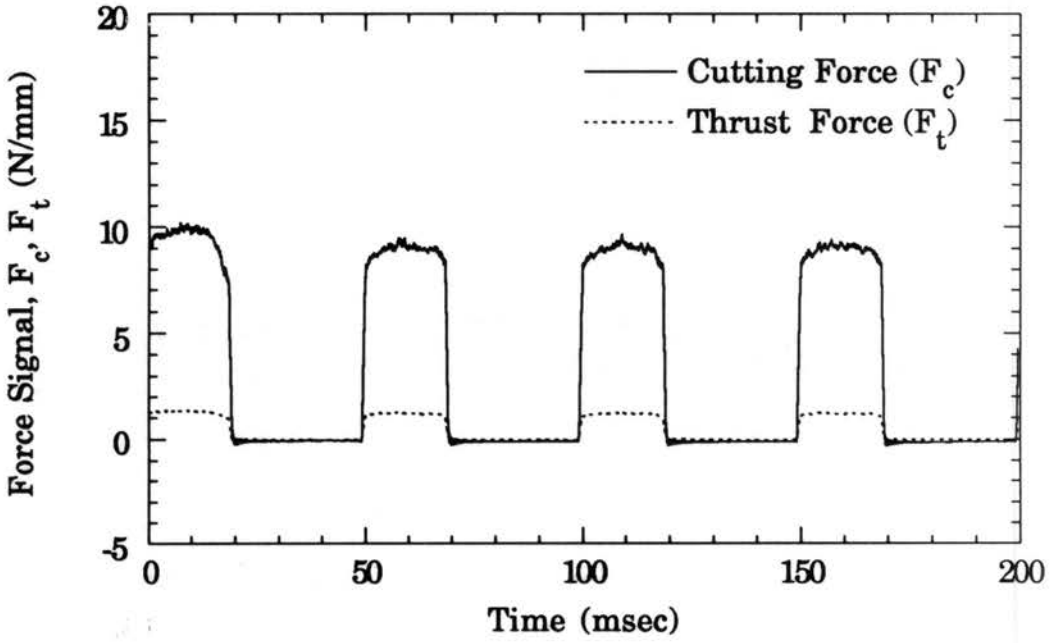

Figure 5-16. Averaged (19 points) Cutting and Thrust Force Signals in Orthogonal Flycutting of Te-Cu at 10 μm Depth of Cut

depths of cut corresponded to about 0.5 ~ 4 times the measured edge radius for the Tool A1. This may be due to the unstable interaction between the tool edge and the material where the material flow is unstable in front of the tool edge relative to the lower and upper end of the depths of cut range. Also, grain boundaries of the Te-Cu specimen in which the grain size would be this range may affect the fluctuation of the force signals.

5.4.2 Reproducibility of Force Components

5.4.2.1 Repeatability. The magnitudes of the cutting and thrust forces were obtained from the average heights in the cyclic force signals during cutting. At identical cutting conditions, two specimens were cut and force components were measured to check the reproducibility of the force components. Cutting experiments were performed starting from a 0.01 μm depths of cut to 20 μm. This process was then repeated for another specimen under the identical cutting conditions. The reproducibility is tested using the variation, Var (%), defined as:

$$\text{Var (\%)} = \frac{(\text{Force}_{\text{2nd specimen}} - \text{Force}_{\text{1st specimen}})/2}{(\text{Force}_{\text{2nd specimen}} + \text{Force}_{\text{1st specimen}})/2} \times 100 \qquad (5\text{-}1)$$

Two cases of reproducibility were investigated, i.e., the repeatabilities due to the change of the rake angle of the tool (tools of A1, B, C, D) of which the overall geometry was quite different, and those due to the change of the cutting distance for the tools having identical overall geometry (tools of A1, A3, A4). The calculated variations of cutting and thrust forces are shown in Figs. 5-17 ~ 5-20 for those two cases respectively. As shown in Figs. 5-17 and 5-18, at depths of cut below about 1 μm, the variations of both the

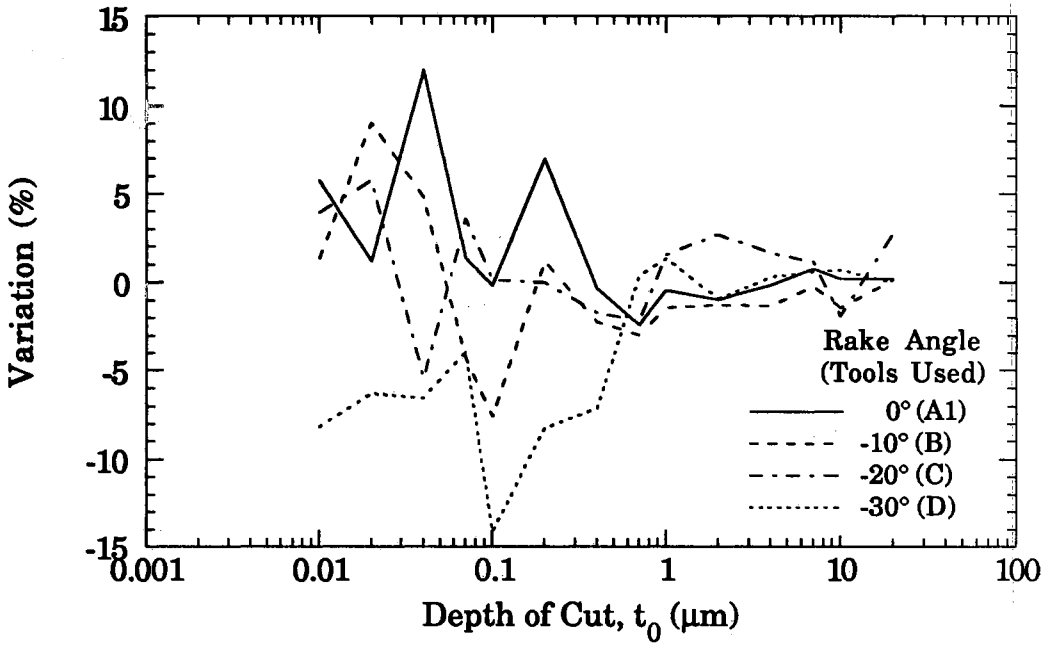

Figure 5-17. Relative Variation of Measured Cutting Forces Between Two Specimens in Micro-Machining of Te-Cu with Various Rake Angle New Tools

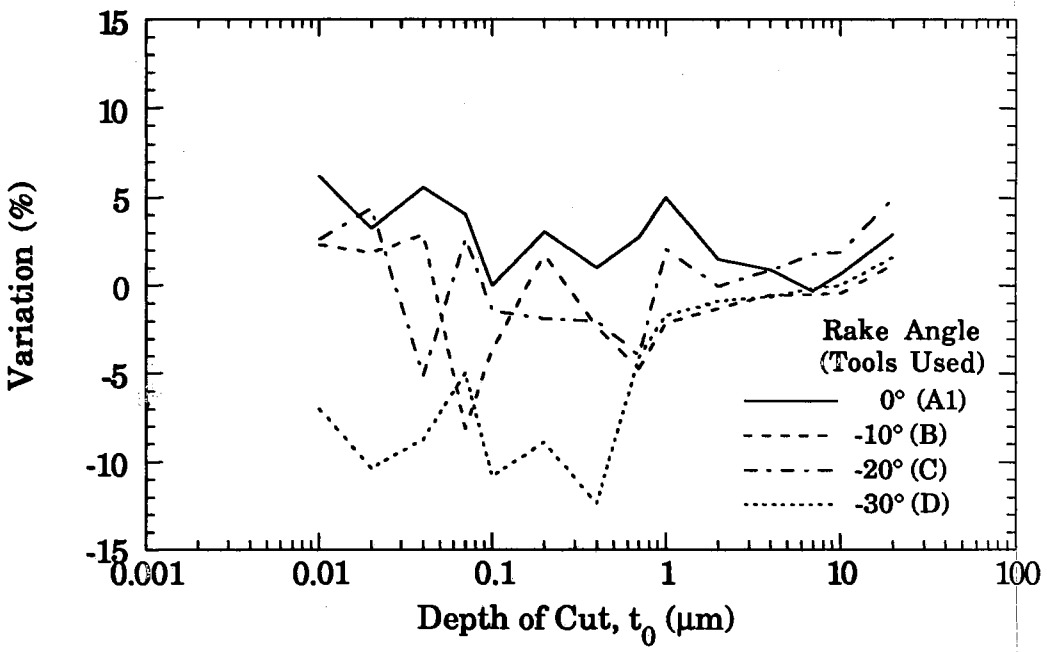

Figure 5-18. Relative Variation of Measured Thrust Forces Between Two Specimens in Micro-Machining of Te-Cu with Various Rake Angle New Tools

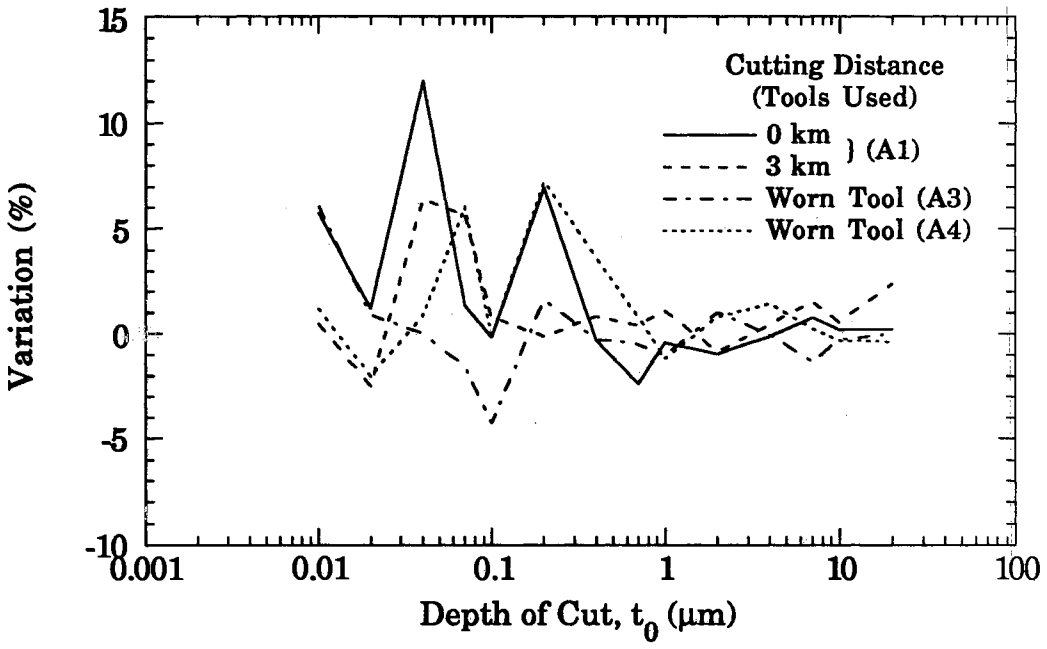

Figure 5-19. Relative Variation of Cutting Forces Between Two Specimens in Micro-Machining of Te-Cu with 0° Rake Tools at Various Cutting Distances

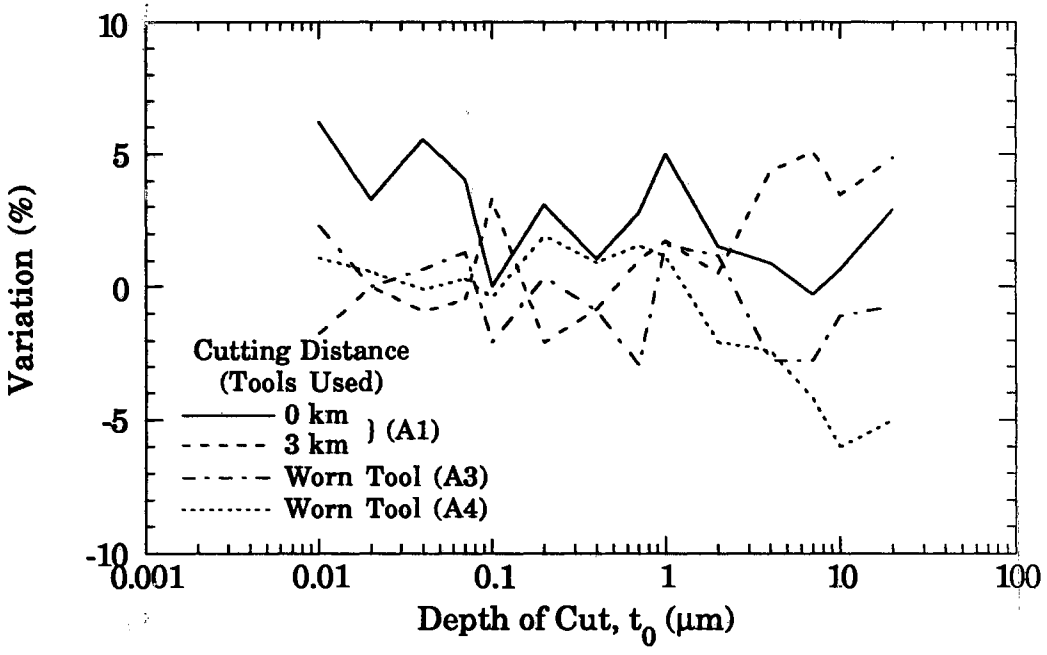

Figure 5-20. Relative Variation of Thrust Forces Between Two Specimens in Micro-Machining of Te-Cu with 0° Rake Tools at Various Cutting Distances

cutting and thrust forces show more scatter than those above 1 μm depth of cut. Even though the -30° rake tool had relatively high fluctuations at submicrometer depths of cut, there seems to be no general trend for the repeatability due to the change of the tool rake angles. Here, it is noted that 1 μm depth of cut is 4 times the measured tool edge radius of 0.25 μm, which is the upper range of the region attributed to rubbing and burnishing by Moriwaki and Okuda [1989] in the micro-cutting of OFHC. Similar trends can be seen from Figs. 5-19 ~ 5-20. For the case of identical overall tool geometries however, the thrust force from specimen to specimen fluctuated regardless of the cutting distance as depth of cut was increased, a different trend from that of the cutting forces. From the investigation of the variations of cutting and thrust forces, the repeatability can be said to be within about ± 5% of the average forces of the two specimens even though some data points are out of this range.

5.4.2.2 Comparison with the Literature. The reproducibility of the overall trends of the forces and energies between the results of the current study and some of those from the literature was examined. The results are shown in Figs. 5-21 ~ 5-24. Included are the results of Moriwaki and Okuda [1989], and Furukawa and Moronuki [1988] for the micro-machining of copper. Here, Tool A1 has a 0.25 μm edge radius and Tool A4 has a double edge radius of 0.28 μm as a primary and 1.0 μm as a secondary edge radius. In contrast to these tools, Moriwaki and Okuda's tool has been estimated to have a 20 ~ 50 nm edge radius with 1.0 mm nose radius. Cutting speed for Moriwaki's experiments was 1380 m/min, whereas it was 7.6 m/min for the current study. Furukawa and

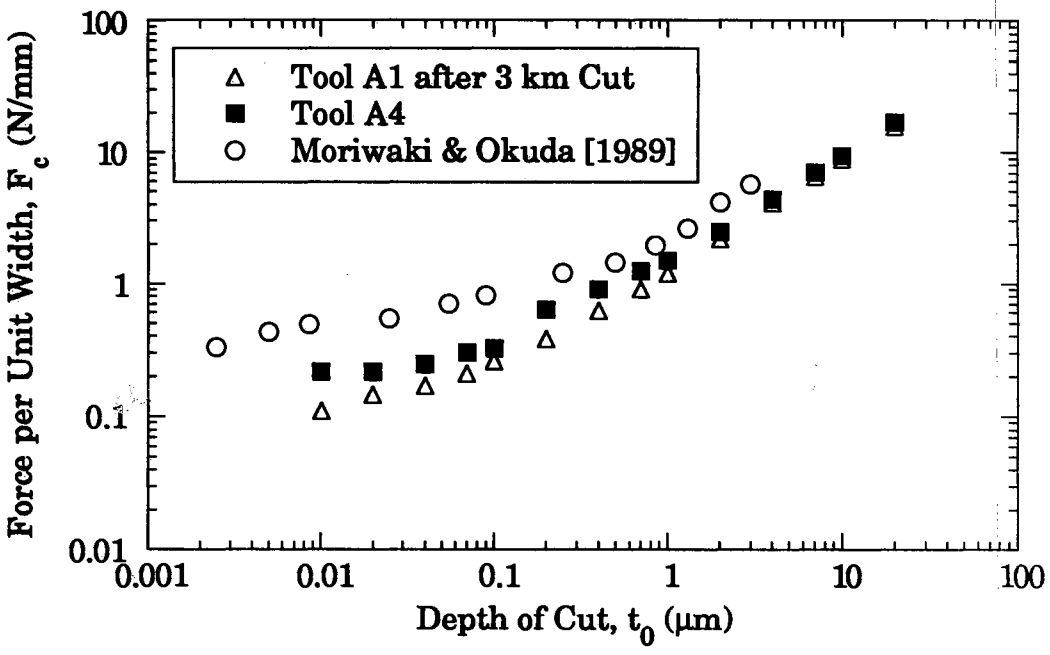

Figure 5-21. Comparison of Cutting Forces Obtained from 0° Rake Angle Tools with the Result of Moriwaki and Okuda [1989] in Micro-Machining of Copper

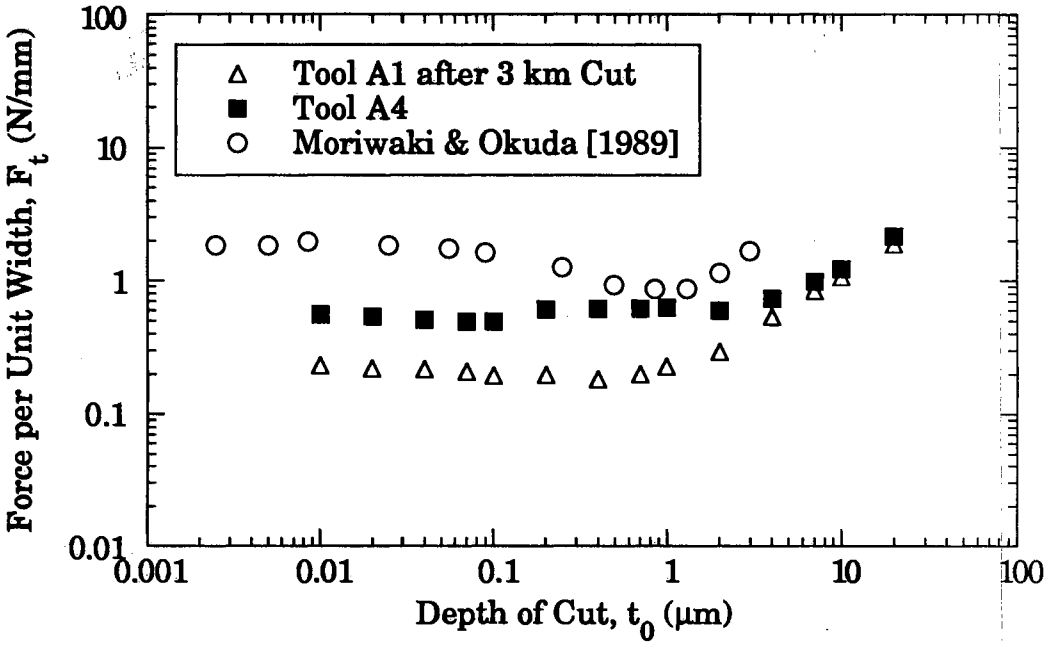

Figure 5-22. Comparison of Thrust Forces Obtained from 0° Rake Angle Tools with the Result of Moriwaki and Okuda [1989] in Micro-Machining of Copper

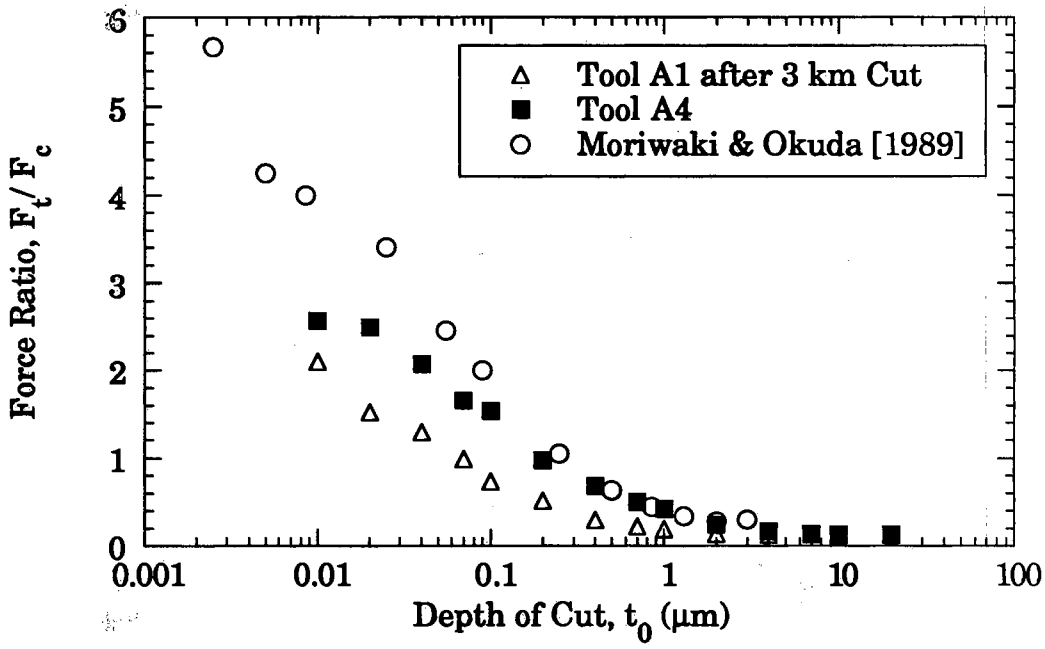

Figure 5-23. Comparison of Force Ratios Obtained from 0° Rake Angle Tools with the Result of Moriwaki and Okuda [1989] in Micro-Machining of Copper

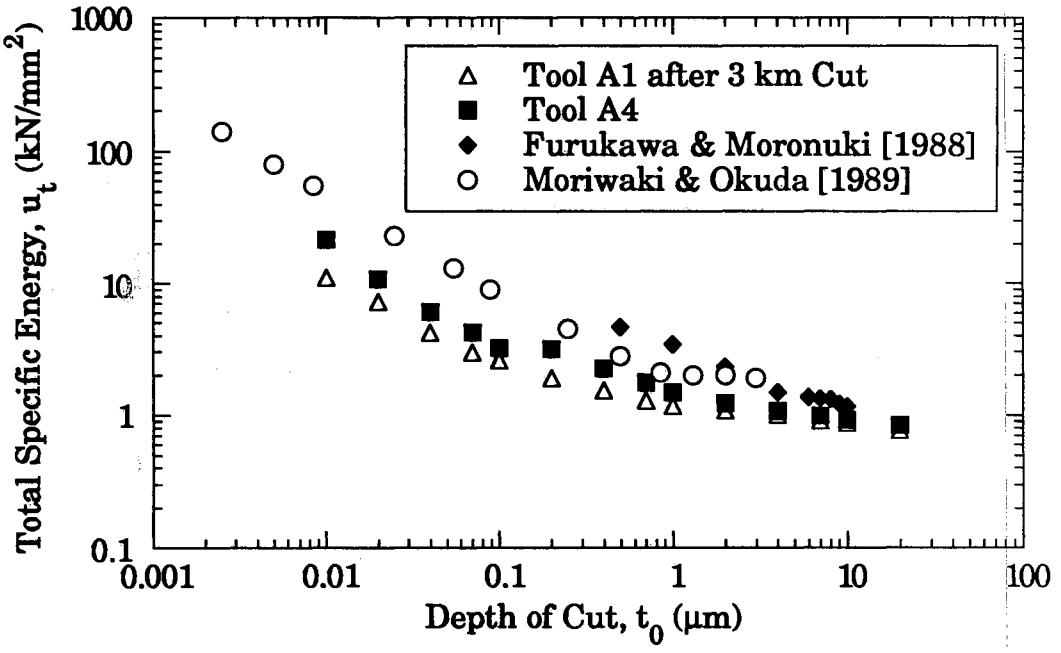

Figure 5-24. Comparison of Total Specific Energy Obtained from 0° Rake Angle Tools with Results from the Literature in Micro-Machining of Copper

Moronuki's cutting speed was 6 m/min, but the tool edge information was not reported.

In Figs. 5-21 ~ 5-23, the effect of depth of cut on cutting force, thrust force, and force ratio obtained from the A1 and A4 tools is compared with the results of Moriwaki and Okuda. Above a depth of cut of 0.7 μm for the cutting force, and about 2 μm for the thrust force, the three results are similar, viz., they are linear with depth of cut, and follow the same trends. These trends are the same for decreased depths of cut also but, they are nonlinear with depth of cut. The force ratios obtained for the worn Tool A4 and for the experiments of Moriwaki and Okuda show a leveling-off at the lower end of depth of cut, and approach values for conventional machining at the high end ($F_t/F_c = 0.2$). In Fig. 5-24, the effect of total specific energy on depth of cut is presented. The size effect can be seen in the figure. The minor differences and shifting of the trends in the figures may be due to the difference in cutting conditions and tool edge geometries.

5.4.3 Effect of Nominal Rake Angles

To study the nominal rake angle effect on energy dissipation, four new tools having 0°, -10°, -20°, and -30° nominal rake angles (Tools A1, B, C, D) were used. Two Te-Cu specimens were cut at 7.6 m/min. The results for the cutting force, thrust force, force ratio, and total specific energy are shown in Figs. 5-25 ~ 5-28. Even though two data sets were obtained from two specimens for all the experiments, data from only one specimen is presented since the repeatability was within ± 5 %. Between the depths of cut of 0.2 and 0.3 μm, the cutting and thrust force were seen to fall off, which is the range of the observed tool edge radius. All are seen

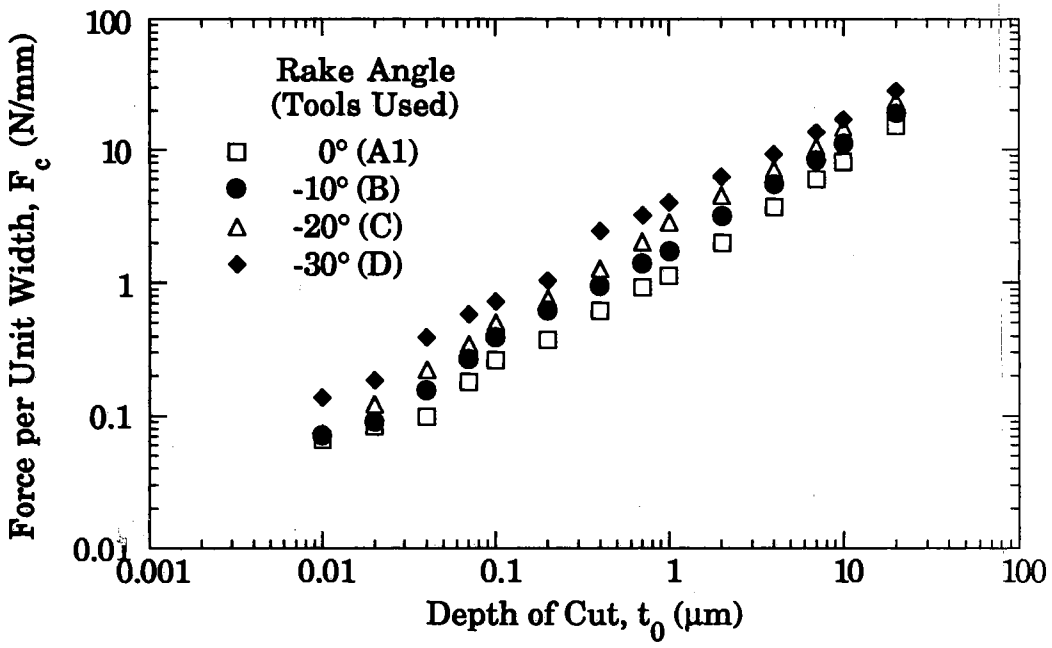

Figure 5-25. Cutting Force vs. Depth of Cut for Various Rake Angles in Micro-Machining of Te-Cu

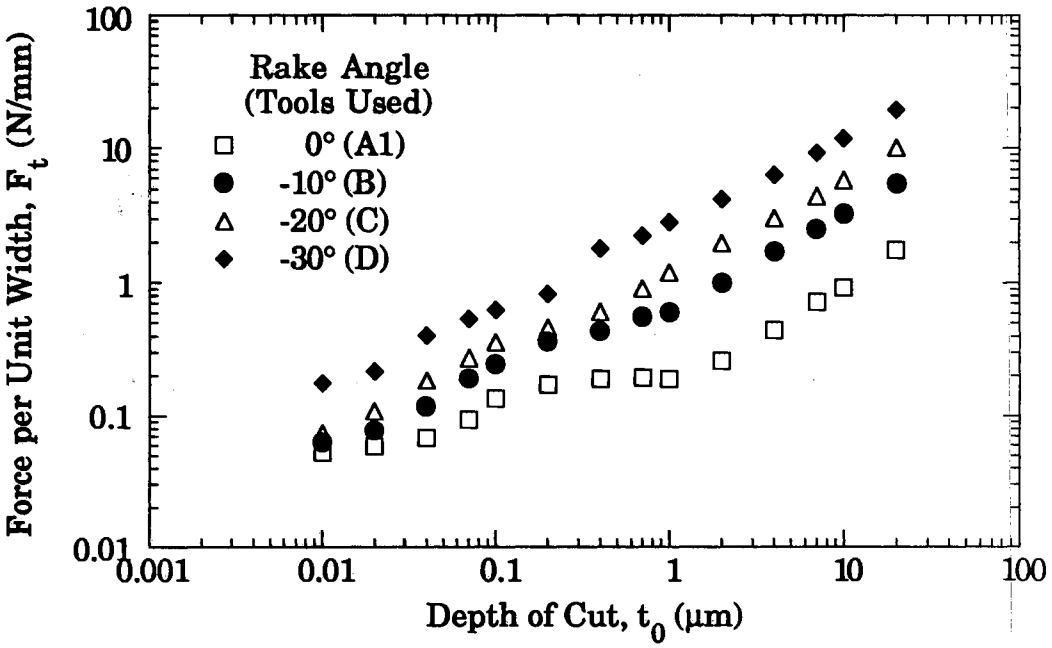

Figure 5-26. Thrust Force vs. Depth of Cut for Various Rake Angles in Micro-Machining of Te-Cu

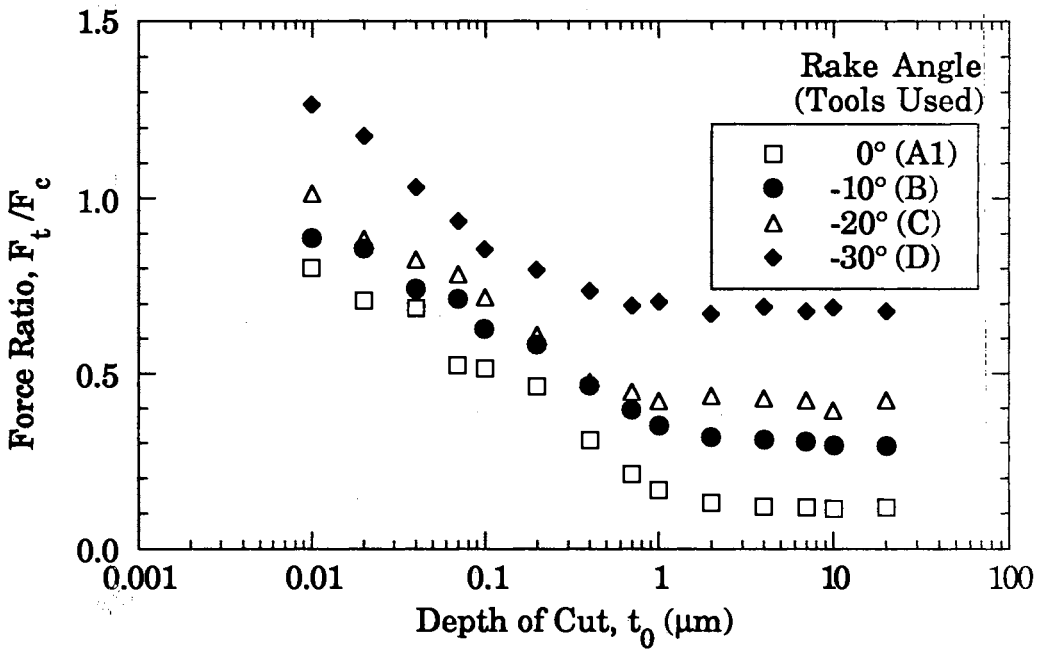

Figure 5-27. Force Ratio vs. Depth of Cut for Various Rake Angles in Micro-Machining of Te-Cu

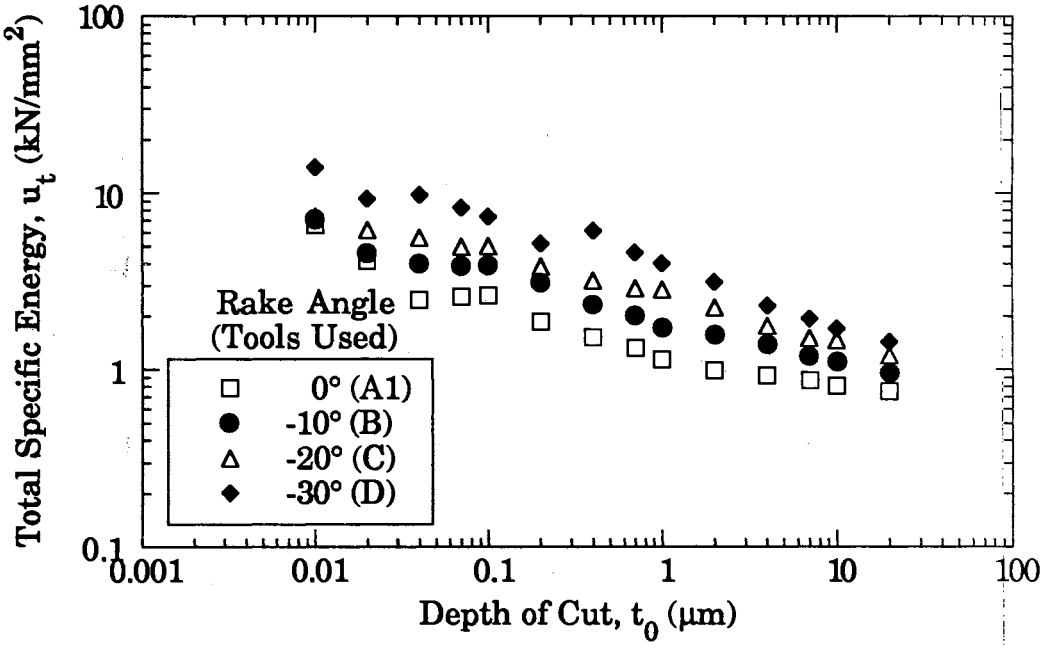

Figure 5-28. Total Specific Energy vs. Depth of Cut for Various Rake Angles in Micro-Machining of Te-Cu

to increase with decreasing rake angle over the entire range of depth of cut.

As shown in Fig. 5-25, the nonlinearity with depth of cut of the cutting force is less pronounced. This is consistent with the use of new tools, in which their edges are sharp and hence, the cutting process is dominant over plowing and sliding process even at submicrometer depths of cut.

In Fig. 5-26, the thrust force curve for the 0 degree rake angle tool exhibits a plateau in the depth of cut range of 0.2 ~ 1.0 μm. This depth of cut correspond to 0.8 ~ 4 times the measured edge radius of 0.25 μm. Although less pronounced, it appears to exist for the negative rake angle tools as well. This trend was seen to occur in many orthogonal micro-cutting experiments. It was most pronounced when cutting with new tools of 0° rake angle, and the same phenomenon has also been observed for the orthogonal ultra-precision flycutting of 6061-T6 aluminum. This behavior could be explained if the contribution to the thrust force due to the edge profile dominates over those contributions associated with the shear zone and rake face. The thrust force is seen to fall off in the range of the measured edge radius of the tool, which would be consistent with the above reasoning. The effect of nominal rake angle on the thrust force decreases as depth of cut decreases. For example, as nominal rake angle decreases from 0° to -30°, the increase of thrust force at 20 μm depth of cut is about 10 times, whereas at 10 nm depth of cut, the increase is only about 4 times the thrust force of the zero degree rake angle tool. This indicates that thrust force is significantly affected by the local tool edge geometry rather than a nominal rake angle at decreasing depths of cut.

In Fig. 5-27, the force ratio is seen to be approximately constant for large depths of cut (above several micrometers), which is consistent with

what is expected for conventional metal cutting. For a zero degree rake angle tool, the force ratio approaches 0.2. When converting the force ratios to the direction of resultant force vector using $\theta = \tan^{-1}(F_t/F_c)$, the increase in the direction at large depth of cut (> 2μm) is approximately the same as the decrease in the nominal rake angle.

For new tools, it was observed that the size effect is less significant than for worn tools regardless of the nominal rake angle. As shown in Fig. 5-28, the increase of specific energy is about one order of magnitude for three orders of magnitude decrease in depth of cut.

5.4.4 Effect of Cutting Distance

It is informative to investigate the change of cutting forces and energies at the early stages of a tool's life since this stage is known to affect the surface roughness greatly [Sugano, 1987]. Some suggest a "break-in" period for a production of parts with better surface finish due to this reason [Atkin, 1986]. Furthermore, the examination of forces and energies as cutting distance increases, could be a good alternative way of studying the effects of tool edge condition on energy dissipation when accurate tool edge characterization is difficult. Based on this reasoning, the very early stages of tool life were examined in terms of the resulting forces and energies up to 3 km in accumulated cutting distance using a 0° rake angle tool (A1).

Immediately after the study of the nominal rake angle effect, the tool edge was characterized under the AFM. To accelerate wear of the tool edge profile, an OFC specimen was cut up to 1 km in cutting distance at 15.2 m/min with light mineral oil as a cutting fluid. The other cutting conditions and the specimen size were the same as when cutting Te-Cu.

Cutting and thrust forces were measured using Te-Cu just after the OFC "wear-in" cutting. This procedure was repeated 3 times to get 3 km in total cutting distance.

Figs. 5-29 ~ 5-32 show the results of the cutting distance history effect on energy dissipation. The forces and energies are seen to increase as cutting distance increases at decreased depth of cut. Above a depth of cut of about 1 μm, the cutting and thrust force remained the same, independent of the cutting distance. Below this depth of cut however, the cutting and thrust forces increased significantly. This trend is consistent with the aluminum cutting described in the previous chapter. The increase of cutting force with cutting distance is less pronounced than that of thrust force. The increase of cutting force at 10 nm depth of cut for a total of 3 km cutting distance, is about 1.7 times that of the new tool however, the increase of the thrust force at the same conditions is about 4.4 times the force of the new tool (0 km).

Form Fig. 5-30, an interesting observation is that the thrust force for depths of cut between 0.1 ~ 1.0 μm decreases as cutting distance increases up to 1 km, whereas at a depth of cut below 0.1 μm, they gradually increase as cutting distance increases. The thrust force in this range begins to increase after cutting distance increases beyond 1 km. Hence, the plateau phenomenon in this range of depth of cut begins to disappear. Here, the zero kilometer cutting data is the same as the data obtained from the study of the rake angle effect. It is also observed that the nonlinearity of the thrust force with depth of cut increases as cutting distance increases. Due to the rapid increase in thrust force as cutting distance increases, the thrust force becomes dominant over the cutting force from the early stages

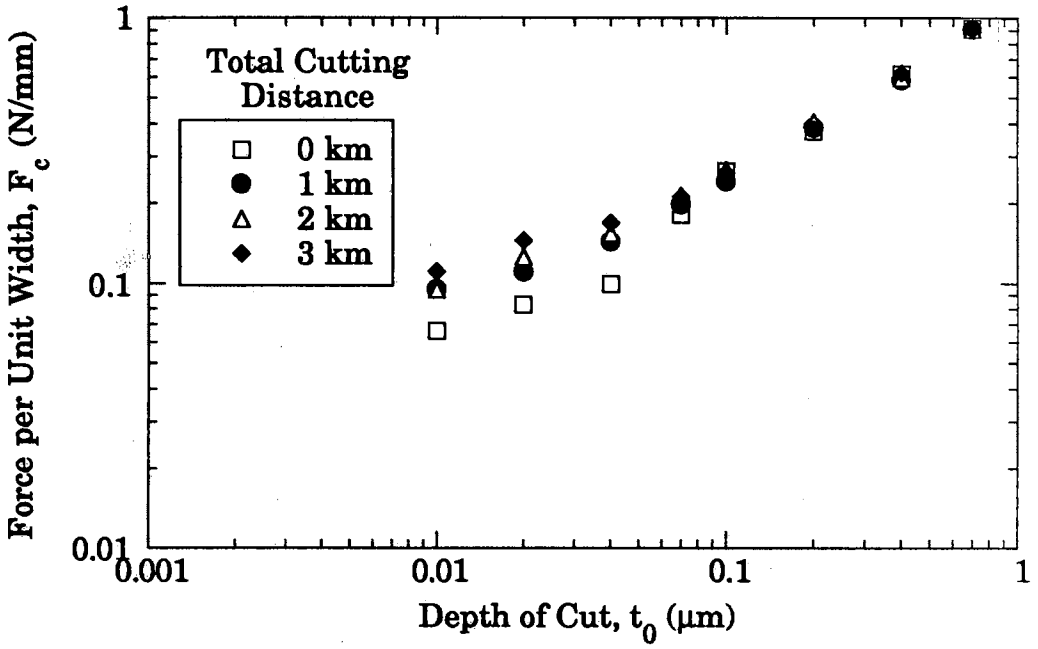

Figure 5-29. Effect of Cutting Distance on Cutting Force in Orthogonal Flycutting of Te-Cu with 0° Rake Angle Tool (Tool A1)

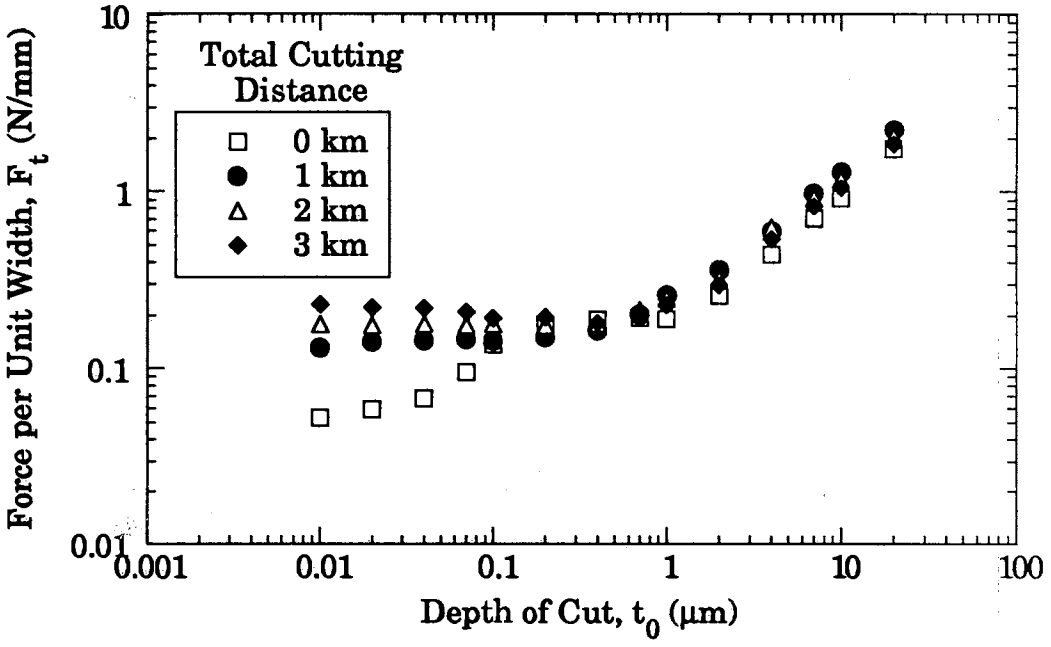

Figure 5-30. Effect of Cutting Distance on Thrust Force in Orthogonal Flycutting of Te-Cu with 0° Rake Angle Tool (Tool A1)

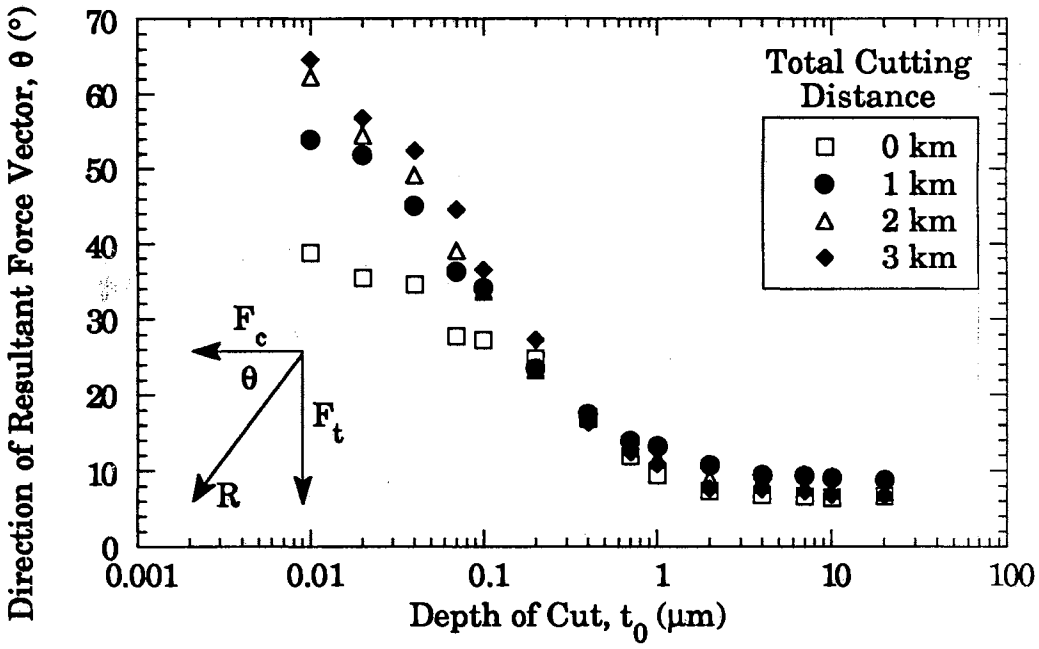

Figure 5-31. Effect of Cutting Distance on Direction of Resultant Force Vector in Orthogonal Flycutting of Te-Cu with 0° Rake Angle Tool (Tool A1)

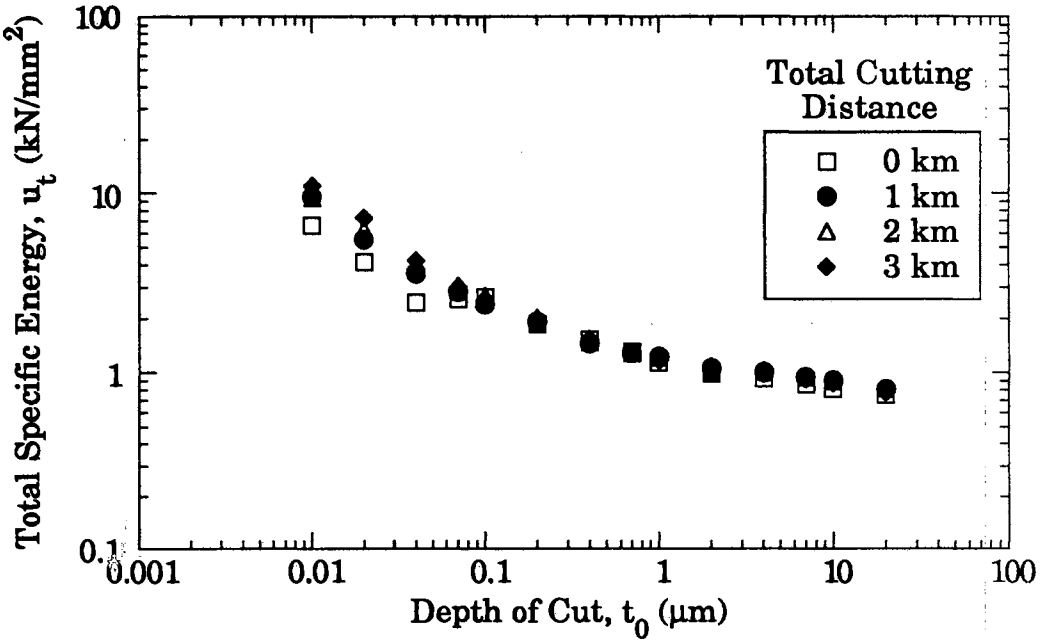

Figure 5-32. Effect of Cutting Distance on Total Specific Energy in Orthogonal Flycutting of Te-Cu with 0° Rake Angle Tool (Tool A1)

of the tool's life at small depths of cut, i.e., the cross-over of cutting and thrust force begins at 10 nm from about 1 km in cutting distance.

From the direction of the resultant force vector vs. depth of cut curve shown in Fig. 5-31, at 10 nm depth of cut, it can be seen that the increment of the force vector is getting smaller as cutting distance increases. This indicates that the tool edge condition is stabilized or smoothened as cutting distance increases. Disappearance of the plateau and the increase of the size effect can also be observed from the total specific energy curve shown in Fig. 5-32.

5.4.5 Effect of Worn Tool

In the previous section, the edge profile used for the study was limited in its shape due to a relatively short cutting distance of 3 km. For further examination of a well-developed tool edge profiles' effect on resulting forces and energies, worn tools which had considerably different edge profiles were used. Fig. 5-33 shows the profiles of two tool edges as characterized by the AFM. The two tools had been used over significantly different cutting distances and had the same overall geometries, i.e., 0° rake and 6° clearance angles. On their rake faces, the tools start to deviate from their nominal rake angle at about 0.25 μm for Tool A1 and approximately 0.5 μm for Tool A4. The new tool has a well-defined edge radius of 0.25 μm however, the worn tool exhibits a gradually sloping flank face. The profile of Tool A4 is seen to be characteristic of the edges of several worn tools examined in this study as shown in Figs. 5-6 and 5-7, and is similar to that reported by Asai et al. [Asai, 1990]. In addition, the edge profiles inferred by the AFM measurements were consistent with previously reported

approximations of edge radii for similar tools determined by SEM examination [Lucca, 1992]. From the flank face of Tool A4, an extensively smoothened contour can be observed relative to that at the rake face.

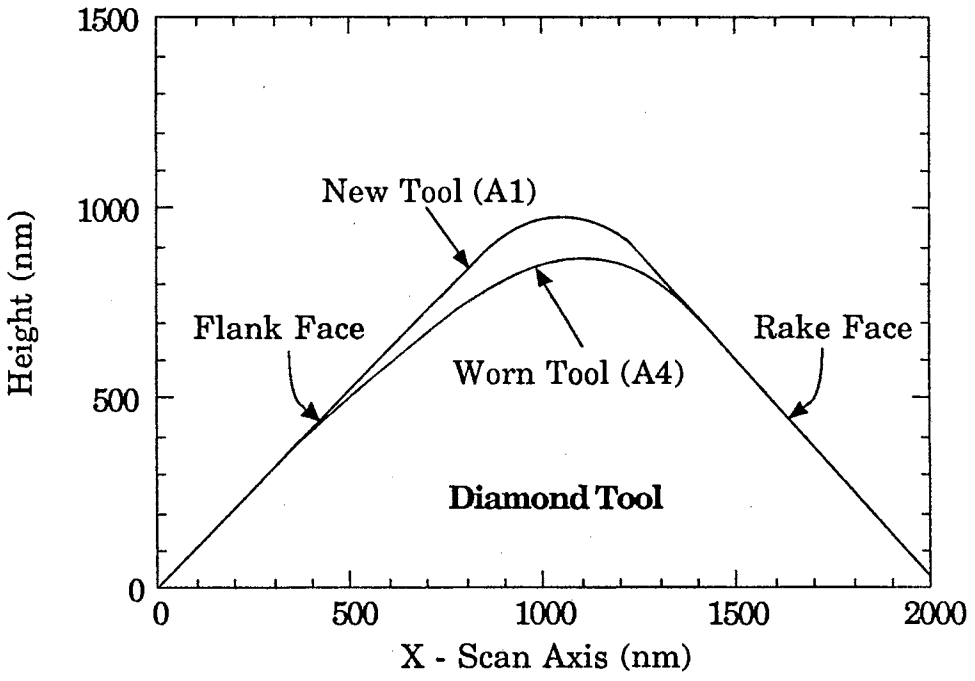

Figure 5-33. Edge Profiles of New and Worn Tools Measured with Atomic Force Microscope

A comparison of the forces and energies which resulted when cutting with Tool A1 and Tool A4 is shown in Figs. 5-34 ~ 5-37. Included is the data from Tool A3, and the edge profile of the tool is shown in Fig. 5-7. This tool seems to be in the middle of developing flank wear, and the rake wear is not yet well established, hence the tool edge radius is similar to the Tool A1 but flank wear is relatively well defined like Tool A4. This was one

of the reasons that Tool A3 is chosen as a worn tool along with Tool A4. As expected, the forces agree reasonably well at relatively large depths of cut where the effect of the nominal geometry dominates.

Fig. 5-34 shows that the cutting force of Tool A4 is higher (about 40 ~ 50 %) than that of Tool A1 for the range of depths of cut between 0.2 μm to 1 μm. This is consistent with the differences in their rake face geometries in this range. Also, the magnitudes of the forces at submicrometer depths of cut are in the order of the edge radii of the three tools, viz., they are in the order of A1<A3<A4. In this range, both tools show a constant thrust force, with Tool A4 exhibiting a higher thrust force as shown in Fig. 5-35. The thrust force from Tool A3 is positioned between the forces of the two tools of A1 and A4 at decreased depths of cut. This again is consistent with their relative flank face geometries. Also, this trend of tool edge geometry at the flank face seems to affect the resulting thrust force more than the cutting force at small depths of cut. Here, for Tool A4, it is observed that the drop off of both the cutting and thrust forces between 0.1 ~ 0.2 μm is consistent with the depth of about 120 nm upward from the bottom of the flank to the point where the primary and secondary edge radii intersect as shown in Fig. 5-8. A constant thrust force here again could be explained if the thrust force component due to the edge profile dominated over cutting and rake face frictional forces.

By using a constant value for the thrust force in this range for each of the tools, the contact length at the tool-workpiece interface can be estimated based on an interfacial pressure of 3 times the uniaxial yield strength of the workpiece material (225 MPa for Te-Cu). This estimate results in lengths of 0.31 μm for Tool A1 and 0.92 μm for Tool A4. Examination of the tool profiles from Fig. 5-33, indicates that the

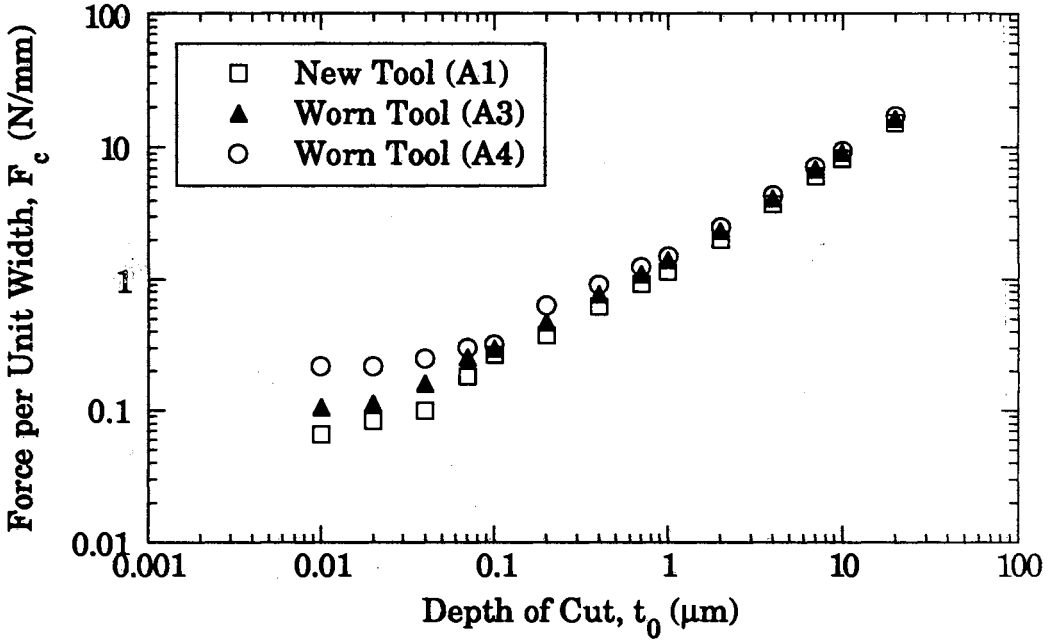

Figure 5-34. Cutting Forces Obtained from New and Worn Tools with Same Overall Geometries in Orthogonal Flycutting of Te-Cu

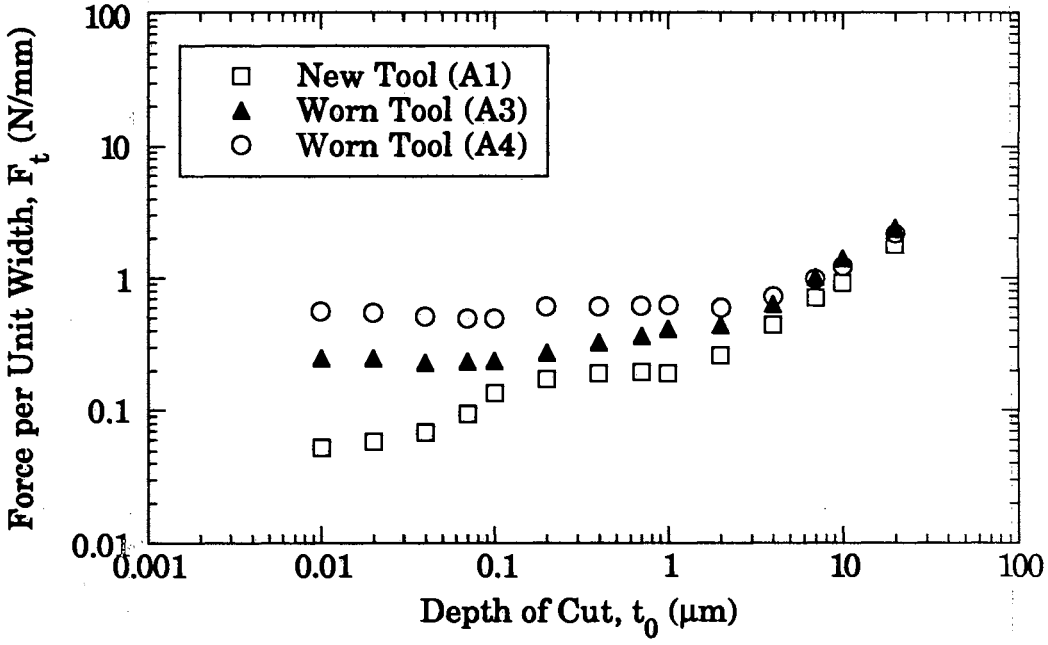

Figure 5-35. Thrust Forces Obtained from New and Worn Tools with Same Overall Geometries in Orthogonal Flycutting of Te-Cu

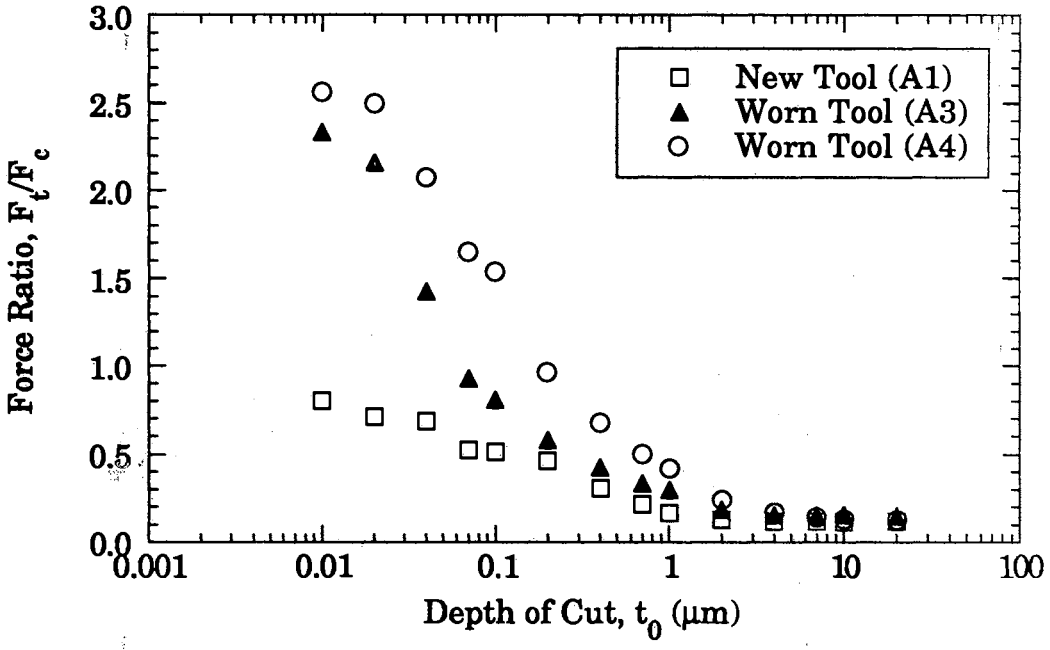

Figure 5-36. Force Ratios Obtained from New and Worn Tools with Same Overall Geometries in Orthogonal Flycutting of Te-Cu

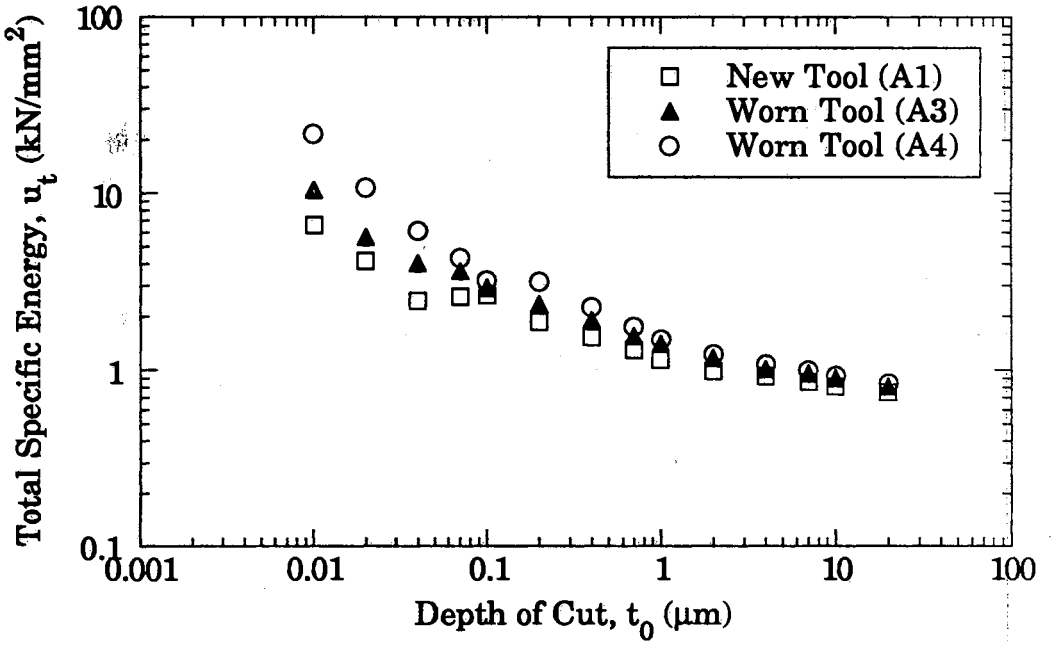

Figure 5-37. Total Specific Energies Obtained from New and Worn Tools with Same Overall Geometries in Orthogonal Flycutting of Te-Cu

minimum lengths at the flank face which would be in contact with the workpiece when cutting are about 0.25 μm and 1.0 μm for Tool A1 and Tool A4 respectively. This result also agrees with the measurements of the contact length at the flank face based on a AuPd coating technique [Lucca, 1992].

Below about 0.2 μm depth of cut, the thrust force is seen to drop off for Tool A1, which should occur if the component of thrust force due to the edge profile dominates. Tool A4 exhibits a slight decrease in thrust force, however, it remains relatively constant down to depths of cut of 10 nm. It is expected that when a chip is no longer being formed, and cutting transitions into pure sliding indentation at the tool-workpiece interface, both the cutting and thrust forces should be approximately constant. Although no attempt was made in this study to determine the depth of cut at which chip formation ceased, force data for the lowest depths of cut examined here indicates such a trend. This will be discussed further in a later section.

Fig. 5-36 represents the force ratio based on the measured cutting and thrust forces. Even at 10 nm depth of cut for Tool A1, the thrust force is still smaller than the cutting force, i.e., the force ratio is smaller than unity. However, for the other two tools A3 and A4, the force ratios are significantly larger. Below about 40 nm depth of cut, the force ratios of the A3 tool are closer to those of A4, and for depths of cut above about 70 nm, the ratios are closer to those of the new Tool A1. This trend can be explained by examining the measured edge profiles. As can be seen from the Fig. 5-7, which represents the tool edge of Tool A3, the sloping of the flank contour gradually approaches the circle representing the edge radius, which is similar to that of Tool A4. This depth is about 50 nm from

the bottom of the flank. The force ratios seem to be reflected by these similar flank contours, viz., the force ratios of the A3 tool below depths of cut of 40 nm are close to those of A4. Above this depth, the edge profile and the edge radii of the tool A1 and A3 are similar, which seems to make the force ratios of A3 tool closer to those of A1. Total specific energy (Fig. 5-37) for the worn tool increases drastically at the lower end of the depth of cut range, which indicates a significant size effect for the worn tools.

5.4.6 Effect of Effective Rake Angle

In the previous section, it was observed that the local tool profile is significant in determining the resulting forces and energies at reduced depths of cut. From this observation, the significance of the role of flank-workpiece interaction on the energy dissipation can be seen. For further examination of the effect of the local tool edge profile, the effect of effective rake angle was studied.

In order to measure the effective rake angle for a given depth of cut, the tool edge contour and a relative scale of the depths of cut were constructed using the edge profile obtained from the AFM examination. The results are shown in Figs. 5-38 and 5-39 for tools A1 and A4.

To estimate the effective rake angle at a given depth of cut, a point was identified on the tool's edge profile, at a distance half the depth of cut up from the workpiece surface. A line tangent to the edge profile at that point was used to determine the effective rake angle. The measured negative effective rake angle (α_e) together with the direction of resultant force vector ($\theta = \tan^{-1}(F_t/F_c)$) is shown in Figs. 5-40 and 5-41 as a function of depth of cut. As shown in Fig. 5-40, the effective rake angle above depths of cut of

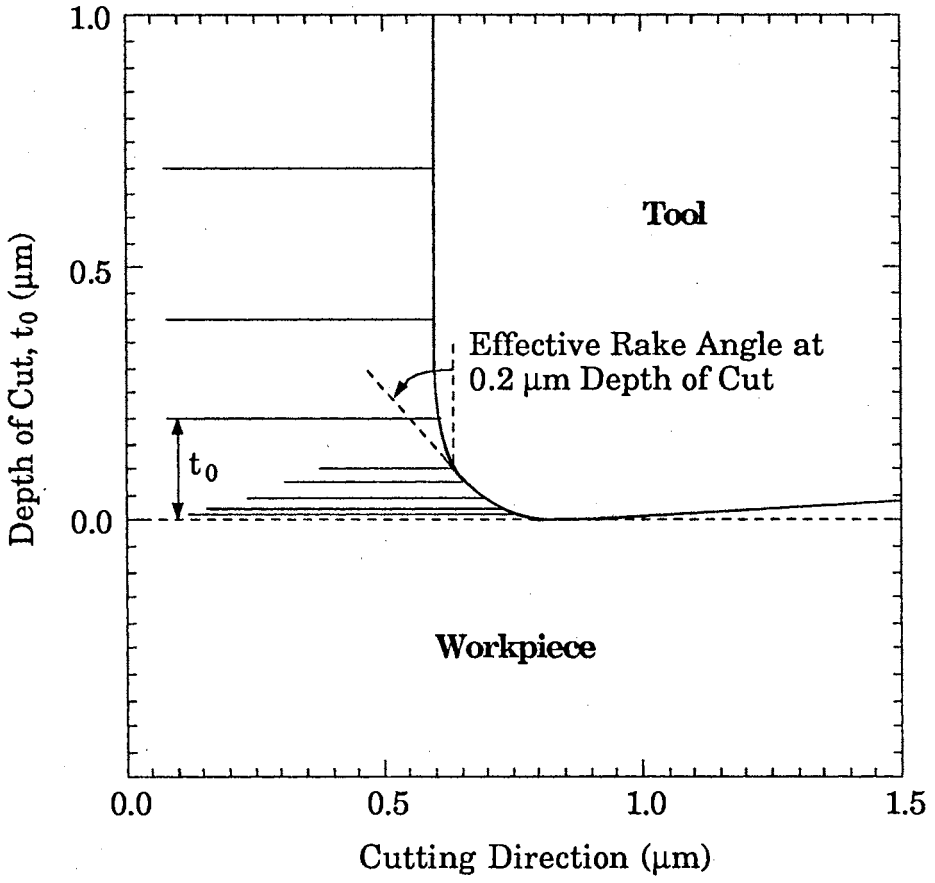

Figure 5-38. Contour of Cutting Edge with Depth of Cut to Measure the Effective Rake Angle of Tool A1 After 3 km in Cutting Distance

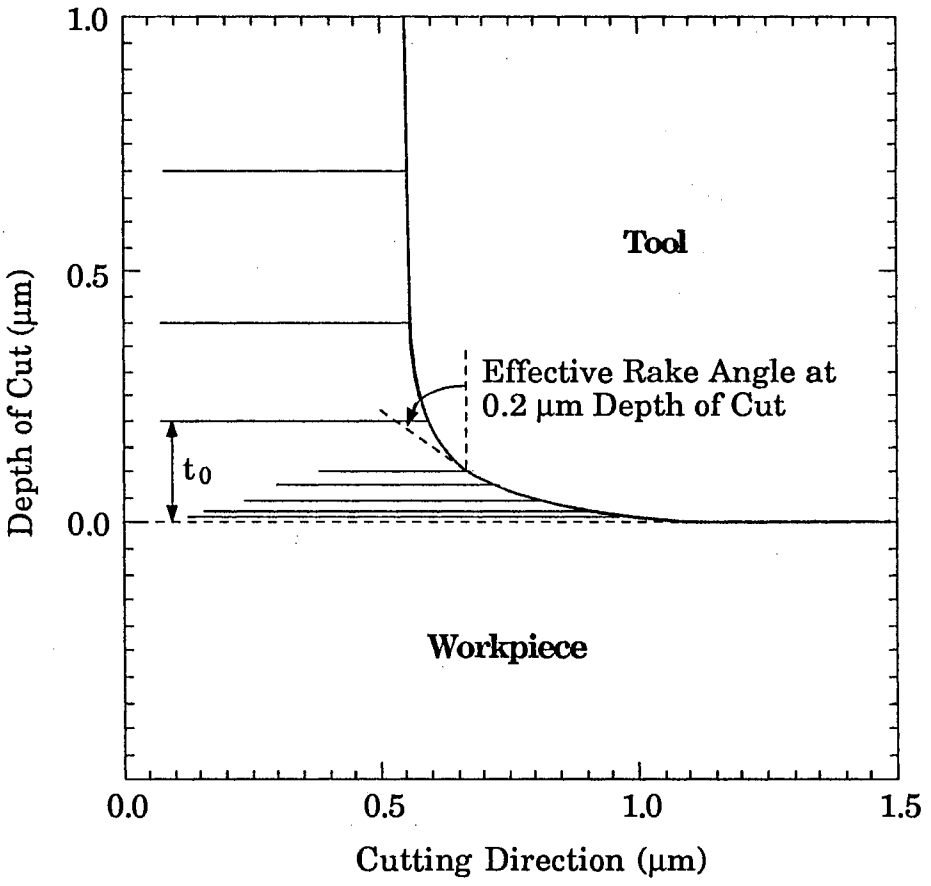

Figure 5-39. Contour of Cutting Edge with Depth of Cut to Measure the Effective Rake Angle of Tool A4

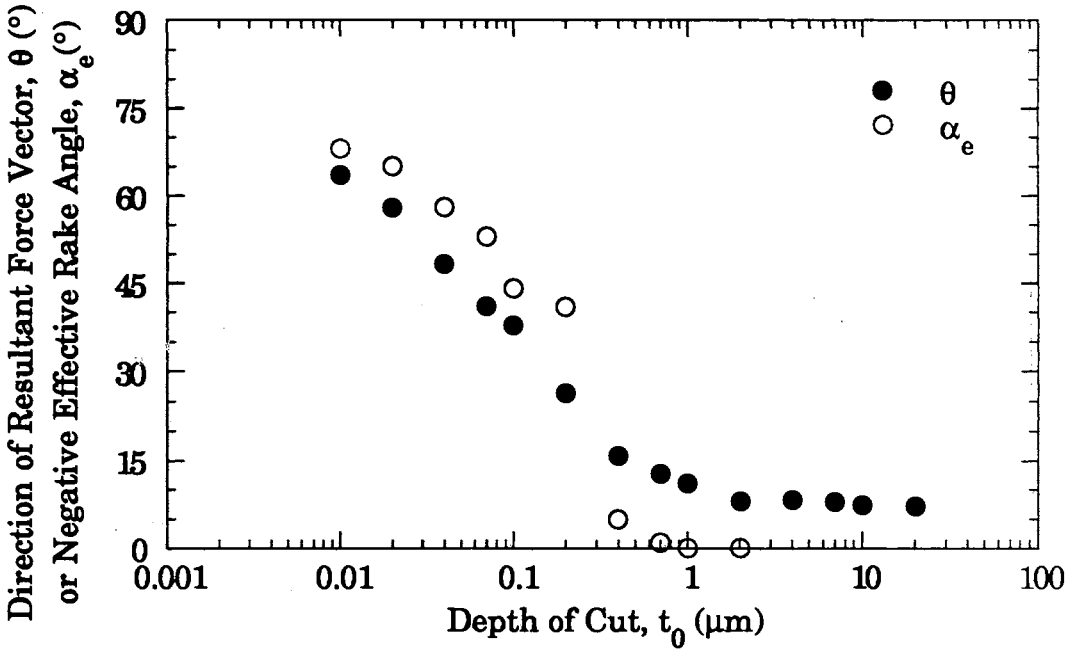

Figure 5-40. Comparison of Direction of Resultant Force Vector and Effective Rake Angle in Micro-Machining of Te-Cu with 0° Nominal Rake Angle New Tool (A1)

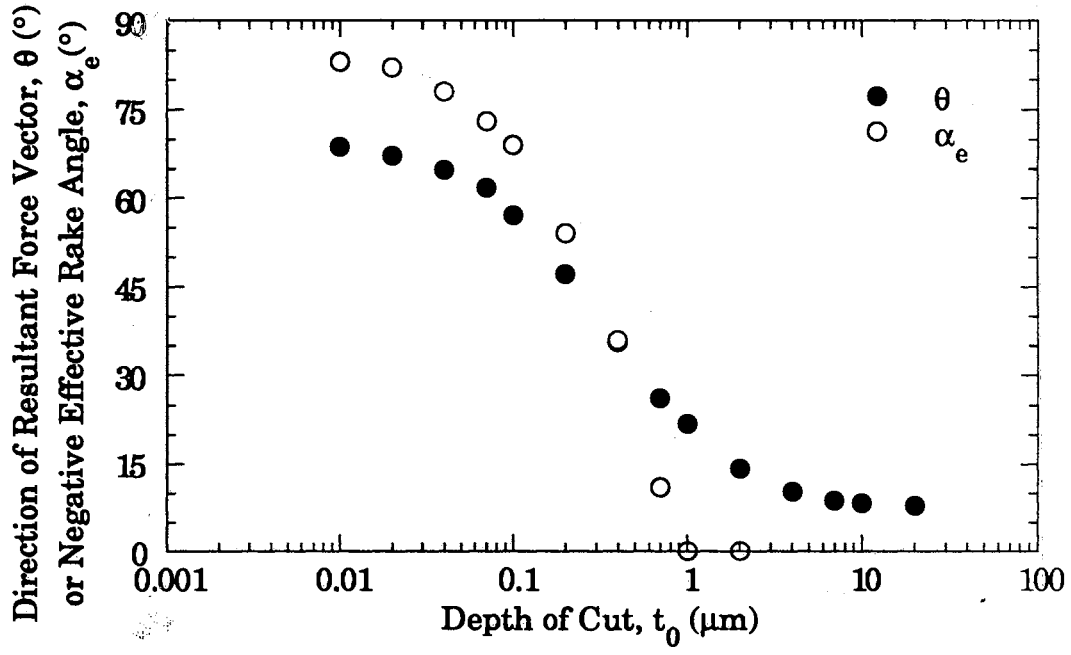

Figure 5-41. Comparison of Direction of Resultant Force Vector and Effective Rake Angle in Micro-Machining of Te-Cu with 0° Nominal Rake Angle Worn Tool (A4)

about 0.5 μm approaches the nominal rake angle of 0° since the measured edge radius was 0.25 μm. Below this depth of cut, the effective negative rake angle increases dramatically as depth of cut decreases. From the depth of cut where the effective rake angle deviates from the nominal rake angle, the direction of the resultant force vector also begins to increase as depth of cut decreases. However, above this depth of cut, θ approaches that for conventional machining (several degrees).

When the tool is further used, a gradual sloping of the tool edge profile and hence a smooth change of the rotation of the resultant force vector can be seen (Fig. 5-41). The overall trends of the curves are the same as before, i.e., as negative effective rake angle increases, the direction of the resultant force vector increases. At the lower end of depth of cut, the effective rake angle approaches -85° and correspondingly, the direction of resultant force vector approaches 70° downward toward the workpiece.

From Figs. 5-40 and 5-41, at submicrometer depths of cut, the effective rake angle can be seen to deviate significantly from the nominal rake angle. This indicates that the nominal rake angle is meaningless at the submicrometer depths of cut below the tool edge radius, viz., the process mechanics in this range of depths of cut is governed by the effective rake angle of a tool. The depth of cut where the direction of the resultant force vector and the negative effective rake angle crosses over is the same for both Tools A1 and A4 at about 0.3 μm. Also, the cross-over angles are about 20° for A1 and 35° for A4. The cross-over angle is greater for worn tools. Hence, this angle could be an index representing a severity of flank wear for various tools.

The leveling off of the effective rake angle and the corresponding change of the vector direction at decreased depth of cut indicates that the

process has changed from a chip formation-dominant process to plowing and sliding-dominant process. This severe rotation of the direction of resultant force vector leads to an inefficient material removal.

It would be informative to compare the force ratio from nominal rake angle tools at large depths of cut with that obtained from tools with effective rake angles at submicrometer depths of cut. For this comparison, the force ratios of various nominal rake angle tools were obtained from the average force ratios at large depths of cut where they are constant. The other force ratios are obtained from the submicrometer depths of cut to which the estimated effective rake angle corresponds. The results are shown in Figs. 5-42 and 5-43 for different tools and various workpiece materials.

In Fig. 5-42, the overall effect of negative rake angle on thrust to cutting force ratio is shown. This figure shows three separate sets of results. First is the average force ratios for nominal rake angle tools (A1, B, C, and D) at depths of cut above 2 μm (Fig. 5-27). The second is the data obtained by estimating the effective negative rake angle which prevailed at a given depth of cut for three tools with a nominal rake angle of 0 degrees (Tools A1, A3, and A4). Finally, these results are compared with the results of Komanduri [1971] for the single point cutting of steel using negative rake angle tools. Both the nominal rake angle diamond tools, when cutting at large depths of cut where the effects of the edge profile are small, and diamond tools cutting at submicrometer depths of cut where the effect of effective rake angle prevails, showed the same trends, viz., as negative effective or nominal rake angle increases, force ratio also increases. The difference between the results of Komanduri and the results of present study seems to be due to the differences in tool and

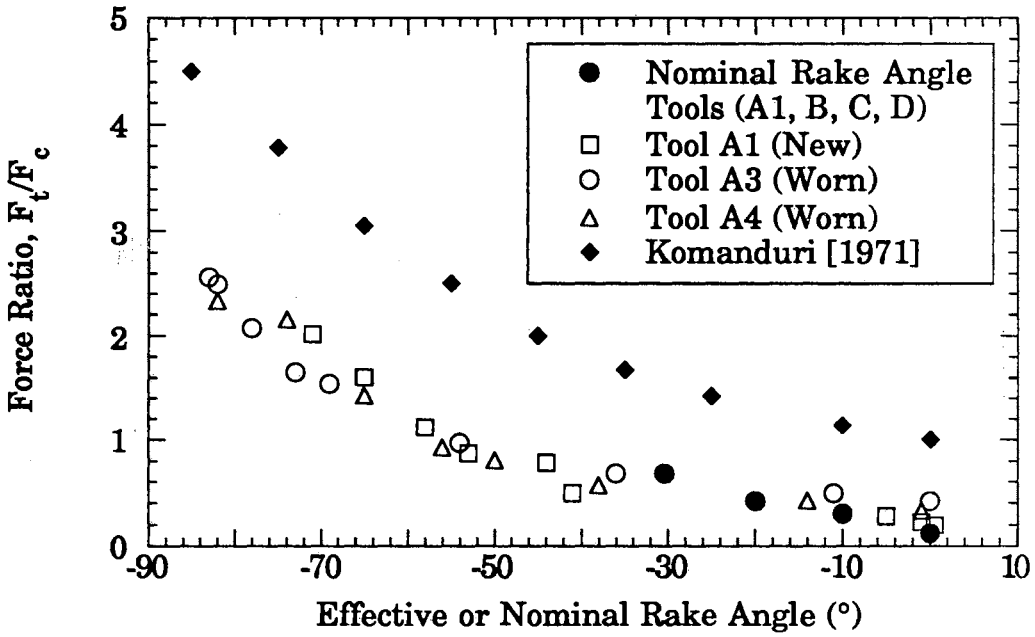

Figure 5-42. Effect of Rake Angle on Force Ratio in Machining with Various Tools

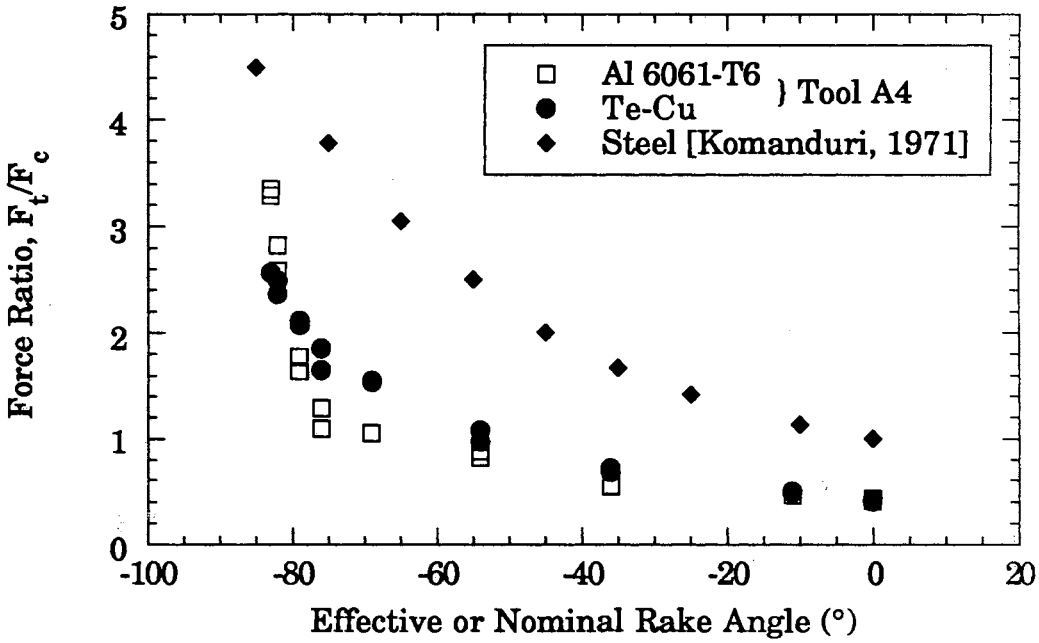

Figure 5-43. Effect of Rake Angle on Force Ratio in Machining of Various Materials

workpiece materials, i.e., Komanduri used steel workpiece cutting with carbide tool at a cutting speed of 183 m/min.

In Fig. 5-43, a similar rake angle effect on force ratios for various materials is shown. The trend for copper is similar to that for aluminum and steel, however the increase of force ratio at very high negative rake angle is dramatic for aluminum.

5.4.7 Effect of Cutting Speed

Debate about the contribution of cutting speed to the dramatic increase in total specific energy as depth of cut decreases is long standing. To study the speed effect on the forces and resulting energies, four different cutting speeds were examined under the identical cutting conditions. Tool A1 was used just after the study for cutting distance effect. The examined cutting speeds were 7.6, 22.9, 38.1, and 76.2 m/min. These speeds corresponded to 100, 300, 500, and 1000 rpm using the present experimental set-up. Two specimens were cut at each cutting speed, and the results are shown in Figs. 5-44 ~ 5-47. The cutting and thrust forces, force ratios, direction of the resultant force vectors, and total specific energies measured at four different cutting speeds are shown. As cutting speed increases, increased oscillations of the force signals in a given step height were observed, however, no discernible differences in force components were observed for up to one order of magnitude greater cutting speed.

In order to investigate the variation of the force components due to the increase in cutting speed, the variation from Specimen 1 to Specimen 2 was calculated at a given cutting speed using eq. (5-1). The variation for cutting and thrust forces are given in Figs. 5-48 ~ 5-49. The variation from

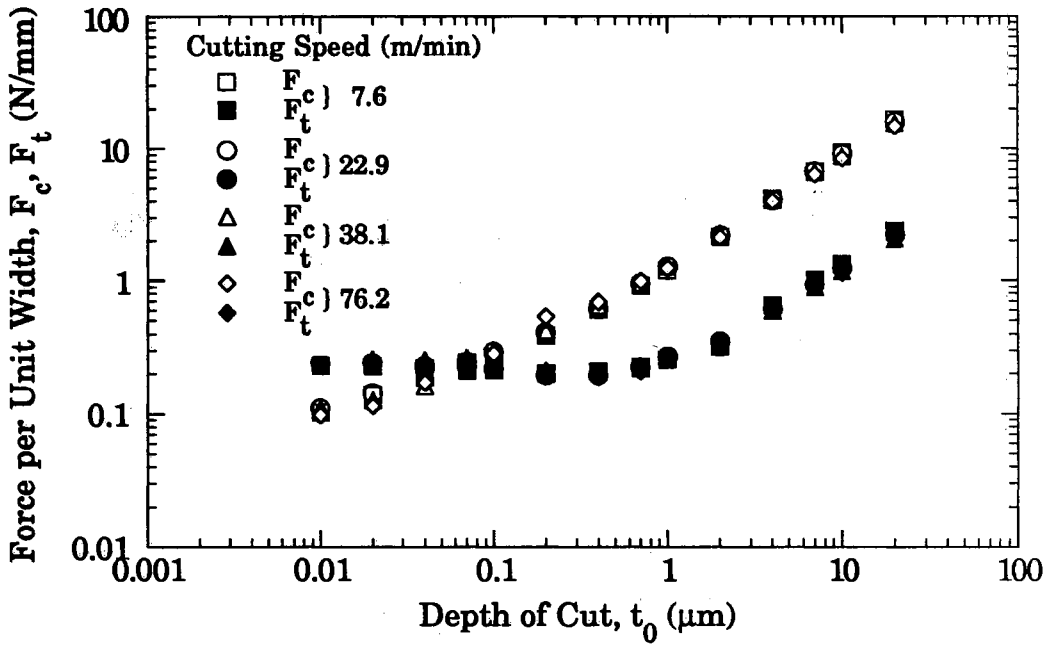

Figure 5-44. Effect of Cutting Speed on Force Components in Orthogonal Flycutting of Te-Cu

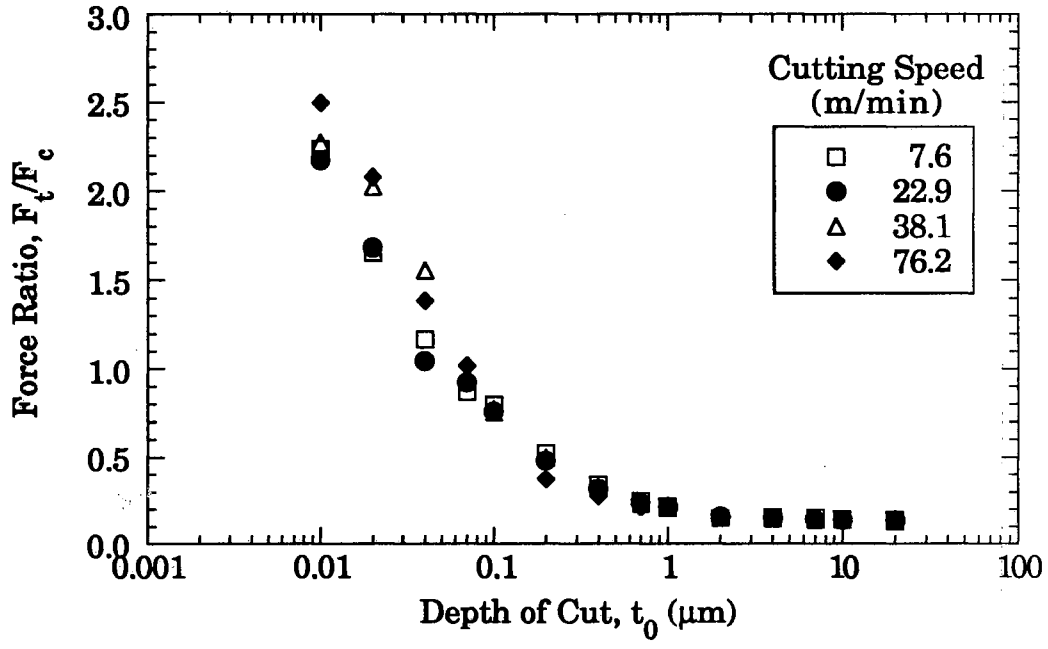

Figure 5-45. Effect of Cutting Speed on Force Ratio in Orthogonal Flycutting of Te-Cu

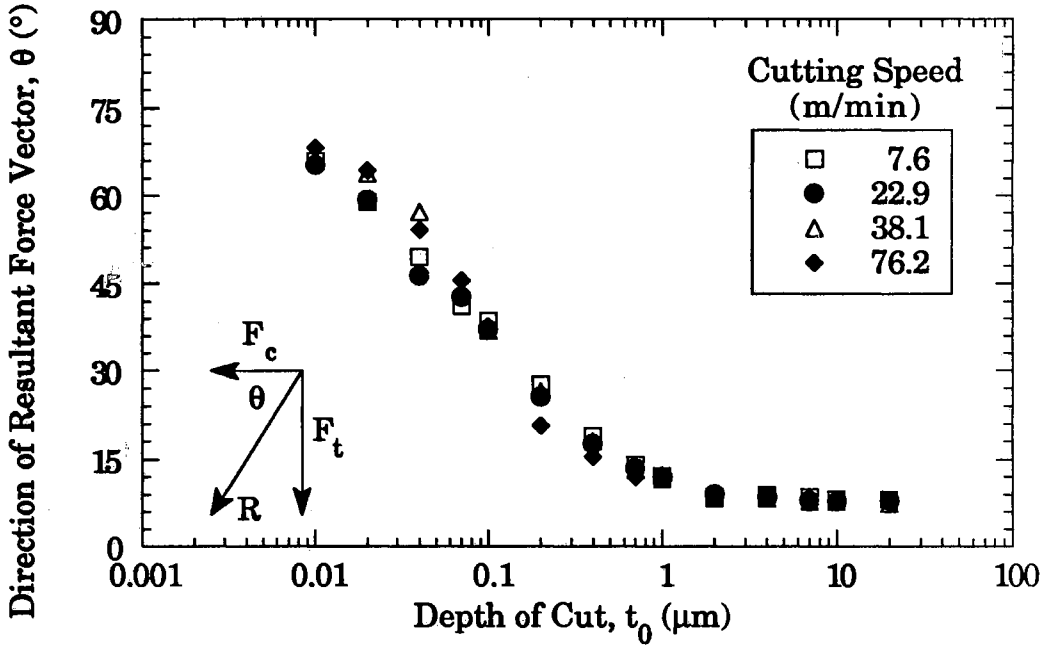

Figure 5-46. Effect of Cutting Speed on Direction of Resultant Force Vector in Orthogonal Flycutting of Te-Cu

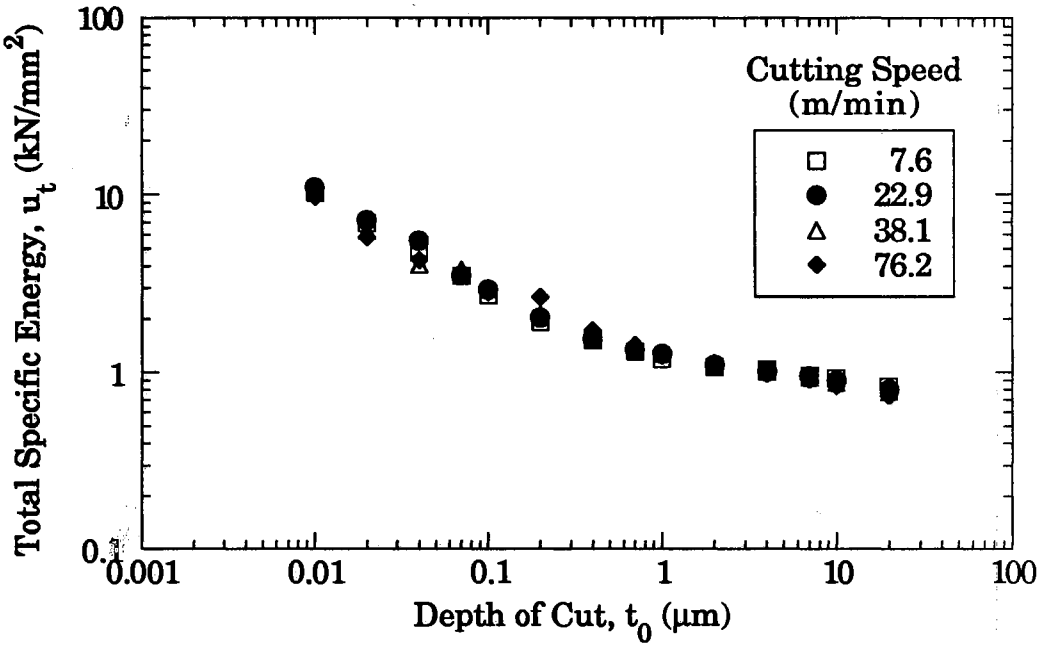

Figure 5-47. Effect of Cutting Speed on Total Specific Energy in Orthogonal Flycutting of Te-Cu

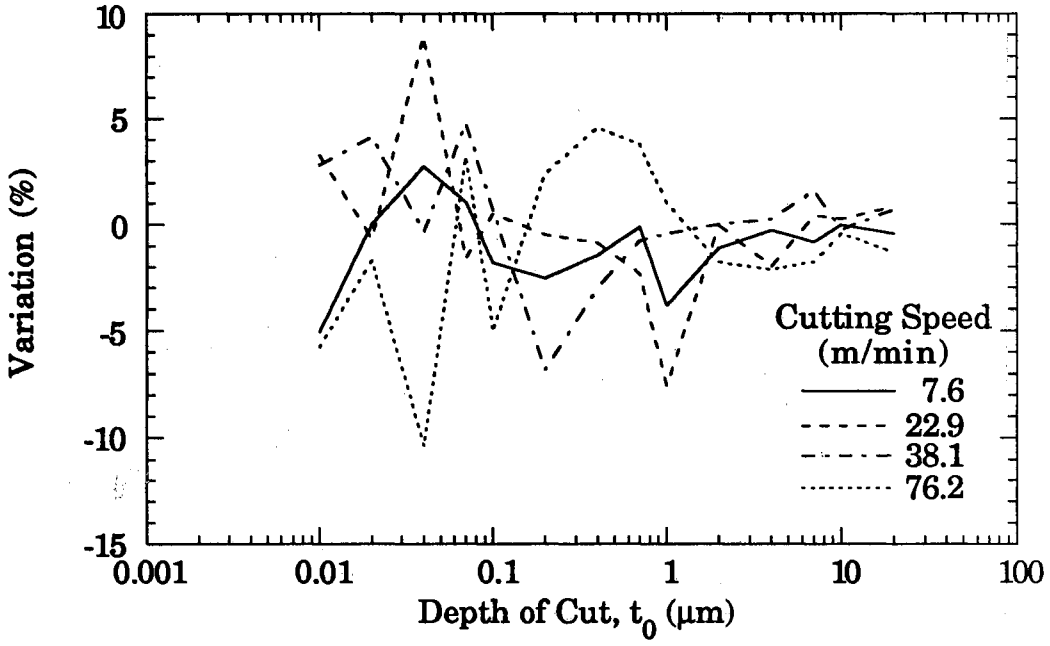

Figure 5-48. Relative Variation of Measured Cutting Forces Between Two Specimens in Orthogonal Flycutting of Te-Cu

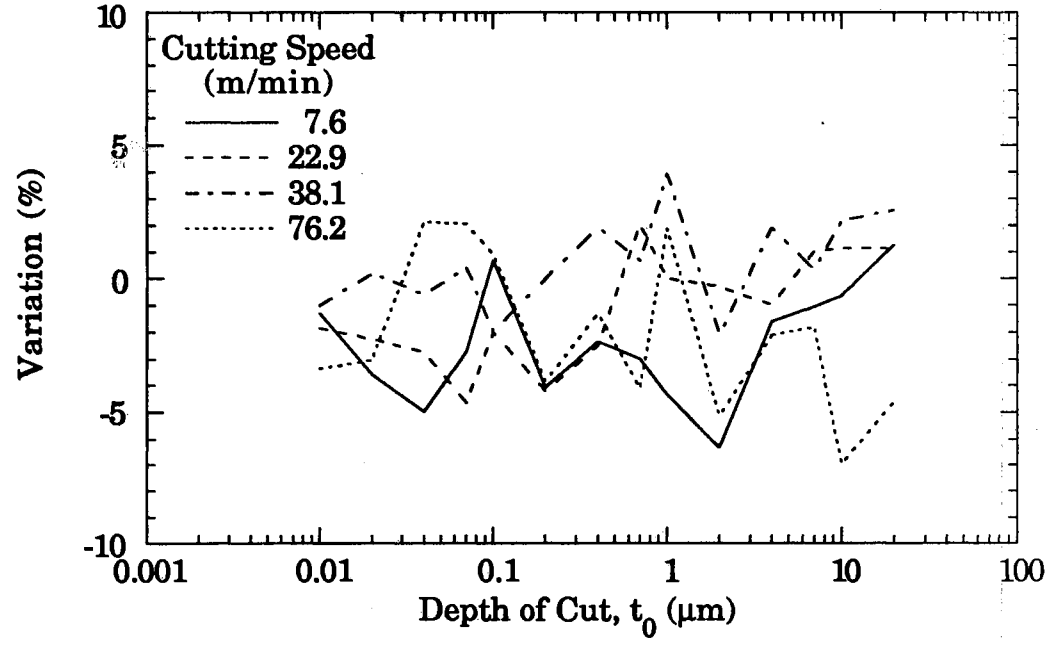

Figure 5-49. Relative Variation of Measured Thrust Forces Between Two Specimens in Orthogonal Flycutting of Te-Cu

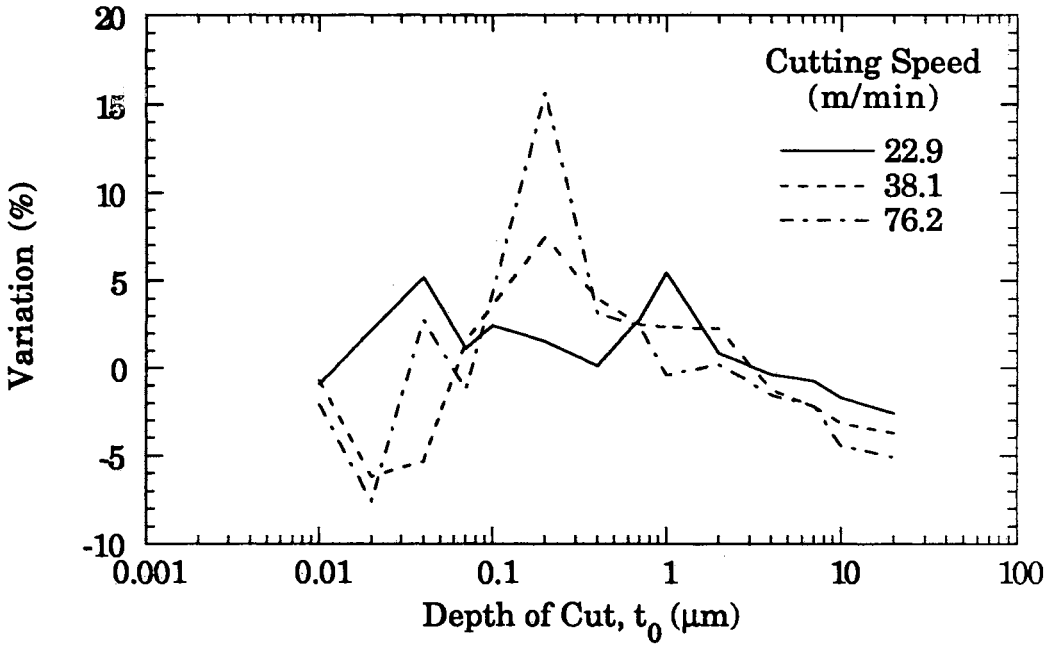

Figure 5-50. Variation of Measured Cutting Forces at Various Cutting Speed with Respect to the Forces at 7.6 m/min in Orthogonal Flycutting of Te-Cu

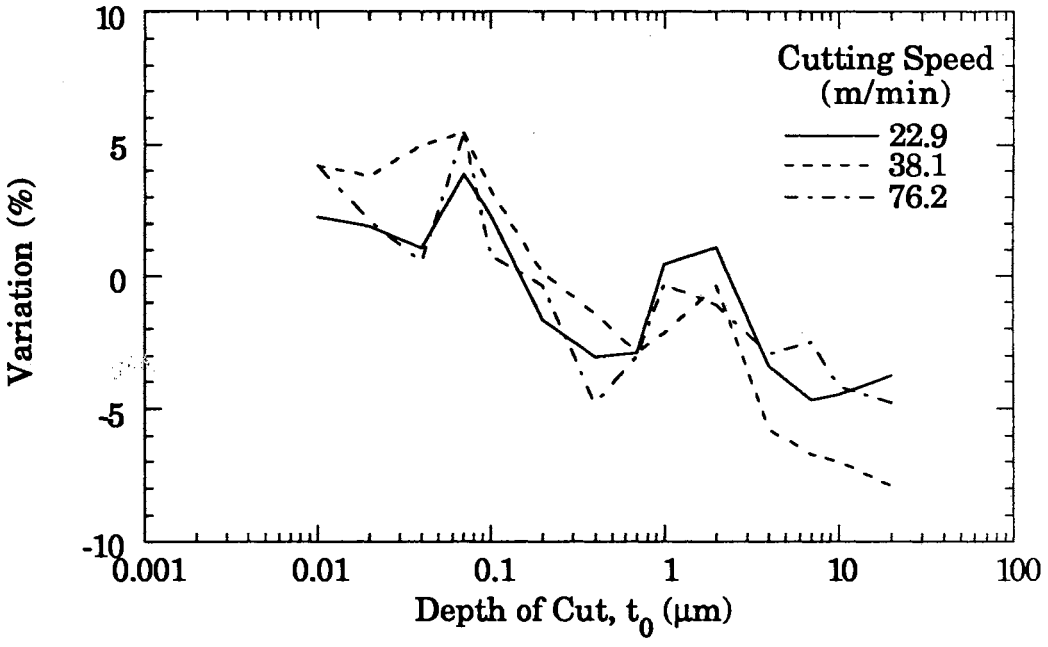

Figure 5-51. Variation of Measured Thrust Forces at Various Cutting Speed with Respect to the Forces at 7.6 m/min in Orthogonal Flycutting of Te-Cu

Specimen 1 to Specimen 2 is within ± 5 %. Then, taking cutting and thrust forces at 7.6 m/min as a basis, the relative increases of the force components at the other three cutting speeds were calculated respectively. Using an average of the measured force components from Specimens 1 and 2, the variation of force components at the i-th cutting speed were calculated as:

$$\text{Var}\,(\%)_{\text{at } i^{\text{th}}\text{ speed}} = \frac{(\text{Force}_{\text{at } i^{\text{th}}\text{ speed}} - \text{Force}_{\text{at 7.6 m/min}})/2}{\text{Force}_{\text{at 7.6 m/min}}} \times 100 \quad (5\text{-}2)$$

The results of the variation due to the change of the cutting speed are shown in Figs. 5-50 and 5-51 for cutting and thrust forces respectively. The results also show ± 5 % variation even though there are some data points outside this range. Any variation in the resulting forces observed over this range were found to lie within the experimental scatter of the data. It can be concluded that cutting speed did not play a role in the resulting forces at these cutting conditions.

5.4.8 Transition from Cutting to Plowing/Sliding

Based on the experimental study of the various tool edge profile effects and cutting conditions on the forces and energies discussed above, the process mechanics of the ultra-precision machining can now be analyzed. An estimate of depth of cut, below which plowing and sliding is dominant, can be made in two ways. The first is to use the direction of resultant force vector. When the direction of resultant force vector is greater than 45° (i.e., $F_t/F_c \geq 1$), the process can be viewed as a plowing/sliding dominant process since the thrust force, which is not effective for material removal, is

greater than the cutting force. This also corresponds to an observed inflection point on the F_t/F_c vs. depth of cut curve, indicating a change in mechanism. The other one is by estimating specific energies. This will be discussed in a later section. Here, plowing is defined as material translation forward at the tool-workpiece interface resultant from either a negative rake angle or an effective negative rake which results when the edge radius of the tool is of the order of the depth of cut. Sliding is due to the subsequent tool-workpiece interaction caused by either flank wear or elastic recovery of the workpiece material. When the plowing/sliding process is dominant over the chip formation process, the surface or subsurface of the machined workpiece may be a major zone of energy dissipation.

5.4.8.1 Depth of Cut vs. Plowing and Sliding. Fig. 5-52 shows directions of resultant force vector for various 0° rake angle tools with different edge profiles in the micro-machining of copper. Included are the results of Moriwaki and Okuda [1989]. For the new tool A1, the resultant force vector direction is less than 45° even at 10 nm depth of cut, which indicates that the chip formation process is still dominant at this depth over the plowing/sliding process as would be expected for sharp edge tools. In contrast to this, as the depth of cut decreases, a severe rotation of the force vector downward towards the workpiece can be observed for all of the worn tools. After a relatively short cutting distance (about 3 km), the direction of the vector increased above 45° from 70 nm depths of cut below for the A1 tool. This implies the plowing/sliding process becomes significant from the early stages of a tool's life. For the worn tool A4, plowing/sliding becomes the dominant process below about 0.2 μm depth of

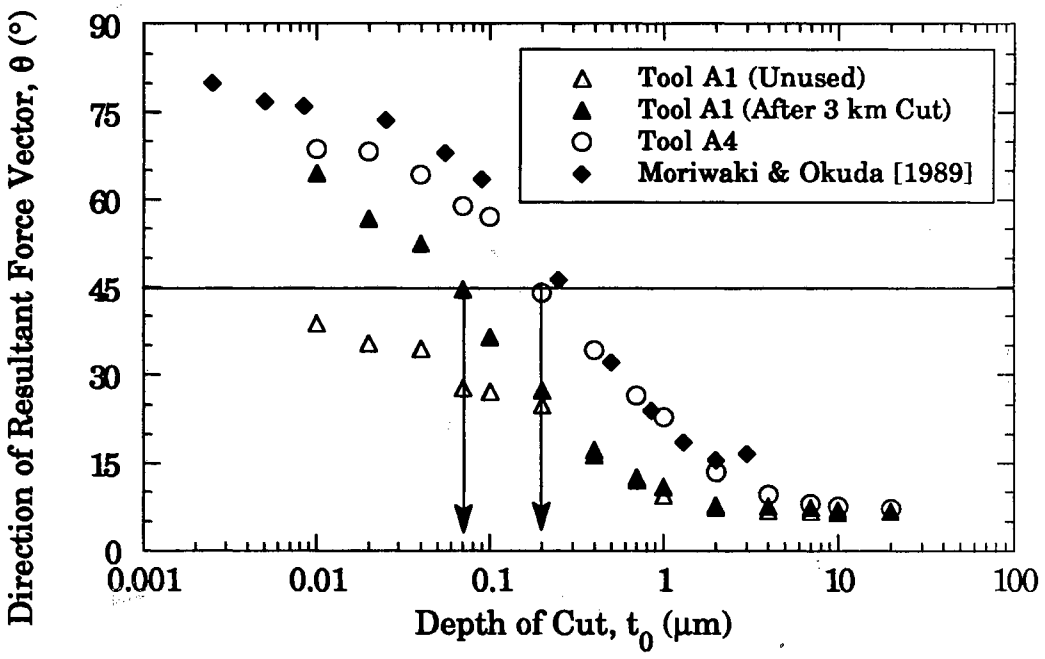

Figure 5-52. Direction of Resultant Force Vector Obtained from Various 0° Nominal Rake Angle Tools in Micro-Machining of Copper

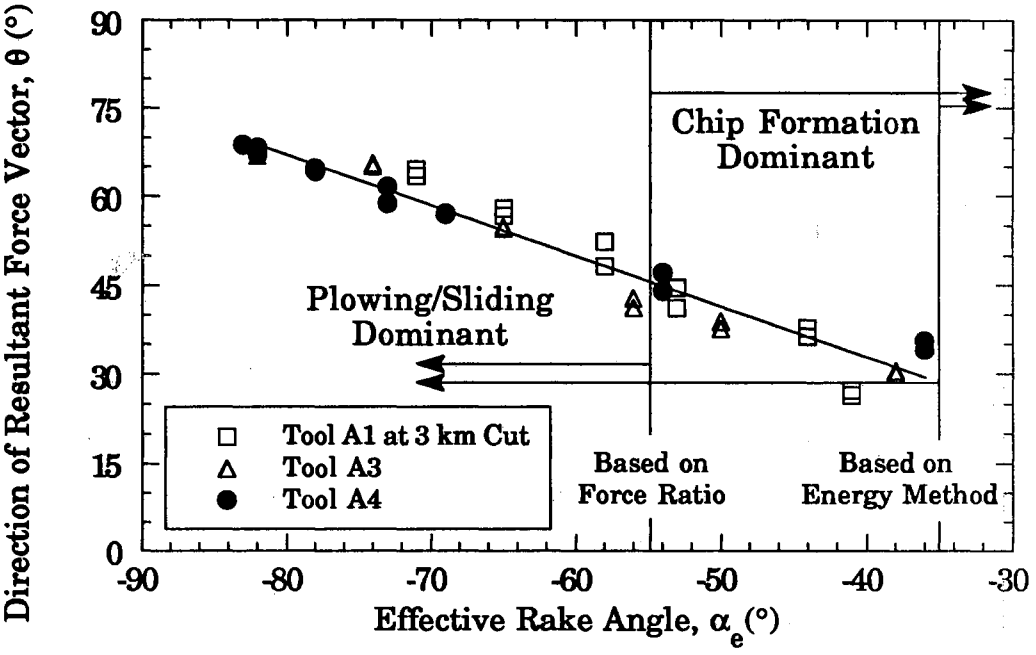

Figure 5-53. Direction of Resultant Force Vector vs. Effective Rake Angle in Micro-Machining of Copper

cut, and similar depths can be seen from Moriwaki and Okuda's result. For the worn tools, the direction of resultant force vector levels off and approaches a constant value. This trend seems to be characteristic of all the experimental results obtained in the microcutting of ductile materials with worn tools. At large depths of cut, above about several micrometers, the direction of the force vector is consistent with what is expected for conventional metal cutting, viz., less than about 10 degrees from the cutting direction.

5.4.8.2 Effective Rake Angle vs. Plowing/Sliding. It has been observed that plowing/sliding becomes significant when the depth of cut is of the order of the tool edge radius. If such is the case, it would be helpful to investigate the effective rake angle effect on the direction of resultant force vector. This is shown in Fig. 5-53 for various tools having 0° nominal rake angle. As can be seen from the figure, as effective rake angle decreases, the direction of the force vector increases almost linearly. With the assumption that above 45°, plowing/sliding is dominant, all the depths of cut below the point of tool edge profile where effective rake angle corresponds to -55°, can be viewed as a range of depths of cut where plowing/sliding is significant. This observation implies that, once the tool edge profile is known, then the depth of cut range where plowing/sliding is significant can be determined without actual cutting. This range can be estimated in two ways:

- For the case of a circular tool edge
- For the case of a general tool edge profile

The first case is for new tools with a circular edge profile where flank wear has not yet developed. In this case, the depths of cut where

plowing/sliding is dominant can be estimated using tool edge radius (r_e) as:

$$t_{0\ pl/sl} \leq r_e (1 - \sin 55^\circ) = 0.18\ r_e \qquad (5\text{-}3)$$

Using this expression, the range of depths of cut where the transition takes place can be estimated. For the A1 tool after 3 km cut having an edge radius of 0.25 μm results in 45 nm whereas reading from Fig. 5-52 is about 70 nm. For A4 tool, taking the secondary edge radius ($r_{e\,2}$) of 1.0 μm since the depth of cut for plowing/sliding would be governed by the secondary edge radius, the depth of cut for the plowing/sliding dominant results in 180 nm, comparable with 200 nm obtained directly from the figure. Also this 180 nm depth of cut is closer to the depth of 120 nm up from the bottom of the flank to the tangent point where two edge radii intersect (Fig. 5-8).

The second case is for a worn tool where the tool edge profile deviates from a circular shape due to well developed flank wear. In this case, there is no well defined tool edge radius, thus a curve fitting technique using the data points in the Fig. 5-53 can be used to estimate the relationship between effective rake angle and the direction of resultant force vector. For the data from the Tools A1, A3 and A4, a linear relationship is obtained using a least squares method as shown in the figure. The equation of the straight line obtained is:

$$\theta = - 0.87\ \alpha_e - 2.39 \text{ (in degrees)} \qquad (5\text{-}4)$$

Using this empirical equation, the direction of the resultant force vector at any point of a tool edge profile can be determined. This equation may be

valid for 0° nominal rake angle tools and can be extrapolated up to 0° effective rake angle since the deviation at $\alpha_e = 0$ is only -2.39 degrees.

5.4.8.3 Minimum Machinable Depth of Cut. When the depth of cut is further decreased below the plowing/sliding dominant depth of cut, "machining" would reach a pure plowing/sliding condition with no chip formation. Many works have attempted to estimate the critical rake angle below which a chip is not formed. Rubenstein [1968] obtained the critical rake angle of -60° ~ -70° for various materials using negative nominal rake angle tools in a low speed shaping operation. Komanduri [1971] observed this angle of -75° in orthogonal cutting of steel with carbide tools having various negative nominal rake angles. Through an extensive review of the literature, Abdel Moneim [1980] suggested that the critical rake angle would be within -62° ~ -57°. Even though the cutting conditions are different between those mentioned above and that of present study, a rough estimation can be made for the minimum machinable depth of cut for the present study. Taking -75° as a critical rake angle, since diamond tools are known to have a very low friction coefficient (at low friction, material flow would be easier than high frictional case hence the chip may not be formed even at high effective negative rake angle), equation (5-4) estimates the directional angle to be $\theta = 63°$. The minimum machinable depth of cut for the two Tools A1 and A4 can be obtained from the Fig. 5-52 by taking the depths of cut when the $\theta = 63°$ intersects the data points of A1 and A4 tools respectively. The minimum depth of cut obtained are about 10 nm and 40 nm for Tools A1 and A4 respectively. This estimate seems to be reasonable since the direction of resultant force vector levels off at this depth of cut for the A4 tool, which possibly indicates no chip formation. Though not

pronounced, the same trend can be observed for the A1 tool at about 10 nm depth of cut. Also a reasonable indication for the estimation is that new tools should have smaller minimum machinable depths of cut as compared to worn tools.

In actual cutting operations however, the minimum depth of cut is extremely difficult to observe since there are many uncertainties. For example, micro-structural behavior of secondary particles, grain boundaries, and some micro-cracks may make the cutting action intermittent. A pop-up when out of the cut and push-down during cutting of the grains and the secondary particles has often been observed in the current experiments by observing the machined surface under the optical microscope and laser interferometric microscope. However, at 10 nm depth of cut, some dust like particles which are difficult to characterize as chips have been observed on the diamond tool tip after several cuts.

5.4.8.4 Plowing/Sliding Transition Based on Specific Energy.

Measured total specific energy can be divided into chip formation energy and plowing/sliding energy [Lucca, 1991b]. In this calculation, chip formation energy consists of shearing energy at the shear plane (u_s) and rake frictional energy (u_r) at the tool-chip interface. The plowing and sliding energy is the remaining energy after subtracting the above two components from the measured total specific energy (based on the measured cutting force). The results are shown in Figs. 5-54 and 5-55 for A1 and A4 tools. From the depth of cut below which the plowing/sliding energy ($u_{pl} + u_{sl}$) is greater than the chip formation energy ($u_s + u_r$), the process can be viewed as plowing/sliding-dominant process. These depths of cut were obtained to be 0.15 μm and 0.25 μm for A1 and A4 tools as

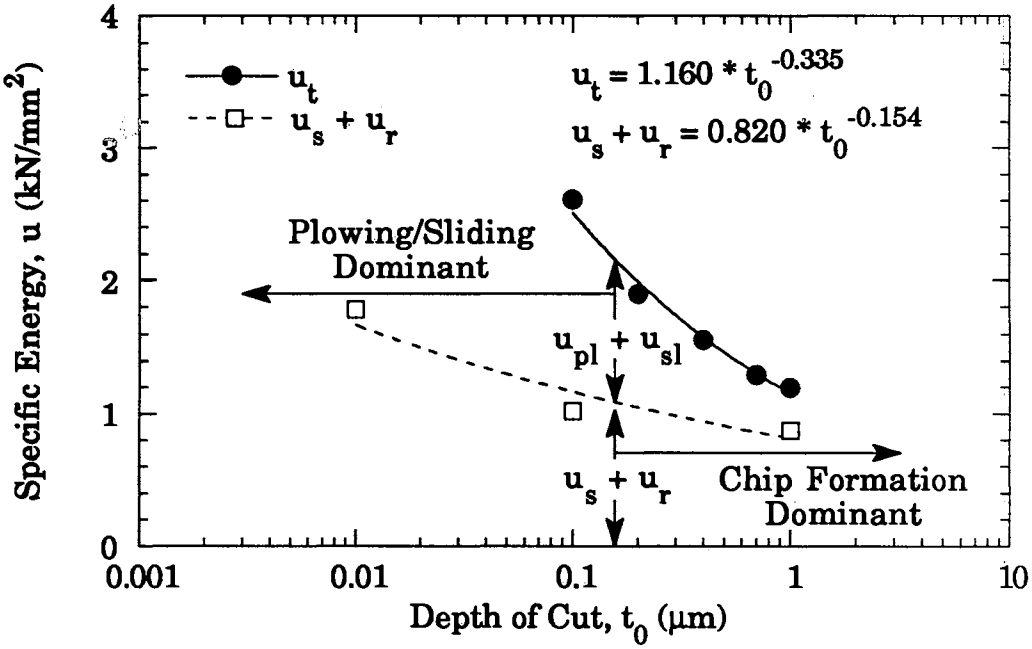

Figure 5-54. Transition from Chip Formation-Dominant Process to Plowing and Sliding-Dominant Process Based on Specific Energy Calculation for Tool A1 (after 3km)

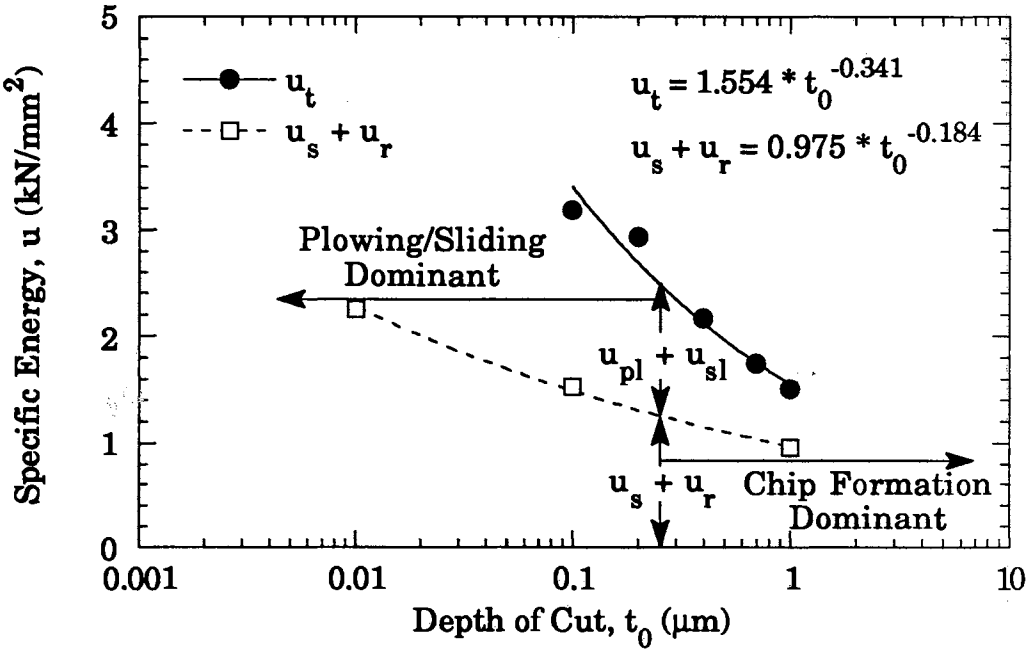

Figure 5-55. Transition from Chip Formation-Dominant Process to Plowing and Sliding-Dominant Process Based on Specific Energy Calculation for Tool A4

shown in the figures. The corresponding direction of resultant force vectors were 30° and 40° (in force ratio, these corresponded to F_t/F_c = 1/1.73, 1/1.13) for A1 tool and A4 tool. Taking 30° as a minimum value, an effective rake angle of -35° was obtained from Fig. 5-53. This energy method seems to estimate a greater depth of cut and smaller effective rake angle than those estimated using force ratio (or direction of resultant force vector) discussed in the previous section.

From the two approaches for the estimate of the transition depth of cut from chip formation to a plowing/sliding-dominant process, the transition seems to occur between 70 nm and 150 nm for A1 tool, and between 200 and 250 nm for A4 tool when cutting Te-Cu at the present cutting conditions. In terms of force ratio, the transition begins to occur when F_t/F_c = 1 ~ 1/1.73, and the corresponding range of effective rake angle is -35° ~ -55°.

5.5 Conclusions

From the experimental study of the tool edge profile effect on the energy dissipation in orthogonal flycutting of Te-Cu, the following observations and findings were made.

5.5.1 Tool Edge Characterization

- Using the atomic force microscope, a total of seven tool edge profiles used in the experiments were characterized in 3D with an accuracy of ± 10 nm.
- The edge profiles of the new tools used were circular shaped and estimated to have 0.25 ± 0.02 μm edge radii. The results of AFM

characterization were consistent with the results of SEM examination.

- Worn tools were double radii shaped with greater wear at the flank face, and were consistent with observations reported in the literature.

5.5.2 Results of Orthogonal Ultra-Precision Flycutting of Te-Cu

- Repeatable cutting and thrust forces were obtained using the orthogonal flycutting geometry for ultra-precision machining of Te-Cu at 7.6 m/min cutting speed and depths of cut from 0.01 μm to 20 μm with light mineral oil as a cutting fluid.
- The reproducibility of the measured forces was within about ± 5 % from specimen to specimen.
- The overall trends of cutting and thrust forces, force ratio, and total specific energy followed results reported in the literature.
- The nonlinearity of force components with depth of cut, severe rotation of the direction of resultant force vector downward toward the workpiece, and dramatic increase in total specific energy as the depth of cut decreases were observed. These were found to be the unique characteristics of the force behavior in ultra-precision machining.

5.5.3 Tool Edge Geometry Effects on Energy Dissipation

5.5.3.1 Nominal Rake Angle

- As nominal rake angle decreases from 0 to -30 degrees, the force components, force ratio, and total specific energy were found to increase over the entire range of depth of cut.
- The thrust force curve for the 0° rake angle tool exhibits a plateau in the depth of cut range of 0.2 ~ 1.0 μm. Though less pronounced as rake angle decreases, this phenomenon was found to be typical for all the new tools employed.
- When the depth of cut is large relative to the extent of the tool edge profile, the resulting forces and energies were seen to be governed by the nominal rake angle.

5.5.3.2 Cutting Distance

- At the early stages of a tool's life (less than 3 km in cutting distance), the increase in forces and resulting energies were significant at submicrometer depths of cut.
- At less than 1 km in cutting distance, thrust force was greater than cutting force at submicrometer depth of cut.

5.5.3.3 Worn Tool

- At submicrometer depths of cut, cutting forces and specific energies were found to be reflected by the tool edge profile. In

particular, the change of thrust force is significantly affected by the contour of the flank face.

- At large depths of cut (above several micrometers) where the tool edge effect is not significant, no discernible differences between the forces from new and worn tools were observed as long as the overall geometries are the same.

5.5.3.4 Effective Rake Angle

- As the depth of cut approaches the size of the edge radius, the effective rake angle appears to determine the resulting forces.
- Both the nominal and effective rake angle effects on force ratio were found to be the same, i.e., as negative effective or nominal rake angle increases, force ratio also increases. This trend was the same for various tools and materials, and was consistent with the literature.

5.5.3.5 Speed Effect

- For one order of magnitude greater cutting speed, the variation of the cutting and thrust forces fell within the scatter of the data, hence the cutting speed did not play a role in the change of the resulting forces at this cutting condition.

5.5.3.6 Plowing/Sliding

- As depth of cut decreases, the direction of resultant force vector increases, levels off and approaches a constant value. At large depths of cut (above several micrometers), the direction is

consistent with that for conventional metal cutting. This trend seems to be a characteristic of all the experimental results obtained in the microcutting of ductile materials.

- From curve fitting of effective rake angle vs. direction of resultant force vector, a range of effective rake angle of -35° ~ -55° is obtained for the corresponding depth of cut below which plowing/sliding becomes significant.
- For tools with circular shaped edge profiles, the depth of cut where plowing/sliding is dominant can be estimated using the tool edge radius, i.e., $t_{0\ pl/sl} \leq 0.18\ r_e$.
- Minimum machinable depth of cut was estimated using the critical rake angle of -75° based on the literature. The depths were about 10 nm and 40 nm for the new and worn tools respectively, and were found to be consistent with the leveling-off of the direction of resultant force vector at those depths of cut.

From Chapter IV, it has been observed that the contact length at the flank face becomes the characteristic length scale for submicrometer depths of cut. This, coupled with the rotation of the resultant force vector towards the workpiece suggests that the process can be thought of as transitioning from a cutting-dominant to a plowing/sliding (or sliding indentation)-dominant process. The process of ultra-precision machining at submicrometer depths of cut can be simplified as a sliding indentation problem to estimate stresses and resulting temperatures of the workpiece material.

CHAPTER VI

ANALYTICAL MODELING OF THE ULTRA-PRECISION MACHINING PROCESS AS A SLIDING INDENTATION PROBLEM

6.1 Introduction

From the experimental study of both the 6061-T6 Al and Te-Cu, it was observed that the process mechanics transitions from a chip formation-dominant to plowing and sliding-dominant process at submicrometer depths of cut. This observation was based on both the severe rotation of the resultant force vector downward toward the workpiece and the dominant length scale becoming the contact length at the tool-workpiece interface in contact. For this case, the ultra-precision machining process may be idealized as a sliding indentation problem.

Finite-element or finite-difference techniques [Strenkowski, 1985; Donaldson, 1985, 1986; Kagiwada, 1988] may give acceptable solutions for general modeling of the problem however, most of the commercial packages do not consider a moving body under surface load and frictional heating simultaneously together with the energy partition at the interface.

Recently, molecular dynamics and quasi-static analyses [Shimada, 1992; Inamura, 1992] simulating the machining process at an atomic scale have been attempted. In these models, interatomic potentials were used to

predict cutting forces and temperatures. However, sliding contact was not considered and extremely lengthy computational time was the limitation.

In this chapter, stress fields at the subsurface of a workpiece due to a stationary or moving surface load, energy partition at the surface of the interface in contact due to the frictional load, and the resulting temperature fields have been studied. For the idealized model, shearing at the shear plane and rake friction were not considered since the contact length at the tool-workpiece is the dominant length scale as observed from the experimental results.

From an optics application point of view, knowledge of the stress fields of the machined parts is critical for stable images and reflectivity due to free electron movement or energy at the surface of the machined parts [Caithness, 1975; Arnold, 1975]. Also, residual stresses at the surface cause dimensional instabilities and "optical blanks" hence, residual stress affects the long term service performance of the machined parts as well as the short term performance in optical applications.

As an initial step in calculating the elastoplastic stress field in the workpiece under machining conditions, the elastostatic stress field due to a concentrated/distributed surface load has been predicted. For the elastodynamic stress fields due to the loading of an elastic half space by a non-insulated rigid slider, a Fourier integral transform technique has been employed in solving the governing field equations. An estimate of the subsurface elastic stress fields and the thickness of the elastic-plastic boundary has been made using the developed model and experimental data for cutting and thrust forces and contact length at the flank face for the orthogonal flycutting of Al 6061-T6 and Te-Cu. Considering the sliding work dissipated at the interface, prediction of the resulting temperatures

has also been made. The elastic model was then extended to include plastic effects. In calculating the elastoplastic stress fields, the Prandtl-Reuss equation was solved using a Runge-Kutta method based on the elastic stress fields obtained from the Fourier integral transform technique. Residual stresses in the moving body were also estimated. In addition to the above approach for obtaining the elastoplastic stress fields, the identical loading conditions have been used with the commercial FEM code ABAQUS and the results were compared. The results of plastically deformed layer thickness, residual stress and temperature have also been compared with some experimental results from the literature.

It was found that both the elastic and elastoplastic solutions can be used for the prediction of stress fields, and the elastic-plastic boundary layer thickness. The temperatures at the tool-workpiece interface were found to be negligible at the cutting conditions studied.

6.2 Elastic Modeling

6.2.1 Geometry of the Model

When the contact length (l_f) dominates the length scale and the resultant force vector (R) rotates downward toward the workpiece, the tool-workpiece contact (Fig. 6-1a) may be idealized as a sliding indentation problem (Fig. 6-1b).

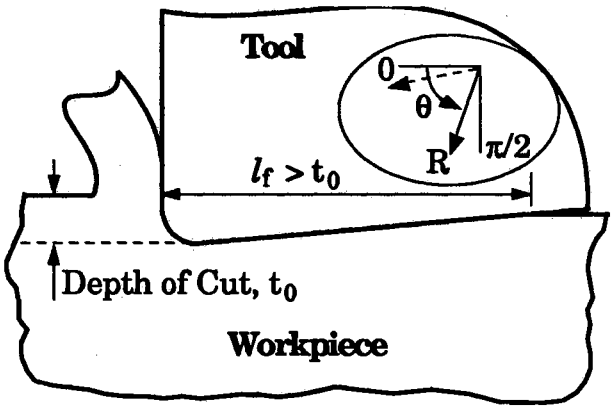

a) Characteristics of Tool-Workpiece Contact and Resultant Force Vector in Orthogonal Ultra-Precision Machining

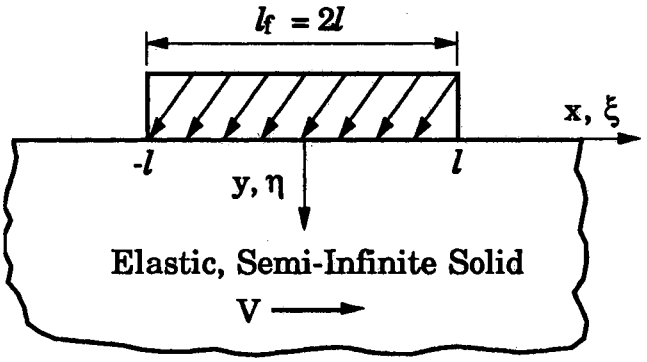

b) Slider Model

Figure 6-1. Idealization of the Tool-Workpiece Interface in Ultra-Precision Machining as a Sliding Indentation Problem

6.2.2 Formulation of the Elastostatic Problem

6.2.2.1 Elastostatic Stress Fields in a Body Due to a Concentrated Surface Load.

As an initial step to estimate the stress fields, a concentrated surface load on a semi-infinite stationary elastic body was considered. In this case, neither dynamic effects nor contact length at the interface was considered. For an arbitrarily inclined concentrated load, the stress fields can be obtained in closed form using a stress function in which the equilibrium and compatibility conditions are satisfied. An Airy's stress function (ϕ) for a concentrated normal force (P) and tangential force (Q) per unit thickness on a semi-infinite body may be expressed as (Boussinesq-Flamant problem) [Timoshenko, 1970]:

$$\phi_P = -\frac{P}{\pi} r_1 \theta_1 \sin \theta_1 \tag{6-1a}$$

$$\phi_Q = -\frac{Q}{\pi} r_2 \theta_2 \sin \theta_2 \tag{6-1b}$$

where r_i, θ_i, i=1,2 are distances from the loading point and included angles from the direction of loading to the point of interest respectively.

Using the geometric relationship shown in Fig. 6-2, the variables can be expressed as:

$$\begin{aligned} r_1 \sin \theta_1 = x,\ r_2 \sin \theta_2 = y \\ \theta_1 = \tan^{-1}(x/y),\ \theta_2 = \tan^{-1}(y/x) \end{aligned} \tag{6-2}$$

Substituting eq. (6-2) into eqs. (6-1a) and (6-1b), the stress function can be obtained as:

$$\phi_P = -\frac{P}{\pi} x \tan^{-1}\left(\frac{x}{y}\right) \tag{6-3a}$$

$$\phi_Q = \frac{Q}{\pi} y \tan^{-1}\left(\frac{y}{x}\right) \tag{6-3b}$$

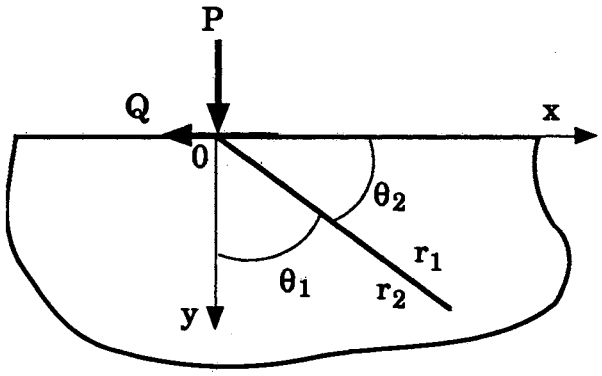

Figure 6-2. Geometry of Inclined Concentrated Load

Elastic behavior is linear thus, superposition is valid for the stress functions. The general stress function for an arbitrarily inclined surface concentrated load can be expressed as:

$$\phi = -\frac{1}{\pi}\{P x \tan^{-1}\left(\frac{x}{y}\right) - Q y \tan^{-1}\left(\frac{y}{x}\right)\} \tag{6-4}$$

Once a stress function is known, the corresponding stress fields, when body forces are neglected, can be obtained as:

$$\sigma_{xx} = \frac{\partial^2\phi}{\partial y^2}, \quad \sigma_{yy} = \frac{\partial^2\phi}{\partial x^2}, \quad \sigma_{xy} = -\frac{\partial^2\phi}{\partial x \partial y} \tag{6-5}$$

From eqs. (6-4) and (6-5), the stress fields in 2D can be given as:

$$\sigma_{xx} = \frac{2P}{\pi}(\mu_f x - y)\frac{x^2}{\{x^2+y^2\}^2} \tag{6-6a}$$

$$\sigma_{yy} = \frac{2P}{\pi}(\mu_f x - y)\frac{y^2}{\{x^2+y^2\}^2} \tag{6-6b}$$

$$\sigma_{xy} = \frac{2P}{\pi}(\mu_f x - y)\frac{xy}{\{x^2+y^2\}^2} \tag{6-6c}$$

where $\mu_f = Q/P$. For plane strain conditions, $\sigma_{zz} = \nu(\sigma_{xx} + \sigma_{yy})$ may be added. For numerical calculation of the stress components, the thrust force F_t can be replaced by the normal force P and the cutting force F_c can be replaced by the tangential force Q since they are forces per unit width applied on the surface of a semi-infinite body.

For the stress fields due to a concentrated surface load, contact length is not involved therefore, the effect of the characteristic length scale can not be investigated. A singularity problem occurs as $x^2 + y^2$ approaches zero near the point of the applied force. This limits the study of the stress fields of the body where the local stress distribution is significant.

6.2.2.2 Elastostatic Stress Fields in a Body Due to a Distributed Surface Load. Considering the contact length, elastostatic stress fields due to a distributed surface pressure can be formulated also by using the Airy's stress function when sliding speed, interfacial temperature and plastic deformation effects are not considered. Using the stress function for a concentrated load, the stress function for an arbitrarily distributed pressure can be obtained for both the horizontal and vertical pressures by superposition. Here, three different types of surface pressures are considered, i.e., linear, constant and elliptical. The solution

for the stress fields due to an elliptical surface pressure is comparable with Smith and Liu's [1953] closed form solution. Details of the derivation of the stress functions are shown in Appendix A for the three surface loading conditions. The resulting stress fields for each of the applied surface pressures are as follows:

- Elastostatic Stress Fields Due to

a Linear Surface Pressure. In this case, both the normal and tangential pressure distributions are triangular shaped with maximum at one end ($-l$) and decaying to zero at the other end (l) of the contact. With the maximum normal pressure p_0 and tangential pressure q_0 which are defined in Appendix A, the stress fields may be expressed as:

$$\sigma_{xx} = \frac{q_0}{\pi l}\int_{-l}^{l}(l-\xi)\frac{(x-\xi)^3}{\left\{(x-\xi)^2+y^2\right\}^2}d\xi - \frac{p_0}{\pi l}\int_{-l}^{l}(l-\xi)\frac{(x-\xi)^2 y}{\left\{(x-\xi)^2+y^2\right\}^2}d\xi \qquad (6\text{-}7a)$$

$$\sigma_{yy} = \frac{q_0}{\pi l}\int_{-l}^{l}(l-\xi)\frac{(x-\xi)y^2}{\left\{(x-\xi)^2+y^2\right\}^2}d\xi - \frac{p_0}{\pi l}\int_{-l}^{l}(l-\xi)\frac{y^3}{\left\{(x-\xi)^2+y^2\right\}^2}d\xi \qquad (6\text{-}7b)$$

$$\sigma_{xy} = \frac{q_0}{\pi l}\int_{-l}^{l}(l-\xi)\frac{(x-\xi)^2 y}{\left\{(x-\xi)^2+y^2\right\}^2}d\xi - \frac{p_0}{\pi l}\int_{-l}^{l}(l-\xi)\frac{(x-\xi)y^2}{\left\{(x-\xi)^2+y^2\right\}^2}d\xi \qquad (6\text{-}7c)$$

- Elastostatic Stress Fields Due to

a Constant Surface Pressure. In this case, the magnitudes of both the normal and tangential applied pressure are uniform throughout the contact ($-l$, l). The resultant stress fields are:

$$\sigma_{xx} = \frac{2q_0}{\pi}\int_{-l}^{l}\frac{(x-\xi)^3}{\left\{(x-\xi)^2+y^2\right\}^2}d\xi - \frac{2p_0}{\pi}\int_{-l}^{l}\frac{(x-\xi)^2 y}{\left\{(x-\xi)^2+y^2\right\}^2}d\xi \qquad (6\text{-}8a)$$

$$\sigma_{yy} = \frac{2q_0}{\pi}\int_{-l}^{l}\frac{(x-\xi)y^2}{\left\{(x-\xi)^2+y^2\right\}^2}d\xi - \frac{2p_0}{\pi}\int_{-l}^{l}\frac{y^3}{\left\{(x-\xi)^2+y^2\right\}^2}d\xi \qquad (6\text{-}8b)$$

$$\sigma_{xy} = \frac{2q_0}{\pi}\int_{-l}^{l}\frac{(x-\xi)^2 y}{\left\{(x-\xi)^2+y^2\right\}^2}d\xi - \frac{2p_0}{\pi}\int_{-l}^{l}\frac{(x-\xi)\, y^2}{\left\{(x-\xi)^2+y^2\right\}^2}d\xi \qquad (6\text{-}8c)$$

- Elastostatic Stress Fields Due to an Elliptical Surface Pressure. The applied pressure distributions are elliptical with maximum at the center and elliptically decaying to zero at both ends of $-l$ and l of the contact. The stress fields are:

$$\sigma_{xx} = \frac{2q_0}{\pi l}\int_{-l}^{l}(l^2-\xi^2)^{1/2}\frac{(x-\xi)^3}{\left\{(x-\xi)^2+y^2\right\}^2}d\xi - \frac{2p_0}{\pi l}\int_{-l}^{l}(l^2-\xi^2)^{1/2}\frac{(x-\xi)^2 y}{\left\{(x-\xi)^2+y^2\right\}^2}d\xi \qquad (6\text{-}9a)$$

$$\sigma_{yy} = \frac{2q_0}{\pi l}\int_{-l}^{l}(l^2-\xi^2)^{1/2}\frac{(x-\xi)y^2}{\left\{(x-\xi)^2+y^2\right\}^2}d\xi - \frac{2p_0}{\pi l}\int_{-l}^{l}(l^2-\xi^2)^{1/2}\frac{y^3}{\left\{(x-\xi)^2+y^2\right\}^2}d\xi \qquad (6\text{-}9b)$$

$$\sigma_{xy} = \frac{2q_0}{\pi l}\int_{-l}^{l}(l^2-\xi^2)^{1/2}\frac{(x-\xi)^2 y}{\left\{(x-\xi)^2+y^2\right\}^2}d\xi - \frac{2p_0}{\pi l}\int_{-l}^{l}(l^2-\xi^2)^{1/2}\frac{(x-\xi)\, y^2}{\left\{(x-\xi)^2+y^2\right\}^2}d\xi \qquad (6\text{-}9c)$$

The stress fields for an elliptical pressure distribution was originally predicted by Hertz for elastic bodies in frictionless contact [Johnson, 1982; Suh, 1986; Johnson, 1987].

The elastodynamic stress fields can be predicted when sliding speed is considered. The result for the elastodynamic stress fields in which temperature effects are not considered has been taken from the literature [Eringen, 1975; Ju, 1982] and is shown in Appendix A together with the above three elastostatic stress fields. The solution for the elastodynamic stress fields are derived by using complex potential functions. A computer program for the three loading conditions was made together with the elastodynamic stress fields for the loading conditions due to constant and elliptical surface pressures. Some stress fields due to the loading conditions representing microcutting of Al 6061-T6 are shown in Appendix A.

From the results of the elastostatic stress fields in the body, it was observed that the overall distribution of the resulting stresses and the elasto-plastic boundary thickness were almost the same for the three different cases of the applied surface pressures. This is due to Saint-Venant's principle where by the stress distribution is locally affected by the type of applied force distribution however, the overall distribution is identical regardless of the type of the applied pressure distribution as long as the total applied force and the geometry of the body remain the same.

6.2.3 Formulation of the Elastodynamic Stress, Temperature and Thermomechanical Stress Fields Using a Fourier Integral Transform Method

For the actual case of a moving body, the elastodynamic effect and corresponding frictional energy at the interface of the two body system was considered. For the model geometry in this case, a rigid, non-insulated slider of length $2l$ fixed in space and loaded against an elastic, semi-infinite body moving with velocity V in the x-direction was considered (Fig. 6-1). The basic assumptions were:

- the relative speed of the body is much less than the Rayleigh wave speed in the body and the material is continuous and homogeneous,
- the apparent contact is equal to the actual contact,
- at the surface, the normal and tangential pressures are uniformly distributed over the contact, and the semi-infinite body is force-free elsewhere,
- heating is due to a planar frictional heat source at the contact and heat is allowed to flow across the plane of contact to either the slider or the half space and there is no heat transfer at the free surface of the half space, thus energy partition is considered at the interface, and
- the linear theory of thermoelasticity is valid, i.e., the superposition principle is applicable.

To estimate the workpiece subsurface stress distribution and the temperature fields due to a mechanical load and frictional heating, a simplified thermomechanical model of the moving contact was formulated

[Ling, 1973; Ju, 1984; Chen, 1988]. Using a Fourier integral transform technique, the partial differential equations of thermodynamic equilibrium and Fourier conduction are transformed into ordinary differential equations. These transformed field equations are solved by imposing transformed boundary equations. Inverse transformation of the solution results in a final form of the stress and temperature fields.

The Fourier integral transform and its inverse transform used are defined as:

$$\tilde{f}(s) = \int_{-\infty}^{\infty} f(\xi) \exp(- is\xi) \, d\xi \qquad (6\text{-}10a)$$

$$f(\xi) = \frac{1}{2\pi} \int_{-\infty}^{\infty} \tilde{f}(s) \exp(is\xi) \, ds \qquad (6\text{-}10b)$$

where $i = \sqrt{-1}$. The detailed governing equations and the derivation for this section are given in Appendix B.

6.2.3.1 Mechanical Stress Components. The Fourier integral transform is applied to the system of Navier's thermoelastic equilibrium equations in terms of displacements together with Hooke's law for the stress and boundary conditions. Before the transformation, all the governing equations are normalized with respect to the half contact length of the slider for the coordinate system and to the applied normal pressure for the stress components. Temperature is non-dimensionalized with respect to the applied heat flux at the frictional interface. The boundary conditions are given as stress components such that the surface normal

and shear stresses are the same as the applied normal and tangential pressures along the normalized contact, i.e., $\xi = x/l = [-1, 1]$. For the mechanical stress fields, the thermal terms in the Navier's equilibrium equation vanish. The resulting ordinary differential equations are solved in the transformed domain. After applying the inverse transform and taking the real parts, the equations for the mechanical stress field are obtained as:

$$\sigma^{M}_{\xi\xi}(\xi,\eta) = \frac{2}{\pi G_1}\Big[-4k\int_0^{\infty}\frac{\sin s}{s}\cos s\xi e^{-js\eta}ds + 2(2-M^2)\mu_f\int_0^{\infty}\frac{\sin s}{s}\sin s\xi e^{-js\eta}ds + (M^2+2k^2)\{(j+\frac{1}{j})\int_0^{\infty}\frac{\sin s}{s}\cos s\xi e^{-ks\eta}ds - 2\mu_f\int_0^{\infty}\frac{\sin s}{s}\sin s\xi e^{-ks\eta}ds\}\Big] \quad (6\text{-}11a)$$

$$\sigma^{M}_{\eta\eta}(\xi,\eta) = \frac{2}{\pi G_1}\Big[4k\int_0^{\infty}\frac{\sin s}{s}\cos s\xi e^{-js\eta}ds - 2(2-M^2)\mu_f\int_0^{\infty}\frac{\sin s}{s}\sin s\xi e^{-js\eta}ds - (2-M^2)\{(j+\frac{1}{j})\int_0^{\infty}\frac{\sin s}{s}\cos s\xi e^{-ks\eta}ds - 2\mu_f\int_0^{\infty}\frac{\sin s}{s}\sin s\xi e^{-ks\eta}ds\}\Big] \quad (6\text{-}11b)$$

$$\sigma^{M}_{\xi\eta}(\xi,\eta) = \frac{2}{\pi G_1}\{(j + \frac{1}{j})\{(2 - M^2)\mu_f \int_0^\infty \frac{\sin s}{s} \cos s\xi e^{-js\eta} ds$$

$$+ 2k \int_0^\infty \frac{\sin s}{s} \sin s\xi e^{-js\eta} ds\}$$

$$+ 2k\{ - 2\mu_f \int_0^\infty \frac{\sin s}{s} \cos s\xi e^{-ks\eta} ds$$

$$- (j + \frac{1}{j}) \int_0^\infty \frac{\sin s}{s} \sin s\xi e^{-ks\eta} ds\}] \qquad (6\text{-}11c)$$

where

$$G_1 = (j + \frac{1}{j})(2 - M^2) - 4k,$$

$$j^2 = 1 - M^2, \quad k^2 = 1 - M^2/N^2,$$

$$M = \frac{V}{C_s}, N = \frac{C_d}{C_s} \text{ and } \mu_f = \frac{F_c}{F_t}$$

and where C_d, C_s are the dilatation and shear wave speeds in the body.

6.2.3.2 Energy Partition. Due to the difference in thermal properties of the sliding body system, a part of the frictional energy generated at the sliding interface goes into the stationary body and the remaining portion flows into the moving body. In order to predict the temperature of the moving body, the partition of frictional energy must be known. A simplified approach could be to invoke Blok's conjecture [Blok, 1937] whereby the energy partition would not be a function of the location along the contact ξ. However, to arrive at a location dependent energy partition, the surface temperatures due to the surface frictional heating of the two bodies in contact are equated, and the partition is calculated. The energy

which goes into the stationary body is (q_0 R) and the remainder q_0 (1-R) enters the moving body.

The heat input $q_0 = F_c V/(2J\, l\, w)$ is due to frictional heating at the flank interface. Here, F_c is the cutting force, V is the sliding speed, w is the width of the slider (w = 2b, B=b/l), l is the half contact length, and J = 1.078 x 10^5 kg-mm/Btu is the mechanical equivalent of heat. The resulting energy partition R to the stationary body can be obtained as:

$$R(\xi) = \frac{\displaystyle\int_{-B}^{B}\int_{-1}^{1} \frac{\exp[-\frac{Pe}{2}\{\sqrt{(\xi-\xi')^2+\zeta'^2}-(\xi-\xi')\}]}{\sqrt{(\xi-\xi')^2+\zeta'^2}}\, d\xi' d\zeta'}{\displaystyle\int_{-B}^{B}\int_{-1}^{1} \frac{r_K+\exp[-\frac{Pe}{2}\{\sqrt{(\xi-\xi')^2+\zeta'^2}-(\xi-\xi')\}]}{\sqrt{(\xi-\xi')^2+\zeta'^2}}\, d\xi' d\zeta'} \qquad (6\text{-}12)$$

The energy partition is expressed as a function of location ξ within the contact ($-1 \le \xi \le 1$), the ratio of thermal conductivities of the moving to the stationary body in contact (r_K), and relative sliding speed in terms of Peclet number Pe.

6.2.3.3 Temperature Fields. In solving the temperature fields of the moving body, the Fourier heat conduction equation [Jaeger, 1942; Carslaw, 1959; Francis, 1970; Terauchi, 1984] was used as a governing equation and the boundary condition applied was frictional heating at the contact length due to a sliding energy per unit time at the interface. The normalized temperature field of the moving body (workpiece) considering the energy partition at the interface is obtained as:

$$\phi_w(\xi,\eta) = \frac{1}{\pi}\int_0^{\infty} \frac{1}{(a+b)s^2}\sum_{m=1}^{n}(1-R_m)[\sqrt{a}\{\sin s(x_1+\Delta\xi) - \sin sx_1\} + \sqrt{b}\{\cos sx_1 - \cos s(x_1+\Delta\xi)\}]e^{-\sqrt{a}s\eta}ds \quad (6\text{-}13)$$

where

$$a = \frac{1+\sqrt{1+(Pe/s)^2}}{2}, \quad b = \frac{(Pe/s)^2}{2(1+\sqrt{1+(Pe/s)^2})}$$

$$x_1 = 1 - m\Delta\xi - \sqrt{b}\eta + \xi$$

and $\Delta\xi$ is the length of each segment of the interval of the non-dimensionalized contact length $\xi = [-1, 1]$ with a total of n segments and R_m is the energy partition at the m-th segmented interface.

6.2.3.4 Thermal Stress Fields. Similar to the mechanical stress fields, the Navier's thermoelastic equilibrium equation is used with the boundary conditions of normal and shear stress free at the surface to calculate the thermal stresses. The resulting thermal stress fields are obtained as:

$$\sigma^T_{\xi\xi}(\xi,\eta) = \frac{\mu}{\pi p_0}\int_0^{\infty} s[2F_{D1}(R_{D1}\cos s\xi - I_{D1}\sin s\xi)e^{-js\eta} + (M^2+2k^2)F_{D2}(R_{D2}\cos s\xi - I_{D2}\sin s\xi)e^{-ks\eta} + F_{D3}\{R_{D5}\cos s(\sqrt{b}\eta - \xi) + I_{D5}\sin s(\sqrt{b}\eta - \xi)\}e^{-\sqrt{a}s\eta}]ds \quad (6\text{-}14a)$$

$$\sigma^T_{\eta\eta}(\xi,\eta) = -\frac{\mu}{\pi p_0}\int_0^\infty s[2F_{D1}(R_{D1}\cos s\xi - I_{D1}\sin s\xi)e^{-js\eta} + (2 - M^2)F_{D2}(R_{D2}\cos s\xi - I_{D2}\sin s\xi)e^{-ks\eta} + (2 - M^2)F_{D3}\{R_{D3}\cos s(\sqrt{b}\eta - \xi) + I_{D3}\sin s(\sqrt{b}\eta - \xi)\}e^{-\sqrt{a}s\eta}]ds \quad (6\text{-}14b)$$

$$\sigma^T_{\xi\eta}(\xi,\eta) = \frac{\mu}{\pi p_0}\int_0^\infty s[(j + \frac{1}{j})F_{D1}(-R_{D1}\sin s\xi - I_{D1}\cos s\xi)e^{-js\eta} + 2kF_{D2}(-R_{D2}\sin s\xi - I_{D2}\cos s\xi)e^{-ks\eta} + 2F_{D3}\{R_{D4}\sin s(\sqrt{b}\eta - \xi) - I_{D4}\cos s(\sqrt{b}\eta - \xi)\}e^{-\sqrt{a}s\eta}]ds \quad (6\text{-}14c)$$

where F_{Di}, I_{Di}, and R_{Di} are shown in the Appendix B.

Finally, the combined total normalized stress fields are the summation of the fields due to the mechanical and thermal fields.

$$\sigma_{ij} = \sigma^M_{ij} + \sigma^T_{ij} \quad (6\text{-}15)$$

6.2.4 Results of Elastic Stress Fields

6.2.4.1 Elastostatic Stress Fields. The stress fields due to a concentrated surface load are not a function of a contact length. In this case, the effect of the contact length on the stress fields can not be investigated, moreover, a singularity of the stress near the point of loading complicates the problem. When the local stress distribution near the point of contact is significant, the stress fields due to a concentrated applied force may not provide an adequate solution.

When temperature rise is negligible, an estimate of the elastic-plastic boundary layer thickness from the surface of the body may be made by

considering the solution of the elastostatic stress fields due to a distributed surface pressure at the interface of the contact. The stress fields for a stationary body due to the three types of loading conditions using the Airy's stress function were calculated for plane strain conditions. As an applied surface load, the measured cutting and thrust forces, and contact lengths (shown in Table 4-4) were used for Al 6061-T6. The material properties shown in Table 6-1 were used for the body (Al 6061-T6) and the rigid slider (diamond tool). For the numerical integration of the equations of the stress

TABLE 6-1

MATERIAL PROPERTIES OF THE WORKPIECES AND SINGLE CRYSTAL DIAMOND TOOL

1. Al 6061-T6 Workpiece	Properties
Young's modulus (E)	72.4 (GPa)
Poisson's ratio (ν)	0.33
Mass density (ρ)	2.821×10^{-10}(kg/mm^3)
Thermal expansion ratio (α)	2.52×10^{-5} (mm/mm/°C)
Thermal conductivity (K_w)	2.247×10^{-4} (Btu/mm/sec/°C)
Thermal diffusivity (κ)	73 (mm^2/sec)
Tensile strength (Y)	363 (MPa)

2. Te-Cu Workpiece	Properties
Young's modulus (E)	120 (GPa)
Poisson's ratio (ν)	0.3
Mass density (ρ)	9.14×10^{-10}(kg/mm^3)
Thermal expansion ratio (α)	1.76×10^{-5} (mm/mm/°C)
Thermal conductivity (K_w)	3.74×10^{-4} (Btu/mm/sec/°C)
Thermal diffusivity (κ)	114.5 (mm^2/sec)
Tensile strength (Y)	225 (MPa)

3. Diamond Tool	Properties
Thermal conductivity(K_t)	2.18×10^{-3} (Btu/mm/sec/°C)

components with a finite range of integration, a 10 point Gaussian quadrature scheme was employed. Using the data sets representing orthogonal flycutting in which the depths of cut are one order of magnitude different, i.e., 0.01 and 0.1 μm, the stress fields were estimated. Above about 0.5 μm depth of cut for Al 6061-T6, the measured thrust force was smaller than the cutting force hence the sliding indentation model may not be appropriate to predict the stress fields since above this depth of cut chip formation may be dominant over plowing and sliding.

Contours of the normalized von Mises equivalent elastostatic stress with respect to the yield strength of the body (σ_{eq}/Y) are shown in Figs. 6-3 and 6-4 for Al 6061-T6 for loading conditions representing orthogonal flycutting at 0.01 and 0.1 μm depths of cut respectively. These stress fields are due to a constant surface pressure. The spatial coordinates have been non-dimensionalized by the measured half contact length (i.e., $\xi=x/l$, $\eta=y/l$). The contours due to linear and elliptical surface pressures are shown in the Appendix A.

From Fig. 6-3, near-circular-shaped equivalent stress contours can be observed away from the contact however, near the contact, the contours deviate from the circular arc. This trend is identical with other surface loading conditions, i.e., linear and elliptical surface pressures. The first yielding occurs at the subsurface and near $\xi = -1$ of the body. This trends is consistent with Merwin and Johnson's results [1963]. As the direction of resultant force vector rotates towards the sliding direction, i.e., as depth of cut increases, the contours of equivalent stress shown in Fig. 6-4 become non-symmetric relative to the contours in Fig. 6-3 and the plastically

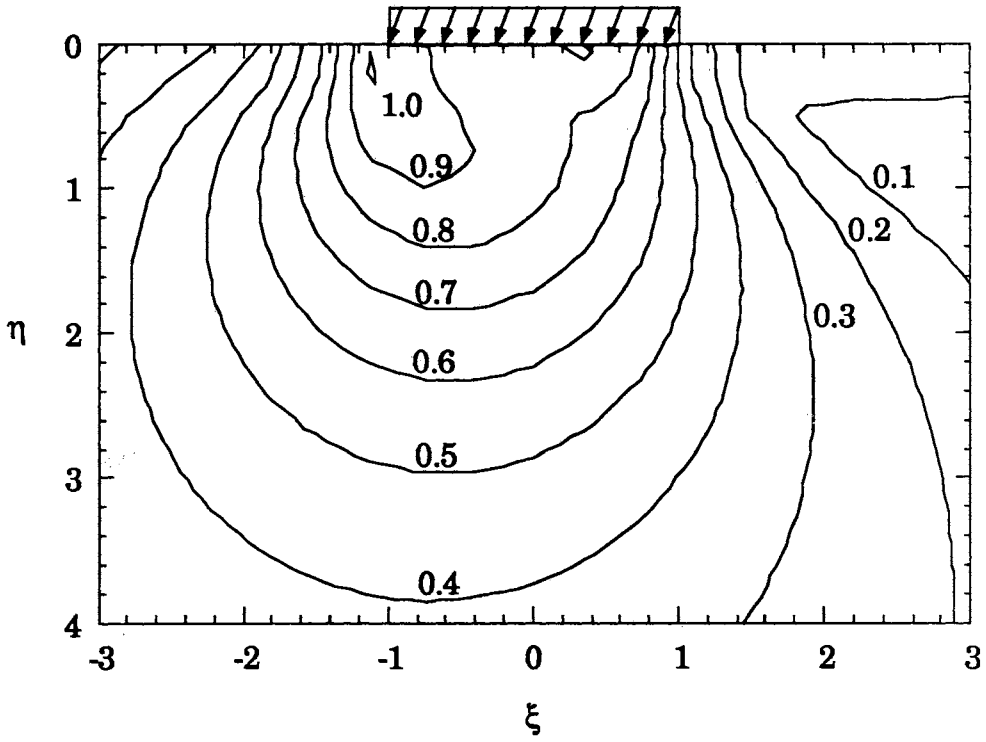

Figure 6-3. Contours of the Normalized von Mises Equivalent Elastostatic Stress with Respect to the Uniaxial Yield Strength of the Body as Predicted by Airy's Stress Function for Loading Conditions Representing the Orthogonal Flycutting of Al 6061-T6 at Depth of Cut of 0.01 μm

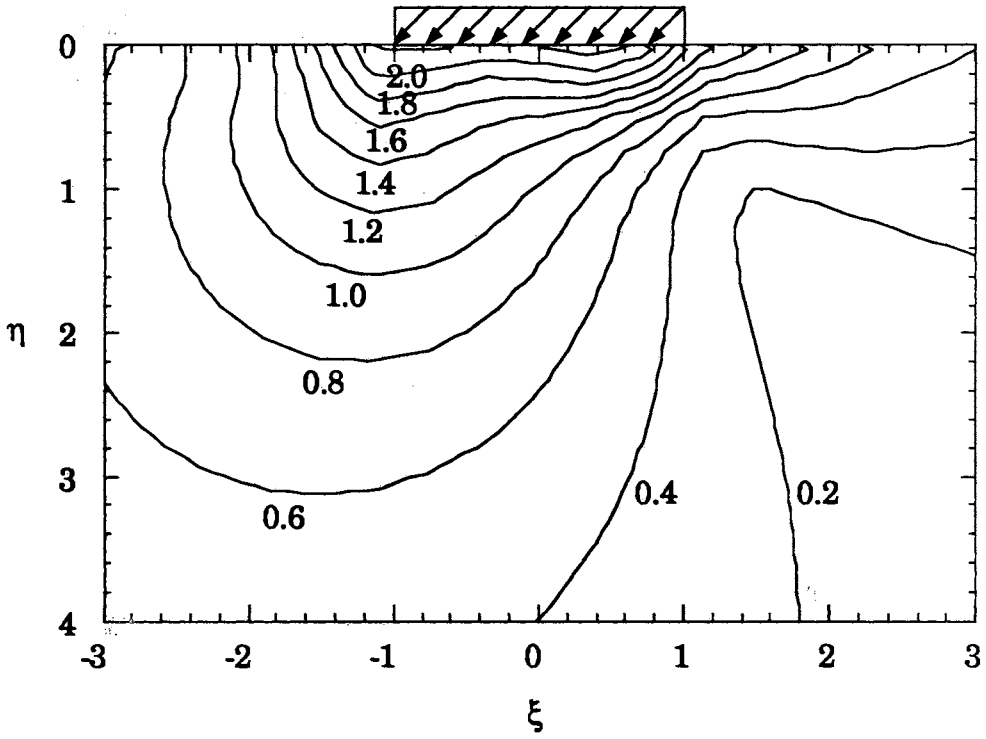

Figure 6-4. Contours of the Normalized von Mises Equivalent Elastostatic Stress with Respect to the Uniaxial Yield Strength of the Body as Predicted by Airy's Stress Function for Loading Conditions Representing the Orthogonal Flycutting of Al 6061-T6 at Depth of Cut of 0.1 μm

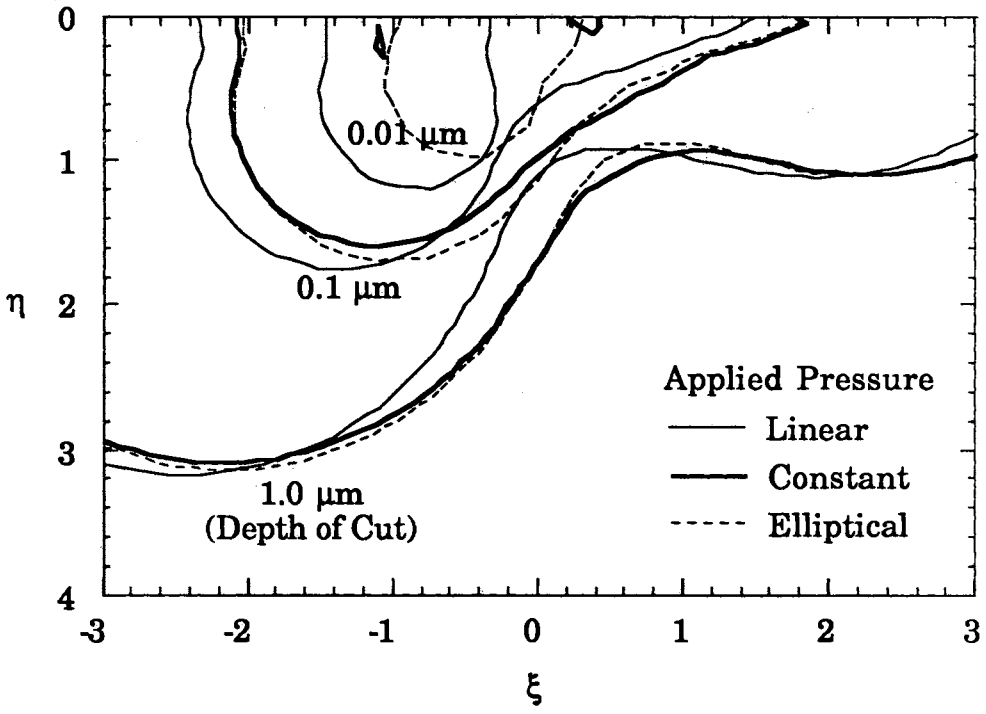

Figure 6-5. Elastic-Plastic Boundaries for Elastostatic Stress Fields due to Various Surface Pressures as Predicted by Airy's Stress Function for Loading Conditions Representing the Orthogonal Flycutting of Al 6061-T6 at Various Depths of Cut

deformed zone ($\sigma_{eq}/Y = 1$) extends further in the negative ξ direction and deeper in the η (depth) direction.

The elastic-plastic boundary contours for three depths of cut due to different types of surface pressures (the total applied forces are the same) are shown in Fig. 6-5. The contours at 1.0 μm were included in the figure as a comparison. Here, the maximum thickness of the boundary from the surface appears to be affected by the applied pressure type (i.e., linear, constant or elliptical). However, the elastic-plastic boundaries which are far from the surface are almost independent of the type of applied pressure consistent with Saint-Venant's principle [Timoshenko, 1970].

From Fig. 6-5, the plastic zone due to a constant pressure seems to be smaller than those due to linear and elliptical pressure at the loading conditions for 0.01 μm depth of cut. However, above yield, the stress state would be re-distributed for plastic deformation. Considering elastic-perfectly plastic material behavior, the contact interface may be supported by the constant yield strength of the material. Hence the contact pressure may be close to the actual state of the applied pressure.

6.2.4.2 Elastodynamic Stress Fields. For the elastodynamic stress fields, the concept of the moving body should be re-considered. The moving body (workpiece) has relative meaning with respect to the stationary body (tool). The entire contact length of the slider is under a sliding load constantly, whereas the moving body is subject to the contact pressure only on a part of its surface. In this case, even if the body is stationary, it can be considered as a moving body relative to the applied load, i.e., contact length is fixed and the material of the semi-infinite body flows toward the location of the contact.

Based on the above reasoning, the workpiece which was stationary for the present experimental study can be considered as the moving body relative to the slider (tool). Strictly speaking, "moving load on a stationary body" may be more appropriate than a "moving body". However, the terminology of "moving body" is used throughout the discussion for the convenience.

- Stress Fields of Al 6061-T6. Using the formulation based on the Fourier integral transform technique, elastodynamic stress fields for a moving body due to a constant surface pressure were estimated for plane strain conditions. The same applied load and material properties as used for the elastostatic stress fields were employed for this estimate. In the numerical integration for the stress fields, a 10 point Gauss-Laguerre integration technique was used, in which the integration limit from zero to infinity with exponential terms is appropriate.

Contours of the normalized von Mises equivalent stress with respect to the yield strength of the body (σ_{eq}/Y) are shown in Figs. 6-6 and 6-7 for Al 6061-T6 under planar loading conditions representing orthogonal flycutting at 0.01 and 0.1 μm depths of cut respectively. In Fig. 6-6, similar equivalent stress contours as those of the elastostatic stress fields shown in Fig. 6-3 can be seen, i.e., circular shaped contours, the first yielding occurs near $\xi = -1$ with skewed contours towards negative ξ direction. Also, as depth of cut increases, the contours of equivalent stress become non-symmetric, and the plastic zone ($\sigma_{eq}/Y = 1$) extends further in the negative ξ direction and deeper in the η direction as shown in Fig. 6-7.

In Fig. 6-8, the comparison of the elastic-plastic boundary contours for the elastostatic and elastodynamic solutions obtained for the same

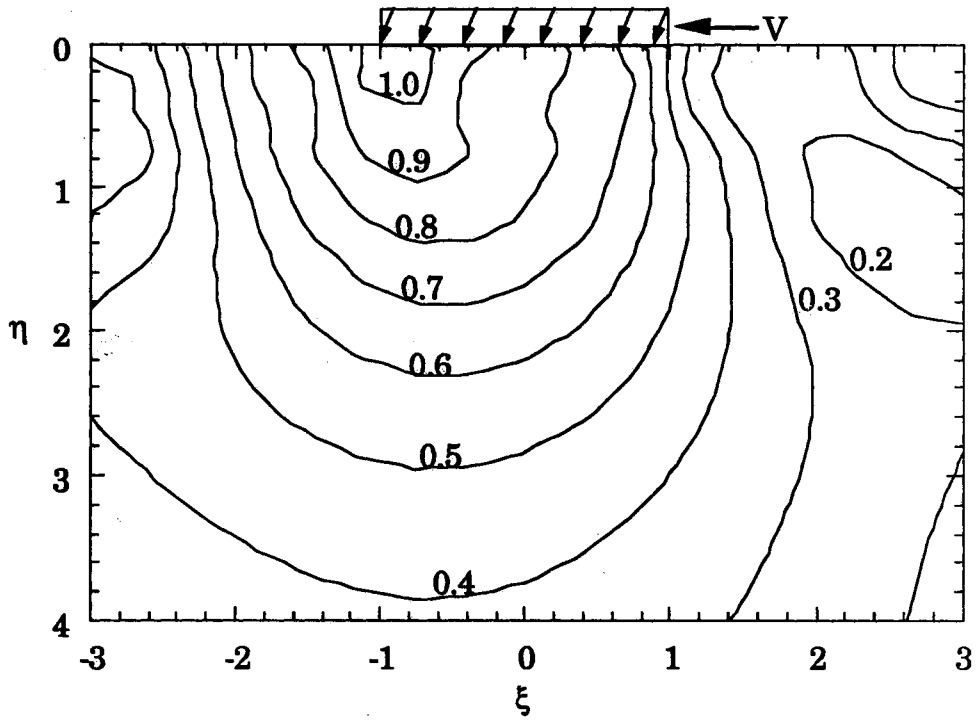

Figure 6-6. Contours of the Normalized von Mises Equivalent Elastodynamic Stress with Respect to the Uniaxial Yield Strength of the Body as Predicted by Fourier Integral Transform for Loading Conditions Representing the Orthogonal Flycutting of Al 6061-T6 at Depth of Cut of 0.01 μm

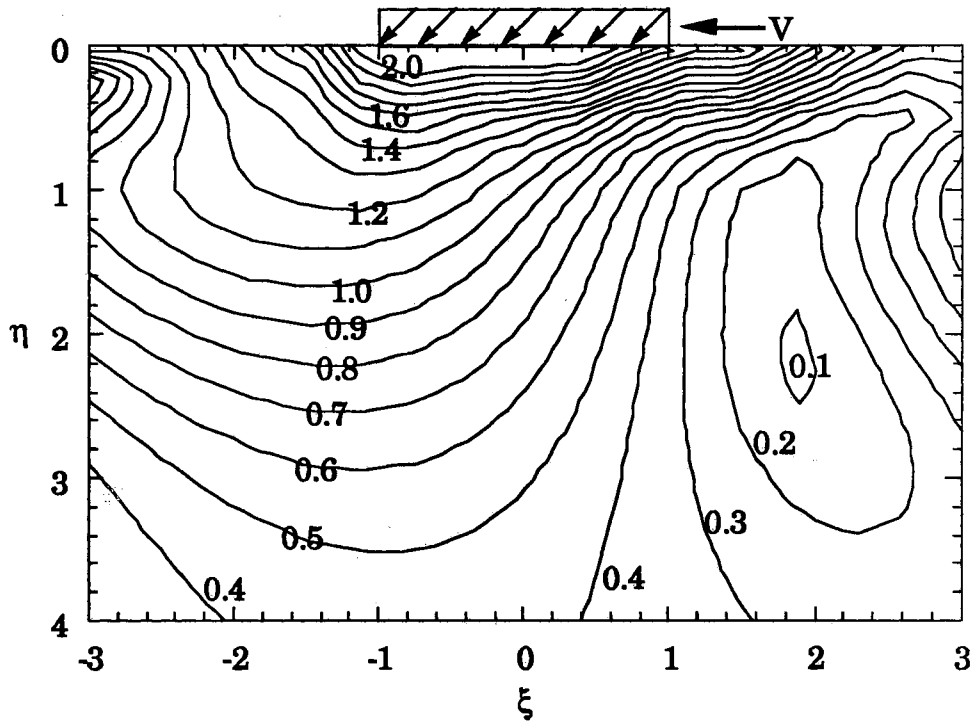

Figure 6-7. Contours of the Normalized von Mises Equivalent Elastodynamic Stress with Respect to the Uniaxial Yield Strength of the Body as Predicted by Fourier Integral Transform for Loading Conditions Representing the Orthogonal Flycutting of Al 6061-T6 at Depth of Cut of 0.1 μm

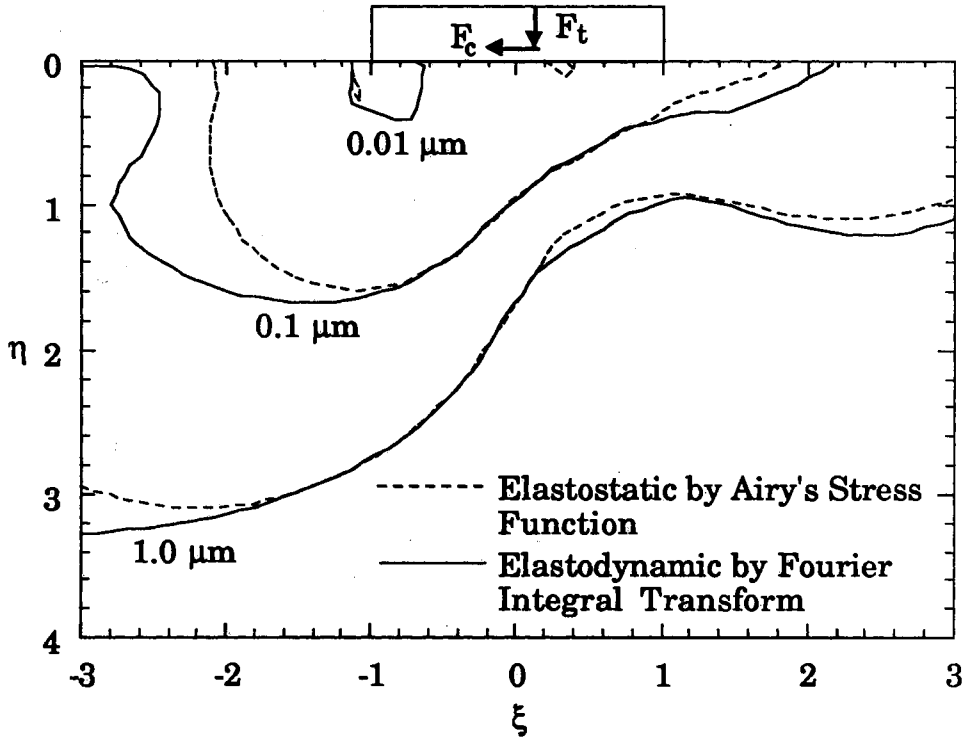

Figure 6-8. Comparison of Elastic-Plastic Boundaries due to Constant Surface Pressure as Predicted by Airy's Stress Function and Fourier Integral Transform Technique for Loading Conditions Representing the Orthogonal Flycutting of Al 6061-T6 at Various Depths of Cut

conditions except the sliding speed (7.6 m/min) are made for three depths of cut. A somewhat broader plastic zone in the sliding direction is predicted by the elastodynamic formulation. This may be due to the differences in formulation and not due to the speed effect. The effect of sliding speed on the stress fields will be discussed later. The plastically deformed thicknesses seem to agree well for the two approaches. As the slider moves, the plastic zone propagates in the sliding direction only, hence the broadening of the plastic zone in the sliding direction is not significant for the estimate of the thickness of the plastically deformed layer. The ratios of plastically deformed thickness predicted by the Airy's stress function to those by the Fourier integral transform technique are 0.73, 0.95 and 0.94 for the loading conditions representing 0.01, 0.1 and 1.0 μm depths of cut for Al 6061-T6. This indicates that the two formulations are in good agreements for the estimate of the elastic-plastic boundary thickness and the speed effect is not significant at this cutting conditions.

In Fig. 6-9, the plastically deformed layer thickness (δ_p) and the normalized thickness with respect to the depth of cut (δ_p/t_0) are shown as a function of depth of cut. In the figure, two data sets are represented for Al 6061-T6. The first one is the plastically deformed thickness estimated by the elastostatic stress field using the Airy's stress function (denoted as "Airy"), and the second is the thickness estimated by the elastodynamic stress fields using the Fourier integral transform technique (denoted as "FIT"). At 10 nm depth of cut, the plastically deformed thickness is about 0.2 μm, and at 1 μm depth of cut, it is about 2 μm for Al 6061-T6 at this cutting condition. This indicates that as depth of cut increases by two orders of magnitude, the plastically deformed thickness increases only 10 times. This seems mainly due to the small increase of the thrust force and

the directional change of the resultant force vector toward the cutting direction as depth of cut increases. When the plastically deformed thickness is normalized with respect to the depth of cut, the normalized thickness at 10 nm depth of cut is about 20 times the depth of cut whereas, the thickness at 1 μm depth of cut is only 2 times the depth of cut. This implies an increasing relative importance of the subsurface plastically deformed layer to the depth of cut at submicrometer depths of cut. Included are the data for Te-Cu and these will be discussed in the next section.

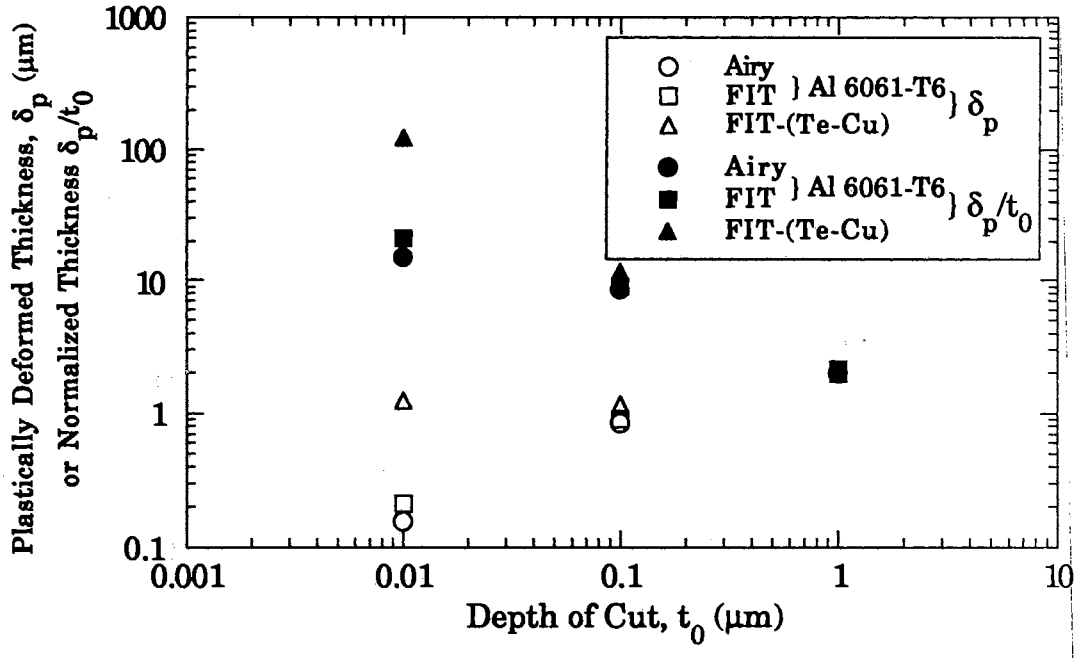

Figure 6-9. Subsurface Plastically Deformed Layer and Normalized Thicknesses Obtained Using Fourier Integral Transform for Loading Conditions Representing the Orthogonal Flycutting of Al 6061-T6 and Te-Cu at Various Depth of Cut

- Stress Fields of Te-Cu. For a calculation of the workpiece stress fields when machining Te-Cu, the measured cutting and thrust forces shown in Table 6-2 were used. These force components were obtained using Tool A4. Here, the contact length of the Te-Cu was measured by the examination of the tool wear at the flank face using the scanned result of the AFM. The wear land at the flank face of the Tool A4 was measured to be about 1.0 μm, and was assumed to have the same length for the depths of cut of 0.01, 0.1 and 1.0 μm since the thrust force for these depths of cut was measured to be almost the same. The resulting stress fields are shown in Figs. 6-10 and 6-11 for these loading conditions when machining Te-Cu at 0.01 and 0.1 μm depths of cut. The stress fields above 0.2 μm depth of cut using the model may be erroneous since the chip formation process may be dominant from above this depth of cut. The overall trend of the stress field is the same as that found for aluminum.

TABLE 6-2

MEASURED FORCE COMPONENTS, ESTIMATED CONTACT LENGTHS, AND CONTACT STRESSES IN ORTHOGONAL FLYCUTTING OF Te-Cu

Depth of Cut (μm)	Test No	F_c (N/mm)	F_t (N/mm)	l_f (μm)	l_f / t_0	σ (MPa)
0.01	1	0.216	0.553			
	2	0.211	0.541			
	Ave	0.214	0.547	1	100	547
0.1	1	0.318	0.489			
	2	0.319	0.493			
	Ave	0.319	0.491	1	10	491
1.0	1	1.485	0.624			
	2	1.521	0.610			
	Ave	1.503	0.617	1	1	617

Contours of the elastic-plastic boundaries estimated by the elastodynamic model for the loading conditions at three depths of cut are shown in Fig. 6-12. The plastically deformed thickness for 0.01 μm depth of cut is seen to be slightly greater than that for a 0.1 μm depth of cut, and the elastic-plastic contours are almost the same. This is due to the loading conditions at the two depths of cut, viz., thrust force when cutting at a 0.01 μm depth is greater than that at a 0.1 μm depth of cut, but cutting force when cutting at a 0.01 μm depth is smaller than that at a 0.1 μm depth of cut.

In Fig. 6-9, the plastically deformed thickness (δ_p) and the normalized thickness (δ_p/t_0) are shown as a function of depth of cut for Te-Cu. At 10 nm depth of cut, the plastically deformed thickness is about 1.2 μm, and at 1 μm depth of cut, it is about 2 μm. This indicates that for two orders of magnitudes increase in depth of cut, the plastically deformed thickness increases less than a factor of two. The normalized thickness at 10 nm depth of cut is about 120 times the depth of cut whereas, the thickness at 1 μm depth of cut is only 2 times the depth of cut. The magnitude of the plastically deformed thickness for Te-Cu is much more significant than that for Al 6061-T6. Two reasons can be considered. First, there is a difference in yield strength of the materials (363 MPa for Al 6061-T6 vs. 225 MPa for Te-Cu) and secondly there is a difference in the nonlinearity of the force behavior with depth of cut when machining those two materials (different tools used for cutting of the aluminum and Te-Cu are responsible for this nonlinearity). When machining Te-Cu, almost constant thrust forces were measured at submicrometer depths of cut (tool edge geometry was shown to be responsible for this nonlinearity as discussed in the previous chapter). The almost constant applied forces at

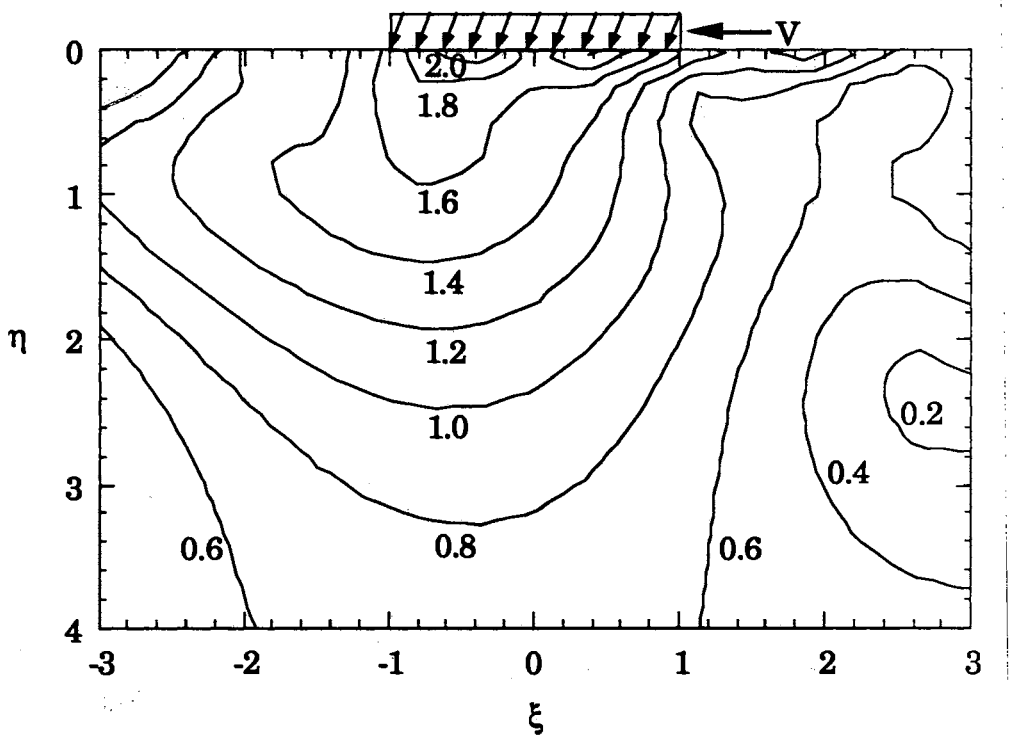

Figure 6-10. Contours of the Normalized von Mises Equivalent Elastodynamic Stress with Respect to the Uniaxial Yield Strength of the Body as Predicted by Fourier Integral Transform for Loading Conditions Representing the Orthogonal Flycutting of Te-Cu at 0.01 μm Depth of Cut

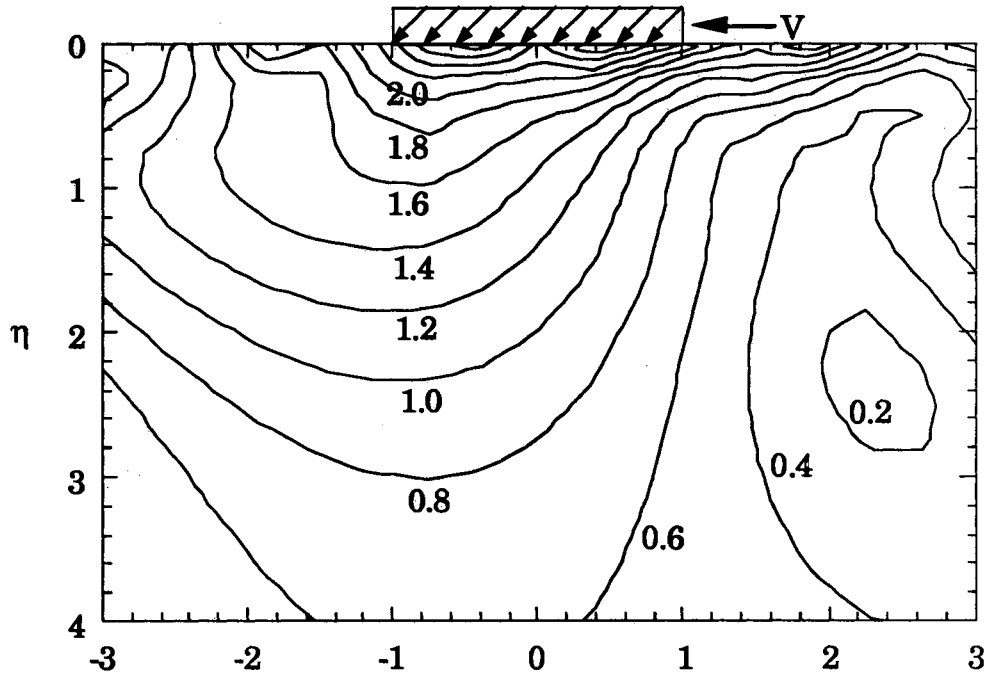

Figure 6-11. Contours of the Normalized von Mises Equivalent Elastodynamic Stress with Respect to the Uniaxial Yield Strength of the Body as Predicted by Fourier Integral Transform for Loading Conditions Representing the Orthogonal Flycutting of Te-Cu at 0.1 μm Depth of Cut

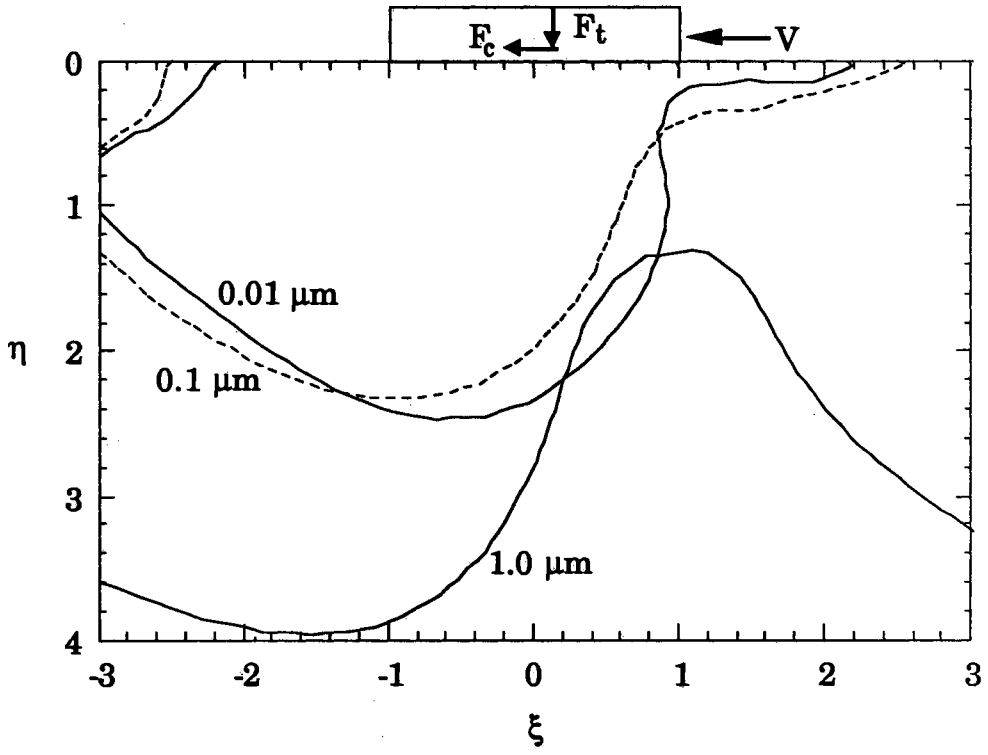

Figure 6-12. Elastic-Plastic Boundaries as Predicted by Fourier Integral Transform for Loading Conditions Representing the Orthogonal Flycutting of Te-Cu at Various Depths of Cut

those two depths of cut of 0.01 and 0.1 μm resulted in similar stress fields. This indicates that the worn tool produces almost the same force components at submicrometer depths of cut, and these force components generate similar stress fields at the subsurface of the workpiece. Hence, for effective material removal with minimum plastically deformed layer thickness, the depth of cut where thrust force ceases to decrease can be taken as a maximum depth of cut for actual machining.

6.2.4.3 Effect of Sliding Speed on Stress Fields. As discussed earlier, for one order of magnitude increase in cutting speed from 0.126 to 1.26 m/sec (7.6 to 76.2 m/min), no discernible change in cutting forces was measured for Te-Cu. Moreover, the trends of measured force with depth of cut at 0.126 m/sec were similar to the results of Moriwaki and Okuda in which machining was performed at 23 m/sec.

For an analytical examination of the speed effect on the stress fields, the elastodynamic stress field when cutting at 42 m/sec was estimated for the force components of 0.1 μm depth of cut for Te-Cu. The speed of 42 m/sec is about 1 % of the dilatation wave speed of Te-Cu. This stress field was compared with the stress field at 0.126 m/sec shown in Fig. 6-11. Almost identical stress fields were obtained. Contours of the elastic-plastic boundaries for both speeds at cutting 0.1 μm depth of cut of Te-Cu are shown in Fig. 6-13. With two orders of magnitude increase in sliding speed, no change in the elastic-plastic boundary can be seen. Also, the similar negligible effect of the sliding speed has been observed from the elastodynamic stress fields by using Eringen and Suhubi's [1975] formulation shown in the Appendix A.

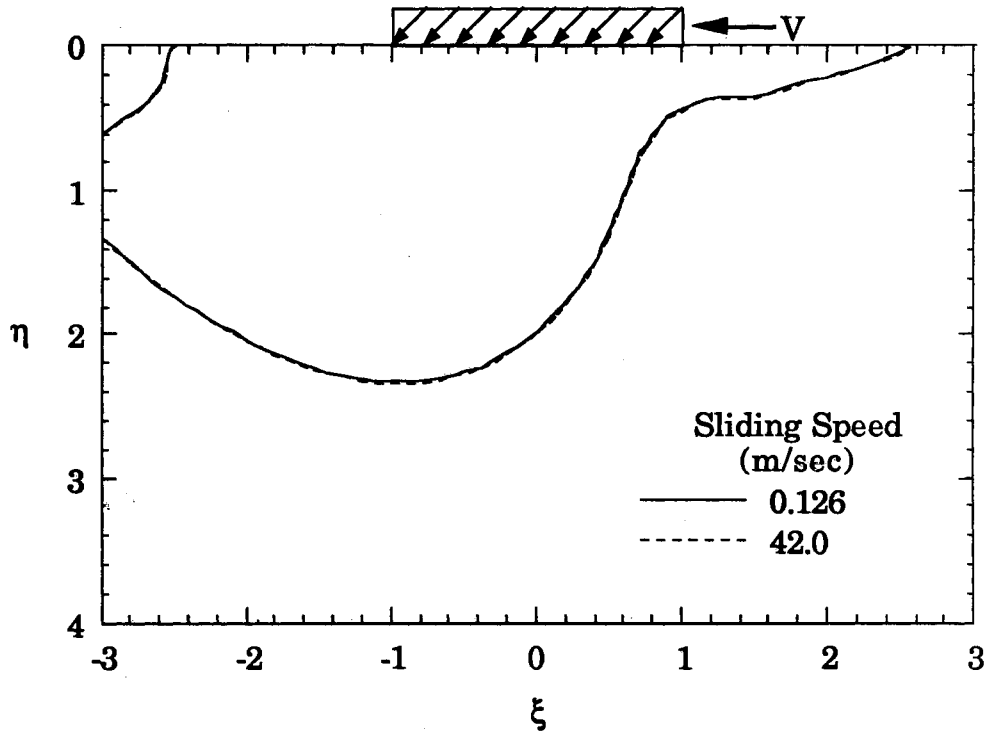

Figure 6-13. Contours of Elastic-Plastic Boundaries as Predicted by Fourier Integral Transform for Loading Conditions Representing the Orthogonal Flycutting of Te-Cu at Various Sliding Speeds

Both the measured force components and the stress fields were not affected by the increase of the cutting speed for up to one order of magnitude. However, as the sliding speed increases further, the temperature rise at the interface would increase linearly, since the frictional energy at the interface of the contact is directly proportional to the sliding speed. At high cutting speed, this temperature rise would affect the process mechanics more significantly.

6.2.5 Results of Temperature

Using tool-workpiece combinations of diamond-aluminum, and diamond-copper, the partition of energy as a function of location along the interface in contact has been predicted. Energy partitions and temperatures at the contact for the two tool-workpiece systems are shown in Figs. 6-14 ~ 6-17. The orthogonal flycutting of aluminum and copper at a speed of 7.6 m/min corresponds to a Peclet number of Pe ≈ 0.001 (for aluminum Pe = 0.0009, and for copper Pe = 0.0006). Hence from a heat transfer point of view, this represents essentially a stationary problem.

As shown in Fig. 6-14 and 6-15 for aluminum and copper, the majority of heat generated at the contact is seen to enter the tool (90.6 and 85.3 % for aluminum and copper) due to diamond's superior thermal properties. In the figures, energy partition, R, is the fraction of frictional energy which goes into the slider (tool). As expected for low Pe cases, the partition of energy is seen to be constant along the contact length. This fraction is seen to decrease as sliding speed is increased, however even at cutting speeds which are considered to be high for diamond turning, e.g., 23 m/sec used by Moriwaki [1989], the majority of heat still goes into the

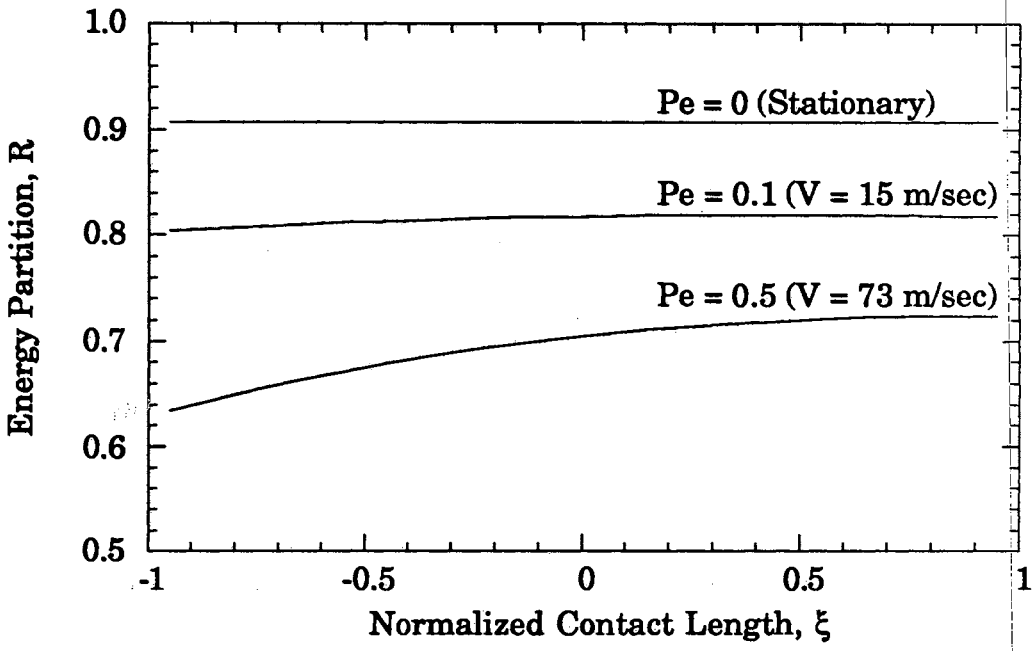

Figure 6-14. Energy Partition at the Contact Interface for the Bodies with Thermal Conductivities like Diamond and Aluminum (κ_{Al} = 73 mm²/sec, l = 0.565 μm)

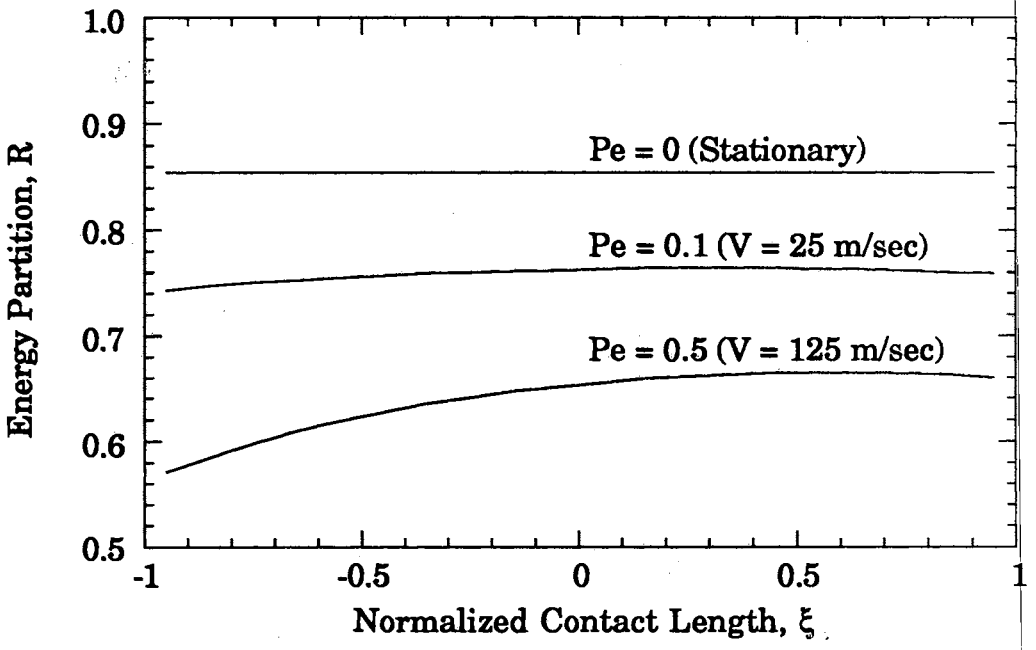

Figure 6-15. Energy Partition at the Contact Interface for the Bodies with Thermal Conductivities like Diamond and Copper (κ_{Cu} = 114.5 mm²/sec, l = 0.50 μm)

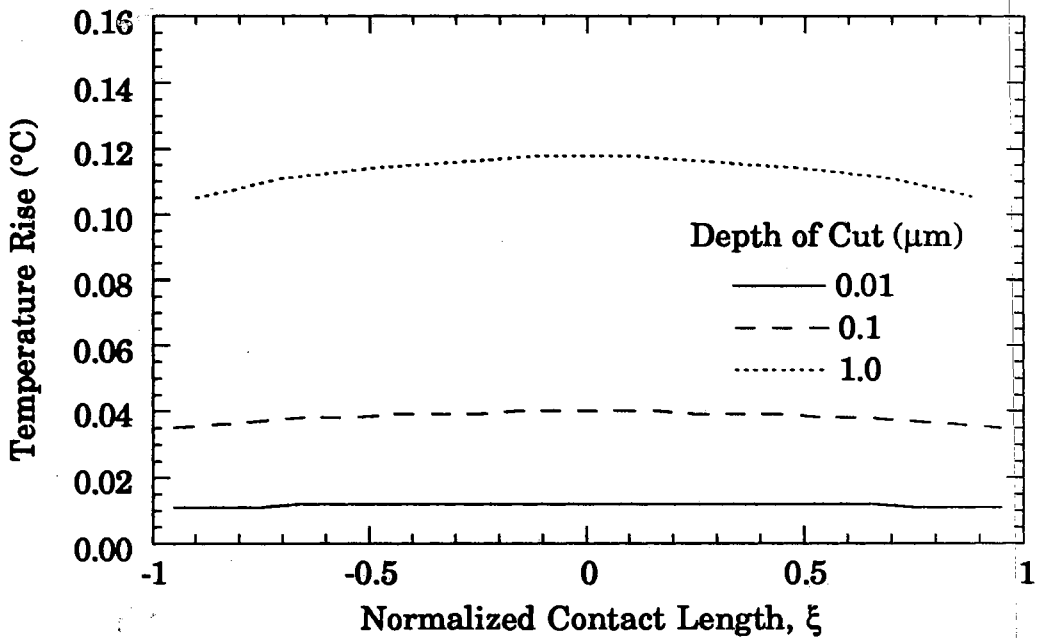

Figure 6-16. Predicted Temperature Rises at the Tool-Workpiece Interface for Conditions Representing the Orthogonal Flycutting of Al 6061-T6 at Depths of Cut of 0.01, 0.1 and 1 μm

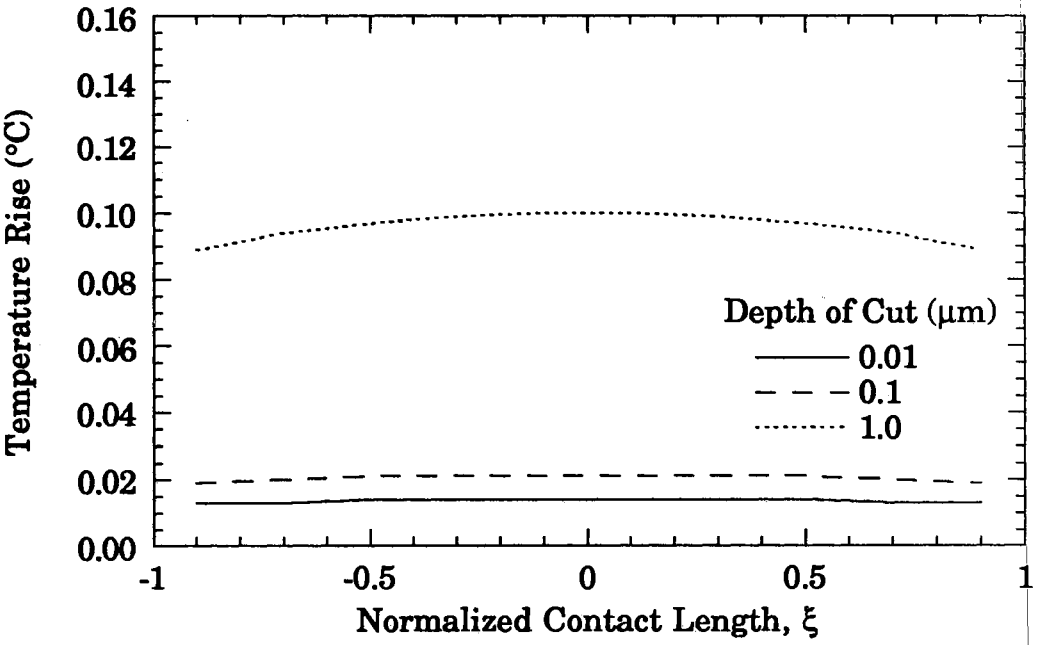

Figure 6-17. Predicted Temperature Rises at the Tool-Workpiece Interface for Conditions Representing the Orthogonal Flycutting of Te-Cu at Depths of Cut of 0.01, 0.1 and 1 μm

tool. Also, as the sliding speed increases, less energy flows into the diamond at the leading edge ($\xi = -1$) as compared to that for the trailing edge ($\xi = 1$).

Using measured cutting forces and the predicted partition of energy, the temperatures at the tool-workpiece interface have been calculated for conditions representing the flycutting of Al 6061-T6 and Te-Cu at depths of cut of 0.01, 0.1 and 1 μm, and are shown in Figs. 6-16 and 6-17. Due to the low Peclet number, the predicted temperatures are symmetric about the center of the contact, and are seen to be small. The maximum temperature increases are 0.12 °C for aluminum and 0.10 °C for Te-Cu at a 1 μm depth of cut. These small increases are due to the extremely small amount of energy which is being dissipated at the sliding contact, viz., cutting forces are only 1.668 and 1.503 N for Al 6061-T6 and Te-Cu for 1 mm wide specimen cutting at 1 μm depth of cut with 7.6 m/min speed.

In the ultra-high precision diamond flycutting experiments of Iwata [1987b] on copper, a maximum temperature rise of 1.0 °C for a cutting velocity of 565 m/min was measured at a depth of cut of 3 μm using micro thermocouple. This cutting speed results in an overall energy which is 2 orders of magnitude greater than the present cutting experiment on aluminum performed at 7.6 m/min. Considering this difference, the predicted temperature rise of the slider model, is consistent with the measured result of Iwata. For example, scaling Iwata's temperature data for the order of sliding energies encountered in the present experiments, would show resultant temperatures of the same order as those predicted by the slider model.

Relative to the concentrated heat source at the interface as discussed above, when the heat source is distributed over some finite

thickness throughout the depth of the body due to plastic deformation, the temperature rise would differ from that due to concentrated surface heat source. Malkin and Marmur [1977] investigated the temperature rise due to a distributed heat source in a thin layer of plastic deformation, and found that the concentrated surface heat source results in significant over-estimates of resulting temperatures. This indicates that a distributed heat flux in the subsurface would lead to even lower predicted temperatures for the present study.

6.3 Elastoplastic Modeling

6.3.1 Prandtl-Reuss Equation using Runge-Kutta Method

In order to simulate the stress fields of a body in a sliding process representing diamond turning at submicrometer depths of cut, it is necessary to extend the elastic formulation to include elastoplastic stress fields. The elastoplastic stress fields can be solved for by combining the elastic fields and using the step-by-step numerical approach of Merwin and Johnson [1963], which was later modified by Jahanmir [1976].

Once the stress fields reach the yield condition, a plastic stress and strain relation may be applied. The basic assumptions are i) the material behavior is elastic-perfectly plastic, ii) plane strain conditions exist, and iii) the elastic deviatoric stress and strain rate are the initial conditions for the plastic stress and strain fields.

Total incremental strain is the sum of the incremental elastic strain and plastic strain and may be given as:

$$\dot{e}_{ij} = \dot{e}^{e}_{ij} + \dot{e}^{p}_{ij} \tag{6-16}$$

The incremental plastic strain can be obtained from the Levy-Mises equation as:

$$\dot{e}^{p}_{ij} = \frac{\dot{w}^{p}}{2k^2} s_{ij} \tag{6-17}$$

where $\dot{w}^p$ is an incremental plastic work per unit volume, s_{ij} are the deviatoric stress components, and k is the flow stress of the body.

Using Hooke's law for the elastic strains, and the Levy-Mises equation for the plastic strains, the elastoplastic Prandtl-Reuss equation in terms of the incremental deviatoric stress and strain may be written as:

$$\dot{e}_{ij} = \frac{\dot{s}_{ij}}{2\mu} + \frac{\dot{w}^{p}}{2k^2} s_{ij} \tag{6-18}$$

where μ is the shear modulus. The energy rate per unit volume can be represented by the plastic energy, i.e, $\dot{w} = \dot{w}^p$. The deviatoric incremental stress can be obtained as:

$$\dot{s}_{ij} = 2\mu \left(\dot{e}_{ij} - \frac{\dot{w}}{2k^2} s_{ij}\right) \tag{6-19}$$

Here, material derivatives are considered as:

$$\frac{Ds_{ij}}{Dt} = \frac{\partial s_{ij}}{\partial t} + V\frac{\partial s_{ij}}{\partial \xi} \tag{6-20}$$

At steady state, the first term on the right hand side in eq. (6-20) vanishes, and the material derivative becomes a spatial derivatives. Other rate terms of strain and work in eq. (6-19) may also be in the form of spatial derivatives. Again, equating the rate terms in eq. (6-19) after taking the material derivatives and eliminating speed V from both sides, the material derivative equation becomes the spatial derivative equation.

For the elastoplastic stress fields, the incremental deviatoric stress can be found using the Runge-Kutta method based on the elastic stress fields starting from the first yield point at a given depth of the body. This stress field is used to calculate the stress field of the next point. This procedure is the process of releasing stresses above the yield point. At the end of a step in a given depth, the calculated stress may not satisfy the equilibrium condition. By introducing residual stress, the equilibrium condition can be satisfied. This procedure is repeated until there is no further changes in residual stresses. For the calculation of the elastoplastic stress fields, the steps shown in Suh's procedure were employed [Jahanmir, 1976; Suh, 1986].

1) Initialize residual stress and strains by setting to zero.
2) Calculate elastic stress along ξ-axis at fixed η.
3) When stress state reaches yield criterion (von Mises), the Prandtl-Reuss equations are used to calculate the stress for successive movement of the point, assuming the total strains are the same as that given by the elastic solution.
4) The Prandtl-Reuss equations are integrated using a Runge-Kutta method up to fourth order. Starting from the first yield point, the stress rates are found from eq. (6-19). These stress rates are used to predict the stress components of the next point.

5) When the yield criterion is not satisfied or the rate of plastic work becomes negative, plastic deformation terminates. The stress at the next point is calculated from the elastic equation.

6) The final state of stress violates the equilibrium condition. At the end of each iteration, the stresses are relaxed elastically to satisfy an equilibrium condition, and residual stresses and strains are calculated.

7) Steps 2)-6) are repeated for the same point using the residual stress from the previous iteration until a steady state is reached. This state is when the residual stresses and strains are not significantly different from those of the previous iteration.

8) Above step is continued for η direction.

6.3.2 Residual Stresses and Strains

The possible residual stress components are independent of ξ due to the nature of the sliding problem and can be written as a function of η only as:

$$(\sigma_{\xi\xi})_r = f_1(\eta),\ (\sigma_{\eta\eta})_r = f_2(\eta),\ (\sigma_{\xi\eta})_r = f_3(\eta) \tag{6-21}$$

The equilibrium equations for residual stress are:

$$\sigma_{ij,j} = 0 \tag{6-22}$$

From eqs.(6-21) and (6-22), the following can be obtained:

$$f_3(\eta) = C_3,\ f_2(\eta) = C_2 \tag{6-23}$$

where C_i, i = 2,3 are constants.

The boundary conditions for residual stresses may be written as:

$$(\sigma_{\eta\eta})_r = (\sigma_{\xi\eta})_r = 0 \text{ at } (\xi, \eta) = (\infty, 0) \tag{6-24}$$

These boundary conditions result in $C_2 = C_3 = 0$. Thus, possible residual stresses for plane strain condition are:

$$(\sigma_{\xi\xi})_r = f(\eta), (\sigma_{\zeta\zeta})_r = \nu f(\eta)$$

$$(\sigma_{\eta\eta})_r = (\sigma_{\xi\eta})_r = 0 \tag{6-25}$$

Since the equilibrium and residual stress boundary conditions are not satisfied at the end of each iteration, the state of stress at the end of each iteration gives nonzero 'pseudo-residual stresses' of $(\sigma_{\eta\eta})_r'$ and $(\sigma_{\xi\eta})_r'$. These 'pseudo' residual stress components are the difference between the elastoplastic stress and elastic stress at the point where the elastic-plastic boundary ends at the trailing edge at each iteration. The corresponding strains are:

$$(\varepsilon_{\eta\eta})_r = -\frac{1-2\nu}{2(1-\nu)G}(\sigma_{\eta\eta})_r'$$

$$(\gamma_{\xi\eta})_r = -\frac{(\sigma_{\xi\eta})_r'}{G} \tag{6-26}$$

Using the stress from each iteration, the residual stresses may be calculated as:

$$(\sigma_{\xi\xi})_r = (\sigma_{\xi\xi})_r' - \frac{\nu}{(1-\nu)}(\sigma_{\eta\eta})_r'$$

$$(\sigma_{\zeta\zeta})_r = (\sigma_{\zeta\zeta})'_r - \frac{\nu}{(1-\nu)}(\sigma_{\eta\eta})'_r \qquad (6\text{-}27)$$

$(\sigma_{\xi\xi})_r$ and $(\sigma_{\zeta\zeta})_r$ are used as initial conditions for the next iteration. This procedure is repeated until there is no further change in $(\sigma_{\xi\xi})_r$ and $(\sigma_{\zeta\zeta})_r$ which means $(\sigma_{\eta\eta})'_r = 0$. However, $(\gamma_{\xi\eta})_r$ approaches a constant value.

6.3.3 Results of Elastoplastic Stress Fields

6.3.3.1 Elastoplastic Stress Fields. The present model should be considered applicable to the ultra-precision machining process only at depths of cut where sliding indentation is dominant (in the submicrometer range and below). Above about 0.5 and 0.2 μm depth of cut for Al 6061-T6 and Te-Cu respectively, the force ratios (F_t/F_c) were less than unity. Hence, the elastoplastic stress fields for depths of cut of 0.01 and 0.1 μm depths of cut were calculated. Also, due to the negligibly small increase of interfacial temperature of about 0.1 °C even at depth of cut of 1 μm, only mechanical stress is considered.

Near the contact where the gradients of stress are abruptly changing, an instability of the numerical convergence was observed. By decreasing the number of integration points, the numerical convergence was achieved. In the numerical integration, a 10 point Gauss-Laguerre scheme was used. For some cases near the surface, a 6 point scheme was used alternatively. Due to the nature of the elastic-perfectly plastic material behavior assumed, the prediction of strain fields may not be appropriate since stress is independent of strain beyond the yield point for this behavior. Hence, the stress fields are considered in the present study so as to predict the elastic-plastic boundary layer thicknesses.

- Stress Fields of Al 6061-T6. Using the elastic solution from the Fourier integral transform technique as a starting point, the elastoplastic stress fields were obtained using a step size of $\Delta\xi = 0.01$. The normalized von Mises equivalent elastoplastic stress fields with respect to the yield strength of the body are shown in Figs. 6-18 and 6-19 for loading conditions representing the orthogonal flycutting of Al 6061-T6 at depths of cut of 0.01 and 0.1 μm. Comparing the elastoplastic stress fields with the elastic stress fields, the plastic zone is seen to be broadened in the direction of sliding. The comparison of the elastoplastic stress field with that of the elastic solution will be discussed in a later section along with the results obtained from ABAQUS. In the figures, the change of stress fields near the top subsurface can be seen, viz., the stress field for 0.01 μm depth of cut has been changed up to $\eta = 0.6$, and up to $\eta = 1.5$ from the surface for 0.1 μm depth of cut, which are the maximum plastically deformed layer thicknesses. Below these depths (increasing η), the stress fields are the same as that of the elastic fields (which is expected). The depths of the plastic zone predicted by both models are seen to be almost the same.

Elastoplastic axial, normal and shear stress at depths of $\eta = 0.1$ and 0.5 are shown in Figs. 6-20 ~ 6-22 for Al 6061-T6. All the stress components are normalized with respect to the yield strength of the material (363 MPa). At the leading edge ($\xi = -1$), the state of axial stress is compressive as is expected, and at the trailing edge ($\xi = 1$), it is tensile. This trend is consistent with the results of Ju [Ju, 1982] and Huang [Huang, 1985] for elastodynamic stress fields. The maximum compressive axial stress occurs near $\xi = -1$ for the case of 0.1 μm depth of cut. However, for 0.01 μm depth of cut, the point of maximum stress shifts toward the trailing edge. This seems to be reflected by the rotation of the resultant force vector

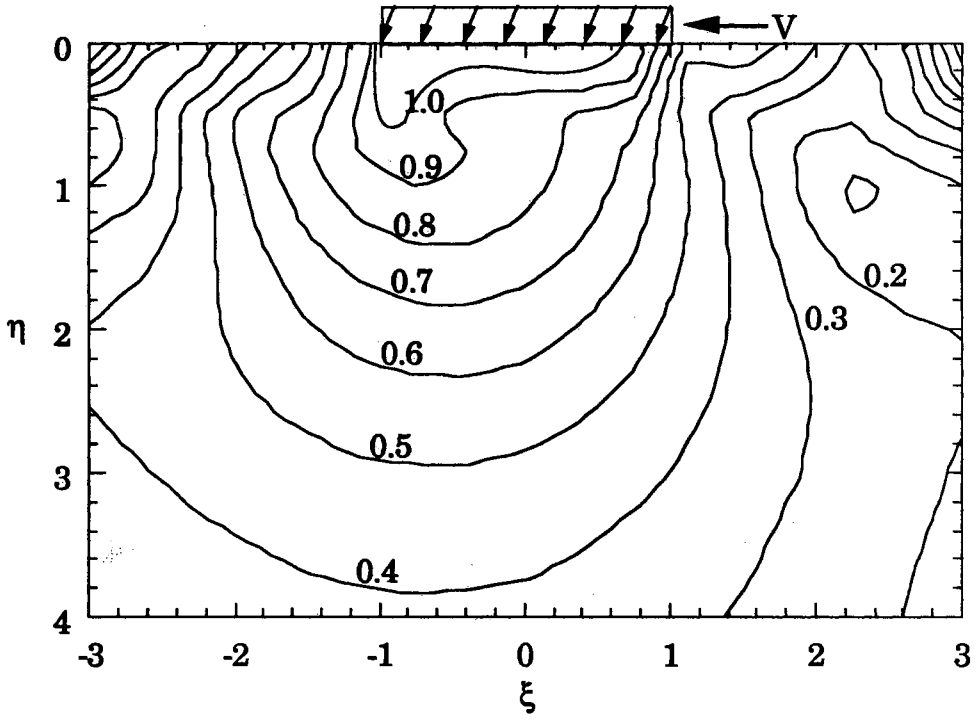

Figure 6-18. Contours of the Normalized von Mises Equivalent Elastoplastic Stress with Respect to the Uniaxial Yield Strength of the Body as Predicted by Fourier Integral Transform and Runge-Kutta Method for Loading Conditions Representing the Orthogonal Flycutting of Al 6061-T6 at Depth of Cut of 0.01 μm

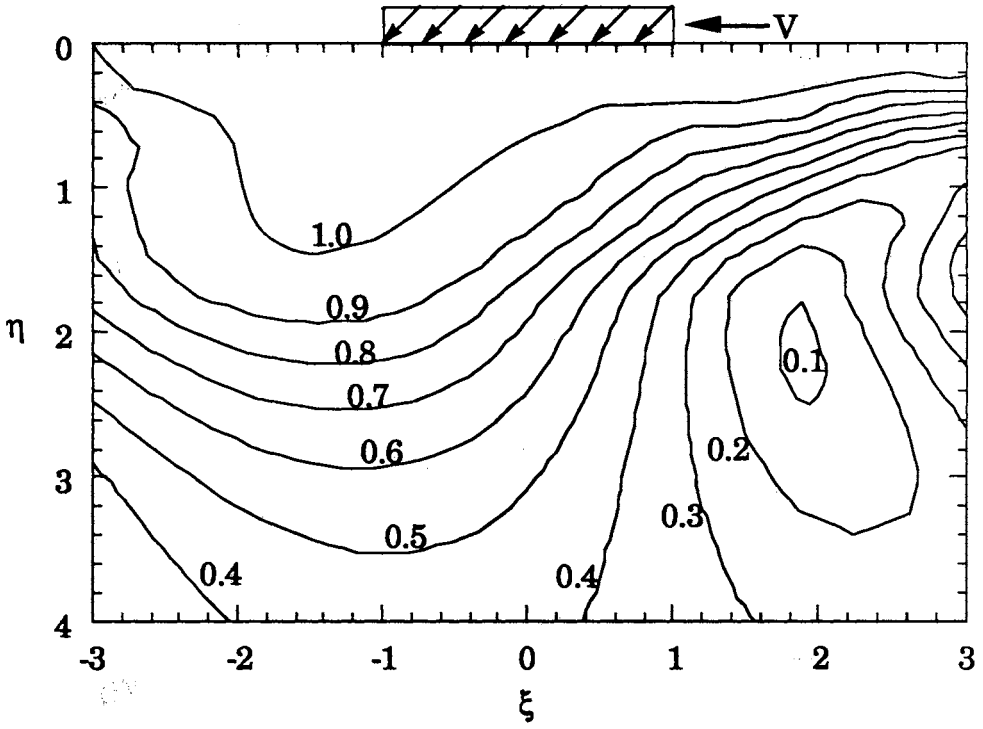

Figure 6-19. Contours of the Normalized von Mises Equivalent Elastoplastic Stress with Respect to the Uniaxial Yield Strength of the Body as Predicted by Fourier Integral Transform and Runge-Kutta Method for Loading Conditions Representing the Orthogonal Flycutting of Al 6061-T6 at Depth of Cut of 0.1 μm

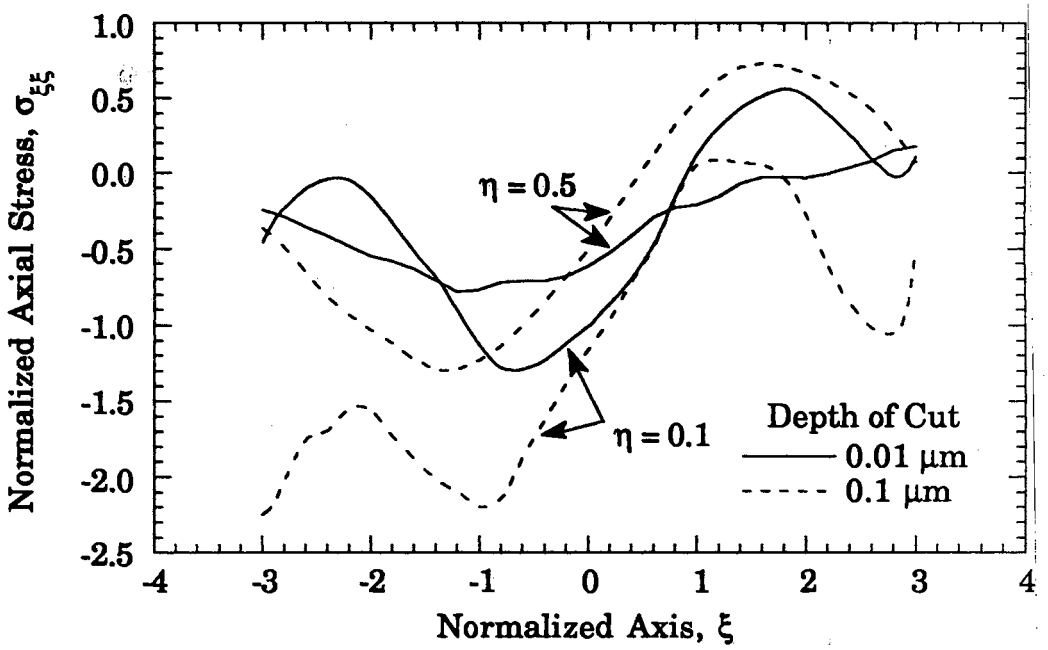

Figure 6-20. Comparison of Normalized Elastoplastic Axial Stresses by the Yield Strength of the Body at the Subsurface of Al 6061-T6 in Micromachining at 0.01 and 0.1 μm Depths of Cut

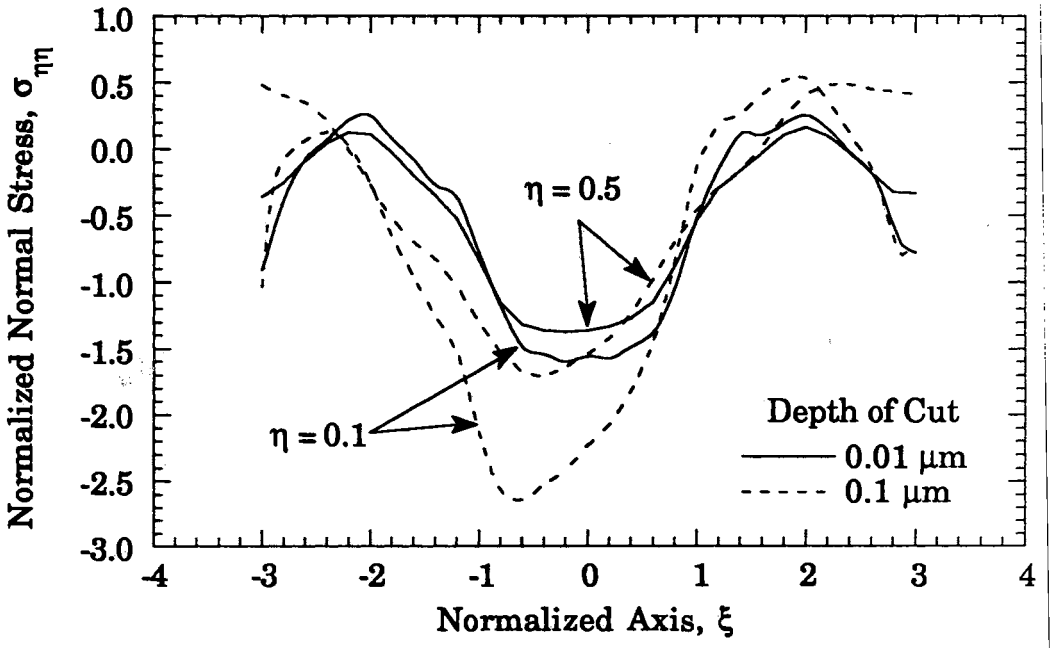

Figure 6-21. Comparison of Normalized Elastoplastic Normal Stresses by the Yield Strength of the Body at the Subsurface of Al 6061-T6 in Micromachining at 0.01 and 0.1 μm Depths of Cut

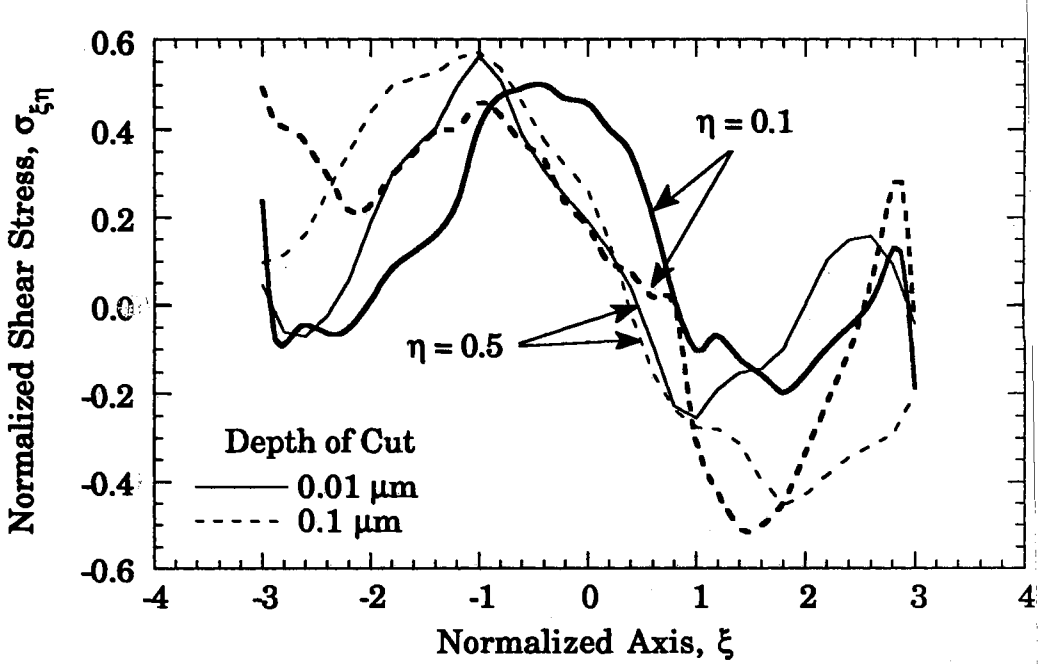

Figure 6-22. Comparison of Normalized Elastoplastic Shear Stresses by the Yield Strength of the Body at the Subsurface of Al 6061-T6 in Micromachining at 0.01 and 0.1 μm Depths of Cut

applied at the surface, viz., at 0.01 μm depth of cut, the direction of resultant force vector is about 72 degrees whereas it is 46 degrees for 0.1 μm depth of cut.

The normal stress shown in Fig. 6-21 represents a typical stress field by an indentation. At 0.01 μm depth of cut, in which the force components resemble pure indentation, the normal stress shows quasi-symmetric with respect to $\xi = 0$ with the maximum normal stress at the center. When the loading direction deviates from that of indentation, the stress contour becomes asymmetric. Tensile stresses around $\xi = \pm 2$ can be observed from the figure.

The normalized shear stresses in Fig. 6-22 show almost the same maximum positive and negative shear stress near $\xi = \pm 1$ for both the loading conditions of 0.01 and 0.1 μm depths of cut even at deeper depths ($\eta = 0.5$) from the surface. The maximum shear stress of about 45 ~ 60 % of the yield strength occurs at the leading edge. At the trailing edge, the direction of the shear stress changes to negative. This change of shear stress is the same as that observed by Hamilton [1963], and Merwin and Johnson [1963]. This implies that energy dissipation would be much greater than that which would be expected from simple shear due to the nature of the loading path.

- Stress Fields of Te-Cu. Similar elastoplastic stress fields to those for aluminum were obtained for Te-Cu. The normalized equivalent stress fields are shown in Figs. 6-23 and 6-24 for loading conditions at depths of cut of 0.01 and 0.1 μm. Comparing with the stress fields obtained for aluminum, a much deeper plastic zone can be observed. This is due to the smaller yield strength of Te-Cu (363 vs. 225 MPa). Due to almost the same applied pressure for the depths of cut of 0.01 and 0.1 μm, almost the same stress fields are obtained for the two cases. However, for the depth of cut at 0.1 μm, the iso-stress lines in Fig 6-24 are shifted toward the leading edge ($\xi = -1$) due to the greater cutting force applied. The stress fields for both depths of cut are different up to about $\eta = 2$, which is the maximum plastically deformed depth from the surface. When $\eta > 2$, the elastoplastic stress fields are the same as the elastic fields. Comparison of the elastic-plastic boundaries estimated using both the elastic and elastoplastic models are shown in Fig. 6-25. For both depths of cut considered, the

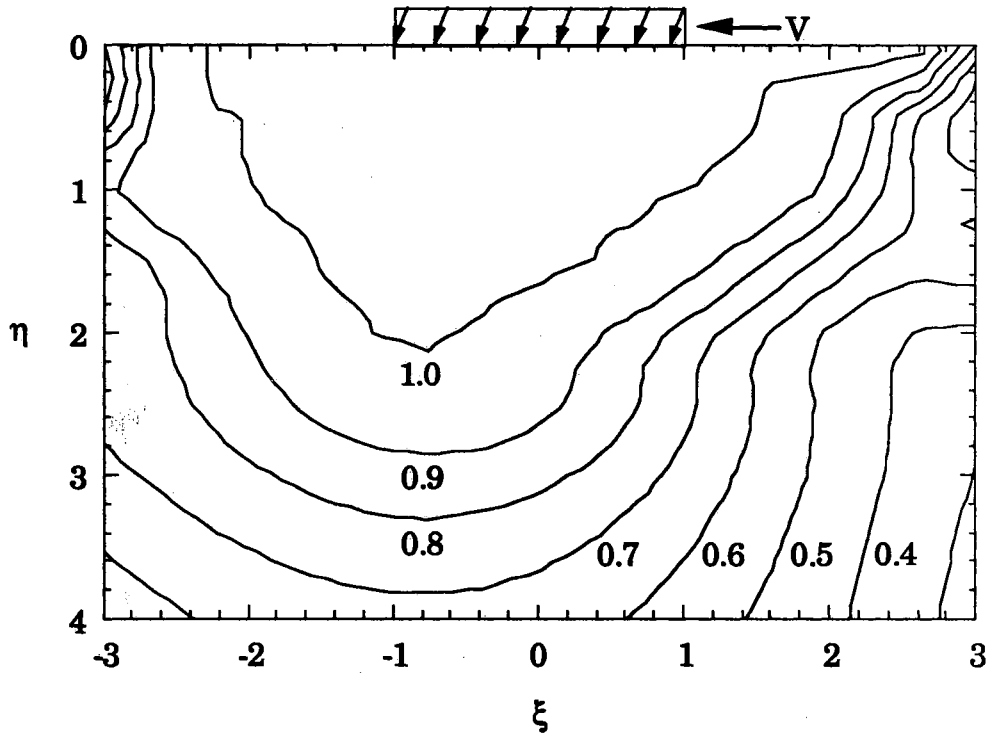

Figure 6-23. Contours of the Normalized von Mises Equivalent Elastoplastic Stress with Respect to the Uniaxial Yield Strength of the Body as Predicted by Fourier Integral Transform and Runge-Kutta Method for Loading Conditions Representing the Orthogonal Flycutting of Te-Cu at Depth of Cut of 0.01 μm

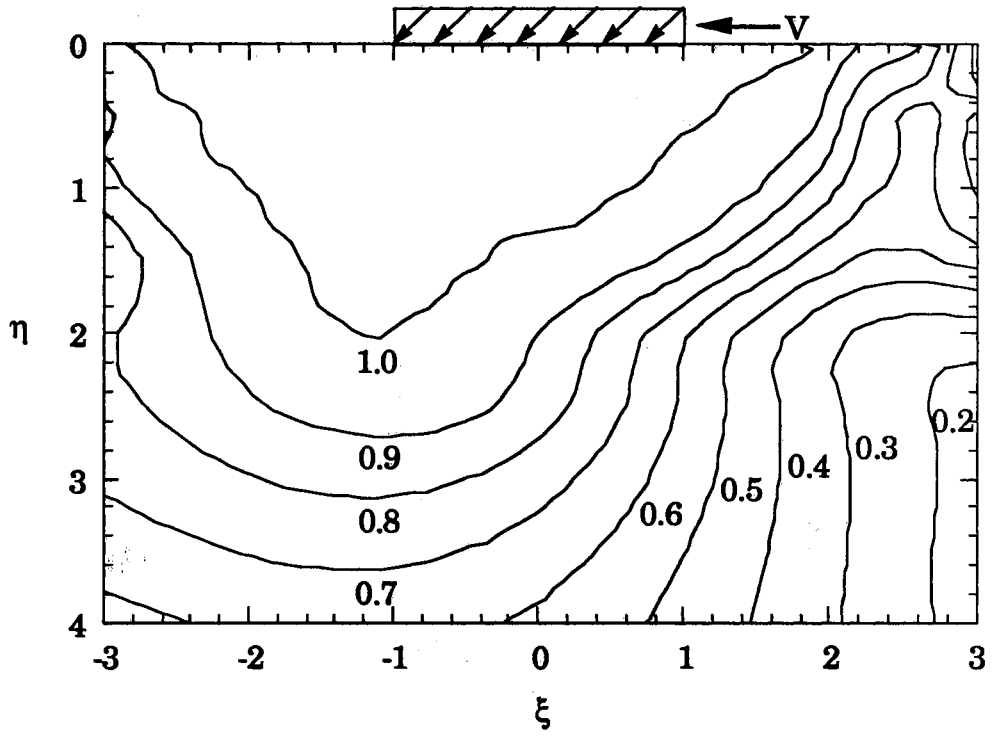

Figure 6-24. Contours of the Normalized von Mises Equivalent Elastoplastic Stress with Respect to the Uniaxial Yield Strength of the Body as Predicted by Fourier Integral Transform and Runge-Kutta Method for Loading Conditions Representing the Orthogonal Flycutting of Te-Cu at Depth of Cut of 0.1 μm

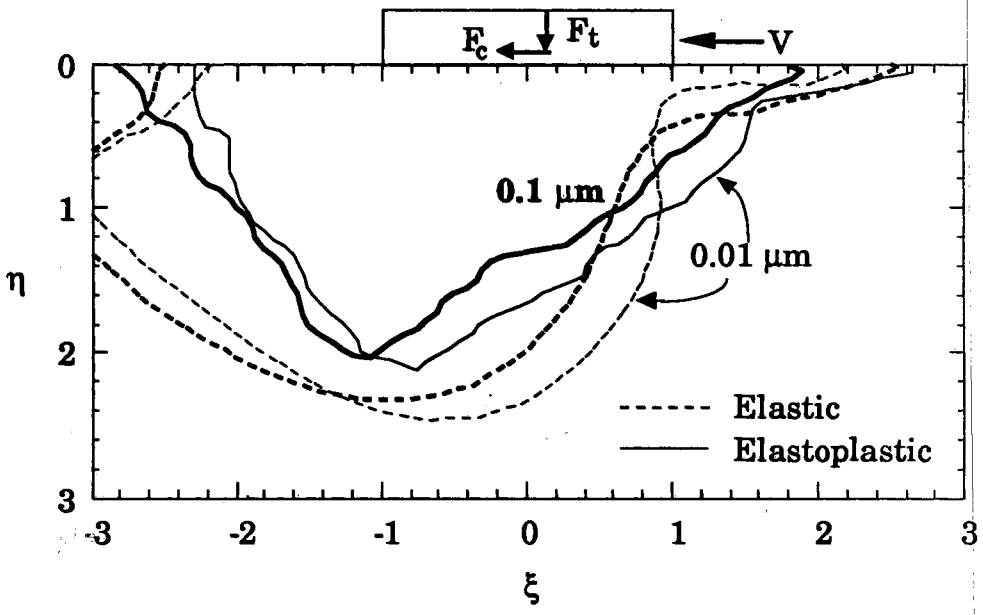

Figure 6-25. Comparison of Elastic-Plastic Boundaries Estimated Using Elastic and Elastoplastic Model for Loading Conditions Representing the Orthogonal Flycutting of Te-Cu at Depths of Cut of 0.01 and 0.1 μm

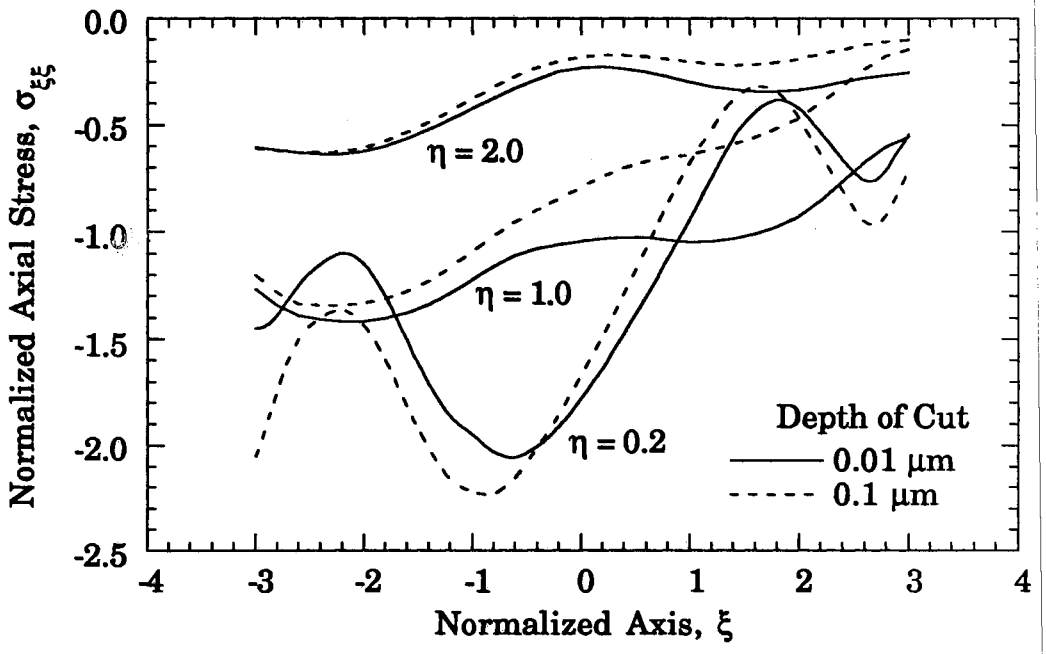

Figure 6-26. Comparison of Normalized Elastoplastic Axial Stresses by the Yield Strength of the Body at the Subsurface of Te-Cu in Micromachining at 0.01 and 0.1 μm Depths of Cut

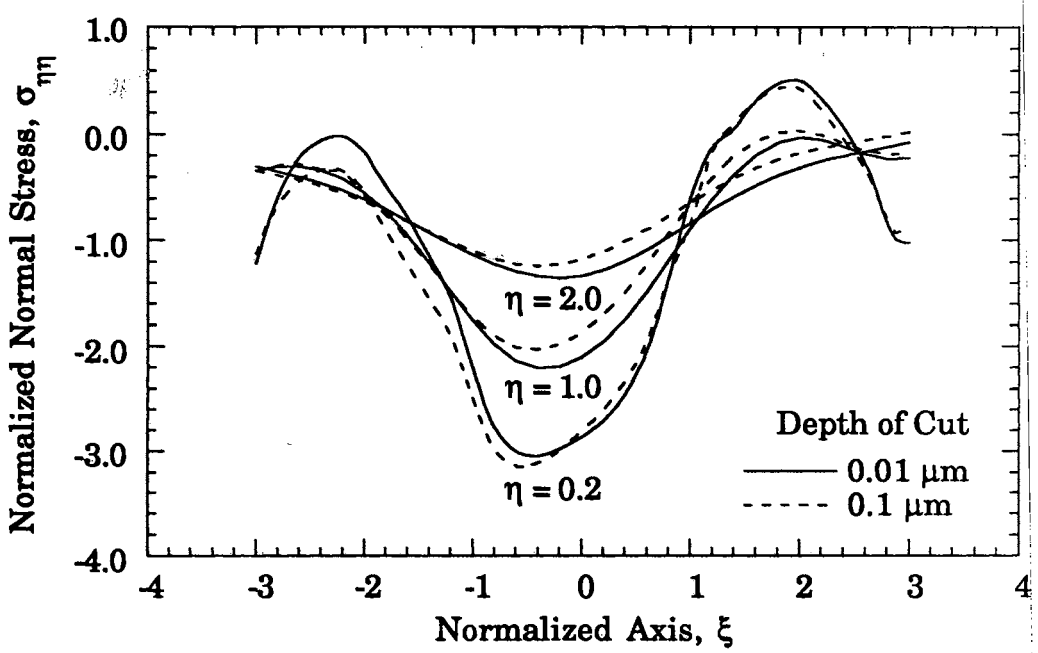

Figure 6-27. Comparison of Normalized Elastoplastic Normal Stresses by the Yield Strength of the Body at the Subsurface of Te-Cu in Micromachining at 0.01 and 0.1 μm Depths of Cut

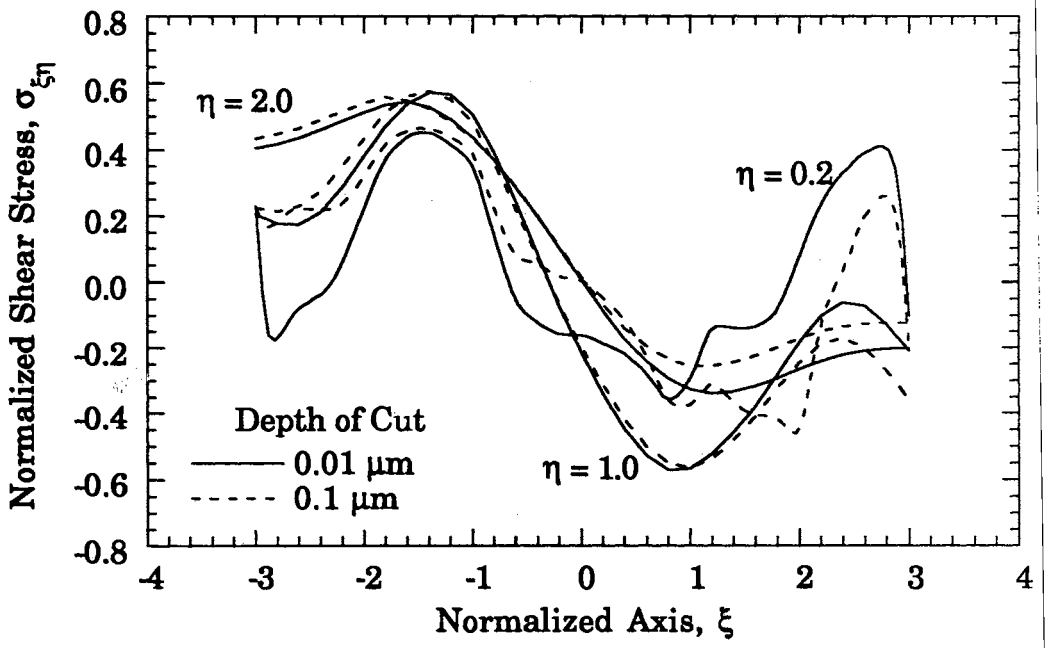

Figure 6-28. Comparison of Normalized Elastoplastic Shear Stresses by the Yield Strength of the Body at the Subsurface of Te-Cu in Micromachining at 0.01 and 0.1 μm Depths of Cut

elastoplastic model estimates a slightly smaller elastic-plastic boundary thickness of about 2 μm.

Normalized elastoplastic axial, normal and shear stress at depths of η = 0.2, 1.0 and 2.0 are shown in Figs. 6-26 ~ 6-28. Similar stress distributions as for those of aluminum can be seen for both the loading conditions of 0.01 and 0.1 μm depth of cut, i.e., maximum axial compressive stress near ξ = -1, almost symmetric normal stress with respect to ξ = 0, and maximum tensile shear stress of 45 ~ 60 % of the yield strength near ξ = -1.

6.3.3.2 Estimated Residual Stresses. Using the slider model for the prediction of the elastoplastic stress fields, residual stresses for Al 6061-T6 and Te-Cu were also estimated for loading conditions representing 0.01 and 0.1 μm depths of cut. Convergence of the residual stresses was investigated to check numerical stability. The convergence of residual stress normalized with respect to the yield strength of the Te-Cu workpiece material vs. number of iterations is shown in Figs. 6-29 and 6-30 representing the loading conditions of 0.01 and 0.1 μm depths of cut. Stable convergence reaching steady state at about 5 to 6 iterations can be seen. Even at a shallow depth of 0.1 η, convergence seems to be fairly good. Similar trends were observed for Al 6061-T6.

Predicted axial residual stress normalized with respect to the yield strength of the material along the depth from the surface is shown in Figs. 6-31 and 6-32 for Al 6061-T6 and Te-Cu. The depth from the surface of the material is normalized with respect to the half contact length, i.e., $\eta = y/l$. For aluminum, compressive residual stresses of about 13 % of the yield

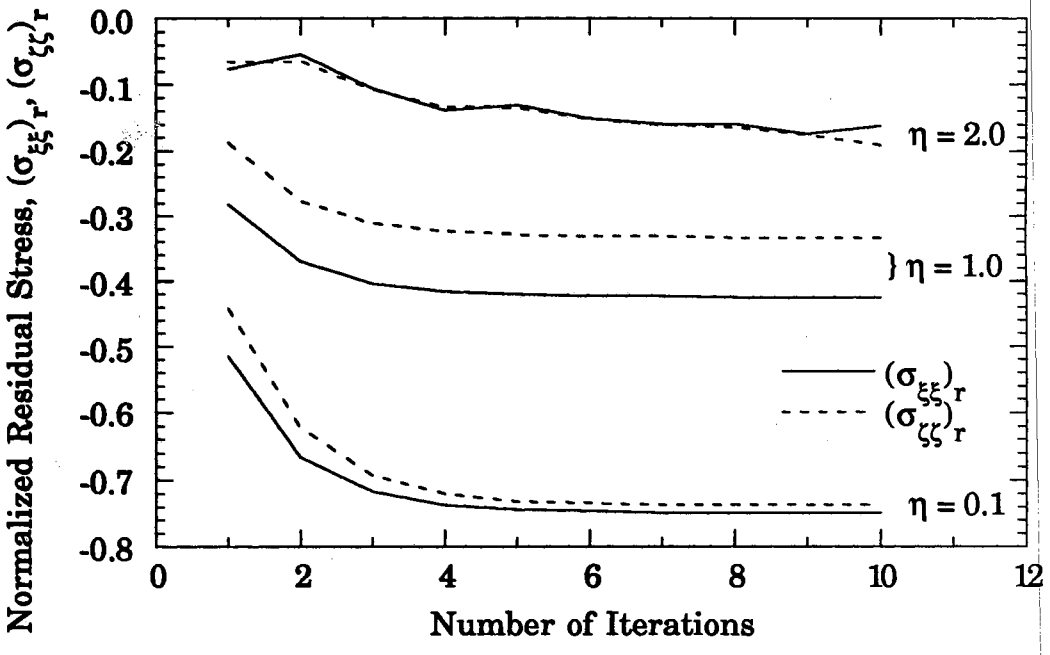

Figure 6-29. Normalized Residual Stresses by the Yield Strength vs. Number of Iterations for Loading Conditions of Microcutting of Te-Cu at 0.01 μm Depth of Cut

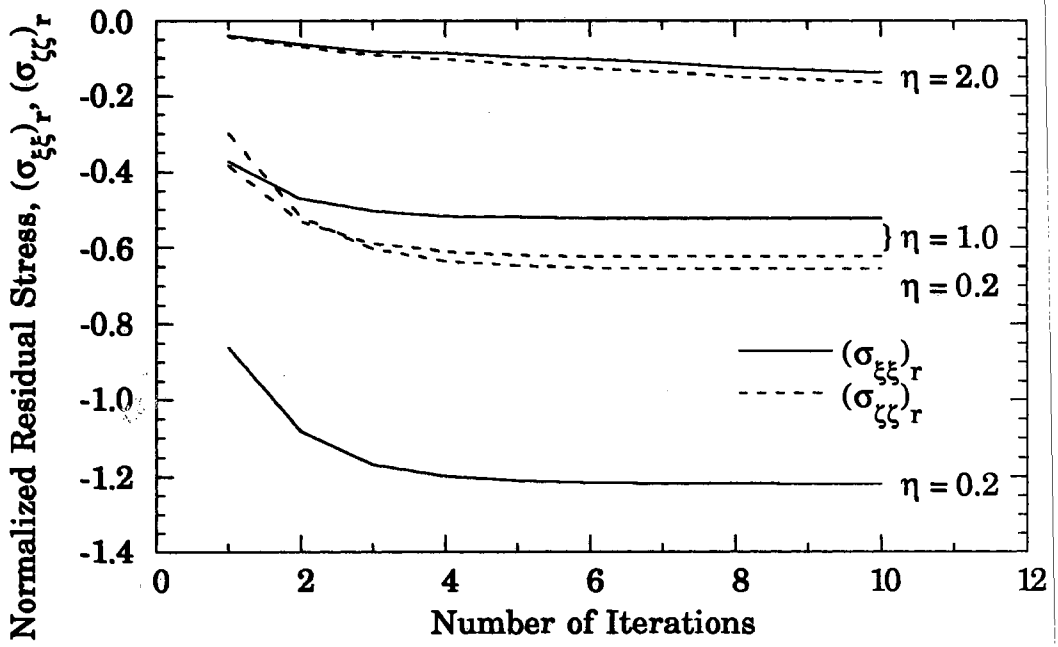

Figure 6-30. Normalized Residual Stresses by the Yield Strength vs. Number of Iterations for Loading Conditions of Microcutting of Te-Cu at 0.1 μm Depth of Cut

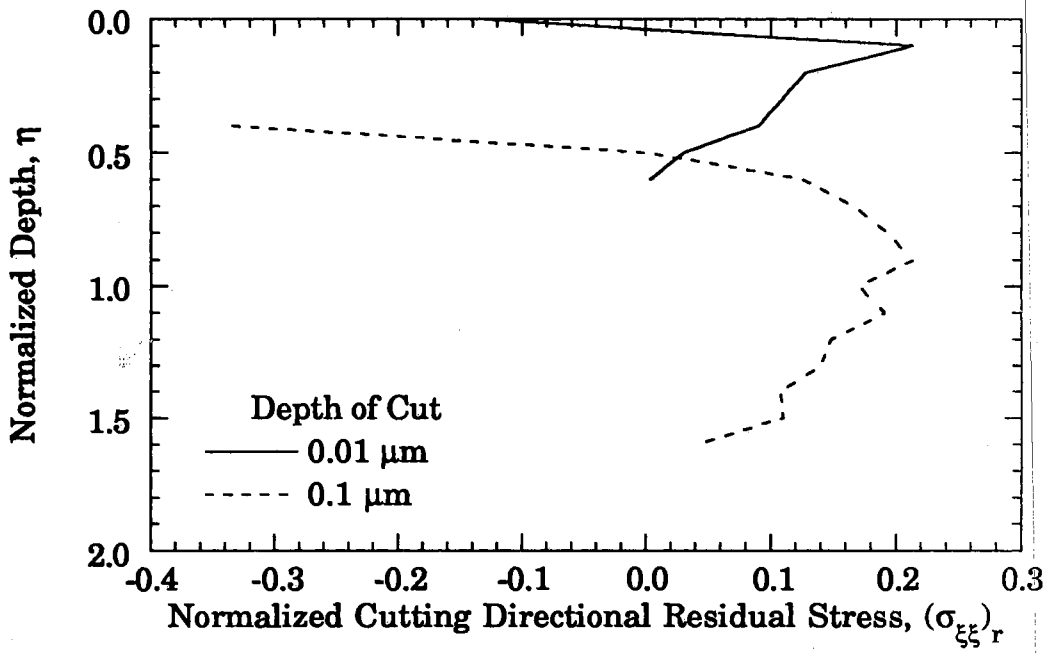

Figure 6-31. Normalized Cutting Directional Residual Stresses of Al 6061-T6 Predicted using Loading Conditions of Micromachining at 0.01 and 0.1 μm depths of cut

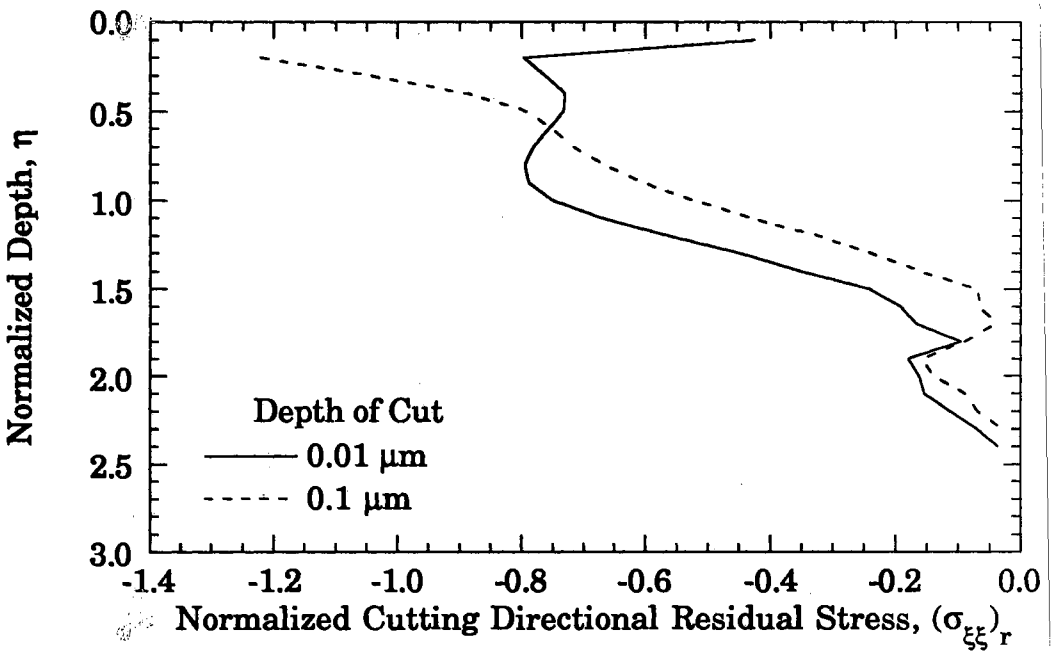

Figure 6-32. Normalized Cutting Directional Residual Stresses of Te-Cu Predicted using Loading Conditions of Micromachining at 0.01 and 0.1 μm depths of cut

strength at 0.01 μm depth of cut and 33 % at 0.1 μm depth of cut, and 80 % ~ 125 % for Te-Cu at those depths of cut are predicted. This corresponds to residual stresses of 50 to 120 MPa for Al 6061-T6, and 95 to 250 MPa for Te-Cu.

For 6061-T6 aluminum, using a dull high speed steel tool having an edge radius of 64 μm, Strenkowski et al. [1990] predicted compressive residual stresses of about 100 MPa at 0.127 mm depth of cut for a cutting speed of 0.1 m/sec. This predicted value was in good agreement with their experimental value obtained by using a deflection etching technique. Sugano et al. [1987] obtained residual stresses of about 60 MPa for the diamond turning of an aluminum alloy using an X-ray diffraction technique. The predicted residual stresses for the present study are consistent in magnitude with those above.

6.3.3.3 Comparison with the Result of ABAQUS. For a comparison of the elastic and elastoplastic mechanical stress fields predicted by the analytical/numerical technique developed for the present study, the stress field resulting from the same slider problem was estimated using the finite element code ABAQUS. The code was not programmed for sliding speed, hence the resulting stress fields are static, elastoplastic stress fields. However, as discussed earlier, the speed effect on the stress field is negligible in the range considered. As a mesh model, 14 x 35 elements were taken, in which an 8 node bilinear plane strain element (CPE4) was employed. The mesh model used for the program is shown in Fig. 6-33. As boundary conditions, the left and right hand side nodes (ξ = -4, and 3) were fixed in the ξ direction and nodes along the bottom of the mesh (η = 0) were fixed in the η direction. The measured cutting and thrust force

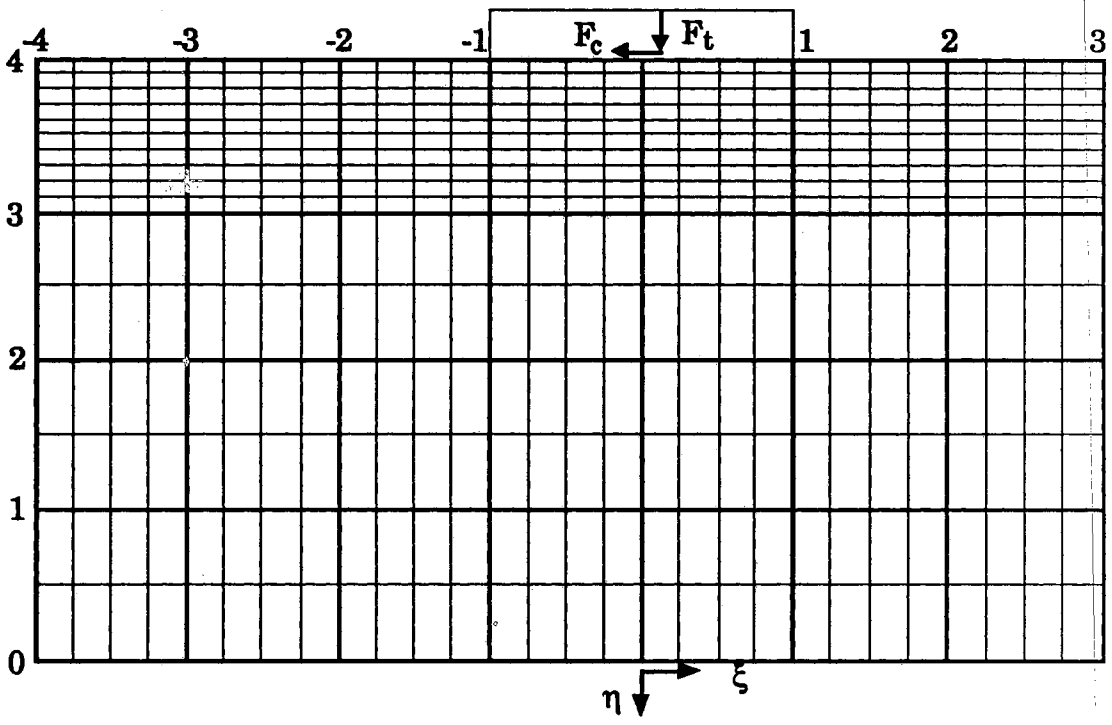

Figure 6-33. Mesh Model for ABAQUS to Predict the Stress Fields of a Body Representing the Orthogonal Flycutting at Submicrometer Depths of cut

components for Al 6061-T6 were divided into the number of the nodes in contact, and applied as concentrated loads in both the normal and tangential directions at the contact surface ($-1 \leq \xi \leq +1$ at $\eta = 4$). The resulting stress fields for 0.01 and 0.1 μm depths of cut are shown in Figs. 6-34 and 6-35. Similar elastoplastic stress fields to those obtained from the slider model can be seen. For a comparison of elastic-plastic boundary layer thicknesses estimated from the elastic model, elastoplastic model and ABAQUS, the boundary contours are shown in Fig. 6-36 for loading conditions of cutting 0.01 and 0.1 μm depths of cut. The maximum plastically deformed layer thicknesses shown in Fig 6-36, obtained from the elastodynamic solution using the Fourier integral transform (A), the elastoplastic slider model (B) and those from ABAQUS (C) are summarized in Table 6-3. The elastic-plastic boundary thicknesses predicted using the elastic model are 0.78 ~ 1.20 and elastoplastic slider model are 1.08 ~ 1.15 times those predicted by the ABAQUS for the loading conditions of machining aluminum at 0.01 and 0.1 μm depths of cut. This implies that the elastic-plastic boundary thicknesses predicted by the elastic model are within ± 20 % and the elastoplastic slider model are slightly larger (8 ~ 15 %) than those predicted by ABAQUS.

For diamond turning of an aluminum alloy, Sugano et al. [1987] observed that the "work-affected" layer is on the order of submicrometers using X-ray diffraction analysis. The predicted plastically deformed layer thicknesses of 0.31 and 0.81 μm for 0.01 and 0.1 μm depth of cut from the elastoplastic slider model seem to be in good agreement with this experimental observation. In a broader sense, this model should be applicable not only for submicrometer cutting conditions but also for general sliding indentation problems.

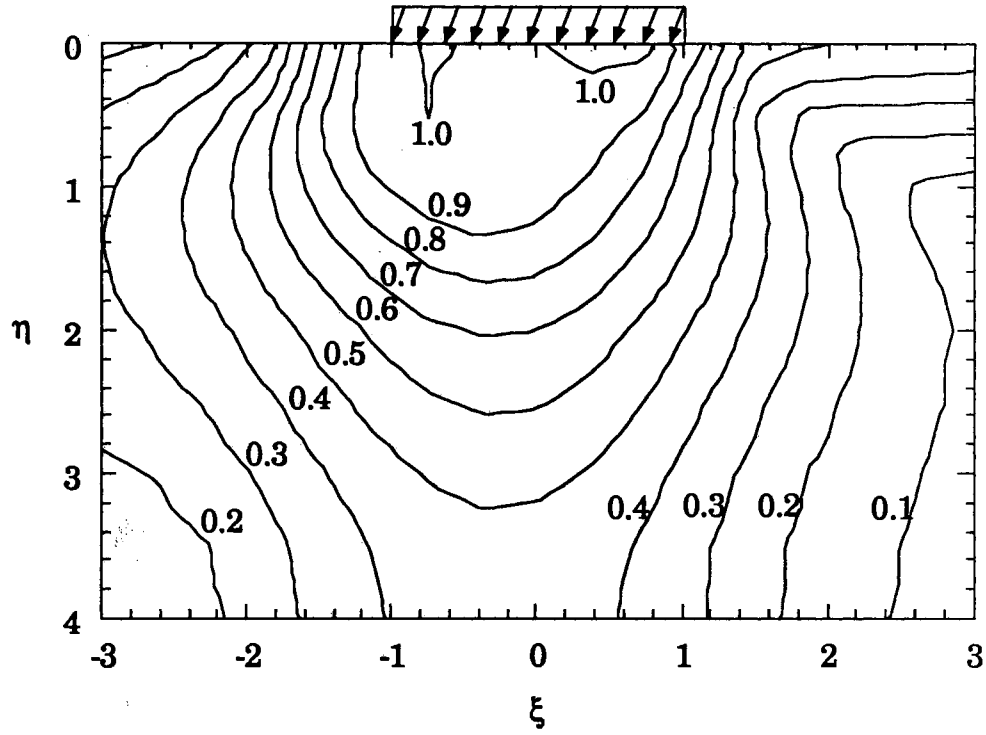

Figure 6-34. Contours of the Normalized von Mises Equivalent Elastoplastic Stress with Respect to the Yield Strength of the Body as Estimated Using ABAQUS for Loading Conditions Representing the Orthogonal Flycutting of Al 6061-T6 at Depth of Cut of 0.01 μm

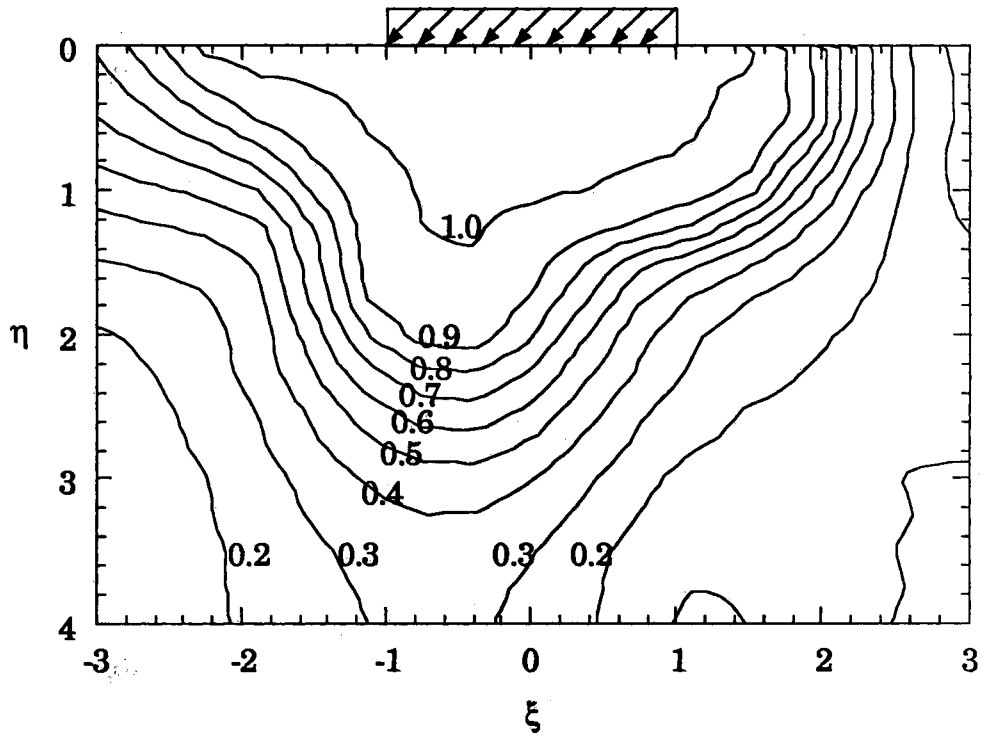

Figure 6-35. Contours of the Normalized von Mises Equivalent Elastoplastic Stress with Respect to the Yield Strength of the Body as Estimated Using ABAQUS for Loading Conditions Representing the Orthogonal Flycutting of Al 6061-T6 at Depth of Cut of 0.1 μm

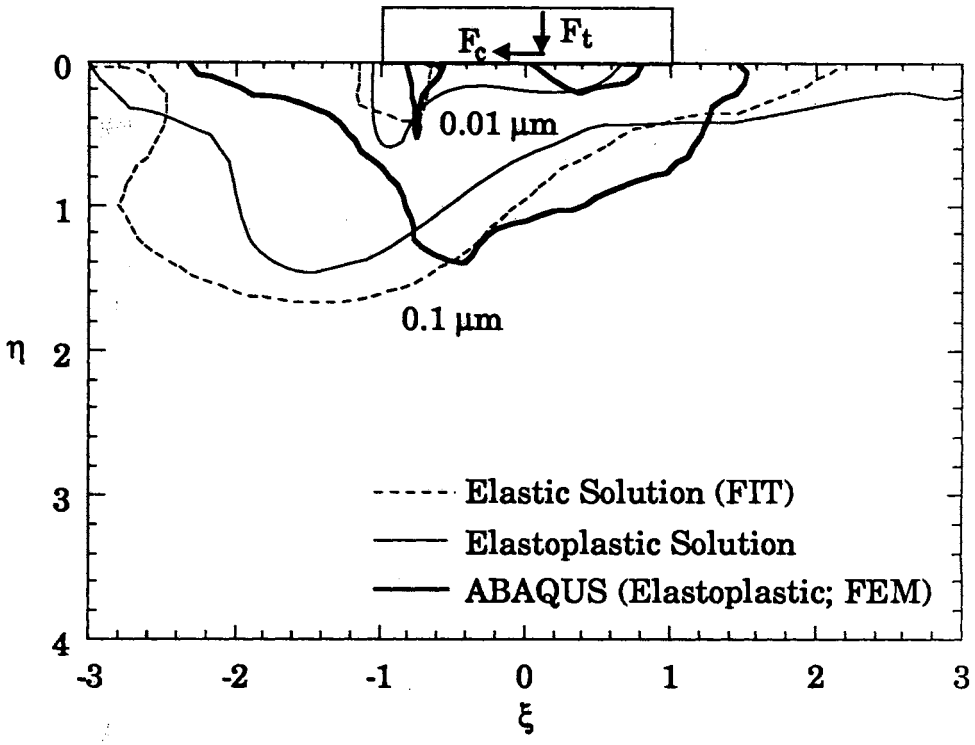

Figure 6-36. Comparison of Elastic-Plastic Boundaries Estimated Using Elastic, Elastoplastic and ABAQUS for Loading Conditions Representing the Orthogonal Flycutting of Al 6061-T6 at Depths of Cut of 0.01 and 0.1 μm

TABLE 6-3

COMPARISON OF THE PREDICTED THICKNESSES OF ELASTIC-PLASTIC BOUNDARIES USING VARIOUS SOLUTIONS FOR THE LOADING CONDITIONS REPRESENTING THE ORTHOGONAL FLYCUTTING OF AL 6061-T6

Depth of Cut (μm)	Elastic (A)	Elastoplastic (B)	ABAQUS (C)	A/C	B/C
0.01	0.21	0.31	0.27	0.78	1.15
0.1	0.90	0.81	0.75	1.20	1.08

For an extended study of the plastically deformed layer, microhardness tests using a nanoindenter can be undertaken. This technique is known to represent a formidable task due to the extremely small spot size and corresponding micromechanical behavior of materials and interaction between the material and indenter.

6.4 Conclusions

Based on the observations of a severe rotation of resultant force vector downward and characteristic length scale of contact length at the tool-workpiece interface at submicrometer depths of cut in orthogonal flycutting of Al 6061-T6 and Te-Cu, the process was found to transition from a chip formation-dominant to plowing and sliding-dominant process. In order to understand some aspects of the process at submicrometer depths of cut, predictions of the stress and temperature fields of the workpiece have been made for the idealized geometry resulting from a sliding indentation problem.

An elastostatic stress field using an Airy's stress function and elastodynamic stress field using a Fourier integral transform technique were studied for the elastic-plastic boundaries at the subsurface of the workpiece. The elastodynamic stress field was then extended for the elastoplastic case using the Prandtl-Reuss equation solved by a Runge-Kutta method. The energy partition and corresponding temperature field at the interface were predicted. Using the measured force components and contact lengths as input data, the stress fields and elastic-plastic boundaries in the workpiece, energy partition and temperature rise at the interface were estimated. Comparison was made between the results of

the developed models and those which result from the use of the FEM code ABAQUS. Through the analytical/numerical formulation and analysis of the elastic, elastoplastic and temperature model, the following observations can be made:

6.4.1 Stress Fields

- The contours of the equivalent iso-stress fields are circular shaped, however near the contact, they deviate from a circular arc.
- As the direction of resultant force vector decreases, i.e., as depth of cut increases, the contours of equivalent stress become non-symmetric and skewed toward the leading edge, consistent with the direction of the applied resultant force vector.
- The first yielding occurs near the leading edge of the contact.
- For Te-Cu, in which the applied forces were obtained from a worn tool, the stress fields at loading conditions of submicrometer depths of cut were almost identical, due to almost the identical force components.
- For about two orders of magnitude increase in sliding speed, no discernible change in the stress fields and elastic-plastic boundary were seen. Hence, the stress field is not affected by the sliding speed in this range.
- Compressive residual stresses of 50 to 120 MPa for Al 6061-T6 and 95 to 250 MPa for Te-Cu were estimated for the loading conditions of 0.01 and 0.1 μm depths of cut.

- The estimated residual stress of 6061-T6 aluminum seems to be in reasonably good agreement with the result of 60 ~ 100 MPa reported in the literature.

6.4.2 Comparison of Stress Fields

- The elastic-plastic boundary thicknesses predicted by the elastic model were within ± 20 % and the elastoplastic slider model was slightly larger by 8 ~ 15 % than those predicted by ABAQUS for the loading conditions of machining 6061-T6 aluminum at 0.01 and 0.1 μm depths of cut.
- The predicted plastically deformed layer thicknesses of 0.31 and 0.81 μm for 0.01 and 0.1 μm depth of cut for Al 6061-T6 were in good agreement with the experimental results taken from the literature.

6.4.3 Energy Partitions and Temperatures at the Contact

- From a heat transfer point of view, the ultra-precision machining at submicrometer depths of cut is essentially a stationary problem since Peclet number is negligibly small.
- The majority of heat generated at the contact (90.6 and 85.3 % for aluminum and copper) was seen to enter the tool due to diamond's superior thermal properties.
- As the sliding speed increases, less energy flows into the diamond at the leading edge ($\xi = -1$) as compared to the trailing edge ($\xi = 1$).

- The maximum temperature rises were 0.12 °C for aluminum and 0.10 °C for Te-Cu at 1 μm depth of cut and at cutting speed of 7.6 m/min, and were consistent with measured results reported in the literature.

The developed elastic and elastoplastic models should be applicable for estimating the stress and temperature fields of a body under sliding conditions in general.

CHAPTER VII

SUMMARY AND RECOMMENDATIONS

7.1 Summary

7.1.1 Motivation of the Research

Ultra-precision diamond turning is currently being used for machining parts producing submicrometer form accuracies and nanometer scale surface roughnesses. In order to improve the machining performance and surface quality in ultra-precision machining, sufficient understanding of the process mechanics is essential. The classical theory of metal cutting needed to be re-examined at decreased depths of cut since the characteristic length scale is several orders of magnitudes smaller in ultra-precision machining. At the transitioning depth of cut range from conventional to ultra-precision machining, the uniqueness and change of the process mechanics is in need of study. In this work, both experimental and analytical investigations have been made to contribute to our understanding some of the process physics in ultra-precision machining of ductile materials.

7.1.2 Research Fields

The mechanics which govern the classical theory of metal cutting have been re-examined at decreased depths of cut down to the order of tool

edge radius. Both experimental and analytical studies for the process at submicrometer depths of cut have been performed. The following have been studied:

- diamond tool edge characterization using scanning electron microscopy (SEM) and/or atomic force microscopy (AFM),
- accurate measurement of the nonlinear behavior of the force components with depth of cut from 20 μm to 10 nm at 7.6 m/min using Al 6061-T6 and Te-Cu,
- effect of the tool edge contour (profile) on measured 2D force components and energies,
- effect of increased cutting speed from 7.6 m/min to 76.2 m/min on the resulting force components and specific energies,
- study of plowing and sliding at submicrometer depths of cut relative to the chip formation process,
- study of the role of tool flank contact and measurements of the contact lengths at the tool-workpiece interface, and
- prediction of the elastoplastic stress fields and temperatures in the workpiece at submicrometer depths of cut using a simplified analytical model.

7.1.3 Initial Experimental Results Using Al 6061-T6

An orthogonal flycutting geometry, where tool is rotating and workpiece is stationary has been employed for all of the experimental study. Tools having edge radii of 0.2 μm (as characterized by the SEM) were used to investigate their effect on the cutting forces, thrust forces and specific energies. Cutting was performed at 7.6 m/min without cutting

fluid at depths of cut from 20 μm to 10 nm. From the initial microcutting of Al 6061-T6, the following observations were made:

- the orthogonal flycutting geometry produced very repeatable cutting forces from 20μm to 10 nm depths of cut,
- at submicrometer depths of cut, thrust force was dominant over cutting force. The force behavior with depth of cut is seen to be nonlinear with a cross-over of the cutting force and thrust force. The size effect was observed and the overall trend was seen to be the same as that reported in the literature,
- a significant rotation of the direction of the resultant force vector downward toward the workpiece as depth of cut decreases was observed,
- a tool-workpiece contact length of the order of about 1 μm was measured using a AuPd coating technique at 0.01, 0.1 and 1.0 μm depths of cut and was the characteristic length scale at submicrometer depths of cut,
- the process was seen to transition from a chip formation-dominant to plowing/sliding-dominant process (sliding indentation) at submicrometer depths of cut, and
- the effect of tool edge radius was found to be significant on the resulting force components at decreased depth of cut.

The significance of the tool edge effect on the energy dissipation and the change of the process mechanics at submicrometer depth of cut suggested a need for further systematic experimental study with a variety of tool geometries and a more reliable 3D tool characterization technique.

7.1.4 Further Experimental Results Using Te-Cu

Using the identical cutting geometry used for Al 6061-T6, machining on Te-Cu was performed. For these experiments, various nominal rake angle tools (0°, -10°, -20°, -30°) were characterized using the AFM and used to study the tool edge profile effect. The effects of cutting distance (up to 3 km), tool condition (new tool and considerably worn tool), and cutting speed (one order of magnitude difference) on the resulting forces and energies were studied. Cutting was performed at 7.6 m/min using a light mineral oil as a cutting fluid at depths of cut from 20 μm to 10 nm. Through the experimental study of Te-Cu, the following observations were made:

7.1.4.1 Tool Edge Characterization.

- using the AFM, a total of seven tools were characterized in 3D with a form accuracy of ± 10 nm,
- the edge profiles of new commercial tools were circular shaped and were estimated to have 0.25 ± 0.02 μm edge radii, consistent with the results of SEM examination, and
- worn tools were double radii shaped with greater wear at the flank face, and this contour was consistent with the results reported in the literature.

7.1.4.2 Results of Orthogonal Ultra-Precision Flycutting of Te-Cu.

- the reproducibility of the measured forces was about ± 5 % from specimen to specimen. The overall trends of cutting and thrust

forces, force ratio, and total specific energy followed the results of Al 6061-T6 and the literature, and

- the nonlinearity of force components, severe rotation of the resultant force vector, and dramatic increase in total specific energy as depth of cut decreases were found to be the unique characteristics of the force behavior in ultra-precision machining.

7.1.4.3 Tool Edge Geometry Effects on Energy Dissipation

7.1.4.3.1 Nominal Rake Angle

- as nominal rake angle decreased from 0 to -30 degrees, force components, force ratio, and total specific energy were found to increase over the entire range of depths of cut,
- the thrust force curve for 0° rake angle tool exhibits a plateau in the depth of cut range of 0.2 ~ 1.0 μm. This phenomenon was found to be typical for all new tools used, and
- when the depth of cut is large relative to the tool edge radius, the resulting forces and energies are governed by the nominal rake angle.

7.1.4.3.2 Cutting Distance

- at the early stages of a tool's life (less than 3 km in cutting distance), the increase of forces and resulting energy was significant at submicrometer depths of cut.

7.1.4.3.3 Worn Tool

- at submicrometer depths of cut, cutting forces, especially the thrust force are significantly affected by the contour of the flank face, and
- at large depths of cut above several micrometers where tool edge effect is not significant, no discernible differences between the forces from new and worn tools were observed for the same overall geometry.

7.1.4.3.4 Effective Rake Angle

- as depth of cut approaches the size of the edge radius, effective rake angle appears to determine the resulting forces and energies, and
- both the nominal and effective rake angle effects on force ratio were found to be the same. As negative effective or nominal rake angle increases, force ratio also increases.

7.1.4.3.5 Speed Effect

- for increased cutting speed from 7.6 to 76.2 m/min, no discernible changes in the resulting forces were observed.

7.1.4.3.6 Plowing/Sliding

- as depth of cut decreases, the direction of resultant force vector increases, levels off and approaches a constant value,
- assuming the depths of cut below which thrust force is greater than cutting force as plowing/sliding dominant depths of cut, a

range of effective rake angle of -35° ~ -55° is obtained for the corresponding depths of cut below which plowing/sliding may be significant, and

- minimum machinable depths of cut were estimated using a critical rake angle of -75° based on the literature. The depths were about 10 nm and 40 nm for the new and worn tools used in the present study.

7.1.5 Analytical Results

The ultra-precision machining process in the submicrometer depth of cut has been idealized as a sliding indentation problem. This was based on the experimental observations of severe rotation of resultant force vector and dominant length scale of the tool-workpiece contact. The model allowed for a prediction of the stress and temperature fields in the workpiece material.

An elastostatic model using an Airy's stress function, and an elastodynamic model using a Fourier integral transform technique for a loaded slider on a semi-infinite moving non-insulated body due to planer surface pressure have been formulated. Extension from the elastodynamic stress solution to elastoplastic stress solution was made by employing the Prandtl-Reuss equation and Runge-Kutta method. For comparison, the same sliding conditions have been modeled with the commercial code ABAQUS. Heat partition at the interface and corresponding temperature rises at both the stationary and moving bodies have been predicted also. Through the analysis of the elastic, elastoplastic

and temperature fields using the slider models, the following observations were made:

7.1.5.1 Stress Fields

- contours of the equivalent iso-stress lines are circular shaped, and near the contact, the contours deviate from a circular arc,
- as the direction of resultant force vector decreases, i.e., as depth of cut increases, the contours of equivalent stress become non-symmetric and skewed toward the leading edge, consistent with the direction of the applied resultant force vector,
- for about two orders of magnitude increase in sliding speed, no discernible changes in the stress fields and elastic-plastic boundaries were seen. Hence, the stress fields were not affected by the sliding speed over this range,
- compressive residual stresses of 50 to 120 MPa for Al 6061-T6 and 95 to 250 MPa for Te-Cu were calculated for loading conditions of 0.01 and 0.1 μm depths of cut, and
- the estimated residual stress of 6061-T6 aluminum is in reasonably good agreement with the result of 60 ~ 100 MPa obtained from the literature.

7.1.5.2 Comparison of Stress Fields

- the elastic-plastic boundary thicknesses predicted by the elastic model were within ± 20 % and those predicted by the elastoplastic slider model were slightly larger (8 ~ 15 %) than those predicted

by ABAQUS for the loading conditions of microcutting of 6061-T6 aluminum at 0.01 and 0.1 μm depths of cut, and

- the predicted plastically deformed layer thicknesses of 0.31 and 0.81 μm from the elastoplastic slider model for 0.01 and 0.1 μm depth of cut were in good agreement with experimental results reported in the literature.

7.1.5.3 Energy Partition and Temperature at the Contact

- the majority of heat generated at the contact (90.6 and 85.3 % for aluminum and copper) is seen to enter the tool due to diamond's superior thermal properties,
- as sliding speed increases, less energy flows into the diamond at the leading edge ($\xi = -1$) as compared to the trailing edge ($\xi = 1$), and
- the maximum temperature increases are 0.12 °C for aluminum and 0.10 °C for Te-Cu at a 1 μm depth of cut and at cutting speed of 7.6 m/min. These are consistent with measured results taken from the literature.

The developed slider model should be good for calculating the stress and temperature fields of a body under general sliding conditions.

7.2 Recommendations

For further study of the current research on energy dissipation of ultra-precision machining, the following recommendations are put forth.

For the present study, straight edge tools were used for all the experimental investigations, additionally the effects of round nosed tool on

energy dissipations at various cutting conditions can be studied as a parallel effort.

Even though reasonable contact lengths were measured using the AuPd coating technique, for improvement of the accuracy, other more reliable techniques may need to be developed. Also, dynamic effects (such as bouncing) can be investigated further at increased cutting speeds.

The minimum machinable depth of cut obtained was based on the experimental result of force components. This minimum depth would be a function of tool geometries, cutting conditions and the properties of workpiece materials (such as rigidity and/or strength). The effect of these factors on the minimum machinable depth of cut can be investigated further.

For the analytical elastoplastic modeling, elastic-perfectly plastic material behavior was assumed. Elastic-strain hardening behavior can be considered for the estimation of the strain fields. Also, expansion from an isotropic material to include anisotropic behavior can be considered for calculating the stress fields of anisotropic single crystal materials.

Measurement of the interfacial temperatures at the tool-workpiece contact can verify the accuracy of the predicted temperatures. However, this is known to be a formidable task due to the small spot size and extremely low level of energy.

The experimental measurement of the stress fields and residual stresses at the subsurface of the machined surface would verify the accuracy of the developed elastic and elastoplastic model. For the experiments, a nanoindenter may be used, however, the micromechanics involved with the indenter and specimen would be a problem together with the oxidation of the machined surface of the specimen.

CHAPTER VIII

CONCLUSION

8.1 Goal of the Study

The goal of the present study was to contribute to our understanding of the process physics in ultra-precision machining. In the range of depths of cut from tens of micrometers to tens of nanometers, the process was seen to transition from conventional machining to ultra-precision precision machining where the process mechanics changes from a chip formation-dominant to plowing and sliding-dominant process. This change is seen to be closely related to the combination of diamond tool edge geometry (edge radius or profile) and workpiece material. To understand the process mechanics better, both experimental and analytical approaches were undertaken. Experiments included the investigation of the effect of energy dissipation due to change of tool edge contours, cutting speed and workpiece materials. Analytical models were developed to investigate the stress and temperature fields of the workpiece. The analytical models were based on the experimental observation of a severe rotation of the measured force vector and characteristic length scale change at reduced depths of cut.

Due to the extremely small dimensions (the range of depth of cut was from 10 nm to 20 μm, the edge radius of commercially available diamond tools was on the order of one half the wavelength of a visible light of about

0.5 μm), and extremely low level of cutting forces (0.1 N for cutting 1 mm wide aluminum specimen at 10 nm depth of cut) encountered in ultra-precision machining, the experimental design and performance were critical. Construction of the experimental set-up, handling of the diamond tool, clamping of the force transducer, even environmental factors such as temperature changes and vibration were also very important. Furthermore, results of the literature (measured force components, stress, and temperature in ultra-precision machining) were nearly non-existent. As a strategy to achieve the goal of the present study, consistency (such as the result of SEM and AFM) and repeatability (specimen to specimen) of the experimental results were examined throughout the study. The results of the developed analytical models were also compared with those of commercially available FEM code ABAQUS.

8.2 Achievements of the Study

Through the experimental and analytical study on energy dissipation in orthogonal ultra-precision machining of ductile materials, the followings were achieved:

- experimental technique to measure accurate force components in orthogonal flycutting,
- a AuPd coating technique for the measurement of tool-workpiece contact length at submicrometer depths of cut,
- technique to identify tool edge radius or tool edge profile (contour) using scanning electron microscopy and/or atomic force microscopy,

- some fundamental cutting force data which is related to the measured edge profile of the tool,
- simplified analytical model to predict stress and temperature fields of the workpiece, residual stress of the workpiece, and energy partition at the tool-workpiece contact, and
- corresponding stress fields, process temperature, energy partition, and residual stresses representing the loading conditions of the ultra-precision machining of Al 6061-T6 and Te-Cu.

From the experimental study, it was observed that the energy dissipation in submicrometer depths of cut is significantly affected by the tool edge profile. The process mechanics transitions from a chip formation-dominant process to a plowing and sliding-dominant process. This transition depth of cut is closely related to the tool edge profile.

The analytical results showed the relative increasing importance of the plastically deformed thickness as depth of cut decreases. For an estimate of the plastically deformed thickness, an elastic model can be used in addition to an elastoplastic model within relatively small error for the ductile material workpieces. For further study of the stress fields of the workpiece, though formidable, microhardness (or nanoindenter) tests were suggested.

REFERENCES

1. Abdel Moneim, M. E. (1980), "Comments on 'Transition from Plowing to Cutting During Machining with Blunt Tools'", Wear, Vol. 64, pp. 385-388.

2. Albrecht, P. (1960), "New Developments in the Theory of Metal-Cutting Process, Part I. The Ploughing Process in Metal Cutting", Trans. ASME, J. Eng. Ind., Vol. November, pp. 348-358.

3. Albrecht, P. (1963), "Mechanics of the Cutting Process", Int. Prod. Eng. Res. Conf., Pittsburgh, Pennsylvania, ASME, pp. 32-41.

4. Altan, T., and Boulger, F. W. (1973), "Flow Stress of Metals and Its Application in Metal Forming Analyses", Trans. ASME, J. Eng. Ind., Vol. 95, pp. 1009-1019.

5. Armarego, E. J. A., and Brown, R. H. (1961), "On the Size Effect in Metal Cutting", Int. J. Prod. Res., Vol. Oct., pp. 75-99.

6. Arnold, J. B., Steger, P. J., and Morris, T. O. (1975), "Machinability Aspects of Diamond-Turned Metal Optics", Metal Optics, San Diego, California, The Int. Soc. Opt. Eng., Vol. 65, pp. 108-117.

7. Asai, S., Taguchi, Y., Horio, K. et al. (1990), "Measuring the Very Small Cutting-Edge Radius for a Diamond Tool Using a New Kind of SEM Having Two Detectors", Annals of the CIRP, Vol. 39, No. 1, pp. 85-88.

8. Atkin, R. B. (1986), "Diamond/Aluminum Interactions that Affect Tool Performance", Ultraprecision Machining and Automated Fabrication of Optics, SPIE, Vol. 676, pp. 127.

9. Backer, W. R., Marshall, E. R., and Shaw, M. C. (1952), "The Size Effect in Metal Cutting", Trans. ASME, pp. 61-72.

10. Binnig, G., Quate, C. F., and Gerber, C. (1986), "Atomic Force Microscope", Phys. Rev. Lett., Vol. 56, No. 9, pp. 930-933.

11. Blake, P. N., and Scattergood, R. O. (1987), "Single-Point Diamond Turning of Silicon and Germanium", Presented at the 2nd Annual ASPE Conf., Columbus, OH, Abstract.

12. Blake, P. N., and Scattergood, R. O. (1988), "Ductile Regime Turning of Germanium and Silicon", Intersociety Symposium of Advanced Ceramic Materials and Components, The Winter Annual Meeting of ASME, Chicago, Illinois, pp. 249-265.

13. Blok, H. (1937), "Theoretical Study of Temperature Rise at Surface of Actual Contact under Oiliness Lubricating Conditions", Proceedings of the General Discussion on Lubrication & Lubricants, pp. 222-235.

14. Brown, N. J., Donaldson, R. R., and Thompson, D. C. (1983), "Fabrication of Machined Optics for Precision Applications", Symposium on Optical Surface Technology, West Germany, The Int. Soc. Opt. Eng., Vol. 381, pp. 48-62.

15. Burnham, M. W. (1976), "The mechanics of Micromachining", SPIE, Advances in Precision Machining of Optics, Vol. 93.

16. Caithness, W. (1975), "Some Fundamentals of Metal Mirrors", Metal Optics, San Diego, California, The Int. Soc. Opt. Eng., Vol. 65, pp. 8-11.

17. Carslaw, H. S., and Jaeger, J. C. (1959), "Conduction of Heat in Solids", Clarendon Press, Oxford.

18. Chapman, G. F. (1988), "Recent Developments in the Generation of Glass Aspherical Surfaces", SPIE, Micromachining Optical Components and Precision Engineering, Hamburg, Germany, Vol. 1015, pp. 36-44.

19. Chen, T. Y., and Ju, F. D. (1988), "Thermomechanical Cracking in the Vicinity of a Near-Surface Void Due to High-Speed Friction Load", Trans. ASME, J. of Tribology, Vol. 110, pp. 306-312.

20. Delingat, E. W. (1983), "The Production of Optical Surfaces, Survey of Present Techniques and Preview on New Developments", Symposium on Optical Surface Technology, West Germany, The Int. Soc. Opt. Eng., Vol. 381, pp. 2-8.

21. Donaldson, R. R. (1983), "Design and Construction of a Large Vertical Axis Diamond Turning Machine", SPIE, Vol. 433, pp. 62-67.

22. Donaldson, R. R., Vandervoort, R. R., Mara, G. L., and Landingham, R. L. (1985), "Chip Science: Research on Single-Point Machining", Fabrication Technology, pp. 19-29.

23. Donaldson, R. R., Syn, C. K., Taylor, J. S., and Riddle, R. A. (1986a), "Chip Science: Basic Study of the Single-Point Cutting Process", Fabrication Technology, pp. 39-48.

24. Donaldson, R. R., Syn, C. K., Taylor, J. S., and Riddle, R. A. (1986b), "Chip Science: Basic Study of the Single-Point Cutting Process", Fabrication Technology, pp. 35-51.

25. Donaldson, R. R. (1992), "Scanning Tunneling and Atomic Force Microscopes", NEWSLINE, Mar. 6, reported by Bashor, J. Univ. of Calif. Lawrence Livermore Nat. Lab., Vol. 17, No. 16.

26. Doyle, E. D., and Dean, S. K. (1980), "An Insight into Grinding from a Material Viewpoint", Annals of the CIRP, Vol. 29, No. 2, pp. 571-575.

27. Dugdale, D. S., and Enahoro, H. E. (1964), "Energy Absorbed in Metal Cutting", Int. J. Mach. Tool Des. Res., Vol. 3, pp. 219-225.

28. Eringen, A. C., and Suhubi, E. S. (1975), "Elastodynamics Volume II Linear Theory", Academic Press, New York.

29. Eugene, F. (1963), "The Influence of the Structural State of Steels upon Machinability and Some Observations on the Physics of Chip Formation", Int. J. Mach. Tool Des. Res., Vol. 3, No. 1, pp. 13-24.

30. Francis, H. A. (1970), "Interfacial Temperature Distribution Within a Sliding Hertzian Contact", ASLE Trans., Vol. 14, pp. 41-54.

31. Franks, A. (1988), "Nanotechnology at the National Physical Laboratory and the UK National Initiative on Nanotechnology", ASPE 3rd Annual Precision Engineering Conf., Atlanta, Ga, pp. 20-21.

32. Furukawa, Y. (1986), "Development of Ultra Precision Machine Tools made of Ceramics", Annals of the CIRP, Vol. 35, No. 1, pp. 279-282.

33. Furukawa, Y., and Moronuki, N. (1988), "Effect of Material Properties on Ultra Precise Cutting Processes", Annals of the CIRP, Vol. 37, No. 1, pp. 113-116.

34. Gerchman, M. C., and McLain, B. E. (1988), "An Investigation of the Effects of Diamond Machining on Germanium for Optical Application", Infrared Optical Materials VI, Orlando, Florida, The Int. Soc. Opt. Eng., Vol. 929, pp. 94-98.

35. Hamilton, G. M. (1963), "Plastic Flow in Rollers Loaded above the Yield Point", Proc. Instn. Mech. Engrs., Vol. 177, No. 25, pp. 667-675.

36. Hastings, W. F., and Oxley, P. L. B. (1974), "Predicting a Material's Machining Characteristics Using Flow Stress Properties Obtained from High-Speed Compression Tests", Proc. Instn. Mech. Engrs., Vol. 188, No. 22/74, pp. 245-252, D47-D49.

37. Heynacher, E. (1983), "Production and Testing of Aspheric Surfaces, State of the Art in the Federal Republic of Germany", Symposium on Optical Surface Technology, West Germany, The Int. Soc. Opt. Eng., Vol. 381, pp. 39-45.

38. Huang, J. H., and Ju, F. D. (1985), "Thermomechanical Cracking Due to Moving Friction Loads", Wear, Vol. 102, pp. 81-104.

39. Hurt, H. H., and Decker, D. L. (1984), "Tribological considerations of the Diamond Single-Point Tool", SPIE, Production Aspects of Single Point Machined Optics, Vol. 508, pp. 126-131.

40. Hurt, H. H., and Showman, G. A. (1986), "Wear Test of a Preselected Diamond Tool", Ultraprecision Machining and Automated Fabrication of Optics, SPIE, Vol. 676, pp. 116-126.

41. Iizuka, K. (1988), "A Brief Description of the Activities in the Yoshida Nano-mechanism Project", ASPE 3rd Annual Precision Engineering Conf., Atlanta, Ga, ASPE, pp. 16-19.

42. Ikawa, N., and Shimada, S. (1977), "Cutting Tool for Ultraprecision Machining", Proc. of the 3rd Int. Conf. on Production. Engineering, Tokyo, Tokyo, Japan, pp. 357-364.

43. Inamura, T., and Takezawa, N. (1992), "Atomic-Scale Cutting in a Computer Using Crystal Models of Copper and Diamond", Annals of the CIRP, Vol. 41, No. 1, pp. 121-124.

44. Iwata, K., Moriwaki, T., and Okuda, K. (1984), "Ultra-High Precision Diamond Cutting of Copper", Memoirs of the Faculty of Engineering Kobe University, Vol. 31, pp. 93-102.

45. Iwata, K., Moriwaki, T., and Okuda, K. (1986), "Precision Machining of Stainless Steel", Mem. Grad. School Sci. & Technol. Kobe Univ., Vol. 4-A, pp. 31-38.

46. Iwata, K., Moriwaki, T., and Okuda, K. (1987a), "Precision Machining of Stainless Steel with CBN Tool", Bull. Japan Soc. of Prec. Engg., Vol. 21, No. 2, pp. 134-135.

47. Iwata, K., Moriwaki, T., and Okuda, K. (1987b), "A Study of Cutting Temperature in Ultra-Precision Diamond Cutting of Copper(OFC)", Proceedings of the 15th North American Manufacturing Research Conference, Vol. May, pp. 510-515.

48. Jaeger, J. G. (1942), "Moving Sources of Heat and the Temperature at Sliding Contact", Proc. Roy. Soc. New South Wales, Australia, Vol. 76, pp. 203-224.

49. Jahanmir, S. (1976), "A Fundamental Study on the Delamination Theory of Wear", Ph. D. Thesis, Massachusetts Institute Technology.

50. Johnson, K. L. (1982), "One Hundred Years of Hertz Contact", Proc., Insn of Mech. Engrs, Vol. 196, pp. 363-378.

51. Johnson, K. L. (1987), "Contact Mechanics", Cambridge University Press.

52. Johnson, K. L., and Jefferis, J. A. (1963), "Plastic Flow and Residual Stresses in Rolling and Sliding Contact", Proc. of the Sym. on Fatigue Engrs., London, England, Instn. of Mech. Engrs., pp. 54-65.

53. Ju, F. D., and Chen, T. Y. (1984), "Thermomechanical Cracking in Layered Media From Moving Friction Load", Trans. ASME, J. of Tribology, Vol. 106, pp. 513-518.

54. Ju, F. D., and Huang, J. H. (1982), "Heat Checking in the Contact Zone of a Bearing Seal", Wear, Vol. 79, pp. 107-118.

55. Kagiwada, T., and Kanauchi, T. (1988), "Numerical Analyses of Cutting Temperatures and Flow Ratios of Generated Heat", JSME Int. Journal, Vol. 31, Series III, No. 3, pp. 624-633.

56. Kobayashi, A. (1988), "Present Activities in Ultraprecision Technology in Japan", ASPE 3rd Annual Precision Engineering Conf., Atlanta, Ga, ASPE, pp. 13-15.

57. Kobayashi, S., and Thomsen, E. G. (1960), "The Role of Friction in Metal Cutting", Trans. ASME, J. Eng. Ind., pp. 324-332.

58. Komanduri, R. (1971), "Some Aspects of Machining with Negative Rake Tools Simulating Grinding", Int. J. Mach. Tool Des. Res., Vol. 11, pp. 223-233.

59. Krauskopf, B. (1984), "Diamond Turning: Reflecting Demands for Precision", Manufacturing Eng., pp. 90-100.

60. Ling, F. F. (1973), "Surface Mechanics", John Wiley & Sons, Inc.

61. Lucca, D. A., and Seo, Y. W. (1989), "Prediction of the Partition of Energies and Temperatures in Orthogonal Ultraprecision Machining", The ASPE/5th International Engineering Seminar, Monterey, CA, Sept. 18-22.

62. Lucca, D. A., Rhorer, R. L., Seo, Y. W., and Komanduri, R. (1991a), "Energy Dissipation in Ultra-Precision Machining", Proceedings of the 1991 NSF Design and Manufacturing Systems Conference, The University of Texas, Austin, TX, Jan. 9-11, Society of Manufacturing Engineers, pp. 263-267.

63. Lucca, D. A., Rhorer, R. L., and Komanduri, R. (1991b), "Energy Dissipation in the Ultraprecision Machining of Copper", Annals of the CIRP, Vol. 40, No. 1, pp. 69-72.

64. Lucca, D. A., Seo, Y. W., and Rhorer, R. L. (1992), "Energies in the Ultra-Precision Machining of Ductile Materials", Proceedings of the 1992 NSF Design and Manufacturing Systems Conference, Georgia Institute of Technology, Atlanta, Georgia, Society of Manufacturing Engineers, Jan. 8-10, pp. 123-129.

65. Lucca, D. A., Seo, Y. W., and Rhorer, R. L. (1993a), "Energy Dissipation in Ultra-Precision Machining", Proceedings of the 1993 NSF Design and Manufacturing Systems Conference Vol 1, The Univ. of North Carolina at Charlotte, Charlotte, North Carolina, Society of Manufacturing Engineers, Jan. 6-8, pp. 225-229.

66. Lucca, D. A., and Seo, Y. W. (1993b), "Effect of Tool Edge Geometry on Energy Dissipation in Ultraprecision Machining", to appear in the Annals of the CIRP, Vol. 42, No. 1.

67. Lucca, D. A., Seo, Y. W., and Rhorer, R. L. (1993c), "Energy Dissipation and Tool-Workpiece Contact in Ultra-Precision Machining", submitted in Transaction of the STLE.

68. Machinability Data Center (1972), "Machining Data Handbook", Metcut Research Associate Inc., Cincinnati, Ohio.

69. Machinability Data Center (1980), "Machining Data Handbook", Metcut Research Associate Inc., Cincinnati, Ohio.

70. Malkin, S. (1974a), "Thermal Aspects of Grinding, Part 1 Energy Partition", Trans. ASME, J. Eng. Ind., pp. 1177-1183.

71. Malkin, S. (1974b), "Thermal Aspects of Grinding, Part 2 Surface Temperatures and Workpiece Burn", Trans. ASME, J. Eng. Ind., pp. 1184-1191.

72. Malkin, S., and Marmur, A. (1977), "Temperatures in Sliding and Machining Processes with Distributed Heat Sources in the Subsurface", Wear, Vol. 42, pp. 333-340.

73. Masuda, M., Maeda, Y., Nishiguchi, T., and Sawa, M. (1989), "A Study on Diamond Turning of Al-Mg Alloy - Generation Mechanism of Surface Machined with Worn Tool", Annals of the CIRP, Vol. 38, No. 1, pp. 111-114.

74. McKeown, P. A. (1982), "The Design and Development of a Large Ultra Precision CNC Diamond Turning Machine", SME Technical Paper MR82-931.

75. McKeown, P. A. (1987), "The Role of Precision Engineering in Manufacturing of the Future", Annals of the CIRP, Vol. Keynote Paper, pp. 495-501.

76. Merchant, M. E. (1945a), "Mechanics of Metal Cutting Process. I. Orthogonal Cutting and a Type 2 Chip", J. Appl. Physics, Vol. 16, No. 5, pp. 267-275.

77. Merchant, M. E. (1945b), "Mechanics of the Metal Cutting Process. II. Plasticity Conditions in Orthogonal Cutting", J. Appl. Phys., Vol. 16, pp. 319-324.

78. Merwin, J. E., and Johnson, K. L. (1963), "An Analysis of Plastic Deformation in Rolling Contact", Proc. Instn. Mech. Engrs., Vol. 177, No. 25, pp. 676-690.

79. Moriwaki, T., and Okuda, K. (1989), "Machinability of Copper in Ultra-Precision Micro Diamond Cutting", Annals of the CIRP, Vol. 38, No. 1, pp. 115-118.

80. Nakayama, K., and Tamura, K. (1968), "Size Effect in Metal-Cutting Force", Trans. ASME, J. Eng. Ind., Vol. Feb., pp. 119-126.

81. Nishiguchi, T., Maeda, Y., Masuda, M. et al. (1988), "Mechanism of Micro Chip Formation in Diamond Turning of Al-Mg Alloy", Annals of the CIRP, Vol. 37, No. 1.

82. Oxley, P. L. B., and Hastings, W. F. (1976), "Minimum Work as a Possible Criterion for Determining the Frictional Conditions at the Tool/Chip interface in Machining", Phil. Trans. R. Soc. Lond., Vol. 282, No. 1310, pp. 565-584.

83. Piezo-Instrument "Operating Instructions: Quartz Force Transducer for 3 Components, Type 9251A", Piezo-Instrument Co.

84. Piispanen, V. (1948), "Theory of Formation of Metal Chips", J. Appl. Phys., Vol. 19, pp. 876-881.

85. Radzimovsky, E. I. (1953), "Stress Distribution and Strength Condition of Two Rolling Cylinders Pressed Together", Univ. of Illinois Bulletin, Urbana, Illinois.

86. Rank-Pneumo (1990), "Operating and Maintenance Manual of ASG-2500 Aspheric Generator", Rank Pneumo - A Division of Rank Taylor Hobson Inc., Keene, NH.

87. Rhorer, R. L. (1986), "A Method for Orthogonal Cutting Experiments with Diamond Tools", SPIE, Ultraprecision Machining and Automated Fabrication of Optics, Vol. 676, pp. 111-115.

88. Richards, J. B. (1966), "Application of Automatic Tool Setting, Air-bearing Spindles, and Laser Interferometer feedback to Contour Machining", Advances in Machine Tool Design and Research, The 7th International MTDR Conference, Univ. of Birmingham, Pergamon Press, pp. 335-349.

89. Rubenstein, C. (1968), "The Mechanism of Orthogonal Cutting with Controlled Contact Tools", Int. J. Mach. Tool Des. Res., Vol. 8, pp. 203-216.

90. Shaw, M. C. (1983), "Metal Cutting Principles", Oxford Series on Advanced Manufacturing 3, Oxford Science Publications, Oxford.

91. Shimada, S., Ikawa, N., Ohmori, G. et al. (1992), "Molecular Dynamics Analysis as Compared with Experimental Results of Micromachining", Annals of the CIRP, Vol. 41, No. 1, pp. 117-120.

92. Smith, J. O., and Liu, C. K. (1953), "Stresses Due to Tangential and Normal Loads on an Elastic Solid with Application to Some Contact Stress Problems", Trans. ASME, J. Appl. Mech., pp. 157-166.

93. Spaans, C. (1967a), "An Exact Method to Determine the Forces on the Clearance Plane", Annals of the CIRP, Vol. XV, pp. 463-469.

94. Spaans, C. (1967b), "The Extra Forces Near the Cutting Edge and Their Implications", Int. Conf. on Mfg. Technol., U. of Michigan, Ann Arbor, Michigan, ASME, pp. 533-552.

95. Spaans, C. (1970), "The Mechanics of Oblique Cutting, Taking into Account the Forces on the Clearance Face", Int. J. Mach. Tool Des. Res., Vol. 10, pp. 213-220.

96. Spaans, C. (1971), "The Fundamentals of Three-Dimensional Chip Curl, Chip Breaking and Chip Control", Ph. D. Thesis.

97. Strenkowski, J. S., and Carroll, I., J. T. (1985), "A Finite Element Model of Orthogonal Metal Cutting", Trans. ASME, J. Eng. Ind., pp. 349-354.

98. Strenkowski, J. S., Bailey, J. A., and Howerton, D. H. (1990), "Prediction of Residual Stress in Orthogonal Cutting of an Aluminum Alloy", Proceedings of NSF Design and Manufacturing Systems Conference, Arizona State Univ., Tempe, Arizona, pp. 463-470.

99. Sugano, T., Takeuchi, K., and Yoshida, Y. (1987), "Diamond Turning of an Aluminum Alloy for Mirror", Annals of the CIRP, Vol. 36, No. 1.

100. Suh, N. P. (1986), "Tribophysics", Prentice-Hall.

101. Syn, C. K., Shimada, S., Taylor, J. S., and Donaldson, R. R. (1988), "Ductile-Brittle Transition of Cutting Behavior in Diamond Turning of Single Crystal Si", Annual Spring Meeting of the JSPE, pp. 1-8.

102. Syn, C. K., Taylor, J. S., and Donaldson, R. R. (1986), "Diamond Tool Wear vs. Cutting Distance on Electroless Nickel Mirrors", Ultraprecision Machining and Automated Fabrication of Optics, SPIE, Vol. 676, pp. 128-140.

103. Tabor, D. (1987), "Friction and Wear-Developments over the Last Fifty Years", Tribology-Friction, Lubrication and Wear Fifty Years On, Vol. 1, pp. 157-172.

104. Taminiau, D. A., and Dautzenberg, J. H. (1991), "Bluntness of the Tool and Process Forces in High-Precision Cutting", Annals of the CIRP, Vol. 40, No. 1, pp. 65-68.

105. Taniguchi, N. (1983), "Current Status in, and Future Trends of, Ultraprecision Machining and Ultrafine Materials Processing", Annals of the CIRP, Vol. 32, No. 2, pp. 573-582.

106. Taylor, J. S., Syn, C. K., and Donaldson, R. R. (1987), "Observations of Brittle-to-Ductile Cutting Mode Transition During Diamond Turning Tests of Single Crystal Silicon", ASPE Conf.

107. Taylor, J. S., Syn, C. K., Saito, T. T., and Donaldson, R. R. (1986), "Surface Finish Measurements of Diamond-Turned Electroless-Nickel-Plated Mirrors", Optical Eng., Vol. 25, No. 9, pp. 1013-1020.

108. Teague, C. E., and Stowers, I. F. (1988), "Overview of Nanotechnology Activities in the U. S.", ASPE 3rd Annual Precision Engineering Conf., Atlanta, Ga, ASPE, pp. 22-23.

109. Terauchi, Y., Nadano, H., and Kohno, M. (1984), "On the Temperature Rise Caused by Moving Heat Sources", Bulletin of JSME, Vol. 27, No. 226, pp. 831-838.

110. Thomsen, E. G., Lapsley, J. T., and Grassi, R. C. (1953), "Deformation Work Absorbed by the Workpiece During Metal Cutting", Trans. ASME, Vol. 75, pp. 591-603.

111. Timoshenko, S. P., and Goodier, J. N. (1970), "Theory of Elasticity", McGraw-Hill Kogakusha, Ltd.

112. Ueda, K., and Iwata, K. (1980), "Chip Formation Mechanism in Single Crystal Cutting of ß-Brass", Annals of the CIRP, Vol. 29, No. 1, pp. 41-46.

113. Venuvinod, P. K., Lau, W. S., and Rubenstein, C. (1983), "The Role of Discrete Contact at the Flank Wear Land in Determining Cutting Tool Temperature in Orthogonal Cutting", Int. J. Mach. Tool Des. Res., Vol. 23, No. 4, pp. 245-261.

114. von Turkovich, B. F. (1967), "Dislocation Theory of Shear Stress and Strain Rate in Metal Cutting", 8th Int. MTDR Conf., pp. 531-542.

115. Wada, R., Kodama, K., Mizutani, Y. et al. (1980), "Wear Characteristics of Single Crystal Diamond Tool", Annals of the CIRP, Vol. 29, No. 1, pp. 47-52.

116. Whitten, L. G., and Lewis, T. G. (1966), "Machining and Measurement to Submicron Tolerances", Advances in Machine Tool Design and Research, The 7th International MTDR Conference, Univ. of Birmingham, Pergamon Press, pp. 491-513.

117. Williams, J. A., and Gane, N. (1977), "Some Observations on the Flow Stress of Metals During Metal Cutting", Wear, pp. 341-353.

APPENDICES

APPENDIX A

FORMULATION OF AN ELASTOSTATIC STRESS FIELD OF A BODY SUBJECTED TO ARBITRARILY DISTRIBUTED SURFACE PRESSURES

A.1 Elastostatic Stress Fields of a Body due to a Surface Pressure

A.1.1 Airy's Stress Function and Elastostatic Stress Fields

The elastostatic stress field under a semi-infinite body due to a surface pressure can be obtained using the Airy's stress function. This problem is known as Boussinesq-Flamant problem in which the normal and tangential loads are superimposed. Airy's stress function satisfies equilibrium and compatibility conditions by itself. Remaining boundary condition depends on the applied surface load. Assuming a semi-infinite body and plane strain conditions due to the relatively large width than the contact length or the depth of cut for the present problem, three different stress fields due to three different surface loadings such as linear, constant and elliptical applied pressure are considered. The Airy's stress function for concentrated normal load P and tangential load Q may be given as:

$$\phi_P = -\frac{P}{\pi} r_1 \theta_1 \sin \theta_1 \qquad \text{(A-1)}$$

$$\phi_Q = -\frac{Q}{\pi} r_2 \theta_2 \sin \theta_2 \qquad \text{(A-2)}$$

This problem is formulated by Flamant for normal load and tangential load is done by Boussinesq later. For the applied loads, it is necessary to measure the angle θ from the direction of the loading as shown in Fig. A-1. The infinitesimal normal load dP and tangential load

dQ can be expressed in terms of distributed pressure. Also the included angle can be expressed in terms of Cartesian coordinate system as:

For normal force

$$dP = p(\xi)\, d\xi$$
$$r_1 \sin\theta_1 = x_1 = x - \xi \qquad \text{(A-3)}$$
$$\theta_1 = \tan^{-1}(x_1/y) = \tan^{-1}((x - \xi)/y)$$

For tangential force

$$dQ = q(\xi)\, d\xi$$
$$r_2 \sin\theta_2 = y_1 = y \qquad \text{(A-4)}$$
$$\theta_2 = \tan^{-1}(y/x_1) = \tan^{-1}(y/(x - \xi))$$

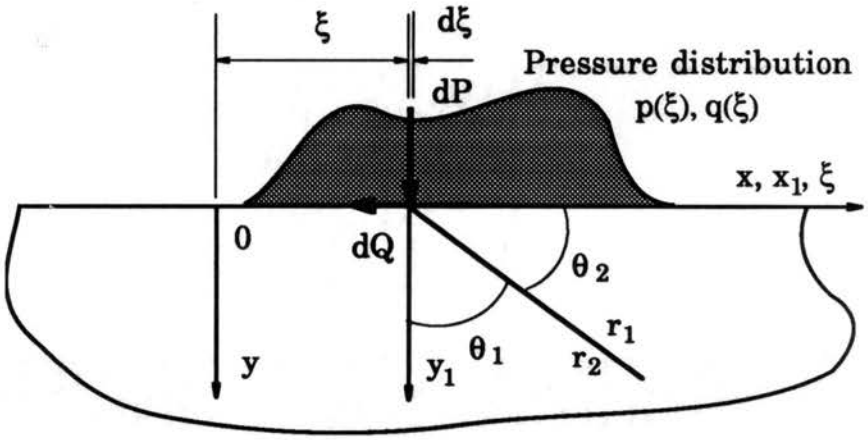

Figure A-1. Geometry for Arbitrarily Distributed Surface Pressure

Substituting eqs. (A-3) and (A-4) into eqs. (A-1) and (A-2) for the stress functions in a semi-infinite body due to the concentrated infinitesimal loads, corresponding stress functions can be obtained as:

$$d\phi_P = -\frac{1}{\pi} p(\xi)\,(x-\xi)\tan^{-1}\left(\frac{x-\xi}{y}\right) d\xi \tag{A-5}$$

$$d\phi_Q = \frac{1}{\pi} q(\xi)\,\xi \tan^{-1}\left(\frac{y}{x-\xi}\right) d\xi \tag{A-6}$$

Elastic behavior is linear thus the superposition is valid for the stress function. The general stress function for arbitrarily distributed surface pressure which is ranging from $-l$ to l can be expressed as:

$$\phi = -\frac{1}{\pi}\int_{-l}^{l} p(\xi)\,(x-\xi)\tan^{-1}\left(\frac{x-\xi}{y}\right) d\xi + \frac{1}{\pi}\int_{-l}^{l} q(\xi)\,\xi \tan^{-1}\left(\frac{y}{x-\xi}\right) d\xi \tag{A-7}$$

Once a stress function is known, corresponding stress fields can be obtained. When a body force is negligible, stress fields may be given as:

$$\sigma_{xx} = \frac{\partial^2\phi}{\partial y^2}, \quad \sigma_{yy} = \frac{\partial^2\phi}{\partial x^2}, \quad \sigma_{xy} = -\frac{\partial^2\phi}{\partial x \partial y} \tag{A-8}$$

For the plane strain condition, out of plane stress component can be written as:

$$\sigma_{zz} = \nu\,(\sigma_{xx} + \sigma_{yy}) \tag{A-9}$$

Three cases of pressure distribution were considered for the stress fields, i.e., linear, constant and elliptical surface pressure distributions in

both the normal and tangential directions to simulate the sliding contact stress fields at the subsurface of the body. The stress functions and corresponding stress fields in a semi-infinite stationary body are obtained in integration forms for the three applied surface pressure types.

A.1.1.1 Elastostatic Stress Fields due to Linear Surface Pressure

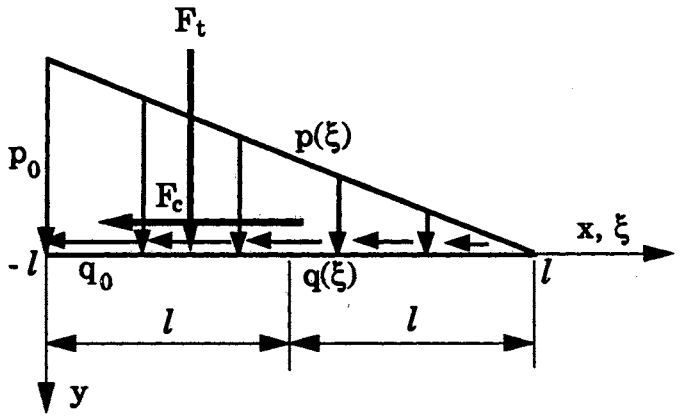

Figure A-2. Linearly Applied Surface Pressure

- Maximum Intensity of Pressure

$$p_0 = \frac{F_t}{l}, \quad q_0 = \frac{F_c}{l} \tag{A-10}$$

- Pressure Distribution

$$p(\xi) = \frac{p_0}{2l}(l - \xi), \quad q(\xi) = \frac{q_0}{2l}(l - \xi) \tag{A-11}$$

- Stress Function

$$\phi = -\frac{p_0}{2\pi l}\int_{-l}^{l}(l-\xi)(x-\xi)\tan^{-1}\left(\frac{x-\xi}{y}\right)d\xi + \frac{q_0}{2\pi l}\int_{-l}^{l}(l-\xi)\,\xi\tan^{-1}\left(\frac{y}{x-\xi}\right)d\xi \qquad \text{(A-12)}$$

Stress fields are given in eq. (6-7) for the semi-infinite stationary body under linear surface pressure.

A.1.1.2 Elastostatic Stress Fields due to Constant Surface Pressure

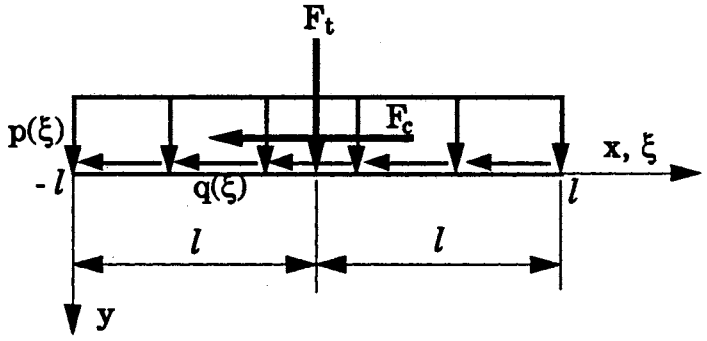

Figure A-3. Constantly Applied Surface Pressure

- Maximum Intensity of Pressure

$$p_0 = \frac{F_t}{2l}, \quad q_0 = \frac{F_c}{2l} \qquad \text{(A-13)}$$

- Pressure Distribution

$$p(\xi) = p_0, \quad q(\xi) = q_0 \tag{A-14}$$

- Stress Function

$$\phi = -\frac{p_0}{\pi}\int_{-l}^{l}(x-\xi)\tan^{-1}\left(\frac{x-\xi}{y}\right)d\xi + \frac{q_0}{\pi}\int_{-l}^{l}\xi\tan^{-1}\left(\frac{y}{x-\xi}\right)d\xi \tag{A-15}$$

Stress fields of a semi-infinite body subjected to a planar surface pressure are shown in eq. (6-8).

A.1.1.3 Elastostatic Stress Fields due to Elliptical Surface Pressure

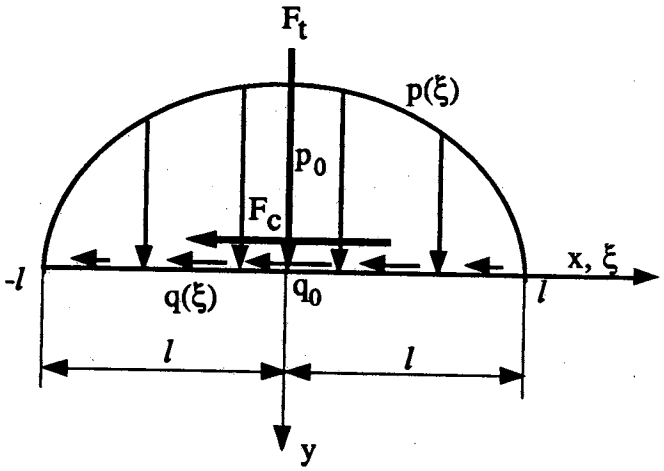

Figure A-4. Elliptically Applied Surface Pressure

- Maximum Intensity of Pressure and Distribution

$$p_0 = \frac{2F_t}{\pi l}, \quad q_0 = \frac{2F_c}{\pi l} \tag{A-16}$$

$$p(\xi) = \frac{p_0}{l}(l^2 - \xi^2)^{\frac{1}{2}}, \quad q(\xi) = \frac{q_0}{l}(l^2 - \xi^2)^{\frac{1}{2}} \tag{A-17}$$

- Stress Function

$$\phi = -\frac{p_0}{\pi l}\int_{-l}^{l}(l^2 - x^2)^{1/2}(x-\xi)\tan^{-1}\left(\frac{x-\xi}{y}\right)d\xi + \frac{q_0}{\pi l}\int_{-l}^{l}(l^2 - x^2)^{1/2}\,\xi\tan^{-1}\left(\frac{y}{x-\xi}\right)d\xi \tag{A-18}$$

Stress fields are given in eq. (6-9) for the body under elliptical surface pressure.

A.2 Elastodynamic Stress Fields of a Body due to a Moving Surface Pressure

A.2.1 Elastodynamic Stress Fields

Elastodynamic stress fields can be formulated using complex stress potential in which speed effect is considered. The result of the stress fields from Eringen and Suhubi [Eringen, 1975] is written as:

$$\sigma_{xx} = \frac{\beta_d \eta}{\pi R}\left[(2\beta_d^2 - \beta_s^2 + 1)(1 + \beta_s^2)\int_{-1}^{1} \frac{p(\lambda)}{(\xi - \lambda)^2 + (\beta_d \eta)^2}\, d\lambda \right.$$

$$\left. - 4\beta_s^2 \int_{-1}^{1} \frac{p(\lambda)}{(\xi - \lambda)^2 + (\beta_s \eta)^2}\, d\lambda\right]$$

$$- \frac{2\beta_s \mu_f}{\pi R}\left[(2\beta_d^2 - \beta_s^2 + 1)\int_{-1}^{1} \frac{p(\lambda)\,(\xi - \lambda)}{(\xi - \lambda)^2 + (\beta_d \eta)^2}\, d\lambda \right.$$

$$\left. - (1 + \beta_s^2)\int_{-1}^{1} \frac{p(\lambda)\,(\xi - \lambda)}{(\xi - \lambda)^2 + (\beta_s \eta)^2}\, d\lambda\right] \qquad \text{(A-19a)}$$

$$\sigma_{yy} = - \frac{2\beta_s \mu_f \eta^2}{\pi R}(\beta_s^2 + 1)(\beta_s^2 - \beta_d^2)\int_{-1}^{1} \frac{p(\lambda)\,(\xi - \lambda)}{\{(\xi - \lambda)^2 + (\beta_d \eta)^2\}\{(\xi - \lambda)^2 + (\beta_s \eta)^2\}}\, d\lambda$$

$$- \frac{\beta_d \eta}{\pi R}\left[(\beta_s^2 + 1)^2 \int_{-1}^{1} \frac{p(\lambda)}{(\xi - \lambda)^2 + (\beta_d \eta)^2}\, d\lambda \right.$$

$$\left. - 4\beta_s^2 \int_{-1}^{1} \frac{p(\lambda)}{(\xi - \lambda)^2 + (\beta_s \eta)^2}\, d\lambda\right] \qquad \text{(A-19b)}$$

$$\sigma_{xy} = - \frac{2\beta_d \eta^2}{\pi R}(\beta_s^2 + 1)(\beta_s^2 - \beta_d^2)\int_{-1}^{1} \frac{p(\lambda)\,(\xi - \lambda)}{\{(\xi - \lambda)^2 + (\beta_d \eta)^2\}\{(\xi - \lambda)^2 + (\beta_s \eta)^2\}}\, d\lambda$$

$$- \frac{\beta_s \eta \mu_f}{\pi R}\left[4\beta_d^2 \int_{-1}^{1} \frac{p(\lambda)}{(\xi - \lambda)^2 + (\beta_d \eta)^2}\, d\lambda \right.$$

$$\left. - (1 + \beta_s^2)^2 \int_{-1}^{1} \frac{p(\lambda)}{(\xi - \lambda)^2 + (\beta_s \eta)^2}\, d\lambda\right] \qquad \text{(A-19c)}$$

where

$$M_i = V/C_i,\ i = d,\ s$$

$$\beta_i = \sqrt{1 - M_i^2}$$

$$R = (1+ \beta_s^2)^2 - 4\beta_d\beta_s$$

$$C_d = \{\frac{gE(1 - \nu)}{\rho(1 + \nu)(1 - 2\nu)}\}^{1/2},\ C_s = \{\frac{gE}{2\rho(1 + \nu)}\}^{1/2} \qquad \text{(A-20)}$$

C_d and C_s are the dilatation and shear wave speeds in a material, E is the Young's modulus, ρ is the weight density, g is the gravitational acceleration, ν the Poisson's ratio, and μ_f is the friction coefficient of the surface load. Typical values of C_d and C_s are given in Table A-1.

TABLE A-1

TYPICAL VALUES OF DILATATION AND SHEAR WAVE SPEED OF SOME MATERIALS

Material	weight density (Kg/m^3)	C_d (m/sec)	C_s(m/sec)
Steel	7800	5900	3200
Aluminum	2700	6168	3107
Copper	8876	4196	2243

A.3 Numerical Analysis

The integration forms in the stress fields may be evaluated using Gaussian quadrature, which is a mapping the arbitrary range of integration into -1 to 1.

$$\int_A^B f(\xi)\, d\xi = \frac{B-A}{2} \Sigma\, w_i\, f(\xi_i) \qquad \text{(A-21)}$$

where

$$\xi_i = \{(B - A)h_i + (B + A)\}/2$$

Here w_i and h_i are the Gaussian weight and abscissa, and maximum i is the number of Gaussian points to be employed.

Using a 10 point Gaussian quadrature technique, the stress fields are computer programmed for both the Airy's function and the Eringen and Suhubi's formulation. The flow chart for the program is shown in Fig. A-5. The program was run on the IBM AIX Version 3.1 for RISC System/6000. Using the data representing microcutting of Al 6061-T6 at 0.01 and 0.1 μm, the resulting stress fields are shown in A-6 and A-8 for linearly pressure, and in A-9 and A-10 for elliptically distributed pressure respectively. In Fig. A-10, the elastic-plastic boundaries estimated using Eringen and Suhubi's formulation are shown. Similar plastically deformed layer thickness as Airy's stress function technique were obtained even though this is representing "w" shaped iso-stress contours. The constant surface pressure results in slightly smaller plastically deformed thickness, similar to the results of Airy's stress function technique. However, plastically deformed thickness of 0.4 ~ 0.7 η from Fig A-10 is comparable with 0.4 η at 0.01 μm depth of cut, and about 1.6 η at 0.1 μm from Airy's function and that of Fourier transform technique in Fig. 6-8. Also the overall trend seems to be quite similar for those three results of stress fields.

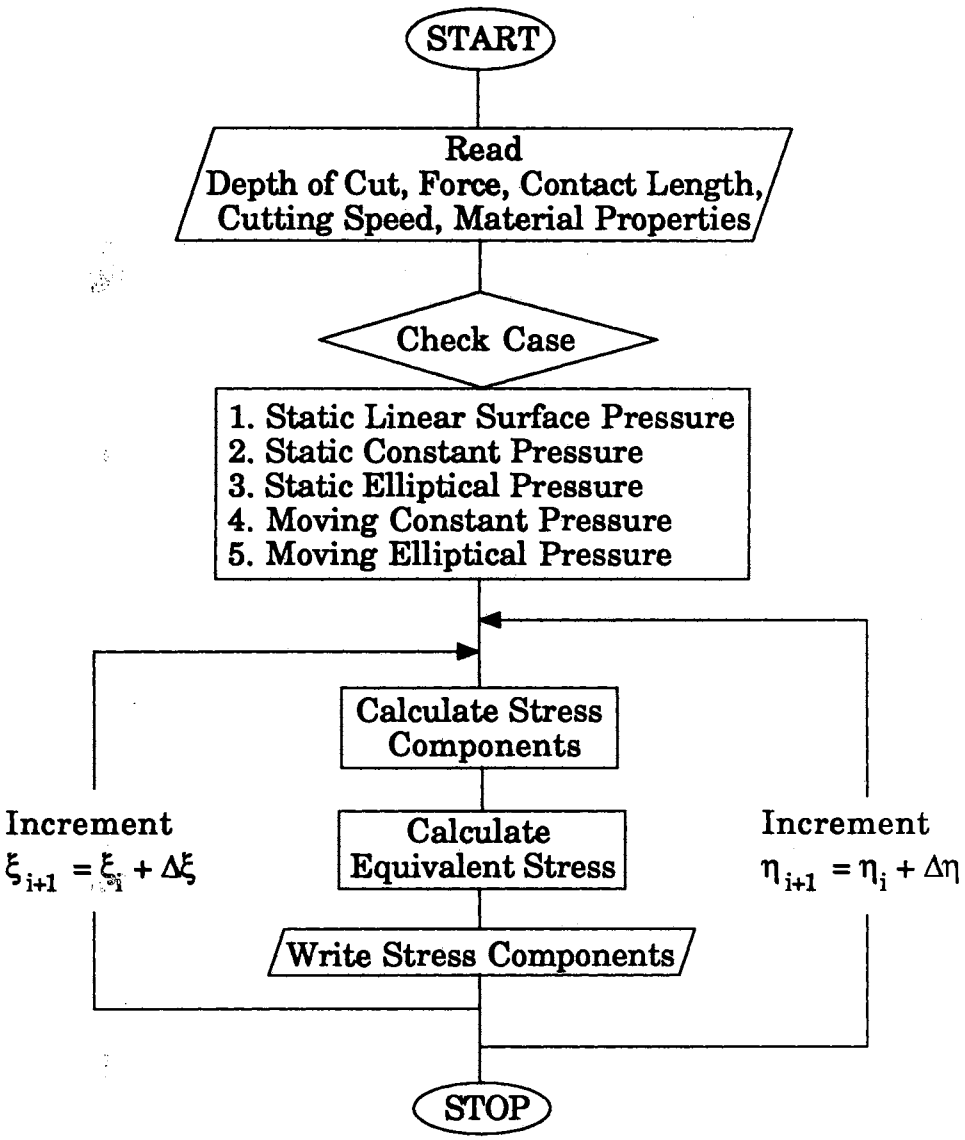

FigureA-5. Flow Chart of the Computer Program for the Elastic Stress Fields

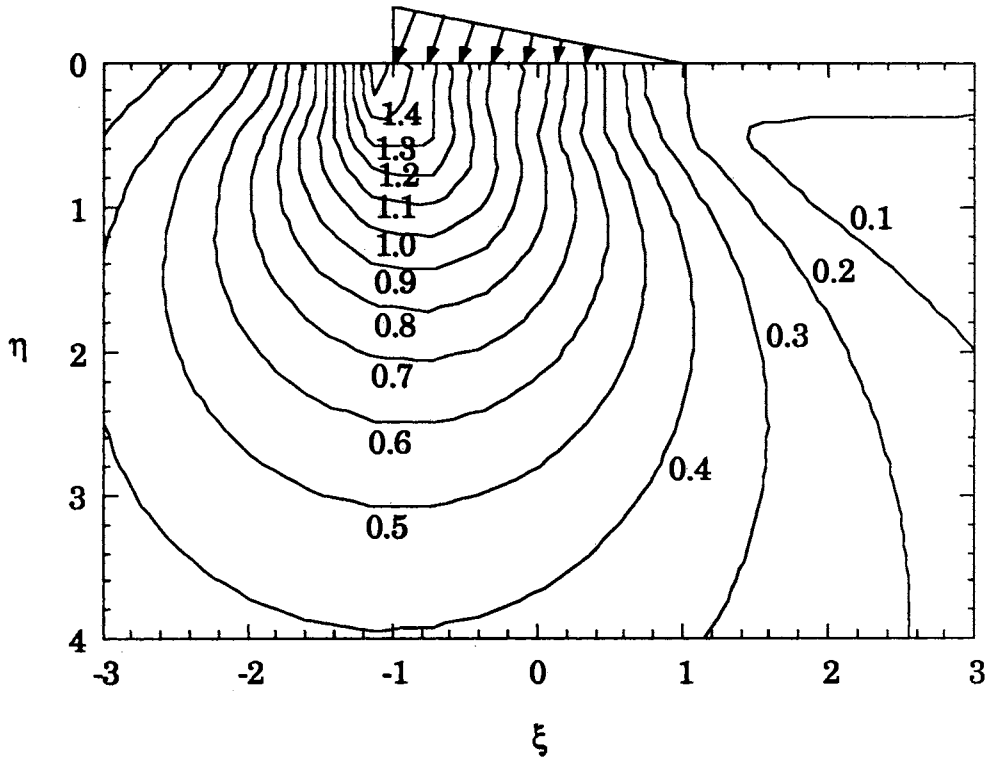

Figure. A-6. Contours of the Normalized von Mises Equivalent Elastostatic Stress with Respect to the Half Space Uniaxial Yield Strength as Predicted by Airy's Stress Function Due to Linear Surface Pressure for Loading Conditions Representing the Orthogonal Flycutting of Al 6061-T6 at Depth of Cut of 0.01 μm

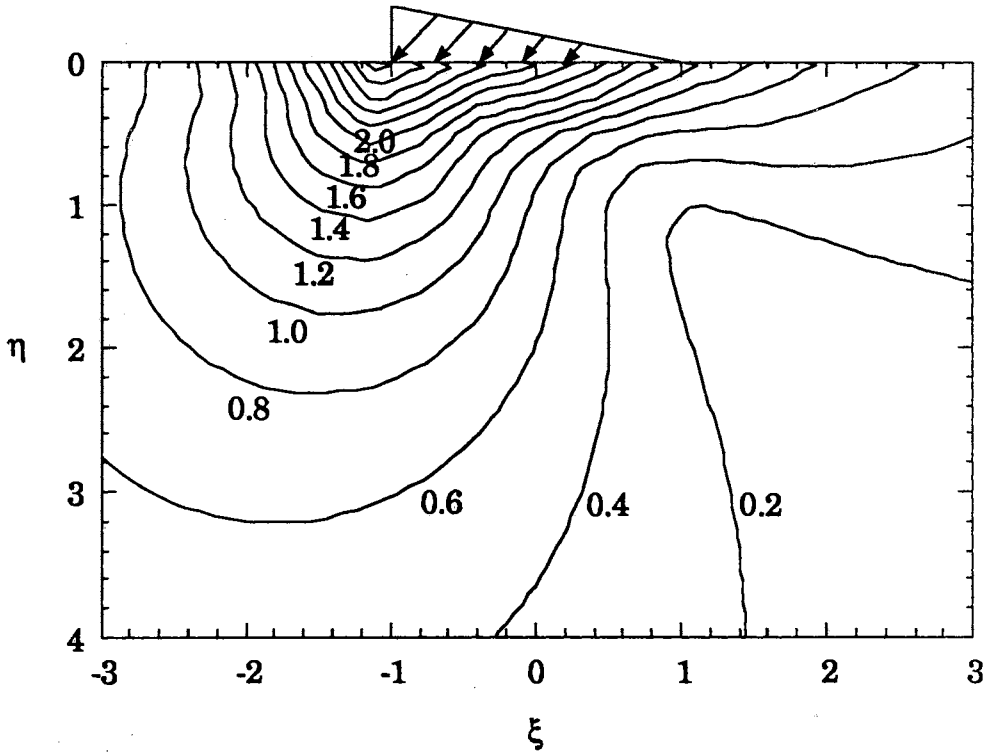

Figure A-7. Contours of the Normalized von Mises Equivalent Elastostatic Stress with Respect to the Half Space Uniaxial Yield Strength as Predicted by Airy's Stress Function Due to Linear Surface Pressure for Loading Conditions Representing the Orthogonal Flycutting of Al 6061-T6 at Depth of Cut of 0.1 μm

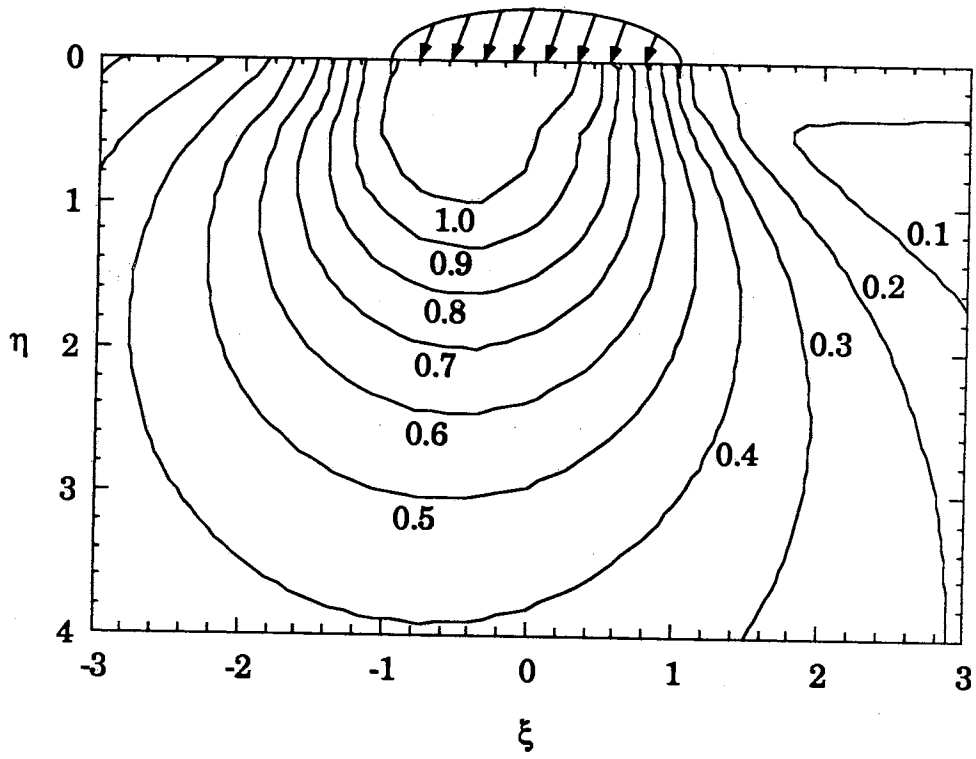

Figure. A-8. Contours of the Normalized von Mises Equivalent Elastostatic Stress with Respect to the Half Space Uniaxial Yield Strength as Predicted by Airy's Stress Function Due to Elliptical Surface Pressure for Loading Conditions Representing the Orthogonal Flycutting of Al 6061-T6 at Depth of Cut of 0.01 μm

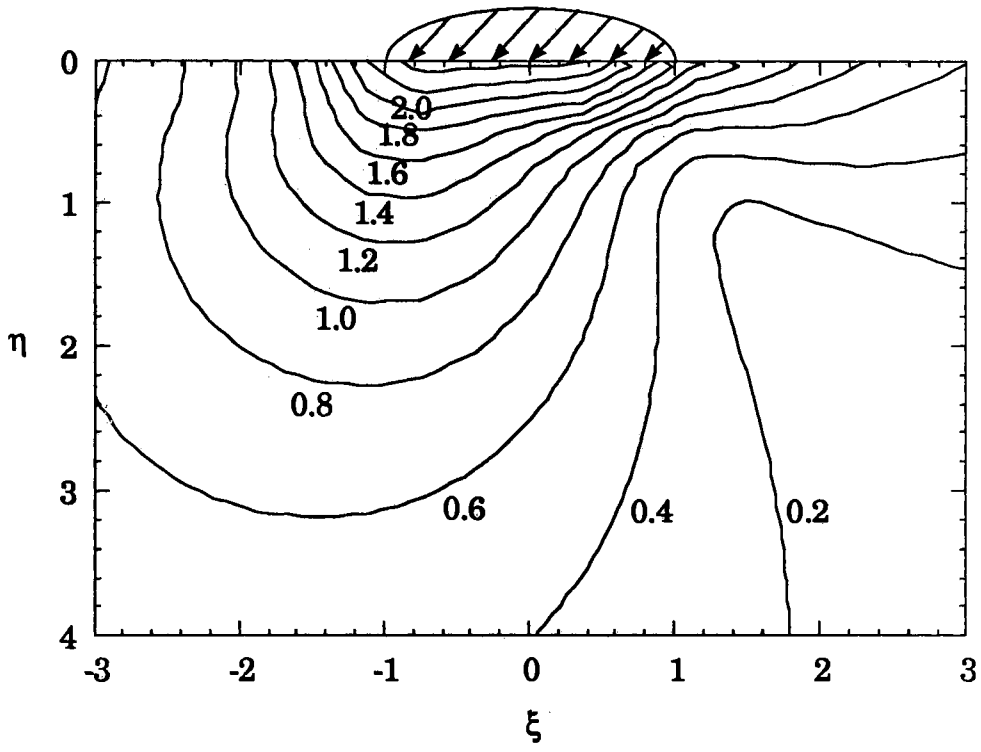

Figure A-9. Contours of the Normalized von Mises Equivalent Elastostatic Stress with Respect to the Half Space Uniaxial Yield Strength as Predicted by Airy's Stress Function Due to Elliptical Surface Pressure for Loading Conditions Representing the Orthogonal Flycutting of Al 6061-T6 at Depth of Cut of 0.1 μm

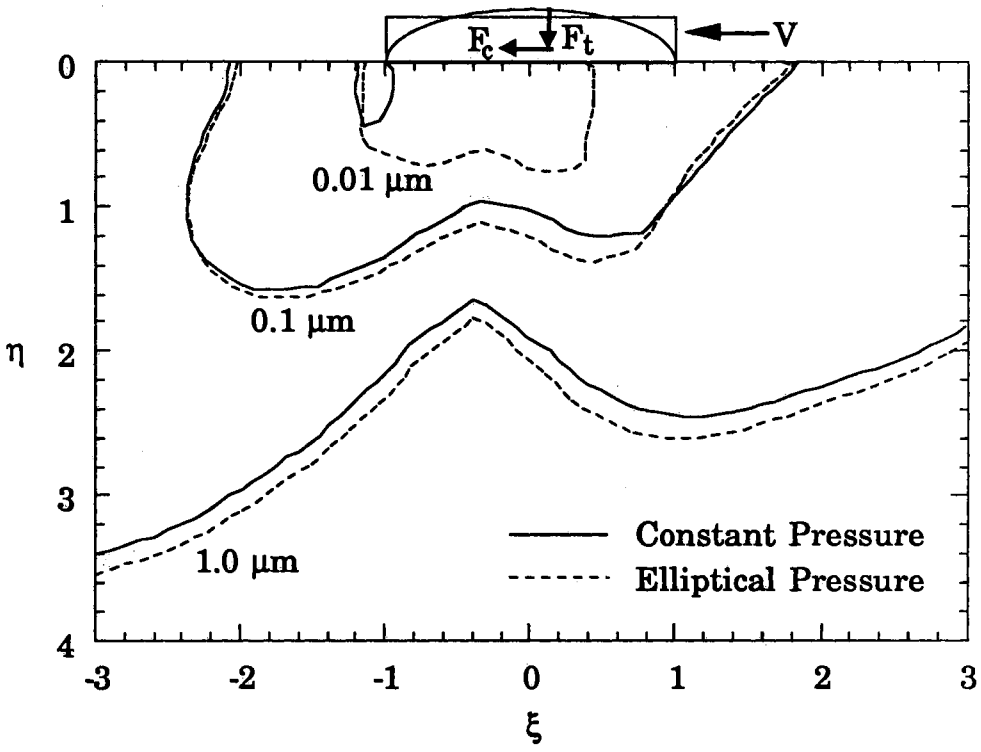

Figure A-10. Contours of Elastic-Plastic Boundaries of Elasto-dynamic Stress Fields as Predicted by Complex Potential Function for Loading Conditions Representing the Orthogonal Flycutting of Al 6061-T6

APPENDIX B

FORMULATION OF ELASTODYNAMIC STRESS, TEMPERATURES, AND THERMOMECHANICAL STRESS FIELDS OF A BODY IN SLIDING INDENTATION

B.1 Introduction

When two bodies are in contact under high loads and speeds, they may result in significant mechanical and thermal problems in the vicinity of contact. These thermomechanical problems occur in mechanical seals, brakes, etc. The source of high contact pressure and temperature is initiating from asperities which have formed at the interface due to secondary inclusions or particles, some may due to deformation of the contact surface. Similar thermomechanical problems occur in manufacturing processes such as metal cutting and forming processes like extrusion. For the study of mechanics involved, it is needed to investigate the thermomechanical behaviors of the bodies in contact.

In order to consider the thermomechanical dynamic stress fields, energy partitions at the interface and temperature rises, the Fourier integral transform technique may be used for the analytical modeling of the process. The procedure of this formulation is as follows:

- The Navier's equilibrium equation and Hooke's law are employed as governing field and constitutive equations of the formulation.
- These partial differential equations are normalized and transformed using the Fourier integral transform to get a set of simultaneous second order ordinary differential equation in terms of two displacement components.
- Solve the ordinary simultaneous differential equations to get the fourth order differential equation of single displacement term, and apply boundary conditions to get stress fields in transformed domain.

- Finally, taking the inverse transformation, the corresponding displacement and stress terms are obtained in integration forms.

B.2 Governing Field Equations

B.2.1 Mechanical Stress Fields

For the mechanical stress, the Navier's thermoelastic equilibrium equations can be employed in terms of displacements without thermal terms as:

$$(\lambda + \mu)u_{k,\,ki} + \mu u_{i,\,kk} = \rho V^2 \frac{\partial^2 u_i}{\partial x_1^2} \tag{B-2.1}$$

The Hooke's law is given as:

$$\sigma_{ij} = \lambda \varepsilon_{kk} \delta_{ij} + 2\mu \varepsilon_{ij} \tag{B-2.2}$$

where λ, μ are the Lamé constant, u_i are the displacement components, ρ is the mass density, V is the sliding speed, σ_{ij} and ε_{ij} are the stress and strain components, and δ_{ij} is the Kronecker delta.

Prescribed surface boundary traction may be given for sliding contact problem as:

$$\sigma_{xy} = \mu_f\, p(x) \qquad |x| \le l,\ y = 0 \tag{B-2.3}$$

$$\begin{aligned} \sigma_{yy} &= -\,p(x) && |x| \le l,\ y = 0 \\ &0 && |x| > l,\ y = 0 \end{aligned} \tag{B-2.4}$$

where μ_f is the friction coefficient, p(x) is the applied pressure, $2l$ is the contact length.

Regularity conditions are given as:

$$\sigma_{ij} = 0, u_i = 0 \text{ as } x^2 + y^2 \to \infty \tag{B-2.5}$$

B.2.2 Temperature Fields

The Fourier heat conduction equation may be given as:

$$\nabla^2 T = \frac{\partial^2 T}{\partial x^2} + \frac{\partial^2 T}{\partial y^2} = \frac{V}{\kappa}\frac{\partial T}{\partial x} \tag{B-2.6}$$

where κ is the thermal diffusivity.

Boundary frictional heat at the surface can be written as:

$$-K\frac{\partial T}{\partial y} = \begin{cases} q(x) & |x| \le l, y = 0 \\ 0 & |x| > l, y = 0 \end{cases} \tag{B-2.7}$$

where K is the thermal conductivity and q(x) is the applied heat flux.

Regularity conditions for temperature fields are as follows:

$$T = 0 \quad \text{as } x^2 + y^2 \to \infty \tag{B-2.8}$$

B.2.3 Thermal Stress Fields

The Navier's thermoelastic equilibrium equation in terms of displacements can be written as:

$$(\lambda + \mu)u_{k,ki} + \mu u_{i,kk} - (3\lambda + 2\mu)\alpha T_{,i} = \rho V^2 \frac{\partial^2 u_i}{\partial x_1^2} \qquad \text{(B-2.9)}$$

The Hooke's law for the thermomechanical stress and strain relationship can be written as:

$$\sigma_{ij} = \lambda\, \varepsilon_{kk}\, \delta_{ij} + 2\mu\, \varepsilon_{ij} - (3\lambda + 2\mu)\, \alpha\, (T - T_0)\delta_{ij} \qquad \text{(B-2.10)}$$

where α is the coefficient of thermal expansion and T_0 is the stress-free reference temperature.

The boundary, and regularity conditions of the thermal stress can be written as:

$$\sigma_{xy} = \sigma_{yy} = 0 \text{ at } y = 0 \qquad \text{(B-2.11)}$$

$$\sigma_{xy} = 0 \text{ for } x^2 + y^2 \to \infty \qquad \text{(B-2.12)}$$

B.3 Normalization of the Governing Equations

The following variables are used to non-dimensionalize the variables involved in the governing field equations.

$$\xi = x/l,\ \eta = y/l,\ u = u_1/l,\ v = u_2/l,$$

$$\phi = \frac{TK}{q_0 l},\ \gamma = \frac{q_0 l \alpha}{K} \qquad \text{(B-3.1)}$$

$$C_d^2 = \frac{\lambda + 2\mu}{\rho},\ C_s^2 = \frac{\mu}{\rho},\ N = \frac{C_d}{C_s},\ M = \frac{V}{C_s}$$

Here, u and v are the displacements in moving and transverse direction.

The equilibrium equation in 2-D case may be expressed as:

$$(N^2 - M^2)\frac{\partial^2 u}{\partial \xi^2} + (N^2 - 1)\frac{\partial^2 v}{\partial \xi \partial \eta} + \frac{\partial^2 u}{\partial \eta^2} - (3N^2 - 4)\gamma\frac{\partial \phi}{\partial \xi} = 0 \qquad \text{(B-3.2)}$$

$$(1 - M^2)\frac{\partial^2 v}{\partial \xi^2} + (N^2 - 1)\frac{\partial^2 u}{\partial \xi \partial \eta} + N^2\frac{\partial^2 v}{\partial \eta^2} - (3N^2 - 4)\gamma\frac{\partial \phi}{\partial \eta} = 0 \qquad \text{(B-3.3)}$$

Similarly, using the normalized stress components below,

$$\sigma_{\xi\xi} = \frac{\sigma_{xx}}{p_0}, \ \sigma_{\eta\eta} = \frac{\sigma_{yy}}{p_0}, \ \sigma_{\xi\eta} = \frac{\sigma_{xy}}{p_0} \qquad \text{(B-3.4)}$$

Hooke's law can be normalized as:

$$\sigma_{\xi\xi} = \frac{\mu}{p_0}\{N^2\frac{\partial u}{\partial \xi} + (N^2 - 2)\frac{\partial v}{\partial \eta} - (3N^2 - 4)\gamma\phi\} \qquad \text{(B-3.5)}$$

$$\sigma_{\eta\eta} = \frac{\mu}{p_0}\{(N^2 - 2)\frac{\partial u}{\partial \xi} + N^2\frac{\partial v}{\partial \eta} - (3N^2 - 4)\gamma\phi\} \qquad \text{(B-3.6)}$$

$$\sigma_{\xi\eta} = \frac{\mu}{p_0}(\frac{\partial u}{\partial \eta} + \frac{\partial v}{\partial \xi}) \qquad \text{(B-3.7)}$$

Non-dimensionalizing the boundary conditions and regularity conditions of the mechanical stress:

$$\sigma_{\xi\eta} = \mu_f\, p(\xi)/p_0 \quad |\xi| \le 1, \eta = 0$$
$$0 \quad |\xi| > 1, \eta = 0 \qquad \text{(B-3.8)}$$

$$\sigma_{\eta\eta} = -\, p(\xi)/p_0 \quad |\xi| \le 1, \eta = 0$$
$$0 \quad |\xi| > 1, \eta = 0 \qquad \text{(B-3.9)}$$

$$\sigma_{ij} = 0 \text{ for } \xi^2 + \eta^2 \to \infty \qquad \text{(B-3.10)}$$

where $\mu_f = F_c/F_t$.

Normalized boundary condition and regularity condition for thermal stress may be given as:

$$\sigma_{\xi\eta} = \sigma_{\eta\eta} = 0 \text{ at } \eta = 0 \tag{B-3.11}$$

$$\sigma_{\xi\eta} = 0 \text{ for } \xi^2 + \eta^2 \to \infty \tag{B-3.12}$$

Normalized heat conduction equation can be obtained as:

$$\nabla^2\phi = \frac{\partial^2\phi}{\partial\xi^2} + \frac{\partial^2\phi}{\partial\eta^2} = \mathrm{Pe}\frac{\partial\phi}{\partial\xi} \tag{B-3.13}$$

where Pe is the Peclet number which is defined as $\mathrm{Pe} = Vl/\kappa$, and the thermal diffusivity, $\kappa = K/\rho c_p$.

Non-dimensionalized boundary and regularity conditions for the heat equation are:

$$-\left[\frac{\partial\phi}{\partial\eta}\right] = \begin{cases} q(\xi) & |\xi| \le 1, \eta = 0 \\ 0 & |\xi| > 1, \eta = 0 \end{cases} \tag{B-3.14}$$

$$\phi \to 0 \text{ as } \xi^2 + \eta^2 \to \infty$$

where $q(\xi) = q(\xi)/q_0$, and q_0 is the heat input here.

B.4 Formulation using Fourier Integral Transform

The Fourier integral transform used is defined as:

$$F(s) = \tilde{f}(s) = \int_{-\infty}^{\infty} f(\xi) \exp(- is\xi) \, d\xi \qquad \text{(B-4.1)}$$

where $i = \sqrt{-1}$.

The transformation of the nth derivatives of the Cartesian coordinate system becomes:

$$F\left\{\frac{\partial^n u}{\partial \xi^n}\right\} = (is)^n \tilde{u} \,, \quad F\left\{\frac{\partial^n u}{\partial \eta^n}\right\} = \frac{\partial^n \tilde{u}}{\partial \eta^n} \qquad \text{(B-4.2)}$$

where tilda(~) is the transformed quantities. The transform is applied to the system of equations and boundary conditions, and the resulting ODEs are solved for the transformed domain. After applying the inverse transform and taking the real parts, the equations for the mechanical stress field and thermal field in the moving body can be obtained.

Due to the mathematical complexities, the range of the Fourier variable can be divided into three domains, i.e., $s > 0$, $s = -w < 0$, and $s = 0$. However, when $s = -w < 0$ the result is found to be the same as the result of the case of $s > 0$ because of their conjugate properties when taking the real parts of the final solutions. When $s = 0$, the Fourier integral transform of a function $f(\xi,\eta)$ becomes:

$$F\left\{\frac{\partial f}{\partial \xi}\right\} = \int_{-\infty}^{\infty} \frac{\partial f}{\partial \xi} \, d\xi = [\, f \,]_{-\infty}^{\infty} \qquad \text{(B-4.3)}$$

Due to the regularity condition, the function value $f(\xi,\eta)$ vanishes as field variable goes to $\pm \infty$. Physical meaning of this equation is that the

stress and temperature fields vanish as the distance from the loading point goes to $\pm\infty$.

B.4.1 Mechanical Displacement and Stress Fields

Substituting the variables as:

$$\bar{u} = i\,\tilde{u},\ \bar{v} = \tilde{v},\ \bar{\phi} = \tilde{\phi}/s,\ \text{and}\ ' = \frac{\partial}{\partial \eta} \tag{B-4.4}$$

the transformed Navier's equation becomes:

$$\bar{u}'' - (N^2 - 1)\, s\, \bar{v}' - (N^2 - M^2)\, s^2\, \bar{u} + (3N^2 - 4)\gamma\, s^2\, \bar{\phi} = 0 \tag{B-4.5}$$

$$N^2\, \bar{v}'' + (N^2 - 1)\, s\, \bar{u}' - (1 - M^2)\, s^2\, \bar{v} - (3N^2 - 4)\gamma\, s\, \bar{\phi}' = 0 \tag{B-4.6}$$

Separating the v term from eq.(B-4.5) and substituting appropriate derivatives of v into eq.(B-4.6) to get the 4th order ordinary differential equation in terms of u and its derivatives only and using simplified variables of

$$j^2 = 1 - M^2,\ k^2 = 1 - \frac{M^2}{N^2},\ h = 3 - \frac{4}{N^2} \tag{B-4.7}$$

the Navier's equilibrium equation becomes:

$$\bar{u}^{IV} - (j^2 + k^2)\, s^2\, \bar{u}'' + j^2 k^2 s^4\, \bar{u} = -h\gamma s^2 (\bar{\phi}'' - j^2 s^2\, \bar{\phi}) \tag{B-4.8}$$

$$\bar{v}^{IV} - (j^2 + k^2)\, s^2\, \bar{v}'' + j^2 k^2 s^4\, \bar{v} = h\gamma s (\bar{\phi}''' - j^2 s^2\, \bar{\phi}') \tag{B-4.9}$$

For mechanical displacement components, the temperature terms are not existent in the above two equations, i.e., homogeneous equations.

The solution of the transformed displacement must be bounded as η goes to infinity due to regularity condition. Thus, the coefficients of positive exponential term vanish and those of negative exponential term remain, hence the coefficients of the solutions are B_i, C_i, i = 1,2.

$$\bar{u}_1^M = B_1 e^{-js\eta} + B_2 e^{-ks\eta} \tag{B-4.10}$$

$$\bar{v}_1^M = C_1 e^{-js\eta} + C_2 e^{-ks\eta} \tag{B-4.11}$$

The unknown four coefficients in eqs. (B-4.10) and (B-4.11) can be obtained using equilibrium equations in eqs. (B-4.8) & (B-4.9) (without thermal terms) and stress boundary conditions.

Substituting eqs.(B-4.10) and (B-4.11) into eqs.(B-4.8) and (B-4.9) respectively without the thermal terms, the relationships between coefficients of B_i and C_i become:

$$C_1 = \frac{B_1}{j},\ C_2 = kB_2 \tag{B-4.12}$$

Taking Fourier integral transform of the Hooke's law in the eqs. (B-3.5) to (B-3.7) to get the transformed stress in terms of the displacements and substituting the variables again using below:

$$\bar{\sigma}_{\xi\xi} = \tilde{\sigma}_{\xi\xi}/s,\ \bar{\sigma}_{\xi\eta} = i\,\tilde{\sigma}_{\xi\eta}/s,\ \bar{\sigma}_{\eta\eta} = \tilde{\sigma}_{\eta\eta}/s,\ \bar{\phi} = \tilde{\phi}/s \tag{B-4.13}$$

the transformed Hooke's law can be written as:

$$\bar{\sigma}_{\xi\xi} = \frac{\mu N^2}{sp_0}\{s\bar{u} + (1 - \frac{2}{N^2})\bar{v}' - h\gamma s\bar{\phi}\} \tag{B-4.14}$$

$$\bar{\sigma}_{\eta\eta} = \frac{\mu N^2}{sp_0}\{(1 - \frac{2}{N^2})s\bar{u} + \bar{v}' - h\gamma s\bar{\phi}\} \quad \text{(B-4.15)}$$

$$\bar{\sigma}_{\xi\eta} = \frac{\mu}{sp_0}(\bar{u} - s\bar{v}) \quad \text{(B-4.16)}$$

Substituting eqs.(B-4.10), (B-4.11) and (B-4.12) into eqs.(B-4.14) ~ (B-4.16) and neglecting thermal terms for mechanical stresses, the transformed mechanical stress fields are obtained as:

$$\bar{\sigma}^M_{\xi\xi 1} = \frac{\mu}{p_0}\{2B_1 e^{-js\eta} + (M^2 + 2k^2)B_2 e^{-ks\eta}\} \quad \text{(B-4.17)}$$

$$\bar{\sigma}^M_{\eta\eta 1} = -\frac{\mu}{p_0}\{2B_1 e^{-js\eta} + (2 - M^2)B_2 e^{-ks\eta}\} \quad \text{(B-4.18)}$$

$$\bar{\sigma}^M_{\xi\eta 1} = -\frac{\mu}{p_0}\{(j + \frac{1}{j})B_1 e^{-js\eta} + 2kB_2 e^{-ks\eta}\} \quad \text{(B-4.19)}$$

In order to obtain the coefficients B_1 and B_2, the stress boundary conditions of eqs. (B-3.8) and (B-3.9) may be applied. Taking Fourier integral transform of the stress boundary conditions with respect to ξ, the transformed boundary conditions become:

$$\left[\tilde{\sigma}^M_{\xi\eta}\right]_{\eta=0} = \mu_f \int_{-\infty}^{\infty} \frac{p(\xi)}{p_0} e^{-is\xi}\, d\xi \quad \text{(B-4.20)}$$

$$\left[\tilde{\sigma}^M_{\eta\eta}\right]_{\eta=0} = -\int_{-\infty}^{\infty} \frac{p(\xi)}{p_0} e^{-is\xi}\, d\xi \quad \text{(B-4.21)}$$

For the constant pressure distribution, i.e., $p(\xi) = p_0$, the unknown coefficients B_1 and B_2 can be manipulated by substituting eqs. (B-4.20) and (B-4.21) into eqs. (B-4.18) and (B-4.19) as:

$$B_1 = -\frac{2i\, p_0 \sin s}{\mu s^2} \frac{\left[(2 - M^2)\mu_f - 2ki\right]}{\left[\left(j + \frac{1}{j}\right)(2 - M^2) - 4k\right]} \tag{B-4.22}$$

$$B_2 = -\frac{2i\, p_0 \sin s}{\mu s^2} \frac{\left[\left(j + \frac{1}{j}\right) i - 2\mu_f\right]}{\left[\left(j + \frac{1}{j}\right)(2 - M^2) - 4k\right]} \tag{B-4.23}$$

By substituting the coefficients above into appropriate mechanical displacement and stress, the transformed quantities can be obtained.

B.4.2 Temperature Fields

B.4.2.1 Energy Partition at the Contact Interface. For the determination of the partition of the frictional energy at the interface, Blok's conjecture may be invoked. The steady state temperature distribution in the moving body due to a point heat source q(x', z') released at (x', z') can be written as [Jaeger, 1942]:

$$dT = \frac{q\, dx'\, dz'}{2\pi K r} \exp\left[-\frac{V}{2\kappa}\{r - (x - x')\}\right] \tag{B-4.24}$$

where

$$r = \sqrt{(x - x')^2 + (z - z')^2} \tag{B-4.25}$$

The temperature field at $z = 0$ along x-direction due to the heat flux $q = q_0$ becomes:

$$T(x) = \frac{q_0}{2\pi K} \int_{z'=-b}^{z'=b} \int_{x'=-l}^{x'=l} \frac{1}{r} \exp[-\frac{V}{2\kappa}\{r - (x - x')\}] \, dx'dz' \qquad \text{(B-4.26)}$$

Non-dimensionalizing the quantities using

$$\phi = \frac{TK}{q_0 l}, \xi = \frac{x}{l}, \xi' = \frac{x'}{l}, \zeta' = \frac{z'}{l}, Pe = \frac{Vl}{\kappa}, B = \frac{b}{l} \qquad \text{(B-4.27)}$$

the normalized temperature becomes:

$$\phi(\xi) = \frac{1}{2\pi} \int_{-B}^{B} \int_{-1}^{1} \frac{\exp[-\frac{Pe}{2}\{\sqrt{(\xi - \xi')^2 + \zeta'^2} - (\xi - \xi')\}]}{\sqrt{(\xi - \xi')^2 + \zeta'^2}} \, d\xi'd\zeta' \qquad \text{(B-4.28)}$$

Considering the energy partition, let (q_0 R) go into the stationary body and q_0(1 - R) flow into the moving body, and using the normalized temperature for the two body system as:

$$\phi_w = \frac{TK_w}{q_0 l}, \phi_t = \frac{TK_t}{q_0 l} r_K \qquad \text{(B-4.29)}$$

where $r_K = K_w/K_t$ is the ratio of the thermal conductivities of the body in contact. The normalized temperature fields of the stationary tool and the moving workpiece can be written as:

$$\phi_t(\xi) = \frac{1}{2\pi} \int_{-B}^{B} \int_{-1}^{1} \frac{R(\xi) r_K}{\sqrt{(\xi - \xi')^2 + \zeta'^2}} \, d\xi'd\zeta' \qquad \text{(B-4.30)}$$

$$\phi_w(\xi) = \frac{1}{2\pi} \int_{-B}^{B} \int_{-1}^{1} \frac{\{1 - R(\xi)\}\exp[-\frac{Pe}{2}\{\sqrt{(\xi - \xi')^2 + \zeta'^2} - (\xi - \xi')\}]}{\sqrt{(\xi - \xi')^2 + \zeta'^2}} d\xi' d\zeta' \quad \text{(B-4.31)}$$

Assuming that the contact is conformal at the interface and the temperatures at the interface are the same for the tool and workpiece:

$$\phi_w(\xi) = \phi_t(\xi) \text{ at } \eta = 0 \quad \text{(B-4.32)}$$

the energy partition R which goes into the tool can be obtained and is shown in eq. (6-12).

B.4.2.2 Temperature Fields. Taking the Fourier integral transform of eq. (B-3.13), the governing equation of the temperature field for the moving body can be obtained as:

$$\frac{d^2\tilde{\phi}}{d\eta^2} - (1 + \frac{i\,Pe}{s})\, s^2\tilde{\phi} = 0 \quad \text{(B-4.33)}$$

Using the quantities below:

$$\beta^2 = 1 + \frac{i\,Pe}{s},\ \bar{\phi} = \frac{\tilde{\phi}}{s},\ ' = \frac{\partial}{\partial\eta} \quad \text{(B-4.34)}$$

Eq. (B-4.33) can be simplified as:

$$\bar{\phi}'' - \beta^2 s^2 \bar{\phi} = 0 \quad \text{(B-4.35)}$$

The solution can be written as:

$$\bar{\phi} = A_0 e^{-bs\eta} \quad \text{(B-4.36)}$$

Due to the regularity condition, only the negative exponential term remains. The unknown coefficient A_0 can be obtained using heat flux boundary condition in eq.(B-3.14). Taking the Fourier integral transform of the boundary conditions as:

$$-\left[\frac{\partial\tilde{\phi}}{\partial\eta}\right]_{\eta=0} = \int_{-\infty}^{\infty} q(\xi)e^{-is\xi}d\xi \qquad \text{(B-4.37)}$$

Considering the heat partition R and the boundary conditions, the coefficient A_0 in eq. (B-4.36) can be obtained as:

$$A_0 = \frac{i}{\beta s^3} e^{is}(1 - e^{is\Delta\xi})\sum_{l=1}^{n}(1 - R_l)e^{-is\Delta\xi l} \qquad \text{(B-4.38)}$$

where n is the number of piecewise linear segments in ξ = [-1, 1] interval where heat flux is applied at the contact and $\Delta\xi$ is the length of each segment.

Similar to the moving body, the temperature of the stationary body may be written as:

$$\frac{d^2\tilde{\phi}}{d\eta^2} - s^2\tilde{\phi} = 0 \qquad \text{(B-4-39)}$$

and the solution can be given as:

$$\bar{\phi} = Ae^{-s\eta} \qquad \text{(B-4.40)}$$

By applying the boundary condition in eq. (B-4.37), the coefficient A in eq. (B-4.40) can be obtained as:

$$A = \frac{i}{s^2} e^{is}(1 - e^{is\Delta\xi}) \sum_{l=1}^{n} R_l e^{-is\Delta\xi l} \qquad \text{(B-4.41)}$$

B.4.3 Thermal Displacement and Stress Fields

The solutions of thermal displacement and stress fields are the sum of the homogeneous solution and the particular solution. Due to the difference in the boundary conditions from the mechanical displacement, the coefficients in the homogeneous solution must be redefined.

Substituting eq. (B-4.36) into the right hand sides of the eqs. (B-4.8) and (B-4.9), the right-hand sides of the expressions become:

$$-h\gamma s^2(\bar{\phi}'' - j^2 s^2 \bar{\phi}) = h\gamma s^4 A_0(j^2 - \beta^2)e^{-\beta s\eta} \qquad \text{(B-4.42)}$$

$$h\gamma s(\bar{\phi}''' - j^2 s^2 \bar{\phi}') = h\gamma s^4 A_0 \beta(j^2 - \beta^2)e^{-\beta s\eta} \qquad \text{(B-4.43)}$$

Let particular solution of eqs. (B-4.8) and (B-4.9) with the right-hand sides substituted with eqs. (B-4.42) and (B-4.43) be:

$$\bar{u}_p = D_0 e^{-\beta s\eta}, \; \bar{v}_p = E_0 e^{-\beta s\eta} \qquad \text{(B-4.44)}$$

Substituting eq. (B-4.44) into eqs. (B-4.8) and (B-4.9), the coefficients D_0, E_0 can be replaced by A_0 as:

$$D_0 = \frac{h\gamma A_0}{(k^2 - \beta^2)}, \; E_0 = \frac{h\gamma\beta A_0}{(k^2 - \beta^2)} \qquad \text{(B-4.45)}$$

Together with the particular and homogeneous solutions, the general thermal displacement solution can be written as:

$$\bar{u}_1^T = \bar{u}_h + \bar{u}_p = D_1 e^{-js\eta} + D_2 e^{-ks\eta} + \frac{h\gamma A_0}{(k^2 - \beta^2)} e^{-\beta s\eta} \tag{B-4.46}$$

$$\bar{v}_1^T = \bar{v}_h + \bar{v}_p = E_1 e^{-js\eta} + E_2 e^{-ks\eta} + \frac{h\gamma\beta A_0}{(k^2 - \beta^2)} e^{-\beta s\eta} \tag{B-4.47}$$

where D_i, E_i, i=1,2 are unknown constants. As a general solution, above eqs. (B-4.46) and (B-4.47) must satisfy the equilibrium equations in eqs.(B-4.5) and (B-4.6), and boundary conditions of thermal stress in eqs.(B-3.11) and (B-3.12).

By substituting eqs. (B-4.46) & (B-4.47) into eqs. (B-4.5) & (B-4.6) and from the coefficients of each exponential term, the following relationship between the unknown coefficients can be obtained:

$$E_1 = \frac{D_1}{j}, \; E_2 = kD_2 \tag{B-4.48}$$

In order to apply the thermal stress boundary conditions, thermal stress fields are expressed in terms of thermal displacements by substituting eqs. (B-4.46) ~ (B-4.48) into the Hooke's law in eqs. (B-4.14) ~ (B-4.16) as:

$$\bar{\sigma}_{\xi\xi 1}^T = \frac{\mu}{p_0} \{2D_1 e^{-js\eta} + (M^2 + 2k^2) D_2 e^{-ks\eta} + \frac{h\gamma A_0}{k^2 - \beta^2} (M^2 + 2\beta^2) e^{-\beta s\eta}\} \tag{B-4.49}$$

$$\bar{\sigma}_{\eta\eta 1}^T = -\frac{\mu}{p_0} \{2D_1 e^{-js\eta} + (2 - M^2) D_2 e^{-ks\eta} + \frac{h\gamma A_0}{k^2 - \beta^2} (2 - M^2) e^{-\beta s\eta}\} \tag{B-4.50}$$

$$\bar{\sigma}_{\xi\eta 1}^T = -\frac{\mu}{p_0} \{D_1 (j + \frac{1}{j}) e^{-js\eta} + 2kD_2 e^{-ks\eta} + \frac{2h\gamma\beta A_0}{k^2 - \beta^2} e^{-\beta s\eta}\} \tag{B-4.51}$$

Applying the thermal boundary conditions in eq. (B-3.11), the unknown coefficients D_1 and D_2 can be obtained as:

$$D_1 = \frac{2h\gamma(2-M^2)A_0}{(k+\beta)\{(j+\frac{1}{j})(2-M^2)-4k\}} \tag{B-4.52}$$

$$D_2 = \frac{h\gamma\{4\beta-(j+\frac{1}{j})(2-M^2)\}A_0}{(k+\beta)\{(j+\frac{1}{j})(2-M^2)-4k\}} \tag{B-4.53}$$

B.4.4 Coefficients for $s = -w < 0$ Domain

Taking the similar procedure for the domain of $s = -w < 0$ ($w > 0$), the corresponding coefficients of the conjugate part of the field equations can be obtained. Here w is the negative Fourier variable.

$$B_1' = -\frac{2i\,p_0 \sin w}{\mu w^2}\frac{\left[(2-M^2)\mu_f + 2ki\right]}{\left[\left(j+\frac{1}{j}\right)(2-M^2)-4k\right]} \tag{B-4.54}$$

$$B_2' = \frac{2i\,p_0 \sin w}{\mu w^2}\frac{\left[\left(j+\frac{1}{j}\right)i + 2\mu_f\right]}{\left[\left(j+\frac{1}{j}\right)(2-M^2)-4k\right]} \tag{B-4.55}$$

$$A_0' = \frac{-i}{\bar{\beta}w^3}e^{-iw}(1-e^{-iw\Delta\xi})\sum_{l=1}^{n}(1-R_l)e^{iw\Delta\xi l} \tag{B-4.56}$$

$$\bar{\beta}^2 = 1 - i\frac{Pe}{w} \tag{B-4.57}$$

$$A' = -\frac{i}{w^2}e^{-iw}(1-e^{-iw\Delta\xi})\sum_{l=1}^{n}R_l e^{iw\Delta\xi l} \tag{B-4.58}$$

$$D_1' = -\frac{2h\gamma(2-M^2)A_0'}{(k+\bar{\beta})\{(j+\frac{1}{j})(2-M^2)-4k\}} \tag{B-4.59}$$

$$D_2' = -\frac{h\gamma\{4\bar{\beta}-(j+\frac{1}{j})(2-M^2)\}A_0'}{(k^2-\bar{\beta}^2)\{(j+\frac{1}{j})(2-M^2)-4k\}} \tag{B-4.60}$$

B.5 Inverse Fourier Integral Transform

For the entire domain of the inverse Fourier integral transform of $s > 0$ and $s = -w < 0$, the subdomains must be added up as:

$$f(\xi) = f_1(\xi) + f_2(\xi) = \frac{1}{2\pi}\left[\int_0^\infty \tilde{f}_1(s)e^{is\xi}ds + \int_0^\infty \tilde{f}_2(w)e^{-iw\xi}dw\right] \tag{B-5.1}$$

B.5.1 Mechanical Displacement and Stress Fields

The non-dimensionalized mechanical displacements may be expressed by substituting corresponding functions and coefficients into eq. (B-5.1) and taking real parts.

The mechanical non-dimensionalized displacement fields can be obtained as:

$$u^M(\xi,\eta) = \frac{2p_0}{\pi\mu G_1}\{-(2 - M^2)\mu_f\int_0^\infty \frac{\sin s}{s^2}\cos s\xi e^{-js\eta}ds$$

$$- 2k\int_0^\infty \frac{\sin s}{s^2}\sin s\xi e^{-js\eta}ds$$

$$+ 2\mu_f\int_0^\infty \frac{\sin s}{s^2}\cos s\xi e^{-ks\eta}ds$$

$$+ (j + \frac{1}{j})\int_0^\infty \frac{\sin s}{s^2}\sin s\xi e^{-ks\eta}ds\} \qquad \text{(B-5.2)}$$

$$v^M(\xi,\eta) = \frac{2p_0}{\pi\mu G_1}\{-\frac{2k}{j}\int_0^\infty \frac{\sin s}{s^2}\cos s\xi e^{-js\eta}ds$$

$$+ \frac{(2 - M^2)}{j}\mu_f\int_0^\infty \frac{\sin s}{s^2}\sin s\xi e^{-js\eta}ds$$

$$+ k(j + \frac{1}{j})\int_0^\infty \frac{\sin s}{s^2}\cos s\xi e^{-ks\eta}ds$$

$$- 2k\mu_f\int_0^\infty \frac{\sin s}{s^2}\sin s\xi e^{-ks\eta}ds\} \qquad \text{(B-5.3)}$$

where

$$G_1 = (j + \frac{1}{j})(2 - M^2) - 4k,\ j^2 = 1 - M^2,\quad k^2 = 1 - M^2/N^2 \qquad \text{(B-5.4)}$$

The non-dimensionalized mechanical stress components is shown in eq. (6-11).

B.5.2 Temperature Fields

The non-dimensionalized temperature fields of the workpiece and tool may be written as:

$$\phi_w(\xi,\eta) = \frac{1}{\pi}\int_0^{\infty} \frac{1}{(a+b)s^2}\sum_{m=1}^{n}(1-R_m)[\sqrt{a}\{\sin s(x_1+\Delta\xi) - \sin sx_1\} + \sqrt{b}\{\cos sx_1 - \cos s(x_1+\Delta\xi)\}]e^{-\sqrt{a}s\eta}\,ds \qquad \text{(B-5.5)}$$

$$\phi_t(\xi,\eta) = \frac{1}{\pi}\int_0^{\infty} \frac{1}{s}\sum_{m=1}^{n} R_m\{\sin s(x_2+\Delta\xi) - \sin sx_2\}e^{-s\eta}ds \qquad \text{(B-5.6)}$$

where a and b are represented in terms of β and $\bar{\beta}$ which are the conjugates each other, and β can be separated into real and imaginary parts as:

$$\beta = \sqrt{a} + i\sqrt{b} = \sqrt{\frac{1+\sqrt{1+(Pe/s)^2}}{2}} + i\sqrt{\frac{(Pe/s)^2}{2(1+\sqrt{1+(Pe/s)^2})}} \qquad \text{(B-5.7)}$$

and $$x_1 = 1 - m\Delta\xi - \sqrt{b}\eta + \xi,\ x_2 = 1 - m\Delta\xi + \xi$$

$\Delta\xi$ is the length of each segment in heat flux boundary, m is the sequential number of the total n segments in ξ = [-1,1].

B.5.3 Thermal Displacement and Stress Fields

Similar to the previous derivations, normalized thermal displacement can be written as:

$$u^T(\xi,\eta) = \frac{1}{\pi}\int_0^\infty [F_{D1}(R_{D1}\sin s\xi + I_{D1}\cos s\xi)e^{-js\eta} + F_{D2}(R_{D2}\sin s\xi + I_{D2}\cos s\xi)e^{-ks\eta} + F_{D3}\{-R_{D3}\sin s(\sqrt{b}\eta - \xi) + I_{D3}\cos s(\sqrt{b}\eta - \xi)\}e^{-\sqrt{a}s\eta}]\, ds \quad \text{(B-5.8)}$$

$$v^T(\xi,\eta) = \frac{1}{\pi}\int_0^\infty [\frac{F_{D1}}{j}(R_{D1}\cos s\xi - I_{D1}\sin s\xi)e^{-js\eta} + kF_{D2}(R_{D2}\cos s\xi - I_{D2}\sin s\xi)e^{-ks\eta} + F_{D3}\{R_{D4}\cos s(\sqrt{b}\eta - \xi) + I_{D4}\sin s(\sqrt{b}\eta - \xi)\}e^{-\sqrt{a}s\eta}]\, ds \quad \text{(B-5.9)}$$

The non-dimensionalized thermal stress fields may be obtained by substituting the displacement into the Hooke's law. The thermal stress fields are shown in eq. (6-14). The coefficients in the equations are defined as:

$$A_0 = F_A(R_A + iI_A),\ A_0' = F_A(R_A - iI_A)$$

$$F_A = \frac{1}{(a+b)s^3}$$

$$R_A = \sum_{m=1}^{n} (1 - R_m)[\sqrt{a}\{\sin s(1 + \Delta\xi - m\Delta\xi) - \sin s(1 - m\Delta\xi)\} + \sqrt{b}\{\cos s(1 - m\Delta\xi) - \cos s(1 + \Delta\xi\Pi - m\Delta\xi)\}]$$

$$I_A = \sum_{m=1}^{n} (1 - R_m)[\sqrt{a}\{\cos s(1 - m\Delta\xi) - \cos s(1 + \Delta\xi - m\Delta\xi)\} + \sqrt{b}\{\sin s(1 + \Delta\xi - m\Delta\xi) - \sin s(1 - m\Delta\xi)\}]$$

$$D_1 = F_{D1}(R_{D1} + iI_{D1}),\ D_1' = -F_{D1}(R_{D1} - iI_{D1})$$

$$F_{D1} = \frac{2h\gamma(2 - M^2)F_A}{G_1\{(k + \sqrt{a})^2 + b\}}$$

$$R_{D1} = (k + \sqrt{a})R_A + \sqrt{b}\, I_A\}, \; I_{D1} = (k + \sqrt{a})I_A - \sqrt{b}\, R_A\}$$

$$D_2 = F_{D2}(R_{D2} + iI_{D2}), \; D_2' = - F_{D2}(R_{D2} - iI_{D2})$$

$$F_{D2} = \frac{h\gamma F_A}{G_1\{(k^2 - 1)^2 + 4ab\}}$$

$$R_{D2} = \{(4\sqrt{a} - G_1 - 4k)(k^2 - 1) - 8b\sqrt{a}\}R_A$$
$$- \{4\sqrt{b}(k^2 - 1) + 2\sqrt{ab}(4\sqrt{a} - G_1 - 4k)\}I_A$$

$$I_{D2} = \{(4\sqrt{a} - G_1 - 4k)(k^2 - 1) - 8b\sqrt{a}\}I_A$$
$$+ \{4\sqrt{b}(k^2 - 1) + 2\sqrt{ab}(4\sqrt{a} - G_1 - 4k)\}R_A$$

$$D_3 = F_{D3}(R_{D3} + iI_{D3}), \; D_3' = F_{D3}(R_{D3} - iI_{D3})$$

$$F_{D3} = \frac{h\gamma F_A}{\{(k^2 - 1)^2 + 4\sqrt{ab}\}}$$

$$R_{D3} = (k^2 - 1)R_A - 2\sqrt{ab}I_A, \; I_{D3} = (k^2 - 1)I_A + 2\sqrt{ab}R_A$$

$$D_4 = F_{D3}(R_{D4} + iI_{D4}), \; D_4' = F_{D3}(R_{D4} - iI_{D4})$$

$$R_{D4} = \sqrt{a}R_{D3} - \sqrt{b}I_{D3}, \; I_{D4} = \sqrt{a}I_{D3} + \sqrt{b}R_{D3}$$

$$D_5 = F_{D3}(R_{D5} + iI_{D5}), \; D_5' = F_{D3}(R_{D5} - iI_{D5})$$

$$R_{D5} = (2 + M^2)R_{D3} - 4\sqrt{ab}I_{D3}$$

Finally, the combined total normalized displacement u_i and stress fields σ_{ij} are the summation of the fields due to the mechanical and thermal stresses.

$$u_i = u_i^M + u_i^T \tag{B-5.10}$$

$$\sigma_{ij} = \sigma_{ij}^M + \sigma_{ij}^T \tag{B-5.11}$$

B.6 Numerical Analysis

The expression of the displacement and stress fields contain infinite range for the integration with exponential terms. In this case Gauss-Laguerre formula can be used, which is defined as:

$$\int_0^\infty e^{-x} f(x)\, dx \approx \sum_{i=1}^{N} A_i f(x_i) \tag{B-6.1}$$

where A_i and x_i are the Gauss-Laguerre weight and abscissa respectively and N is the number of Gauss-Laguerre points to be employed. For 6 and 10 points of N, the abscissa and weights are shown in Table B-1 together with those of Gaussian quadrature.

The mechanical elastodynamic, elastoplastic stress fields, energy partition and temperature fields are computer coded and the flow chart for the program is shown in Fig. B-1.

TABLE B-1

ABSCISSA AND WEIGHTS FOR GAUSSIAN AND GAUSS-LAGUERRE QUADRATURE

Gaussian Quadrature		Gauss- Laguerre	
6 Points			
H	W	x_i	A_i
-0.9324695142	0.1713244924	0.22284660	0.45896467
-0.6612093865	0.3607615730	1.18893210	0.41700083
0.2386191861	0.4679139346	2.99273633	0.11337338
0.2386191861	0.4679139346	5.77514357	0.01039920
0.6612093865	0.3607615730	9.83746742	0.00026102
0.9324695142	0.1713244924	15.98287398	0.00000090
10 Points			
-0.9739065285	0.0666713443	0.13779347	0.30844112
-0.8650633667	0.1494513492	0.72945455	0.40111993
-0.6794095683	0.2190863625	1.80834290	0.21806829
-0.4333953941	0.2692667193	3.40143370	0.06208746
-0.1488743390	0.2955242247	5.55249614	0.00950152
0.1488743390	0.2955242247	8.33015275	0.00075301
0.4333953941	0.2692667193	11.84378584	0.00002826
0.6794095683	0.2190863625	16.27925783	0.00000042
0.8650633667	0.1494513492	21.99658581	0.00000000
0.9739065285	0.0666713443	29.92069701	0.00000000

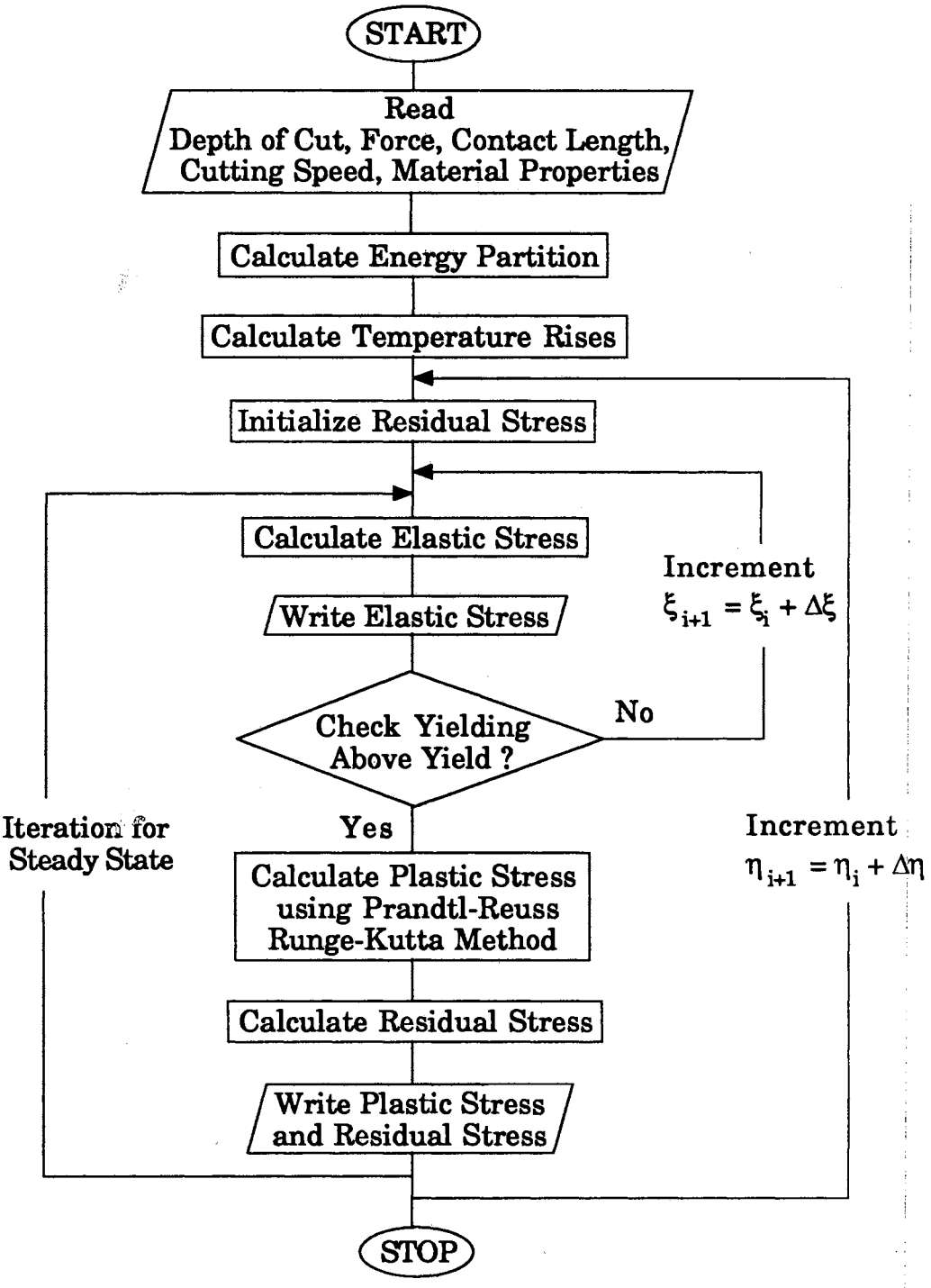

Figure B-1. Flow Chart of the Computer Program for Elastoplastic Stress Fields

VITA

Yongwie Seo

Candidate for the Degree of

Doctor of Philosophy

Thesis : ENERGY DISSIPATION IN ORTHOGONAL ULTRA-PRECISION MACHINING OF DUCTILE MATERIALS

Major Field : Mechanical Engineering

Biographical :

Personal Data : Born in Korea, November 23, 1954, the son of Jongsup Seo and Insoon Moon.

Education : Graduated from Korea University, Seoul, Korea, in February 1976; received Bachelor of Engineering in Mechanical Engineering from the Korea University, Seoul, Korea; Graduated from the Ohio State University, Columbus, Ohio, in May 1990; received Master of Science in Engineering Mechanics from the Ohio State University, Columbus, Ohio; completed requirements for the Doctor of Philosophy degree at Oklahoma State University in May, 1993.

Professional Experience : Research Engineer, the Agency for Defence Development, Taejon, Korea, March 1976 to August 1983.
Visiting Research Engineer, Army Materials Mechanics Research Center, Watertown, Massachusetts, September 1983 to August 1984.
Senior Research Engineer, the Agency for Defence Development, Taejon, Korea, September 1984 to August 1987.
Research Assistant, Department of Engineering Mechanics, the Ohio State University, September 1987 to May 1990.
Research Assistant, Department of Mechanical Engineering, Oklahoma State University, July 1990 to May 1993.